A Structural Approach to Reveal the Cryoprotective Action of Glycerol

James Joseph Towey

School of Physics and Astronomy

University of Leeds

Submitted in accordance with the requirements for the degree of

Doctor of Philosophy

September 2013

Declaration

The candidate confirms that the work submitted is his own, except where work which has formed part of jointly authored publications has been included. The contribution of the candidate and the other authors to this work has been explicitly indicated below. The candidate confirms that appropriate credit has been given within the thesis where reference has been made to the work of others. Chapters 3, 4 and 5 are based on the results of previously published work jointly authored by the candidate (see the bibliography below). The neutron diffraction experiments were devised by Dr Lorna Dougan and completed by Dr Lorna Dougan and Prof Alan Soper. The analysis of the data was performed by the candidate with the support of Dr Lorna Dougan and Prof Alan Soper. The articles were written by the candidate and Dr Lorna Dougan. This copy has been supplied on the understanding that it is copyright material and that no quotation from the thesis may be published without proper acknowledgement.

Bibliography

(1) J.J. Towey, A.K. Soper, and L. Dougan, The structure of glycerol in the liquid state: A neutron diffraction study, *Physical Chemistry Chemical Physics*, **13**(20), pp. 9397-9406 (2011).

(2) J.J. Towey, A.K. Soper, and L. Dougan, Preference for isolated water molecules in a concentrated glycerol-water mixture, *Journal of Physical Chemistry B*, **115**(24), pp. 7799-7807 (2011).

(3) J.J. Towey and L. Dougan, Structural examination of the impact of glycerol on water structure, *Journal of Physical Chemistry B*, **116**(5), pp. 1633-1641 (2012).

(4) J.J. Towey, A.K. Soper, and L. Dougan, Molecular insight into the hydrogen bonding and micro-segregation of a cryoprotectant molecule, *Journal of Physical Chemistry B* **116**(47), pp. 13898-13904 (2012).

(5) J.J. Towey, A.K. Soper, and L. Dougan, What happens to the structure of water in cryoprotectant solutions?, *Faraday Discussions*, **167**(Accepted Manuscript) (2013). **DOI:** 10.1039/C3FD00084B

This thesis is dedicated to the loving memory of Mary Towey.

Acknowledgements

Abstract

Glycerol-water liquid mixtures are intriguing hydrogen-bonded systems that are essential to many fields; from basic molecular research to their wide spread use in industrial and biomedical applications as cryoprotective solutions. This thesis details a study of the structure and bonding of this important system as a function of concentration and temperature. Here, aqueous glycerol has been investigated using a combination of neutron diffraction and computational modelling.

When studying pure liquid glycerol no evidence for intra-molecular hydrogen bonding is found. It is shown that, contrary to previous theories, water-glycerol hydrogen bonds compensate for the loss of water-water hydrogen bonds with increasing glycerol concentration. The molecular scale clustering of the system is also investigated. It is found that there is a preference for isolated water molecules in a concentrated glycerol-water mixture and for monomeric glycerol molecules in dilute aqueous glycerol. At intermediate concentrations, the system forms a structure with percolating clusters of both glycerol and water. Interestingly, this bi-percolating structure is found over the concentration range at which many extremes of thermodynamic functions are found.

On cooling, the water network adopts a more tetrahedral structure that is more ice-like. However, the molecular scale clustering persists as the system is cooled. It is, therefore, proposed that it is the mixing characteristics that allow glycerol-water systems to form a structure that prevents extended water network formation. It is likely that it is this structuring that retards ice formation as the temperature is lowered.

Contents

List of Figures

List of Tables

Abbreviations

Length Scales
m   One metre
mm 1×10^{-3}m
μm 1×10^{-6}m
nm 1×10^{-9}m
Å 1×10^{-10}m
barn $100 \times fm^2$

Energy Scales
eV   One electron volt $= 1.602 \times 10^{-19}$J
meV 1×10^{-3} eV
keV 1×10^{3} eV
MeV 1×10^{6} eV

Other Solutes
DMSO   Dimethyl Sulfoxide
Tert-Butanol   Tertiary butanol
TMAO   Trimethylamine oxide

General Abbreviations
ATLAS   Analysis of Time-of-flight diffraction data
                               from Liquid and Amorphous Samples
DFT   Density Functional Theory
EPSR   Empirical Potential Structure Refinement
IR   Infra Red (light with a wavelength of 700 nm - 1 mm)
LJP   Lennard-Jones Potential
MC   Molecular Dynamics Simulation
MD   Monte Carlo Simulation
RDF   Radial Distribution Function
SANDALS   Small Angle Neutron Diffractometer for
                               Amorphous and Liquid Samples

J   Joules
k_B Boltzmann's constant
$k_B T$ Thermal energy
K   Degree Kelvin (equal to °C + 273.15)
wt %   Weight percent

Chapter 1

Introduction

Liquid water is ubiquitous, important in all aspects of life, from protein structure to quenching thirst. An understanding of the structure of the liquid state and the interactions between the solvent and solute are fundamental to unravelling the mysteries of life and all biologically relevant processes. Significant amongst these liquids are water and aqueous mixtures. Attempts to understand the properties of aqueous systems require that the interactions between water and the molecules that are found in aqueous mixtures are investigated. This thesis explores the properties of one of these important solutes, glycerol. Recent advances in experimental techniques allow unprecedented structural information to be found. This allows the structure of liquid and amorphous samples to be probed at the atomistic level. These structural investigations can be used to explore the molecular scale interactions within these liquids. An understanding of the structure and bonding that is found in important liquid samples can be used to further the insight into these essential fluids. Therefore, this thesis details a study of the structure of aqueous glycerol with the aim of explaining the relationships between structure and function.

1.1 Background

Glycerol (also known as glycerine) contains three carbon atoms each bonded to a hydroxyl group containing one oxygen and one hydrogen atom. Therefore, glycerol is part of a class of molecules known as sugar alcohols[1]. Glycerol has been of significant sci-

---

[1] All sugar alcohols have the formula $H[CHOH]_nH$ such as methanol (CH_3OH) ethylene glycol ($CH_2OH\ CH_2OH$) and glycerol ($CH_2OH\ CHOH\ CH_2OH$).

entific and industrial interest for many years. This attention has, in part, been due to glycerol's ability to form a glass (6). Here, a glass is a viscous liquid that has been cooled sufficiently quickly to avoid crystallisation to the point where its dynamic viscosity becomes larger than 10^{12} Pa s (7). Glycerol is used by a broad range of different types of organisms. These include bacteria, desert plants, fish, insects, reptiles, and yeast (8). The use of glycerol in these organisms is thought to be due to it maintaining the structure of biological macromolecules and promoting self-assembly through preferential hydration (9). Significantly, glycerol is often used as a cryoprotectant molecule (see Sections 1.1.2 and 1.1.3). Indeed, it was one of the first cryoprotectants to be identified (10).
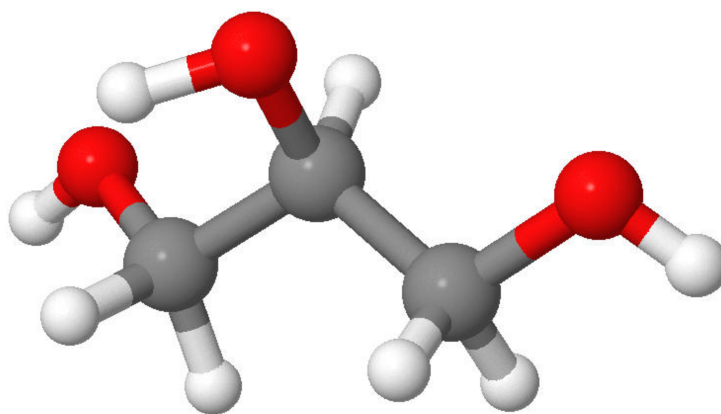
Figure 1.1: A ball and stick diagram showing the glycerol molecule.

The importance of glycerol is discussed in detail in Sections 1.1.1 and 1.1.2. There follows a section describing liquids and liquid structure in general, with emphasis placed on the interactions within liquids (Section 1.2.3) and an introduction to radial distribution functions (RDF). Here, RDFs are used to quantify liquid structure (see Section 1.2.2). The methods that have been used to access liquid structure are introduced in Section 1.3, with some recent studies reviewed in Section 1.4. Finally, the aims and objectives of the work within this thesis are described in Section 1.5.

1.1.1   The Importance of Glycerol and its Aqueous Solutions

Glycerol receives a great deal of interest from an industrial perspective due to its high viscosity (11; 12) and hygroscopic (6) properties. In the pharmaceutical and medical

fields glycerol is used in cough syrups, medicine capsules, topical lotions and lozenges to improve their smoothness and moisturising properties. Glycerol is used as a component for the production of larger polymers (such as polyglycerol methacrylates) that are used in wood treatment and as lubricants. Toiletries and cosmetic products also often include glycerol as an emollient (13).

A recent increase in the interest in glycerol has stemmed from the decrease in the price of glycerol (see Figure 1.2). This is due to the production of biodiesel via transesterification. This process begins with the fats taken from plants and animals, known as triglycerides. These molecules contain a glycerol head group bonded to three long chain fatty acids. The fatty acids are separated from the glycerol to produce the long chain molecules required for use as biodiesel. Therefore, the glycerol that is produced is a bi-product.
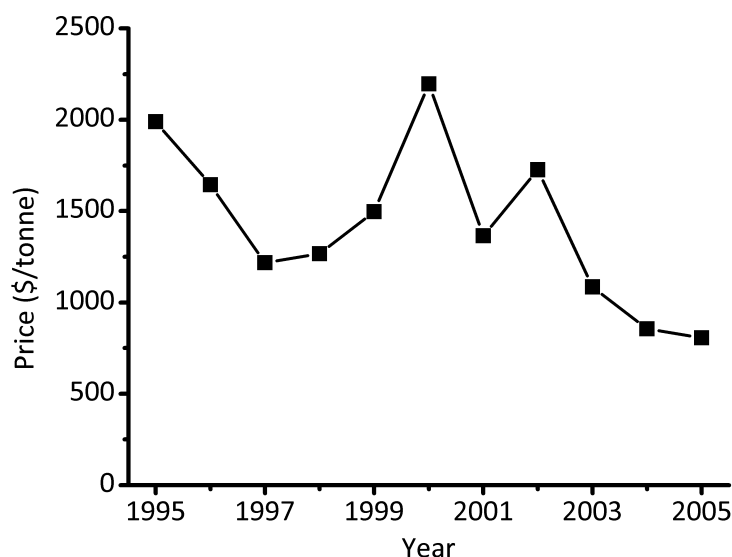
Figure 1.2: Graph showing the changes in the US market price of 99.5% pure glycerol over recent years. A clear downward trend can be seen with the price per tonne falling from the 1995 value of around $2,000 to around $800 in 2005. This decrease in price is a driving factor behind the growing interest in glycerol. The data used to produce this plot are taken from previously published data (13).

The decrease in the cost of glycerol shown in Figure 1.2 has lead to new uses of glycerol being suggested (14–18). Different methods have been proposed to convert glycerol to an ether molecule. Here, an ether molecule contains a carbon-oxygen-carbon bond. It is suggested that these ethers be used as additives for biodiesel or standard diesel (14). It has also been proposed that glycerol could be used to produce either a

solid fuel or mixed with gasoline to produce a spark ignition fuel (15).

The potential uses of glycerol go beyond being a fuel. Another potential use of glycerol is as a feedstock for micro-organisms (such as yeast, fungi and bacteria) to produce useful chemicals such as 1,3-propanediol, 2,3-butanediol, ethanol, n-butanol, organic acids, polyols and many others (17). The crude glycerol by-product from biodiesel production can also be used as a feedstuff for animals including pigs and lambs (18). This is not surprising, as glycerol is also used as an additive in human food. By commercialising such uses of glycerol, it should be possible to further reduce the price of biodiesel production (16). One longstanding industrial use of glycerol is as a cryoprotectant. Indeed, the earliest deliberate addition of a molecule to aid in cryoprotection utilised glycerol (10). This is discussed in greater detail in the following section.

1.1.2 Cryopreservation

Many people use cooling to aid preservation on an everyday basis. For example, putting milk in the refrigerator means that it can be stored for an increased length of time. Physically, this can be quantified using an empirical relationship known as the Arrhenius equation (19),

$$k = Ae^{-\frac{E_a}{k_B T}} \tag{1.1}$$

where k is the rate of the reaction and will have the same units as the pre-factor A, E_a is activation energy, k_B is Boltzmann's constant and T is the temperature in Kelvin. From Equation 1.1 it can be seen that an increase in T will cause a decrease in $\frac{E_a}{k_B T}$. This makes $e^{-\frac{E_a}{k_B T}}$ larger, and therefore the rate of reaction must increase. Similarly, decreasing the temperature decreases the rate of the reaction. Therefore, Equation 1.1 shows that the rate of a reaction can be altered by changing the temperature. This is the motivation behind the use of cooling to extend the storage life of products and samples.

Low temperatures have been used for over 60 years to store biological molecules such as semen (10) and oocytes (20)[1]. These samples are stored at temperatures lower than 200 K in a process known as cryopreservation. This allows the biological samples to be stored over the time-scale of years. Samples that are cryopreserved are often in

---

[1]Oocytes are immature unfertilised ova (egg cells).

an aqueous state (21). Therefore, moving below the freezing temperature of water can cause new problems for the viability of the sample in question. There are two main challenges for effective cryoprotection, both of which are associated with the formation of ice.

When preserving biological molecules or tissues, ice crystals are thought to form first in the extracellular medium surrounding the cells (21). This means that initially ice is formed around cells rather than inside them. This has the effect of significantly increasing the concentration of the solutes around a cell as water is locked away as ice. This increases the osmotic pressure between the cell and its surroundings[1]. As the cells are now surrounded by highly concentrated solutions, the cells lose water to their surroundings by osmosis. This effect is known as freeze dehydration and leads to damage via an increase in the solute (often salt) concentrations within the cell. The other main damaging event caused by water crystallisation in tissue samples is due to intra-cellular ice formation. The mechanism here is less clear, but may include disruption of the sub-units of the cell (organelles) or the cell membrane (22) due to the expansion of water as it forms ice. Here, the cell membrane is a semi-permeable layer that separates the interior of a cell from its surroundings. These damaging factors can be limited by the inclusion of molecules known as cryoprotectants (10). The following section details theories that have been proposed as explanations of the behaviour of these cryoprotectant molecules.

1.1.3 Glycerol as a Cryoprotectant

The discovery of glycerol as a cryoprotectant was made by Polge *et al.* in the 1940s (10). In their work they cooled samples of spermatozoa to 194 K in different buffer solutions with varying concentrations of glycerol. After these samples were thawed the viability of the sperm was measured using a microscope to study their mobility. It was found that the addition of glycerol concentrations of up to 30 wt% lead to increased viability of spermatozoa after thawing (10). This work was followed by a study of the cryoprotective action of glycerol on red blood cells (23). Here, Smith showed that red blood cells that were cooled to 194 K and held there for an hour before re-heating to 313 K showed marked haemolysis when the glycerol concentration was less than 5 wt%.

---

[1]Osmosis is the process by which solvent molecules cross a semi-permeable membrane towards a region of higher solute concentration in order to equalise the solute concentration either side of the membrane.

Here, haemolysis refers to the rupture of red blood cells. However, when the glycerol concentration was increased to 15 wt% glycerol little haemolysis was present (23). Smith also showed that these red blood cells could be stored for up to 3 months at 194 K in a glycerol solution and still maintain their shape. Since these seminal works glycerol has been used as a cryoprotectant in many systems (24). Despite the widespread use of glycerol, the molecular mechanisms behind its action are yet to be elucidated. This lack of understanding is a limiting factor to the future development of cryopreservation protocols. However, there are some qualitative descriptions of the methods employed by cryoprotective molecules that have been suggested.

James Lovelock proposed an early theory regarding cryoprotective action of glycerol (25). He measured the effect of NaCl concentration on the haemolysis of red blood cells when they are cooled. However, when glycerol was added to the solutions much higher salt concentrations could be tolerated by the red blood cells (25). From this work, Lovelock argued that glycerol may reduce the osmotic stress by preventing the high concentrations of solutes within the cells and thus prevent haemolysis (25). Later work by Nash attempted to qualitatively describe the quality of a cryoprotectant using its "protectant coefficient " (26). Here, Nash's coefficient was calculated based on the solubility and molar volumes of different solutes. This work was a useful step forward as it was the earliest attempt to use physical chemistry knowledge to quantify the ability of a cryoprotectant. However, the use of Nash's "protectant coefficient" is limited, as it does not include important factors. These include, the toxicity of the solute, the structure and mixing of the solution and the rate of cooling/heating.

It has been argued that future improvements in cryoprotection protocols will require an understanding of the fundamental properties of the cryoprotectant biomolecule system (27). Therefore, it is important for the scientific community to move beyond qualitative descriptions of cryoprotection (28). From the early years of the study of cryoprotection, molecules such as glycerol were known as "solute moderators" due to their perceived impact on the structure of water (29). This mind-set has persisted when studying cryoprotective molecules (21). Before discussing ways in which the structure of liquids have been studied, it is important to understand what is meant by the structure of a liquid. The following section provides an introduction to the method that will be used throughout this thesis to define the structure of the liquids studied.

1.2 The Liquid State

1.2.1 Introduction to Liquids

The liquid state can be defined as being intermediate between the gaseous and solid states (30). Both of these states can be approximated closely using either the ideal crystal or ideal gas models. In an ideal crystal, the particles[1] which make up the structure are arranged in a periodic lattice (see Figure 1.3(a)). This regular structure can be defined using the unit cell shown by the square with a side length of a. This unit cell is repeated to build the 3-dimensional crystal structure; therefore, the structure of a pure crystal can be defined using the unit cell. These crystals can be of the order of metres in length. The most significant factor in this ideal crystal model is that structural order is only slightly modified by the thermal motion of the particles. The ideal gas model, however, is dominated by random fluctuations of the particles[2] of the gas due to thermal effects. In an ideal gas, there are no interactions (collisions or repulsion) between the particles and the ideal gas law is obeyed. The ideal gas law is given by,

$$PV = nRT \tag{1.2}$$

where, P is the pressure, V is the volume, n is the number of moles of the substance, R is the gas constant, and, T is the temperature. Equation 1.2 is a good approximation as it holds for gases at high temperatures and low pressures. However, the ideal gas law tends to fail at higher particle densities and at lower temperatures.

In a liquid, the structural effects that dominate the crystal state as well as the thermal interactions of the gas phase must both be included. This leads to a complication when one is aiming to quantify the structure of a liquid. The approach of using a repeating unit cell (as utilised for a crystal) is no longer valid as the structure found in a liquid only extends to the nm scale. The assumption of a lack of interactions between the particles (as used for the ideal gas) is similarly inappropriate. The interactions that are found in the liquid state are introduced in Section 1.2.3. The following section addresses the method that is used to quantify liquid structure. This discussion will begin by considering systems that are either atomic crystals or liquids. The description

---

[1] The word particle is used here as crystals can be either atomic or molecular.
[2] See footnote above.

will end by generalising the treatment to more complex systems.

1.2.2   Quantifying Liquid Structure

As stated in Section 1.2.1 the structure of a perfect crystal can be described fully by the unit cell (see Figure 1.3(a)). This description can be used for macroscopic single crystals. For example the Czochralski process can be used to grow cylinders of monocrystalline silicon of up to 2 m in length. These cylinders, therefore, have atomic scale structure repeated over a length scale of metres. Liquids, however, have structural correlations that typically act over length scales of around 1-2 nm (nine orders of magnitude lower than that found in monocrystalline silicon). A snapshot of the structure of a crystal and liquid are shown in Figures 1.3(a) and 1.3(b) respectively.
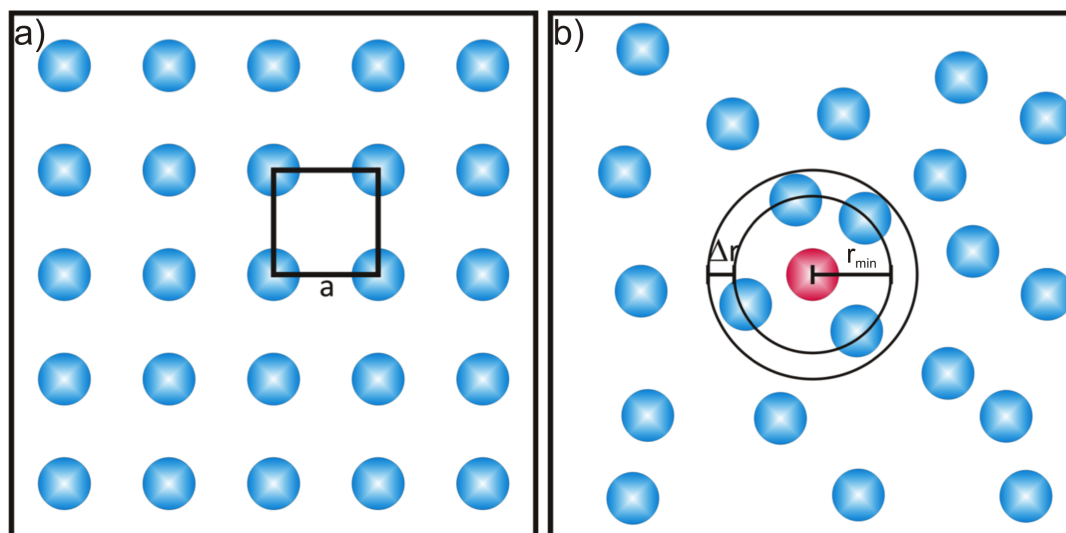
Figure 1.3: Schematic diagram showing the difference between the crystal structure (a) and the structure of a liquid (b). The crystal structure is defined using the unit cell shown with a black square and is repeated to form the macroscopic crystal. The method of quantifying the liquid structure relies on splitting the volume around a central atom into sections Δr as there is no significant long-range structure.

Figure 1.3 shows the difference between the levels of structure in a crystal and liquid sample. The method used to quantify the structure in a liquid is shown by the concentric circles that delineate the volume found in the region Δr in Figure 1.3(b). The circles lie at radial distances of r_{min} and r_{max} where $r_{max} = r_{min} + \Delta r$. The number of atoms found in this volume section is then measured. This is repeated using concentric volume elements at increased radial distances. This is repeated with a different atom used as

the central point, until the distribution around each atom has been found.

These values are used to produce a histogram of the average number of atoms found in each of the volume segments as the radial distance away from the central atom is increased (see Figure 1.4(a)). These values are then normalised by dividing by the distribution that would be found if the atoms were ideally distributed in the system. The ideal distribution is calculated using,

$$\text{Ideal Distribution} = \rho \left(\frac{4}{3} \pi r_{max}^3 - \frac{4}{3} \pi r_{min}^3 \right) \tag{1.3}$$

where ρ is the atomic number density of the system. The radial distribution function is written as $g(r)$ and produced using the following equation,

$$g(r) = \frac{\text{Measured Distribution}}{\text{Ideal Distribution}} \tag{1.4}$$
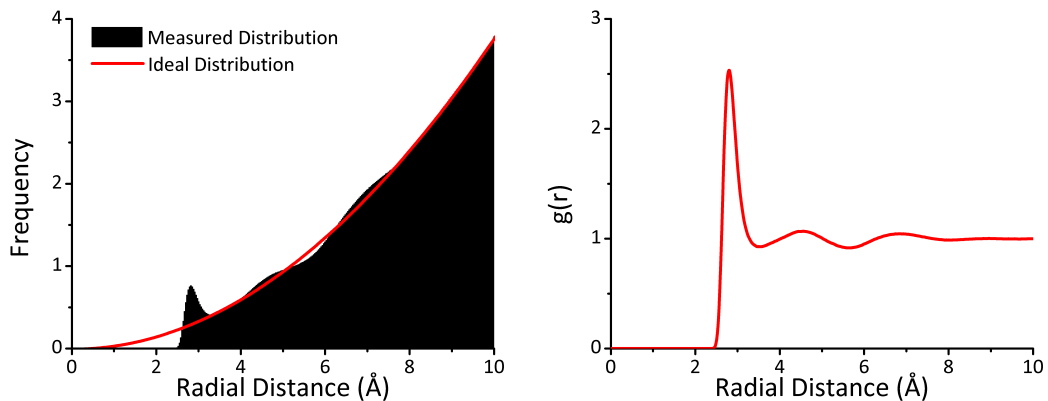
Figure 1.4: A diagram showing the method used to calculate a radial distribution function. (a) The measured atomic distribution is compared to the ideal distribution calculated using Equation 1.3. (b) An example radial distribution function calculated using Equation 1.4.

The radial distribution function given in Figure 1.4(b) shows some important features. The region where $g(r) = 0$ at low radial distances indicates the area where the repulsive nature of the atoms is prevalent. An interesting feature can be found at a separation of around 2.8 Å. This shows the first coordination shell around the central atom for this system. Similarly, the peak at around 4.5 Å indicates the second coordination shell. These peaks indicate the structure found within this particular liquid. As r is increased, $g(r)$ tends to one (Figure 1.4(b)). At these distances, there is a ran-

dom arrangement of atoms and the measured distribution is equal to the ideal atomic distribution (see Figure 1.4(a) and Equation 1.4).

So far, this discussion has been concerned with atomic crystals and liquids. The samples used in this thesis, however, are all molecular in nature. When investigating a molecular system, it is instructive to use partial radial distribution functions, $g_{\alpha\beta}(r)$ to allow the interactions between individual atoms within the molecular liquid to be explored. A partial radial distribution function describes the density of atoms of type β around atoms of type α and is calculated in the manner detailed above with one additional constraint: The species of the atoms that are counted. The calculation of the ideal distribution is modified to become,

$$\text{Ideal Distribution}_\beta = \rho c_\beta \left(\frac{4}{3}\pi r_{min}^3 - \frac{4}{3}\pi r_{max}^3 \right) \tag{1.5}$$

where c_β is fraction of atoms in the system that are of type β. These partial radial distribution functions show levels of structure that are comparable to that found in Figure 1.4(b). Again, the first peak indicates the first coordination shell. The number of atoms within this shell can be found by integration under this peak using,

$$n_{\alpha\beta} = 4\pi\rho c_\beta \int_{rmin}^{rmax} r^2 g_{\alpha\beta}(r)\mathrm{d}r \tag{1.6}$$

Here, $n_{\alpha\beta}$ is known as the coordination number. Changes in the coordination number provide information regarding the bonding that is present within a system of interest. A clear peak in the partial radial distribution function in an indication of a coordination shell. This shell can be caused by steric effects or interactions between the relevant atoms. Some of the important interactions that lead to such structures are discussed in the following section.

1.2.3   Interactions within Liquids

As described in Section 1.2.1, the interactions between and within molecules in a liquid are an important factor in the understanding of the liquid state. In this section three important interactions are discussed, namely, covalent bonding, hydrogen bonding and hydrophobic effects. The first interaction to consider is the covalent bond as this is the strong interaction that leads to molecules being formed. Here, an electron from

one atom is shared with another atom. This allows each of the atoms to reach a state where they have a completed electron shell, leading to a stable electronic configuration. This stability is due to the balance between the attractive interaction caused by the completion of electron shells and the repulsive interaction of bringing the positively charged atomic nuclei into close proximity. It is these stable bonds that lead to the formation of molecules from atoms (see Figure 1.5). Covalent bonds can lead to a polarity within the molecule that is formed. This is due to an imbalance in the positions of the shared electrons leading to the separation of electric charges and the formation of electrostatic poles (dipoles or multipoles).
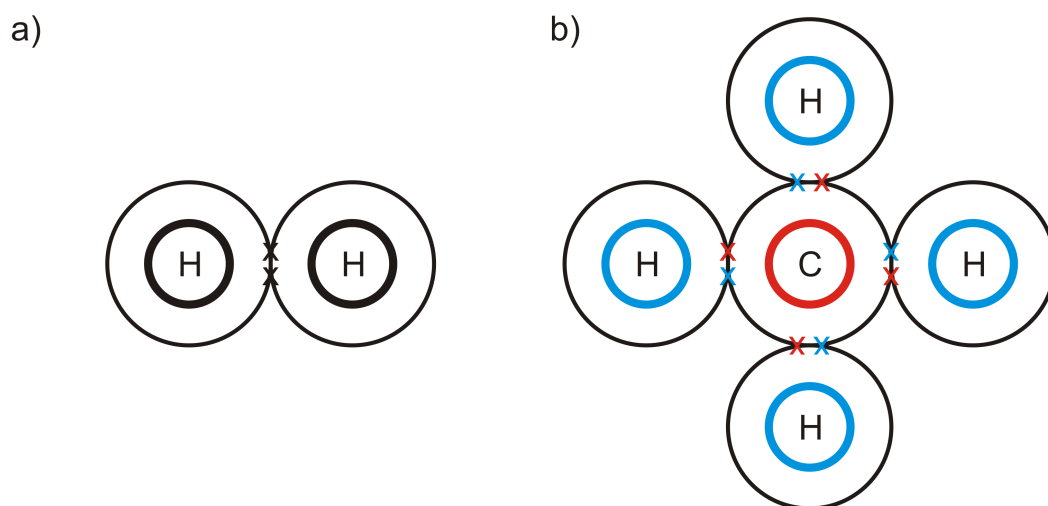
Figure 1.5: Schematic diagram showing the covalent bonding found within two different molecules. (a) A hydrogen molecule. Here, the black colour indicates a covalent bond that is non-polar. This non-polar nature is due to equally shared electrons within the hydrogen molecule. (b) A methane molecule. Here, the red colour indicates an electronegative atom and the blue colour indicates electropositive atoms. The four covalent bonds are all slightly polar in nature, but the net effect is a non-polar molecule as the bonds are arranged tetrahedrally.

A non-polar covalent bond is produced when both of the bonded atoms are of the same element, such as in a hydrogen molecule (see Figure 1.5(a)). Therefore, a hydrogen molecule is non-polar. Other non-polar molecules can be formed when multiple polar covalent bonds are present. In the case of methane (CH_4) the four covalent bonds are arranged tetrahedrally, which leads to a non-polar molecule as the four polar covalent bonds achieve balance (see Figure 1.5(b)).

Water, however, contains two hydrogen atoms covalently bound to an oxygen atom.
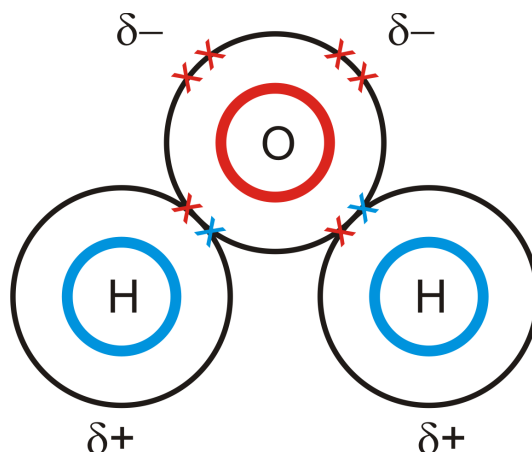
Figure 1.6: Schematic diagram showing the covalent bonds within a water molecule. Each of the bonds is polar. This leads to partial positive charges ($\delta+$) on the hydrogen atoms and negative charges ($\delta-$) on the lone pairs of electrons found on the oxygen atom. These separate partial charges mean that water is a polar molecule.

These bonds are polar in nature, which leads to the water molecule being polar. In water, the positive partial charges ($\delta+$) are found on the hydrogen atoms and the negative partial charges ($\delta-$) on the lone pairs of electrons on the oxygen atom (see Figure 1.6). The polar nature of water means that the inter-molecular interactions can be due to electrostatic effects. These factors lead to anomalous effects in water, such as the density maximum found at around 4 °C.

Most substances increase in density as they are cooled. For water, however, the density decreases as the temperature is decreased below 4 °C. This property allows the water at the surface of a river or lake to freeze first, meaning that liquid water can exist below. The ice at the surface then insulates the water below from further freezing. This is essential to the evolution and survival of life, as it allows organisms to survive below the surface of the water. The density maximum of water can be attributed to the orientation dependant inter-molecular forces that are present. The most powerful of these is hydrogen bonding.

An inter-molecular hydrogen bond is an attractive interaction between a hydrogen atom that is covalently bound to one molecule, and an electronegative atom attached to a separate molecule. Intra-molecular hydrogen bonds are very similar, but are formed between different atoms within the same molecule rather than between separate molecules. As such, intra-molecular hydrogen bonds are essential in the forces determining the structure of large molecules such as proteins. The two molecules (or molecular frag-

ments) involved in a hydrogen bond are named the donor and acceptor (see Figure 1.7). Within this study, only hydrogen bonds of the form oxygen-hydrogen$\cdots$oxygen will be considered. Here the hydrogen bond donor is the oxygen atom that is covalently bonded to the relevant hydrogen atom. The hydrogen bond between the acceptor oxygen atom and hydrogen atom is shown by the dotted line "$\cdots$".

Figure 1.7: Schematic diagram showing a hydrogen bond between two water molecules. The donor and acceptor molecule are labelled.

The hydrogen bond is similar to a covalent bond in that there is a balance between the attractive and energetically costly interactions. The attractive interaction is due to bringing the partially positive hydrogen atom towards the partially negative oxygen atom. The energetically costly part of this is that it also brings the two partially negative oxygen atoms closer together. This leads to strong hydrogen bonds having a conformation where the hydrogen atom to acceptor oxygen atom distance is short and the donor oxygen to acceptor oxygen atom separation is as long as possible. This is achieved by having a linear (or close to linear) arrangement of the oxygen - hydrogen$\cdots$ $\cdot$oxygen triplet.

Hydrogen bonding leads to bulk water molecules being connected in an extended three-dimensional network, with the molecules acting as both donors and acceptors. An area of interest comes from considering what happens to this network when a solute is added to the water. These solutes can be broken down into three groups: hydrophobic, hydrophilic, and, amphiphilic molecules[1]. Hydrophobic molecules are generally non-

---

[1]These names come from the Greek words: hydros (water), amphis (both), phobia (fear) philia (love).

polar (*e.g.* methane) and therefore cannot form hydrogen bonds. Hydrophilic molecules often have a polar nature, or contain a portion of the molecule that is polar. The third group of molecules are known as amphiphiles as they contain both a hydrophilic and hydrophobic portion.

When a hydrophilic solute is added to water, the network of interactions between molecules continues to be dominated by the interactions of the dipoles. However, when a hydrophobic molecule is added to water, the attractive water-solute interactions are much weaker. It is important at this point to recognise that the interaction between a hydrophobic solute and water is attractive and therefore these molecules do not "fear" water as their name would suggest. However, the interaction between the water molecules is much stronger than the water-solute interactions for hydrophobic solutes. Therefore, it is the loss of water-water interactions rather than a repulsive interaction between the solute and the water molecules that is the dominant interaction when a hydrophobic solute is added. This leads to the aggregation of hydrophobic solutes as this maximises the number of water-water interactions. These interactions are the forces that lead to the structure that is found within liquid samples. There are many different techniques that have been used to find structural information regarding liquid and disordered systems. These are discussed in the following section.

1.3   Determining Liquid Structure

The aim of this section is provide an introduction to the different methods that can be used to access liquid structure. These can be split into two main groups: computational modelling, and experimental techniques. Section 1.3.1 gives a brief account of the simulation-based techniques, and Section 1.3.2 provides an introduction to experimental techniques used to study liquids. It is not the aim of this section to provide an exhaustive introduction to computational modelling or the experiments that can be performed on liquids. Further information on the topics introduced here can be found elsewhere (for example in the references that are cited here).

1.3.1   Modelling Techniques

Here, the term "modelling techniques" refers to a computational representation of a liquid sample. When using this technique, a representation of the interaction potentials between the components of the system of interest is required. The combination of these potentials provides the force field of the simulation. This is the computational representation of the potential energy surface of the system that is being studied. Generally the interaction potentials can take two forms. Classical simulations use empirical force-fields whereas *ab initio* simulations use quantum mechanical calculations, from theoretical principles, to calculate the force-field.

Empirical potentials can be assigned to each atom in the system (all-atom simulation) or some level of course graining can be used. In a course-grained simulation different atoms/molecules are combined and become one entity from the viewpoint of simulation. An example of this is the use of "united atom" models which assume that carbon atoms and the hydrogen atoms that are covalently bonded to them can be modelled as if they were one atom (31). This greatly reduces the level of complexity within the simulation and allows larger systems to be modelled. However, this reduction in complexity also reduces the amount of information that can be extracted from the simulation. In an "all-atom" model each of the atoms are assigned a specific potential (32). This approach is more computationally costly than "united atom" models but does allow the interactions between each of the atoms in the system to be probed.

Once the force field for a simulation has been setup the simulating can begin. Again, there are two general types of simulation that are relevant for this thesis: Molecular Dynamics (MD), and Monte Carlo (MC). In a MD simulation, the time dependant behaviour of the particles in the simulation is found by solving Newton's laws of motion. In a MC simulation a modification of the system that is being modelled is attempted, such as, a molecular rotation or translational movement. This modification is accepted or rejected based on whether or not it leads to the potential energy of the system being lowered[1] (33; 34). The atomic/molecular movements that are used in MC models are not necessarily physical. This means that MC simulation does not allow access to the dynamics of the system. However, information regarding the static properties of the system can be found. Therefore, the choice of using MD or MC depends on the

---

[1]Monte Carlo modelling is discussed in greater detail in Section 2.5.

information that is being sought.

These modelling techniques have many advantages over traditional experimental techniques. These include access to atomistic level information as well as the ability to access regions of the phase diagram that are problematic to access experimentally (35). However, simulation based techniques are not without drawbacks. The size of the simulation and the length of time that it is run over limit the scale of the interactions that are being probed (36). Using larger simulations that are run for a longer time can alleviate this. However, the use of large simulations run for a long time can lead to any small errors in the force-field leading to erroneous results (37).

An important point with pure simulation based studies is that the result of the simulation is only as good as the interaction potentials that constitute the force field. The effects of the choice of potential have been investigated in detail by Guillot (37). Here, a large range of interaction potentials that are commonly used to simulate water, were investigated. Guillot compared the results taken from simulations with the macroscopically measurable properties of water, such as the temperature of the density maximum (see Section 1.2.3) (37). Some potentials, such as TIP5P, gave results close to those of the experiments while others provided temperatures in the supercooled region (such as SPC/E and TIP4P). Some water potentials, including SPC and TIP3P, do not show a density maximum with the density increasing monotonically with decreased temperature. The deficiencies of these potentials suggest that there is an important part of the water interactions that are not being adequately accounted for in these simulations.

It is, therefore, imperative that an appropriate model potential is known or can be calculated for accurate computational modelling. The method that is used throughout the work detailed in this thesis to obtain an appropriate potential is given in Section 2.5. Previous examples of computational simulation based studies are given in Section 1.4 and in the relevant results chapters later in this thesis.

1.3.2   Experimental Techniques

The experimental techniques that have been used to study the structure of liquids can be split into three groups. The first method uses spectroscopic measurements, which deal with effects such as absorption, impedance and resonance, to probe interactions within a sample. Another method uses macroscopically measurable properties, such as the

temperature change on mixing (calorimetry), compressibility or excess molar volume. These properties are then used as an indication of the molecular scale interactions within the sample. The final experimental technique to discuss is diffraction. This technique is discussed in detail in Section 2.1. Therefore, only a brief introduction will be given here.

In spectroscopic experiments, the measured quantity is the scattered or absorbed intensity as a function of wavelength (across a spectrum). These data are then used to infer the molecular scale interactions within the sample. Infrared (IR) and Raman spectroscopy are of particular interest to the study of liquid systems (for example (38; 39)). IR spectroscopy deals with the interaction of electromagnetic radiation in the Infrared region with wavelengths in the region of 700 nm to 1 mm. These wavelengths are of interest because they correspond to the resonant energy of the vibrations associated with chemical bonds[1]. When the energy of the incident radiation corresponds to the energy of the vibration of the chemical bond it will be absorbed. Raman spectroscopy relies on the inelastic scattering of light (often in the visible wavelength region). When the light is incident on the sample it excites the molecule to a virtual energy level. The molecule then relaxes to a new energy state and a photon is given off with a different energy to the incident photon. The difference between the energy of the incident and scattered photons is measured. This difference in energy corresponds to the change in energy required to move from vibration mode to another.

The resonant energies of the molecular vibrations are dependent on their surroundings. Therefore, IR and Raman spectroscopy can be used to probe the environment around aqueous molecules (38; 39). In liquid samples the molecules are continually diffusing around due to Brownian motion. This leads to the spectral features measured by IR and Raman being diffuse. These broad peaks are interpreted by fitting a number of Gaussian peaks. Extracting structural information from these fitted peaks is nontrivial. Indeed, different authors have argued that these Gaussian peaks can be assigned to different structural correlations (see reference (40) and those found within).

An excellent review of thermodynamic investigations of aqueous glycerol has been published by Yizhak Marcus (41). The experimental values of these properties, such as

---

[1]Here, the word vibrations is used to mean all of the rotations, stretches and twisting that occurs within molecules.

vapour pressure and calorimetric measurements, are then used to calculate concentration regions where different interactions are expected to be prevalent. Other studies have concentrated on using a single technique to investigate aqueous glycerol *e.g.* calorimetric (42; 43) and volumetric studies (44; 45).

Diffraction experiments are similar to spectroscopic investigation as they both involve measurements of the way that radiation interacts with a sample. In a diffraction experiment, however, it is the relative angles of the incident and scattered waves that is measured rather than a change in energy of the radiation. These values are then used to find the relative atomic positions within the sample under investigation. Diffraction based techniques are discussed in greater detail in Section 2.1. Examples of each of these different techniques are given in Section 1.4 and in the relevant results chapters later in this thesis.

1.4 Previous Studies that are Relevant to the Study of Aqueous Glycerol

Due to the interest in glycerol and its aqueous mixtures (detailed in Section 1.1.1) a number of studies have been performed to investigate the structure and bonding of this important system. This research has focused on different areas of significance and an introduction to each of these areas is given here. The effects of temperature and pressure on water structure are introduced in Section 1.4.1. Section 1.4.2 discusses the studies that have investigated the structure of pure glycerol. The hydrogen bonding within glycerol-water mixtures has also been researched and some interesting results are shown in Section 1.4.3. Section 1.4.4 details studies in to the different mixing regimes that are present in aqueous glycerol. Finally, the results from previous studies that have used neutron diffraction and EPSR are discussed in Section 1.4.5. It is the aim of this section to provide an introduction to the different types of information that has been investigated regarding glycerol and its aqueous mixtures. More detailed discussion of this research is included in the relevant chapters later in the thesis.

1.4.1   Pure Water

The structure of water is of great importance to the general understanding of the liquid state and has, therefore, received a great deal of research interest (46–53). These investigations include studies of: the nature of the hydrophobic effect (46; 47), the structure of water in no-man's land[1] (48), and, the effect of ions on water (49). It is well beyond the scope of this thesis to cover each of these topics in detail. Therefore, this section will focus on the structure of pure water at room temperature and the modifications that occur when the temperature and pressure are modified. These are relevant topics to the study of aqueous glycerol as they provide important reference systems. The structural changes that occur when glycerol is added to the system are compared to these systems later in this thesis.

The structure of water at ambient conditions is not without controversy (50–52)[2]. It has been argued from spectroscopic data that ambient water is composed of strings of molecules (50) and that this leads the structure of water to have an inherent heterogeneity (51). Conversely it has been argued that this heterogeneity is indistinguishable from the density fluctuations that are present in any liquid system (52). In a more recent article, it is suggested that the different interpretations of the structure of water are dependant on the timescale over which the system is being probed (53). Kuhne and Khaliullin argue that the heterogeneity is only accessible when studying water structure on timescales shorter than a femtosecond (10^{-15} s). The method that is used throughout the work in this thesis allows access to the time averaged structure of the system (see Chapter 2). This means that if femtosecond scale heterogeneity is present in the system, it would not be accessible using this technique. Therefore, the research that is discussed in this section refers to previous time averaged structural investigations as these are comparable to the neutron diffraction studies detailed in Chapters 3, 4, 5, and, 6.

Liquid water has been studied using diffraction for over 70 years (54). The early studies used X-ray diffraction and assumed that the signal is almost completely due to the scattering from the oxygen atom of water. This is a justifiable assumption as the X-ray scattering cross section (a measure of the size of the signal) from oxygen is

---

[1]The phrase no mans's land is used to describe the region of the phase diagram that is currently unexplored experimentally between 160 and 232 K.

[2]Indeed, reference (52) discusses references (50; 51) and is entitled "Recent Water Myths".

around 450 times larger than that of hydrogen (see Table 2.1 and Section 2.2.1). The radial distribution function is then found using the Fourier transform[1] of this scattering data (54). From their analysis, Morgan and Warren find that the first peak of the water oxygen-water oxygen RDF is shifted outward and becomes less well resolved as temperature is increased from 1.5 to 83 °C (54). They also conclude that the tetrahedral nature of water, as shown by the second peak in the water oxygen-water oxygen RDF, is broken as the temperature is increased. A more recent X-ray diffraction investigation of the structure of water has been used to produce Figure 1.8(a) (55). This work is in agreement with the conclusions of Morgan and Warren. The first peak becomes less well defined as temperature is increased. Also, the second peak is shown to decrease in magnitude and is shifted outward on heating. Therefore, as the temperature of water is increased the first and second peaks both become less well defined.

The effect of pressure on the water structure has been investigated by Alan Soper using neutron diffraction and EPSR (56). Figure 1.8(b) shows the water oxygen-water oxygen radial distribution functions taken from EPSR analysis of water at 298 K and pressures of 0.1 MPa (red) and 200 MPa (black). It can be seen that the first peak of the RDF is shifted outward with the increase in pressure. The second peak shows a more pronounced change being shifted inward with increased pressure. Interestingly, the inward movement is accompanied by the difference in height between the first peak peak and the following trough being decreased with increased pressure. This indicates that there are more oxygen atoms found at a radial separation of around 3.4 Å in the higher pressure system. This data shows that as the pressure is increased the water second peak is shifted inwards and the trough at around 3.4 Å becomes less pronounced. The modifications to the structure of water with increased temperature or pressure are compared to those found in aqueous glycerol in subsequent chapters.

1.4.2 Pure Glycerol

Section 1.1.1 includes a discussion of the ways that glycerol is used. In order to optimise these procedures it is important to understand the structure and bonding that is found in pure glycerol. Therefore, pure glycerol has been studied using both experimental (*e.g.* (57)) and computational methods (*e.g.* (58)). This research has been interested in

---

[1]This is discussed in greater detail in Section 2.2.3.
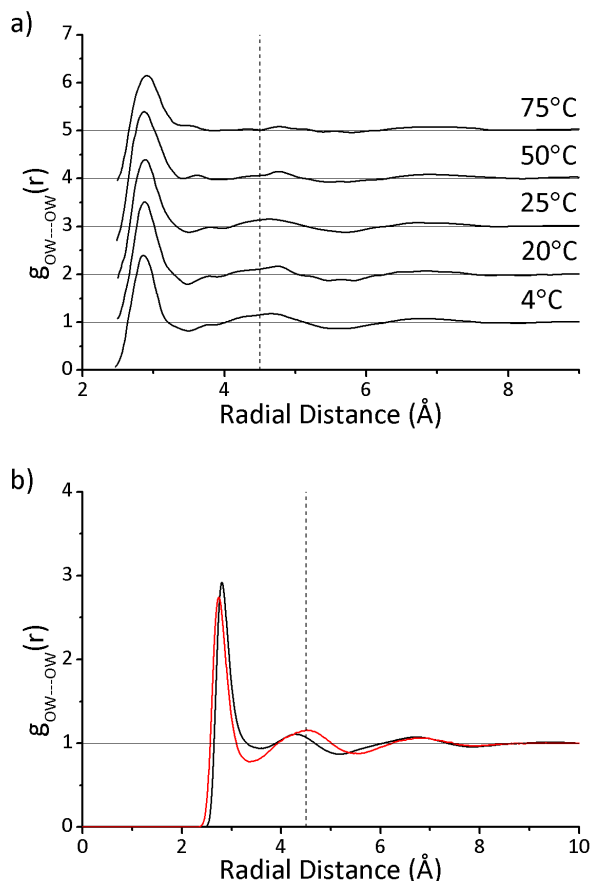
Figure 1.8: The effect of temperature and pressure on the water oxygen-water oxygen radial distribution functions. The thin black lines show the position of g(r) = 1 for each of the RDFs shown and a dashed black line indicates a radial distance of 4.50 Å. (a) The effect of temperature as measured by X-ray diffraction by Narten and Levy (55). (b) The effect of pressure as measured by the neutron diffraction study of Soper (56). Here, the red line indicates water structure at a pressure of 0.1MPa and the black line shows data taken at 200 MPa with both systems being at a temperature of 298 K.

determining the balance between the intra-molecular and inter-molecular interactions. This is a feature common to all liquids and is introduced in Section 1.2.1.

The structure of glycerol can be quantified using the relative positions of the heavy atoms (carbon and oxygen) within the molecule (59) (see Section 3.1.1). Here, the dihedral angles that are formed by the two oxygen-carbon-carbon-carbon quartets are measured. Each of these is then assigned a Greek letter (α, β or γ) based on the size of the dihedral angle (see Equation 3.1 and Figure 3.2). This method has been used to describe the crystalline structure of glycerol which has been found using X-ray diffraction (60) and the gas phase structure that was studied using computational simulations (61). It is the similarity between the liquid state result and these results

that provides information regarding whether the intra- or inter-molecular interactions are dominant.

Previous investigations into the structure of liquid glycerol have been conducted using neutron diffraction[1] (57; 62), and X-ray diffraction (63). Computational studies have used both classical (58; 64) and quantum mechanical calculations (61; 65; 66) to study the structure of glycerol. These previous studies are discussed in greater detail in Section 3.1.1. The results of the present investigation into the structure of liquid glycerol are given in Section 3.2.2.

Another method of studying the intra- and inter-molecular forces that act upon glycerol is to investigate the hydrogen bonding. Here, intra-molecular bonding in the liquid state would indicate that the system is in a similar situation to the gas phase. Previous computational simulation based studies have found that intra-molecular hydrogen bonding is present in liquid glycerol. However, the number of hydrogen bonds per molecule varies widely from 0.16 (67; 68) up to 3 (65) with other studies finding values in between (58; 64; 66). These values, and the definition of the hydrogen bond are listed in Table 3.1 and discussed in Section 3.1.2. The results of the present study are discussed in Section 3.3.2.

Similarly, there have been a number of studies investigating the number of inter-molecular hydrogen bonds that are present in liquid glycerol. The values from simulation based techniques vary between 3.09 (67) up to 5.70 hydrogen bonds per molecule using both quantum mechanical calculations (66) and classical molecular dynamics (69; 70). Again, other studies have found values between these and are summarised in Table 3.2 and discussed in Section 3.1.3. The results of the present study are discussed in Section 3.3.3. As well as an understanding of the balance between intra- and inter-molecular forces, a study of pure glycerol allows any modifications on dilution to be studied. These modifications are discussed in the following section.

1.4.3   Structural Modifications on Mixing of Glycerol and Water

Section 1.2.3 described how the bonding within a liquid is key to a description of its properties. It is, therefore, natural to explore how modifications to this bonding may be

---

[1]The motivation behind conducting a new neutron diffraction based investigation is given in Section 3.1.1.

linked to changes in macroscopic properties as a function of concentration in aqueous glycerol. Indeed, some studies have used macroscopic measurements such as compressibility (71) or molar volume (44; 72) to infer the atomistic level interactions. This section is split into three parts: simulation-based studies of the intra-molecular structure of glycerol molecules in aqueous mixtures, studies of the inter-molecular structure, and, bulk measurements that are used to understand molecular level interactions.

Changes in the intra-molecular structure of glycerol on dilution have been studied using simulation-based techniques. A molecular dynamics study has suggested that there is a range of glycerol conformations that are present (73). Also, there is disagreement over the presence of intra-molecular hydrogen bonding. A quantum mechanical calculation has suggested that intra-molecular hydrogen bonding is found in aqueous glycerol (74) and a more recent classical simulation has questioned this result (75).

It has been suggested that the addition of glycerol diminishes the ability of water to form hydrogen bonds. This would mean that each water molecule would be forming less hydrogen bonds in aqueous glycerol than pure water (76). However, other investigations have found an increase in the number of water-glycerol hydrogen bonds as glycerol concentration is increased. This would compensate for the loss of water-water hydrogen bonds (77; 78). This result is questioned by a more recent simulation study that found that each glycerol molecule is hydrated by four water molecules at each of the concentrations studied (79). The structure of the hydrogen bonds has also been studied with differing results. It has been found that the tetrahedral nature of water hydrogen bonding is diminished with the addition of glycerol which was attributed to the formation of two types of hydrogen bond (78). Politi *et al.* found two populations of hydrogen bonds with average lengths of 2.8 Å and 3.4 Å. Another interesting result from simulation was the suggestion that glycerol will form more hydrogen bonds as an acceptor than a donor (75). These results are discussed in greater detail in Section 4.1.3 with the results from the present study given in Section 4.3.

Aqueous glycerol mixtures have been studied using macroscopic measurements. These investigations have studied the excess molar volume (44; 72), isothermal compressibility (71) and Gibbs energy (41). The aim of these studies was to find the values of the excess functions associated with mixing water and glycerol. Here, an excess function is given by

the difference between the measured and ideal values of a specific variable[1]. It has been found that aqueous glycerol has a negative excess molar volume (44; 72). Cristancho *et al.* and Xu *et al.* both conclude that this is due to the formation of glycerol-water hydrogen bonds upon mixing (44; 72). Fort and Moore have argued that the sign and magnitude of the excess isothermal compressibility of binary aqueous liquids is indicative of the molecular scale interactions (71). They argue that excess isothermal compressibility of liquid mixtures becomes less positive and then increasingly negative as the strength of the interactions between unlike molecules increases. Aqueous glycerol shows a negative excess isothermal compressibility across the complete concentration range (41). Marcus has used measurements taken from the literature (such as vapour pressure measurements of To *et al.* (42)) to calculate the excess Gibbs energy (41). He concludes that the negative values of Gibbs energy (see Figure 5.7) indicate a "...predominance of the mutual attractive interactions over the self-interactions" (41). The interactions between glycerol and water molecules are discussed in Section 4.3.5. To gain a full understanding of the effects of mixing the different molecular species together it is important to study these changes as a function of concentration from pure water to pure glycerol. Section 1.4.4 discusses the effect that these interactions have on the molecular-scale mixing of aqueous glycerol as a function of concentration.

1.4.4   Molecular Mixing in Aqueous Glycerol

Molecular mixing provides information regarding the hydrophobic and hydrophilic nature of the interactions between molecules in a liquid (see Section 1.2.3). The concentrations where different mixing regimes are found can provide information about the relative strength of these interactions. The scenarios that have been proposed to illustrate the different mixing regimes can be split into three arrangements, shown in Figure 1.9.

At low glycerol concentrations, the water network has been found to persist (as shown in Figure 1.9(a)) using titration calorimetry (42), broadband dielectric spectroscopy (43), and raman spectroscopy (38). A spin probe investigation also found that the glycerol and water were incompletely mixed at low glycerol concentrations (80). There is also a general agreement about the intermediate phase comprising de-mixed regions containing

---

[1]The concept of ideal mixing is discussed in more detail in Section 5.1.1.
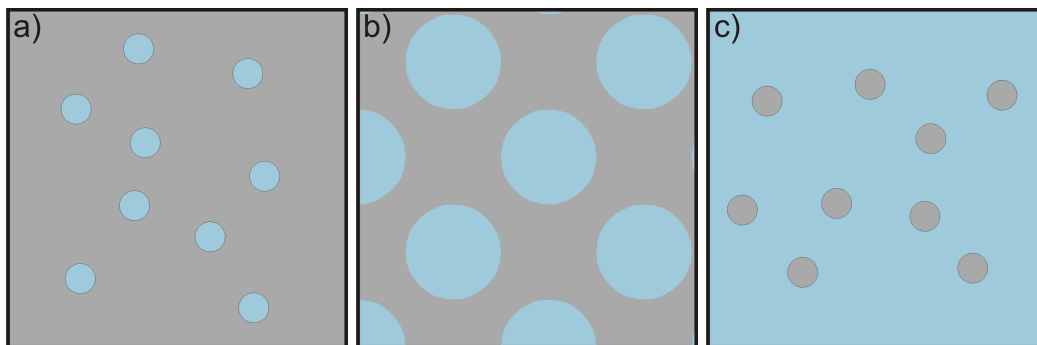
Figure 1.9: A diagram showing the different mixing regimes that have been suggested for aqueous glycerol as a function of concentration from high glycerol (a) to high water content (c). Here, water is shown by the blue region and glycerol by the grey areas. (a) At high glycerol content there are no large (multiple nanometre length) water clusters and the glycerol molecules have similar properties to the pure liquid. (b) At intermediate concentrations there are domains that include either high glycerol or high water concentrations. (c) At high water concentration the water resembles the pure liquid and there are no large (multiple nanometre length) glycerol clusters.

high concentrations of either water or glycerol (see Figure 1.9(b)). To *et al.* suggest that this is in the concentration range defined by glycerol mole fractions (X_g) of 0.15 to 0.35. The Raman spectroscopy work of Mudalige & Pemberton give similar values stating that this happens at concentrations between $X_g = 0.12$ and $X_g = 0.32$. Hayashi *et al.* as well as Banerjee & Bhat both state that this region occurs at concentrations between $X_g = 0.20$ and $X_g = 0.40$.

The mixing regime of water monomers in a pure-like glycerol liquid (see Figure 1.9(c)) is found at high glycerol concentrations in a number of studies. To *et al.* state that this occurs at concentrations greater than $X_g = 0.35$, Mudalige & Pemberton give similar value of $X_g = 0.32$. Again, Hayashi *et al.* are in agreement with Banerjee & Bhat when they state that this mixing regime is found at concentrations above $X_g = 0.40$. Other studies have also proposed different mixing scenarios. Dashnau *et al.* found that water forms a two-dimensional hydration layer around glycerol molecules at a concentration of $X_g = 0.27$ using molecular dynamics simulations (77). Above $X_g = 0.27$ they found that glycerol-glycerol interactions dominate. In another simulation based study it was found that glycerol and water are not well mixed at a low glycerol concentration of $X_g = 0.07$ (81). This is not in agreement with the spectroscopic studies detailed above. The mixing found within aqueous glycerol is discussed in Chapter 5.

1.4.5   Using Neutron Diffraction and Computational Modelling to Study Liquid Mixtures

In this study, glycerol and its aqueous mixtures are studied using a combination of neutron diffraction and computational modelling (see Chapter 2). In this method, neutron diffraction with isotopic substitution is coupled with a computational modelling program called empirical potential structure refinement (EPSR). This section focuses on the studies that have investigated small organic molecules known as osmolytes using neutron diffraction and EPSR. An osmolyte is a molecule that affects the osmotic pressure within a cell. Osmotic stress is an important factor within cryoprotection (see Section 1.1.2) and therefore many of the osmolytes in this section are also used as cryoprotectants. The osmolytes in this section include: the sugar trehalose (82; 83), the amino acid proline (84), a sugar alcohol, sorbitol (85), and two other osmolytes (dimethyl sulfoxide (86) and trimethylamine oxide (87)). Schematic representations of these molecules can be found in Figure 1.10. The results from these previous studies include structural modifications on mixing with water (similar to Section 1.4.3) and the level of mixing that is found in the aqueous mixtures (similar to Section 1.4.4).

Trehalose is a disaccharide sugar, and is formed when two glucose molecules are bonded together. It is known to accumulate as a response to temperature stress (21). This was the motivation behind the investigations conducted by Pagnotta *et al*. They found that when trehalose is added to water in a mole fraction of 0.01, each sugar molecule is hydrogen bonded to either two or three water molecules (82). This result was lower than expected due to the number of hydroxyl groups (-OH) that are present in each trehalose molecule (see Figure 1.10). The water structure, as measured by the three water-water radial distribution functions[1] was not altered, to the first neighbour distance when compared to pure water. However, the second peak in the water oxygen-water oxygen distribution was altered being shifted inward by 0.3 Å compared to pure water (82). In a later article, the trehalose concentration was increased to a mole fraction of 0.04 and similar results were found (83). Pagnotta *et al* conclude that the low number of trehalose-water hydrogen bonds per sugar molecule could indicate that the action of trehalose in preventing osmotic stress is due to trehalose-solute, rather

---

[1]Here, the three radial distribution functions are water oxygen-water oxygen, water oxygen-water hydrogen, and, water hydrogen-water hydrogen.
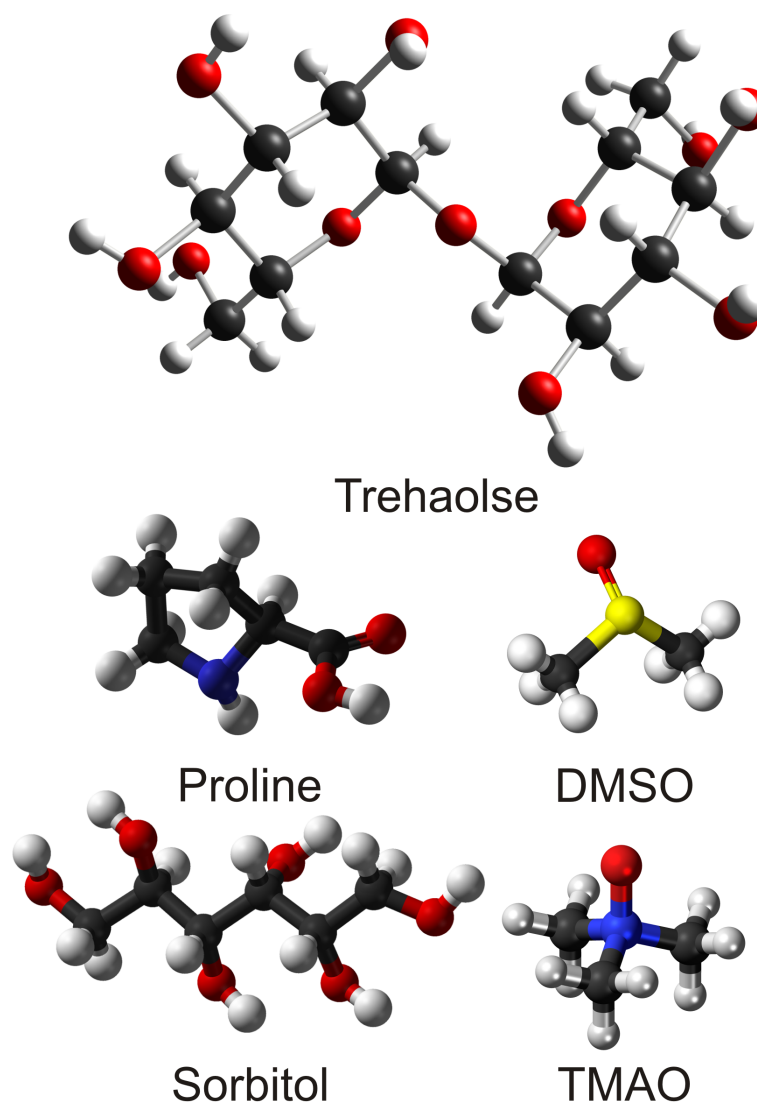
Figure 1.10: Ball and stick diagrams showing the range of solutes discussed in Section 1.4.5 that have been studied using neutron diffraction and EPSR.

than trehalose-water, interactions (83).

McLain *etal.* have studied the amino acid proline using neutron diffraction and EPSR (84). In their investigation, proline concentrations of between mole fractions of 0.05 and 0.09 were probed. It was found that, as the proline concentration is increased, the second peak of the water oxygen-water oxygen distribution was shifted to larger radial distances and became less pronounced. This modification was attributed to there being an insufficient number of water molecules in the system to form a complete second neighbour shell as the proline concentration was increased (84). McLain *et al.* also studied the number of hydrogen bonds formed by each water molecule. The method used

to define a hydrogen bond in their study was a maximum separation of 2.4 Å between the relevant oxygen and hydrogen atoms (different methods of defining a hydrogen bond are discussed in Section 3.3.1). It was found that the number of hydrogen bonds per water molecule decreased as the proline concentration was increased (84). Due to the aromatic ring structure in proline (see Figure 1.10) it had been suggested that it would form a stacking structure due to ring-ring interactions. No evidence for this was found by McLain *et al.*, but this may be due to the concentration of proline not being high enough for such stacked structures to form.

Chou and co-workers studied aqueous sorbitol with a mole fraction of 0.19 at different temperatures between 298 and 100 K (85). They found that the water-water interactions, as shown by the height of the first peak in each of the RDFs, became more prominent as temperature was decreased. They also found that the second peak of the water oxygen-water oxygen RDF was at a shorter radial distance for the sorbitol-water mixtures, at each of the temperatures studied, compared to pure water, a similar result to that found for the trehalose water system (83). The number of hydrogen bonds formed by each water molecule was also calculated. In their study, Chou *et al.* use the same method as is used in this thesis to define a hydrogen bond (see Section 3.3.1). They find that each water molecule forms around half as many hydrogen bonds to other water molecules as is found in pure water (1.86 as opposed to 3.41) and the number of water-water hydrogen bonds formed increases with a decrease in temperature (85). Unfortunately, they do not discuss water-sorbitol hydrogen bonds, therefore, the total number of hydrogen bonds formed by water cannot be investigated. Their work also found that, at these concentrations of aqueous sorbitol there was partial de-mixing of the molecules, leading to regions of high sorbitol concentration surrounded by water rich regions (similar to the mixing regime shown in Figure 1.9(b)).

Smaller osmolytes have also been studied using neutron diffraction and EPSR. Aqueous trimethylamine oxide (TMAO) has been investigated at a mole fraction of 0.053 (2.5M) (87). An inward shift in the second peak of the water oxygen-water oxygen RDF was found when compared to pure water. Thus, it can be concluded that TMAO and trehalose alter the structure of water in a similar fashion. However, this is not the case for dimethyl sulfoxide (DMSO). Aqueous mixtures of DMSO were studied at mole fractions of between 0.05 and 0.09 by McLain *et al.* They found that the second water

oxygen-water oxygen peak is shifted to larger radial distances and becomes less pronounced with an increase in the concentration of DMSO. It was also found that DMSO does not segregate in the manner to that reported by Chou *et al.* for sorbitol-water mixtures (85) but rather forms DMSO-water complexes (86). From the results detailed in this section, a number of general conclusions can be drawn. For each of the osmolytes that has been studied previously, the water structure is not dramatically altered to the first neighbour distance. There is, however, a difference in the effects that have been found in the position of the second neighbour water molecules. Trehalose, sorbitol and TMAO have been found to shift the second neighbour peak inwards, whereas proline and DMSO both act to broaden this peak and increase its radial separation.

To understand the different effects that these solutes have on water structure it is instructive to look at the effects of temperature and pressure introduced in Section 1.4.1. It has been shown that an increase in pressure causes an inward shift of the second water oxygen-water oxygen peak (56). An increase in temperature has been shown to lead to the second water oxygen-water oxygen peak shifting outwards (54; 55). Therefore, it can be concluded that the osmolytes that have been studied use one of two strategies. Proline and DMSO produce a water structure that is similar to higher temperature water, whereas, trehalose, sorbitol and TMAO act by driving the water to a structure that is similar to that found at high pressures. Contrasting results have been found for the molecular level mixing in these systems. This could be due to the limited number of different concentrations studied in each case.

1.5   Aims and Objectives

This project is designed to study the structure of glycerol and its aqueous mixtures at a range of different concentrations and temperature (see Figure 1.11). The experimental method used is a combination of neutron diffraction and computational modelling and is described in Chapter 2. This method allows atomistic level information to be extracted from neutron diffraction experiments. This technique has been used before to study a range of different solutes in aqueous solution (82–87). However, these studies have been limited in the number of different concentrations and temperatures that have been studied. This thesis describes a study across the complete concentration range from

pure glycerol to pure water. The effect of temperature is also investigated by measuring the structure of pure and aqueous glycerol at temperatures close to the relevant freezing temperatures. These data are used to investigate the validity of the results that are taken from previous studies (detailed in Section 1.4).

Initially the structure of pure glycerol is studied (see Chapter 3). This allows an investigation into whether intra- or inter-molecular forces are dominant in pure glycerol as well as being an important first step in the analysis of the aqueous glycerol mixtures. The effects of adding glycerol to water and *vice versa* are investigated in Chapter 4. Chapter 5 will investigate the structural modifications as a function of concentration for each of the room temperature experiments shown in Figure 1.11. The effects of a decrease in the temperature will be studied in Chapter 6 for each of the low temperature experiments shown in Figure 1.11. Finally, Chapter 7 will provide a conclusion to the thesis as well as suggestions for interesting future research that could be conducted.
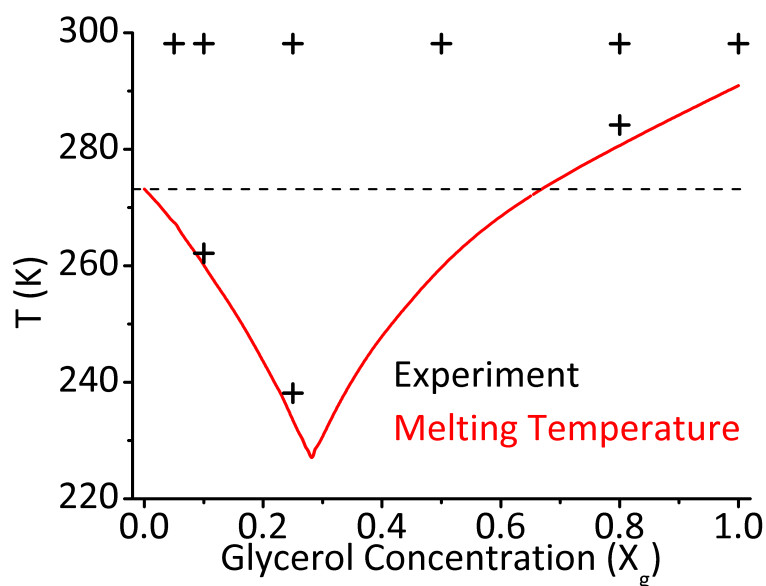
Figure 1.11: Graph showing the freezing temperature of aqueous glycerol (red line) as a function of glycerol mole fraction (Xg) (88). The concentrations and temperatures where neutron diffraction experiments have been completed are shown with black crosses. A dashed line is included at a temperature of 273.15 K (0° C).

Chapter 2

Neutron Diffraction and Computational Modelling

As discussed in Chapter 1, there is large variability within the computational research and a lack of direct experimentally derived data regarding glycerol-water mixtures. This chapter describes the techniques that have been used to address the paucity of such information. An introduction to diffraction and an examination of the information that can be accessed using this powerful techniques is found in Section 2.1. Section 2.2 describes the motivation for using neutron diffraction over other forms of diffraction (such as X-Ray diffraction). Section 2.3 introduces the basic theory behind the use of neutron diffraction. There follows an overview of neutron diffraction techniques and how they have evolved through the years in Section 2.4. The chapter concludes with an explanation of the computational modelling program Empirical Potential Structure Refinement (EPSR) and the ways that it can be used to probe liquid structure (see Section 2.5). It should be noted that it is not the aim of this chapter to be a comprehensive report on crystallography, scattering techniques or computational simulations in general. Further information is available regarding crystallography (89), scattering techniques (90), and simulations of liquids (33).

2.1 Introduction to Diffraction

Section 1.2.2 begins with a description of the structure of a crystal and describes how liquid structure differs from this. In a similar way, this section first describes the diffrac-

tion from a crystal and then a discussion of the diffraction pattern from a liquid follows. Diffraction is an experimental tool that probes the structure of a sample by measuring waves that have interacted with the sample. An everyday example of diffraction can be found by looking at the underside of a CD or DVD. The rainbow pattern that is seen is due to light of different wavelengths (colours) being reflected from the surface of the disc in different ways. By studying this rainbow pattern, information regarding the structure of the spiral features of the disc can be found.

2.1.1 The Interference of Waves

A key component of diffraction is interference, which is the combination of two or more waves that are in the same spatial region. Here, the amplitude that is measured at any point is given by the sum of the amplitudes of all the waves at that point, a phenomenon known as superposition. Figure 2.1 shows this process for waves that are in phase (Figure 2.1(a)) and anti-phase (Figure 2.1(b)). These are the two extremes of superposition. When two waves are in phase, the resultant total wave has the same wavelength and frequency as each of the original waves, but the amplitude is the sum of the amplitudes of the two original waves. This process is known as constructive interference. When the two waves are completely out of phase (anti-phase) there is no resultant wave: a characteristic known as destructive interference. It is this process of constructive/destructive interference that leads to a diffraction pattern.

2.1.2 Bragg Diffraction

The theory of constructive and destructive interference, described in Section 2.1.1, is at the heart of Bragg's law of diffraction, which is given by,

$$n\lambda = 2dsin\theta \tag{2.1}$$

where n is an integer, λ is the wavelength of the incident (and scattered) wave, d is separation of scattering planes and θ is the angle of scattering[1]. Equation 2.1 can be explained using the schematic diagram shown in Figure 2.2.

The path length difference (X) is shown with a solid red line in Figure 2.2. This

[1]the value 2θ is usually measured in diffraction experiments as this is the angle between the incident and scattered waves (k_i and k_f respectively).
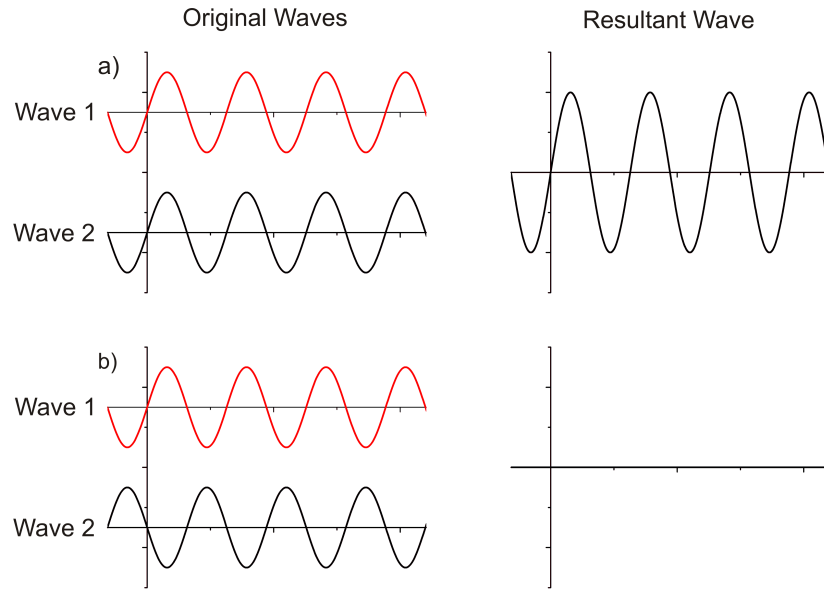
Figure 2.1: A diagram showing superposition: (a) Constructive interference occurs when two waves are in phase; the resultant wave has the same wavelength and frequency as each of the original waves and the amplitude is the sum of the two original waves. (b) Destructive interference occurs when two waves are completely out of phase (anti-phase) and leads to the waves cancelling each other.

length must be an integer number of wavelengths for the wave from the lower scattering plane to interfere constructively with the wave from the top scattering plane. When the path length difference plus $\lambda/2$ is equal to an integer the waves will interfere destructively and no signal will be measured. This can be written as,

$$n\lambda = X \qquad \text{Constructive Interference}$$
$$n\lambda = X + \lambda/2 \qquad \text{Destructive Interference} \tag{2.2}$$

Figure 2.2 shows that the path difference is double the length of the opposite side of the right-angled triangle (shown with dotted lines). Trigonometry can be used to calculate the length of the opposite side of a right-angled triangle using,

$$\text{Opposite Side Length} = dsin\theta \tag{2.3}$$

Using Equation 2.2 and doubling Equation 2.3 we are left with Equation 2.1. Therefore, the combination of the path difference (shown in Figure 2.2) and Equation 2.1 allows the separation of scattering planes to be calculated by measuring the angles θ at which
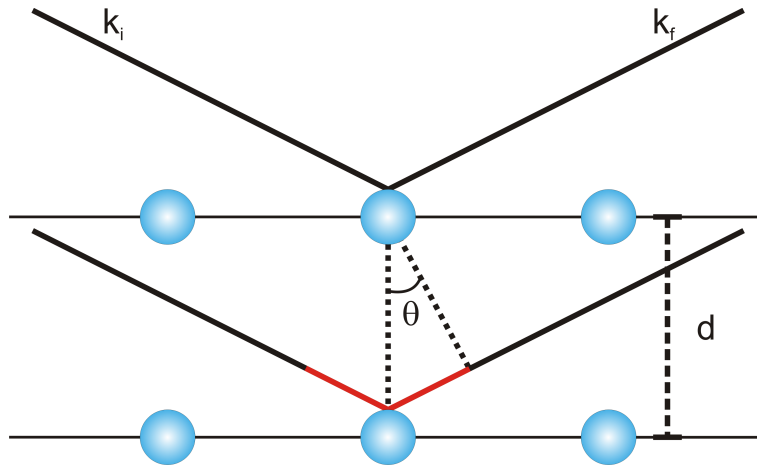
Figure 2.2: Schematic diagram of Bragg diffraction. Here, two waves from the same source are incident on consecutive scattering planes. When the path length difference (shown in red) is equal to an integer number of wavelengths the interference between the two waves will be constructive and a signal will be measured.

constructive interference occurs.

This holds for Fraunhofer, or far-field, diffraction. Here, the diffraction pattern is viewed at a distance much greater than the wavelength of the radiation and the two waves reaching the same point on the screen are essentially parallel and are subject to the interference detailed above. The aim of a diffraction experiment is to measure the angles (θ) at which constructive interference of waves with a known wavelength (λ) occurs. This is known as a diffraction pattern. The key factor here is that information regarding the separation of the sources of scattering can be found from the diffraction pattern.

2.1.3 Length Scales for Diffraction

Different types of diffraction experiment can be used depending on the length scale that is being probed, namely small angle and wide angle. In order to understand the difference between small and wide-angle experiments we recall that Equation 2.1 shows that the separation of scattering planes (d) is inversely proportional to $sin(\theta)$. In a diffraction experiment, the value that is usually measured is 2θ as this is the difference between the incident (k_i) and scattered (k_f) waves. The largest possible value of 2θ is π radians. Therefore, the largest possible value for of θ is $\pi/2$. Figure 2.3 shows the values of $sin(\theta)$ as a function of angle (θ).

Equation 2.1 shows that the largest scale structures (high d) will be found at the
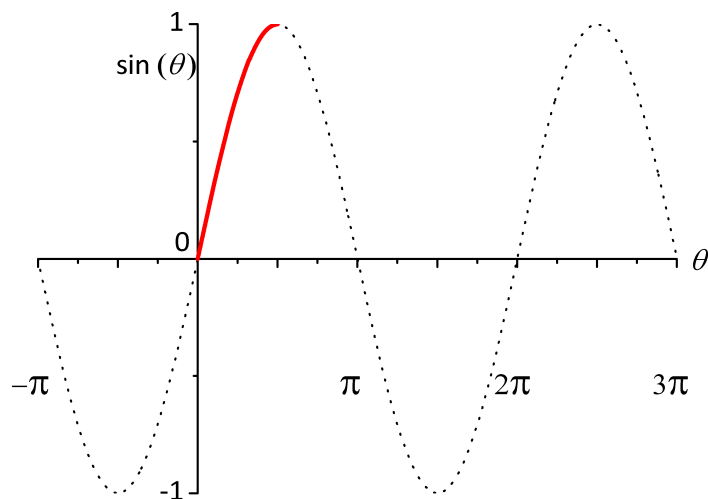
Figure 2.3: Graph showing the values of $\sin(\theta)$ as a function of angle θ. The solid red region shows the possible values of θ for a diffraction experiment. The maximum value of the red region of $\sin(\theta)$ is given when $\theta = \pi/2$ and the minimum value is found when $\theta \to 0$.

lowest values of $sin(\theta)$ for a constant value of $n\lambda$. The lowest values of $sin(\theta)$ are found at low values of θ (see Figure 2.3). Consequently, small angle diffraction is used to measure structures with larger scale features. Similarly, wide-angle diffraction measurements have large values of $sin(\theta)$ and thus small values of d. Therefore wide-angle diffraction measurements probe smaller scale features. To understand the scale of small and wide-angle measurements the value of λ must be known. This value depends on the type of wave that is being used to probe the structure and is discussed in the following section.

2.1.4   Diffraction Probes

Diffraction requires that the probe be a wave and as such be subject to interference. The other constraint on diffraction is that the wavelength of the probe be of a similar scale to structure that is being measured. Therefore, any wave, with appropriate wavelength, can be used for a diffraction experiment.

The waves that are commonly used include electromagnetic waves, such as X-rays, and matter waves, such as electrons or neutrons. A matter wave is a stream of particles that act as waves. The ability of a particle (specifically an electron) to act as a wave and produce a diffraction pattern was shown in two independent experiments by George Paget Thomson (working in Aberdeen) and Clinton Davisson and Lester Germer (work-

ing at Bell Labs in the USA) in the 1920s. G.P. Thomson and Davisson were awarded the Nobel Prize in Physics in 1937 for this discovery. The importance of their work lies in that it confirms the existence of wave-particle duality; an idea first put forward by Louis de Broglie (91). Here, de Broglie relates the wavelength of an object, λ, its momentum, p, and Planck's constant, h, using,

$$\lambda = \frac{h}{p} \tag{2.4}$$

Equation 2.4 shows that sub-atomic particles, such as electrons or neutrons, can be described as waves and as such are subject to interference. Consequently electrons and neutrons can be used as diffraction probes. The following section describes why neutron diffraction has been chosen for the work within this thesis.

2.2 Why Use Neutron Diffraction?

2.2.1 Interaction of the Probe with the Sample

In Section 2.1.4 it is stated that diffraction experiments can be completed with any probe that acts as a wave and undergoes interference. This section describes the motivation behind the use of neutrons as the diffraction probe for the work detailed within this thesis by comparing neutron diffraction with X-ray diffraction techniques. The choice of diffraction probe depends on the information that is being sought. As outlined in Section 1.1.1, hydrogen bonding is of particular interest when investigating glycerol-water mixtures. Therefore, a diffraction probe that is sensitive to the position of hydrogen atoms is essential for this study.

The sensitivity of a diffraction probe is governed by its interaction with the sample. Consider the simplest sample possible, that is, a single atom. The way that this atom scatters radiation (X-rays or neutrons) is called the atomic form factor, and is written as $f(\lambda, \theta)$, where λ is the wavelength of the radiation and θ is the scattering angle. Here it is assumed that the scattering is elastic, which means that the scattering atom is at a fixed position and the incident and scattered waves have the same kinetic energy but different directions of propagation.

For neutrons, the interaction of the wave is with the nucleus of the sample via the

strong nuclear force. This force operates at very small length scales compared to the wavelength of the neutron. Neutrons used in diffraction experiments have a wavelength of around 1 Å (10^{-10}m) and the strong force operates at a length scale of around 10^{-15}m. Consequently, the nucleus is effectively a point source of scattered neutrons, which means that the scattering occurs equally at all angles and is not dependent on the wavelength. This holds for atoms where neutron absorption does not occur at the relevant wavelengths. This means that the atomic form factor for neutron scattering is a constant for each atom and isotope. This constant is known as the scattering length b and is shown in Table 2.1. Therefore, the value of b is dependent on the isotope of the scattering atom. This important factor is discussed in greater detail below.

For X-rays, however, the interaction is with the electron cloud of the scattering atom, and therefore acts over much longer distances. Thus, the size of the signal in X-ray diffraction experiments is proportional to the number of electrons around the atom. For neutral atoms this is given by the atomic number, Z. Therefore, the scattering atom does not act as a point source in an X-ray diffraction experiment. The atomic form factor for X-rays, $f(\lambda, \theta)$ is given by,

$$f(\lambda, \theta) = Zg(\mathbf{Q})r_e \tag{2.5}$$

where, r_e is the classical radius of the electron (2.8 x 10^{-15}m) and $g(\mathbf{Q})$ is a factor dependent on the value $\mathbf{Q}$. Here $\mathbf{Q}$ is the exchanged wave vector and is a measure of the difference between the incident (k_i) and scattered (k_f) wave vectors (see Figure 2.4). The factor $g(\mathbf{Q})$ equals one when $\mathbf{Q}$ equals zero and decays to zero as $\mathbf{Q}$ goes to infinity. This leads to the X-ray atomic form factor being dependent on the angle of scattering.
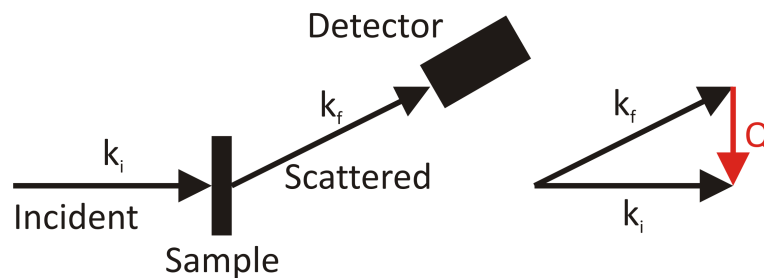
Figure 2.4: Diagram showing the incident wave, k_i, scattered wave, k_f, and the difference between the incident and scattered wave vectors, Q.

The difference between the interactions that lead to the scattering is shown in Figure 2.5. The scattering of neutrons is analogous to water waves reaching a bay with a small opening (Figure 2.5(a)). The water inside the bay has semi-circular waves. The scattering of X-rays, however, is analogous to water waves reaching a bay with a larger aperture (Figure 2.5(b)). The waves inside the bay are propagated predominantly in the forward direction *i.e.* the scattered waves have an angular dependence.
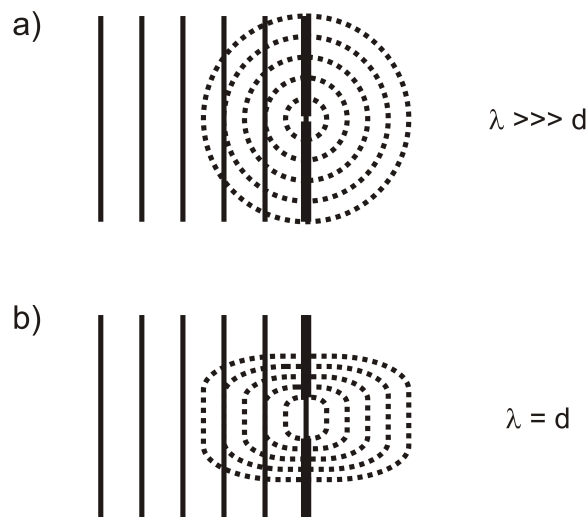
Figure 2.5: The difference between scattered neutrons and X-rays: (a) Scattered neutrons act as if the scattering atom is a point source. Therefore, there is no angular dependence on the scattering, similar to a bay with a small opening. (b) Scattered X-rays do have an angular dependence, similar to a bay with a large opening where the waves propagate predominantly in the forward direction.

Figure 2.5 and Equation 2.5 show that the scattering of X-rays is dependent on the angle of scattering. Consequently, to compare the scattering of X-rays with that of neutrons, the scattering cross-section (σ) of X-rays is used. The difference between scattering lengths and cross-sections is discussed in greater detail in Section 2.2.2. Table 2.1 shows the X-ray scattering cross-sections and neutron scattering lengths for the atoms contained in aqueous glycerol, namely hydrogen, deuterium, carbon and oxygen. The values shown in Table 2.1 are for the coherent scattering of neutrons and X-rays and are taken from Sears Tables (92) and McMaster Tables (93) respectively.

Table 2.1 shows that the X-ray scattering cross-section of oxygen (297.9 barns[1]/atom) is around 450 times larger than that of hydrogen (0.64 barns/atom). This means that

[1]Here, 1 barn is equal to 100 fm^2 or 10^{-28}m^2.

the signal from hydrogen atoms is difficult to extract when X-ray diffraction is used as it forms a very small proportion of the total signal. This is not the case for neutron diffraction as the signal sizes are similar for each of the atom types within this experiment[1].

Table 2.1: Diffraction Signal Sizes for X-rays and Neutrons

Atom	X-ray diffraction cross-section (σ_{coh}) barns atom^{-1}	Neutron diffraction scattering length (b_{coh}) fm
Hydrogen	0.64	-3.74
Deuterium	0.64	6.67
Carbon	85.63	6.65
Oxygen	297.92	5.80

It should be noted that the values in Table 2.1 refer to coherent scattering cross-sections of X-rays and scattering lengths of neutrons. The difference between the incoherent and coherent scattering is that incoherent scattering contains no structural information. The information contained within the incoherent scattering is due to randomly distributed variations in the sample. These randomly distributed variations arise from the thermal fluctuations within the sample for X-rays and isotopic and spin states for neutron scattering. Some atoms, such as vanadium, and alloys, such as titanium zirconium, give a neutron scattering signal that is dominated by incoherent scattering. This makes such materials very useful for neutron diffraction experiments, and is discussed in Section 2.4.4.

2.2.2 Comparing Scattering Cross-Sections from Neutron and X-Ray Diffraction

In Section 2.2.1 neutron scattering lengths are used to describe the scattering from a sample consisting of a single atom. In a neutron diffraction experiment the value that is measured is the differential cross-section of scattering (given by $d\sigma/d\Omega$). Therefore it is important to understand how the scattering length, b, relates to the scattering cross-section, σ. The scattering cross-section is a hypothetical area calculated using the incident flux of neutrons, Φ (units of $s^{-1}m^{-2}$) and the relevant rate of scattering, R

---

[1]It should be noted that the sign (positive or negative) of the scattering length refers to the phase change associated with the scattering. Here, a negative scattering length shows that the scattered neutron is out of phase with the incident neutron. The phase of the scattered neutrons is not measured in the experiments detailed in this thesis.

(units of s^{-1}) using,

$$\sigma = \frac{R}{\Phi} \tag{2.6}$$

The relationship between scattering length and cross-section can be calculated when neutrons are the probe. This is because, as stated previously, the atomic form factor for neutron scattering is not dependent on the scattering angle. Consequently, the neutron scattering cross-section is given by,

$$\sigma = 4\pi b^2 \tag{2.7}$$

The factor of 4π comes from the integration being over all possible scattering angles, which is given by a sphere. Using the neutron scattering cross-section allows the size of the signal from different kinds of atom to be shown schematically, shown in Figure 2.6. The relative sizes of the circles shown in Figure 2.6 are produced using the coherent scattering cross-sections of neutrons and X-rays, again, taken from Sears Tables (92) and McMaster Tables (93) respectively.
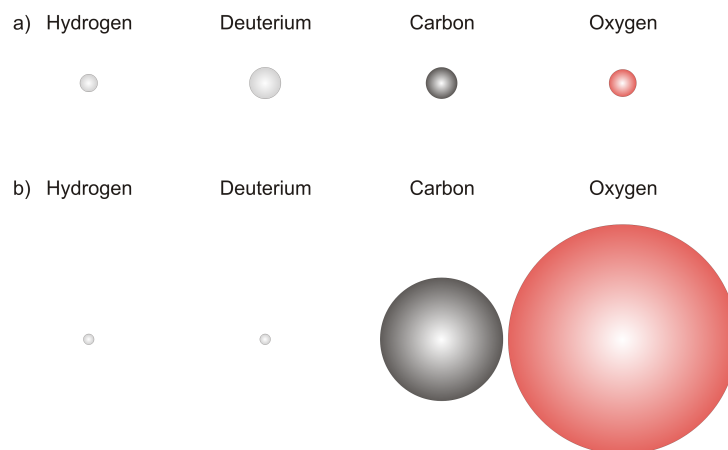
Figure 2.6: Diagram showing the relative scattering cross-sections for different atoms in (a) neutron and (b) X-ray diffraction experiments. It can be seen that the scattering cross-sections for hydrogen and deuterium are different for neutron diffraction and the same for X-ray diffraction.

As mentioned previously (Section 1.1.1) hydrogen bonding is of particular interest when investigating glycerol-water mixtures. Therefore, an experimental technique that is sensitive to the position of hydrogen atoms is required. Figure 2.6 shows that the data

taken from an X-ray diffraction measurement of aqueous glycerol would be dominated by the signal from the oxygen atoms. Therefore, neutron diffraction (rather than X-ray diffraction) is used because it is an atomistic experimental tool that is sensitive to the position of hydrogen atoms.

2.2.3 Reciprocal Space and Fourier Transforms

An important factor when conducting a diffraction experiment is that the signal is measured in reciprocal space (also called k-space or Q-space). To understand this, consider Young's double slit experiment (94) (see Figure 2.7). Here, light illuminates a plate that includes two slits and is recorded on a screen.
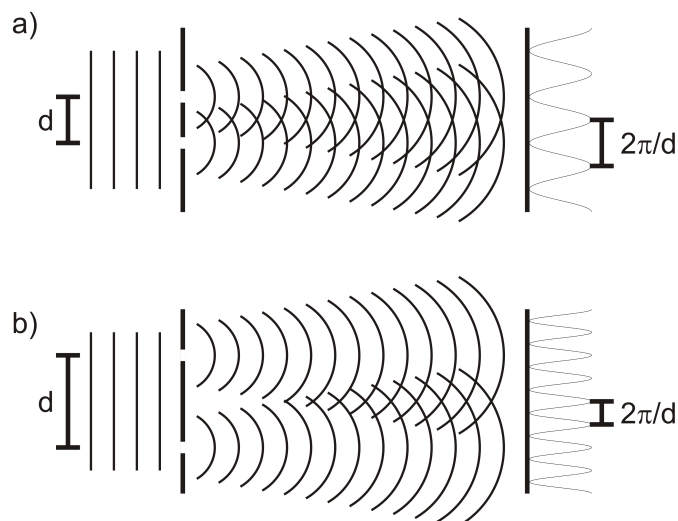
Figure 2.7: Diagram showing Young's double slit experiment where the spacing between the slits, d, is (a) small, and, (b) large. It can be seen that the separation between the peaks in the signal on the screen is given by $2\pi/d$.

The pattern shown on the screen can be explained using the superposition of waves emanating from the slits in the plate. This experiment, performed over 200 years ago, was a key finding that provided support for the wave nature of light (94). An important factor shown in Figure 2.7 is that the distance between peaks on the screen is given by $2\pi/d$. Consequently the separation of peaks in the signal is inversely proportional to the separation of the sources of the radiation; they have a reciprocal relationship. This characteristic leads to the diffraction pattern being in reciprocal space. Consequently a mathematical method to move from the diffraction data to structure of the sample is required. This procedure is known as the Fourier Transform and allows the function

measured by a diffraction experiment to be converted into a mathematical description of the sample and *vice versa*.

The plate used in a double-slit experiment can be described mathematically using an aperture function containing Dirac delta functions, which are written as $\delta(x)$[1]. The separation of the slits is d and they can be represented by delta functions at positions of $x = \frac{d}{2}$ and $x = -\frac{d}{2}$ therefore, the aperture function $A(x)$ is given by,

$$A(x) = \delta\left(x - \frac{d}{2}\right) + \delta\left(x + \frac{d}{2}\right) \tag{2.8}$$

The Fourier Transform of the aperture function shown in Equation 2.8 is given by,

$$\psi(\mathbf{Q}) = \psi_0 \int_{-\infty}^{\infty} A(x)e^{i\mathbf{Q}x}dx \tag{2.9}$$

where $\psi(\mathbf{Q})$ is the scattered wave function, ψ_0 is a constant of proportionality and i is the square root of minus one. The integral from minus infinity to infinity of a Dirac delta function is equal to one and thus Equation 2.9 can be re-written as,

$$\begin{aligned}\psi(\mathbf{Q}) &= \psi_0 \left(e^{i\mathbf{Q}d/2} + e^{-i\mathbf{Q}d/2}\right) \\ &= \psi_0 \, 2cos\left(\frac{\mathbf{Q}d}{2}\right)\end{aligned} \tag{2.10}$$

The measured diffraction pattern is not the complex wave function, $\psi(\mathbf{Q})$, but rather its intensity, denoted as $I(\mathbf{Q})$, which is given by,

$$I(\mathbf{Q}) = |\psi(\mathbf{Q})|^2 = \psi(\mathbf{Q})\psi(\mathbf{Q})^* \tag{2.11}$$

where $\psi(\mathbf{Q})^*$ is the complex conjugate of the scattered wave function, $\psi(\mathbf{Q})$. Combining Equations 2.10 and 2.11 yields

$$I(\mathbf{Q}) \propto \left[cos\left(\frac{\mathbf{Q}d}{2}\right)\right]^2 \propto 1 + cos(\mathbf{Q}d) \tag{2.12}$$

Equation 2.12 shows that the measured diffraction pattern is proportional to $1 + cos(\mathbf{Q}d)$ and has equally spaced peaks of uniform intensity as shown in Figure 2.7. This is a key

---

[1]The Dirac delta function is zero at all points apart from $x = 0$ and has an area of one.

result for diffraction. Equation 2.12 shows that Fourier Transforms can be used to find a function describing the structure of a sample from the measured diffraction pattern. Therefore, diffraction is an experimental tool, which allows access to the atomic level structure of the sample.

2.3 Studying Structure with Neutron Diffraction

2.3.1 Introduction to Neutron Diffraction

The aim of this section is to give a brief introduction to the theory behind neutron diffraction experiments. It is hoped that this description of the fundamentals will enable the reader to understand the motivation behind the steps that are taken in a neutron diffraction experiment. As mentioned in Section 2.1, for a pronounced diffraction pattern to be produced, the wavelength of the incident radiation must be of a similar length scale to the target structure. The intensity of the scattered radiation as a function of angle then provides information regarding the structure of the sample under investigation. The aim of a diffraction experiment is to obtain the interference structure factor, $F(Q)$, which is a description of how a sample scatters incident radiation.

It is stated in Section 2.2.2 that the quantity measured in a diffraction experiment is the total differential scattering cross-section. This is a measure of the proportion of the scattered neutrons per unit solid angle per time and is given by,

$$\left(\frac{d\sigma}{d\Omega}\right)_{tot} = \frac{R_{tot}}{N\Phi d\Omega} \tag{2.13}$$

where R_{tot} is the rate at which neutrons are scattered through the solid angle, $d\Omega$, N is the number of scattering centres in the sample and Φ is the icident neutron flux (units of $s^{-1}m^{-2}$). This can be divided into two contributions called the self $\left(\frac{d\sigma}{d\Omega}\right)_{self}$ and distinct $\left(\frac{d\sigma}{d\Omega}\right)_{dist}$ terms using,

$$\left(\frac{d\sigma}{d\Omega}\right)_{tot} = \left(\frac{d\sigma}{d\Omega}\right)_{self} + \left(\frac{d\sigma}{d\Omega}\right)_{dist} \tag{2.14}$$

The "distinct" part of the structure factor contains information regarding scattering from pairs of atoms. The "self" part of the structure factor contains no structural information and provides a featureless background signal. The different terms that

make up the total differential scattering cross-section are given by,

$$\left(\frac{d\sigma}{d\Omega}\right)_{self} = \sum_{\alpha} c_{\alpha} b_{\alpha}^2$$

$$\left(\frac{d\sigma}{d\Omega}\right)_{dist} = \sum_{\alpha \leq \beta} (2 - \delta_{\alpha\beta}) c_{\alpha} c_{\beta} b_{\alpha} b_{\beta} S_{\alpha\beta}(\mathbf{Q}) - 1 \qquad (2.15)$$

where c_{α} is the concentration and b_{α} is the scattering length of component α and $S_{\alpha\beta}(\mathbf{Q})$ denotes the partial structure factor between atom types α and β. To prevent double counting, a Kronecker delta function $\delta_{\alpha\beta}$ is included.

For some systems the static approximation can be used. Here, the contributions due to attenuation, multiple scattering and inelastic scattering are assumed to be so small they can be ignored. Therefore, the total differential scattering cross-section is assumed to be equal to the elastic differential scattering cross-section. In the static approximation the differential scattering cross-section is considered to be a function of the exchanged wave vector, $\mathbf{Q}$ (see Figure 2.4). The static approximation, however, only holds for solid samples because their atomic structure can be assumed to be constant. When a liquid sample is under investigation, such as in this thesis, a method to correct for attenuation, multiple scattering and inelastic scattering must be employed. The method that has been used here is described in Section 2.4.4.

The samples used in this work are all liquids and can be assumed to have isotropic structure. For isotropic systems it is only the magnitude of the vector $\mathbf{Q}$, given by $Q = |\mathbf{Q}|$, that is important. Using the magnitude of Q leads to the differential scattering cross-section being equal to the total structure factor, $F(Q)_{tot}$. This can be written as,

$$\begin{aligned} F(Q)_{tot} &= F(Q)_{self} \quad + F(Q)_{dist} \\ &= \left(\frac{d\sigma}{d\Omega}\right)_{self} + \left(\frac{d\sigma}{d\Omega}\right)_{dist} \\ &= \sum_{\alpha} c_{\alpha} b_{\alpha}^2 \quad + \sum_{\alpha \leq \beta} (2 - \delta_{\alpha\beta}) c_{\alpha} c_{\beta} b_{\alpha} b_{\beta} S_{\alpha\beta}(Q) - 1 \end{aligned} \qquad (2.16)$$

The most important consequence of Equation 2.16, for this research, is that it shows that the total structure factor is given by the sum of the partial structure factors ($S_{\alpha\beta}(Q)$)

weighted by the concentration (c) and scattering length (b) of the relevant components α and β. This is key because the Fourier transform (see Section 2.2.3) of $S_{\alpha\beta}(Q)$ can be taken to produce the pair radial distribution functions, RDFs (see Section 1.2.2) using,

$$S_{\alpha\beta}(Q) - 1 = 4\pi\rho \int_0^\infty (g_{\alpha\beta}(r) - 1)\frac{sinQr}{Qr}\mathrm{d}r \tag{2.17}$$

where ρ is the atomic number density of the system, r is the radial distance and $g_{\alpha\beta}$ is the RDF. An RDF shows the density of atoms of type β around a central atom of type α. Therefore, in principle, if a sufficient range of isotopes with different scattering lengths are used a complete range of partial structures can be measured allowing Equation 2.17 to be used to find each of the RDFs, $g_{\alpha\beta}(r)$. This is, however, not practical for the system under investigation in this thesis (see Section 2.4.5). Once the RDFs have been calculated, the structure can then be further examined by using integration to find the number of atoms of type β which fall within a radial distance, r, of a central atom, α using,

$$n_{\alpha\beta} = 4\pi\rho c_\beta \int_{rmin}^{rmax} r^2 g_{\alpha\beta}(r)\mathrm{d}r \tag{2.18}$$

Here, $n_{\alpha\beta}$ is known as the coordination number and can be used to investigate the number and type of bonds being formed (discussed in greater detail in Chapters 3, 4 and 6).

The static approximation is not valid for the systems that are studied here and therefore corrections for attenuation, multiple scattering, and inelastic scattering must be taken in to account. These corrections (see Section 2.4.4) are dependent on the diffractometer that is used, so are discussed after the choice of instrument has been described. This section has shown that atomistic level data can be accessed using neutron diffraction. Therefore, neutron diffraction has been used as the experimental tool for this research.

2.4   The Neutron Diffraction Experiment

2.4.1   Neutron Production and Moderation

James Chadwick performed the earliest experimental neutron production in 1932 while he was working at the Cavendish Laboratory in Cambridge (95; 96). Chadwick bom-

barded a beryllium target with α particles emitted by a polonium source (^{120}Po) to produce neutrons via the (α, n) reaction,

$$^{9}Be + \alpha \rightarrow\ ^{13}C \rightarrow\ ^{12}C +\ ^{1}n \tag{2.19}$$
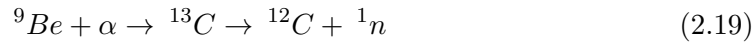
The use of this method earned Chadwick the 1935 Nobel Prize in Physics for the discovery of the neutron. This finding was instrumental in the understanding of the nucleus, and for the development of nuclear fission. However, the quantity of neutrons produced by the reaction shown in Equation 2.19 is much too low for neutron scattering experiments.

The next great step forward was made 10 years later with the production of the first nuclear reactor, Chicago Pile-1, as part of the Manhattan Project. Here uranium-235 (^{235}U) was used to produce a self-sustaining reaction that lead to the production of neutrons. Modern day fission reactors work in a similar way by harnessing the interaction of a neutron with ^{235}U. One such reaction is shown below,

$$^{235}U +\ ^{1}n \rightarrow\ ^{236}U \rightarrow\ ^{134}Xe +\ ^{100}Sr + 2\ ^{1}n \tag{2.20}$$
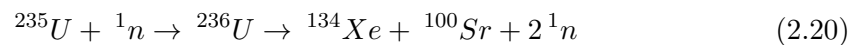
Equation 2.20 shows that this fission reaction results in the production of neutrons. These neutrons are then used to cause the reaction to begin again with a different ^{235}U nucleus. However, the neutrons produced by this reaction are very energetic. The cross-section for neutron-induced fission of ^{235}U is very small for neutrons at this high energy, and becomes larger with decreasing neutron energy. Consequently, the probability of another ^{235}U nuclei capturing a neutron and undergoing the same reaction is low for neutrons at high energies. Therefore, moderators are used to slow the neutrons from the MeV range to the meV range required for the probability of being captured by another ^{235}U nucleus to be high enough for the reaction to become self-sustaining. At this point, the system is said to have become critical.

A moderator is a substance that is designed to produce a large number of inelastic scattering events between the free neutrons and the nuclei of the moderator. In an inelastic neutron scattering event momentum transfer takes place between the incident neutron and the scattering particle leading to the free neutron losing some of its energy. The momentum transfer of an inelastic collision is maximised when the two particles

involved have a similar mass. Consequently moderators contain a large number of low mass nuclei. Chicago Pile-1 used carbon as a moderator, but more modern moderators contain large amounts of hydrogen or deuterium (often in water or methane molecules[1]).

As mentioned previously (Equation 2.4), the energy of a particle is linked to its wavelength (λ) via the de Broglie equation, which for a neutron is written as,

$$\lambda = \frac{h}{m_n v} \tag{2.21}$$

where h is Planck's constant, m_n is the mass of a neutron and v is its velocity ($m_n v$ is the momentum p given in Equation 2.4). Thus, decreasing the velocity of a neutron increases its wavelength. An advantage of having to moderate the neutrons down to meV values is that this increases the wavelength of the neutrons to the Å scale, which is the scale being probed in the neutron diffraction experiments in this thesis. Therefore, the moderators at a reactor source of neutrons can be used to simultaneously maintain the reaction that is producing neutrons and adjust their wavelength to the required magnitude. Modern neutron sources that use fission reactions are found at the Institut Laue-Langevin (ILL) in France and the High Flux Isotope Reactor (HFIR) at the Oak Ridge National Laboratory in the USA. These sources produce a constant white beam (broad range of wavelengths) of neutrons. This is problematic for neutron diffraction experiments as the difference between the incident and scattered wave vectors is being measured (see Figure 2.4). Consequently, the beam must be monochromated (limited to a narrow wavelength spread), leading to only a small proportion of the neutrons that are produced during the fission reactions actually being used for experiments. This is an inefficient use of the neutrons that are being produced.

A more recent development in the production of neutrons is the use of spallation sources. In spallation, pulses of charged particles are accelerated to high energy and impacted upon a target. The interaction between the high-energy particles and the nuclei in the target leads to an excitation of the target nuclei. This causes an internal cascade that leads to high-energy particles, such as neutrons, being ejected from the nuclei. The ejected neutrons have energies that are too high to be used in diffraction experiments, but leave the nuclei of the target atoms in an excited state. The final part

---

[1]The moderator used at ISIS is discussed in Section 2.4.2
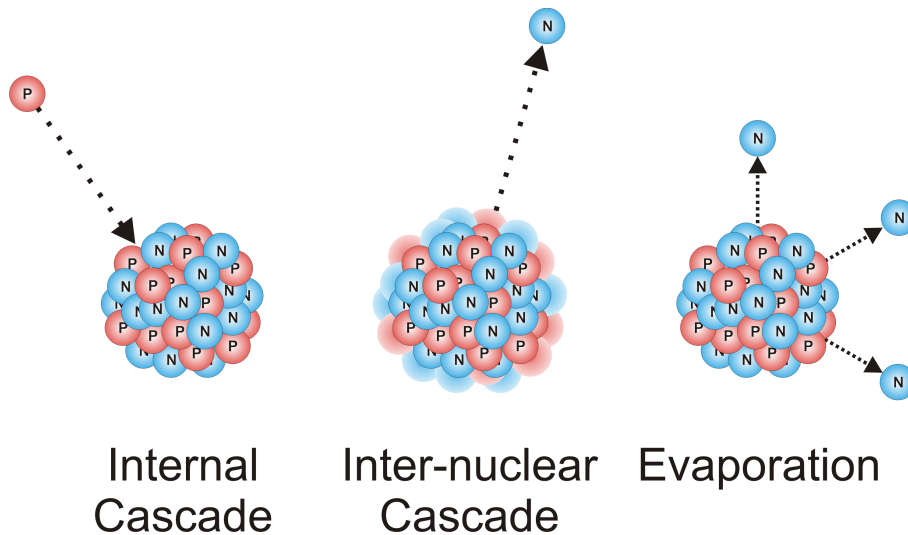
Figure 2.8: Schematic diagram showing the spallation process. The process begins with a high-energy proton being impacted upon a target nucleus. This causes the nucleus to release high-energy sub-atomic particles (such as neutrons). The final part of the process involves the de-excitation of the nucleus and the release of lower energy neutrons. It is the low-energy neutrons from nuclear evaporation that are used for neutron diffraction experiments.

of spallation involves the de-excitation of the nuclei via a process known as evaporation. Here, lower energy neutrons are released by the nuclei during de-excitation. The lower energy neutrons are then used for scattering experiments (see Figure 2.8).

There are two different types of spallation source; continuous and pulsed. At the SINQ neutron source in Switzerland, a constant beam of neutrons is produced via spallation, leading to a white beam of neutrons, which require monochromation. The neutron sources at ISIS[1] in the UK and the Spallation Neutron Source (SNS) in the USA also produce neutrons with a range of wavelengths. The important difference here is that ISIS and SNS are pulsed neutron sources. Therefore, the protons that lead to spallation (Figure 2.8) at these sources arrive in packets (pulses) which causes the neutrons that are produced to be of a pulsed nature. This allows kinematics to be used to determine the wavelength, λ, of the neutrons calculated using,

$$\lambda = \frac{h\,(t + t_o)}{m_n\,(L + L_o)} \qquad (2.22)$$

[1]ISIS is not an acronym but is the name of a Greek goddess who could restore life to the dead. The ISIS neutron source was given this name as it was constructed using parts from older accelerators. The Isis is also a name given to a part of the River Thames that flows through Oxford.

where t is the time between the proton pulse hitting the target nuclei (Figure 2.8) and the neutrons being detected at a distance, L from the moderator. t_o and L_o are time and distance offsets that are calibrated for each instrument being used. Equation 2.22 allows the time-of-flight of the neutrons to be measured and this to be used to calculate their wavelength. The measurement of the scattering angle and the time-of-flight rather than the scattering angle alone enables pulsed neutron sources to use a broad range of different wavelengths simultaneously without the need to monochromate the neutrons.

2.4.2 ISIS and the SANDALS Diffractometer

The experiments detailed in this thesis have been conducted using the Small Angle Neutron Diffractometer for Amorphous and Liquid Samples (SANDALS) at the ISIS neutron source within the Rutherford Appleton Laboratory, UK. Therefore, the following description will focus on this spallation neutron source. A schematic diagram of the SANDALS instrument is shown in Figure 2.9. Table 2.2 compares the particles and energies during neutron production at ISIS and Figure 2.10 shows the layout of the components.

Table 2.2: Neutron Production at ISIS

Component	Particle	Energy
LINAC	H^-	70 MeV
Synchrotron	H^+	800 MeV
Proton Beam Line	H^+	800 MeV
Tungsten Target	H^+	800 MeV
Methane Moderator (100K)	N	1 MeV

The production of neutrons at ISIS begins with H^- ions (containing one proton and two electrons) drifting towards the linear accelerator (LINAC). These negative hydrogen ions are bunched together and accelerated using copper electrodes within the LINAC from energies in the region of 650 keV to around 70 MeV, producing bursts lasting 500 μsec every 20 msec (a frequency of 50 Hz). This ion beam then enters the synchrotron and the electrons are removed by passing the H^- ions through a sheet of alumina to produce protons (H^+ ions). The synchrotron is then used to accelerate the proton bunches from 70 MeV up to 800 MeV. These protons are then steered using magnets and collide with the tungsten target where spallation occurs (see Figure 2.8). After spallation, the neutrons are moderated using a methane moderator. This methane
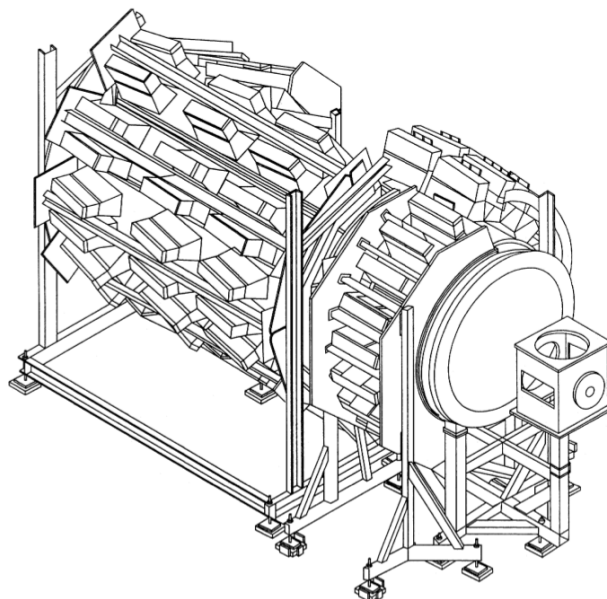
Figure 2.9: Schematic diagram showing the Small Angle Neutron Diffractometer for Amorphous and Liquid Samples (SANDALS) at the ISIS neutron source.

moderator decelerates the neutrons at SANDALS to have a wavelength in the range of 0.05 to 4.50 Å. The pulsed nature of the neutrons that are produced in this manner means that time of flight measurements can be made without the need for the neutrons to be monochromated (See Equation 2.22 and the latter part of Section 2.4.1). Therefore, a larger proportion of the neutrons can be used for measurements compared to reactor-sourced neutrons.

Since 2009, a second target station has been operational at ISIS. Now, every 5th proton pulse is sent to this second target station. Therefore, the neutron pulses arrive at instruments on Target Station 1 (such as SANDALS) with an average frequency of 40 Hz and at Target Station 2 with an average frequency of 10 Hz. There is a range of different experimental techniques that can be used at ISIS, including instruments designed for, neutron reflectometry (*e.g.* Crisp and Offspec), neutron spectroscopy (*e.g.* MARI and Let), small angle scattering (*e.g.* LoQ and Sans2D) and neutron diffraction (*e.g.* NIMROD and SANDALS). Neutron reflectometry measurements are used to study the structure of thin films, a particular interest of the materials science field. Neutron spectroscopy measurements are used to study the atomic and magnetic motions of atoms. Small angle scattering and neutron diffraction measurements study the structure of samples at different length scales. Table 2.3 details the Q-range (reciprocal space) and
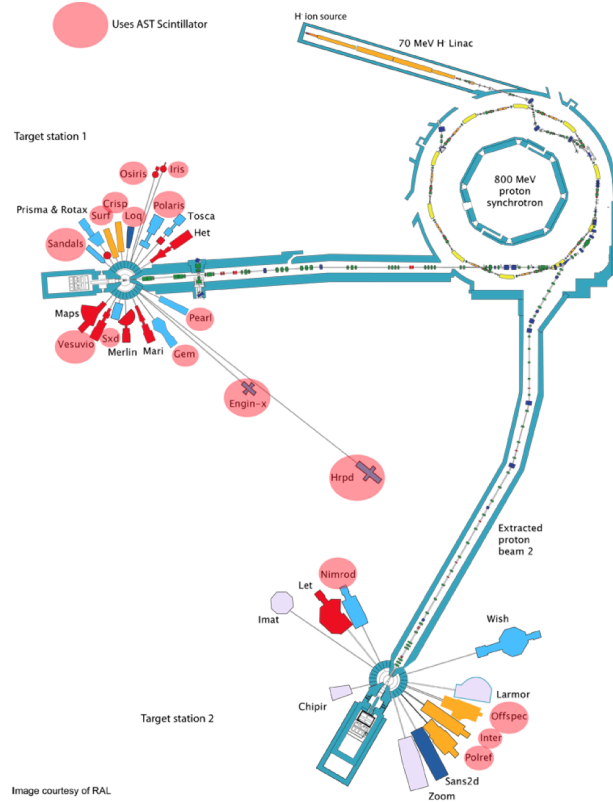
Figure 2.10: Diagram of the ISIS spallation neutron source.

corresponding r-range (real space) that can be found using neutron diffraction (NIMROD and SANDALS) and small angle scattering (LoQ and SANS2D) instruments[1].

Table 2.3: Neutron Diffraction and Scattering Detectors at ISIS

Detector	$Q_{min}(\text{Å}^{-1})$	$Q_{max}(\text{Å}^{-1})$	$r_{min}(\text{Å})$	$r_{max}(\text{Å})$
LoQ	0.06	1.4	4.49	1,047.2
SANS2D	0.002	3.0	2.09	3,141.6
SANDALS	0.10	50	0.13	62.8
NIMROD	0.02	100	0.06	314.2

Hydrogen bonds are of particular interest in this study and have an oxygen-hydrogen separation of $\sim$ 1.8 Å. The small angle scattering instruments (LoQ and SANS2D) do not have access to the length scales required for this. Neither LoQ nor SANS2D can obtain information at this length scale as they have minimum length scales (r_{min}) of 4.49 and 2.09 Å respectively. This is the motivation behind using neutron diffractometers rather than small angle scattering instruments for the work detailed in this thesis.

---

[1]Diffraction and scattering are not separate things. Rather, diffraction is coherent and elastic scattering.

2.4.3 Neutron Detection

Neutrons are highly penetrating particles, which is extremely useful when one is intending to study the bulk structure of a system of interest. The challenge, however, comes when the aim is to detect the neutrons. Detection requires the neutron to be captured by a nucleus within the detector, typically leading to one of the following reactions,

$$^{3}He + n \rightarrow {}^{3}H + p + 0.8 \,\text{MeV}$$

$$^{10}B + n \rightarrow {}^{7}Li + {}^{4}He + 2.3 \,\text{MeV}$$

$$^{6}Li + n \rightarrow {}^{4}He + {}^{3}H + 4.8 \,\text{MeV}$$

(2.23)
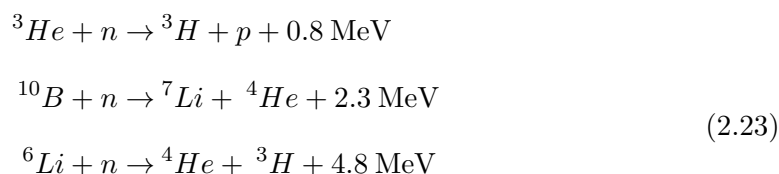
The SANDALS instrument uses ZnS scintillation detectors, which are doped with silver (Ag) and lithium ions (^{6}Li). The ^{6}Li ions absorb a neutron and emit an α -particle, a tritium particle (^{3}H) and a large amount of energy (see Equation 2.23 and Figure 2.11).
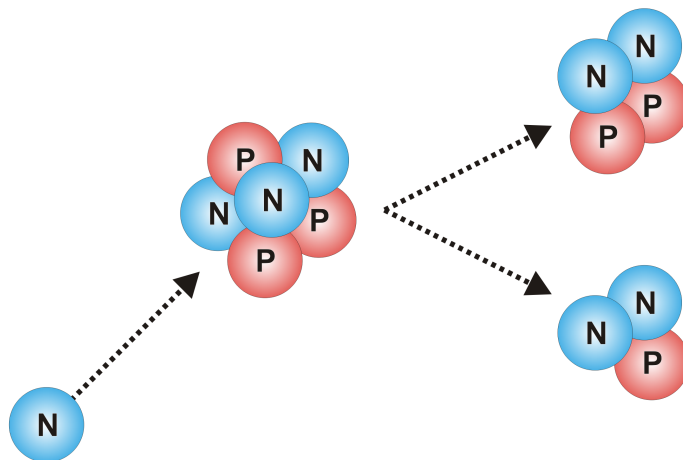
Figure 2.11: Schematic diagram showing the particles given off when a lithium atom absorbs a neutron. This reaction is required for neutrons to be measured in a detector.

The energy released causes an excitation of an electron within the ZnS lattice. This excited electron combines with a hole to create a quasi-particle known as an exciton, which travels along the ZnS lattice until it reaches an impurity activator; in this case the activator is a silver atom. The electron and hole recombine at the Ag atom site and a photon is emitted. This photon is of a lower energy than that required to excite the ZnS atoms, and thus passes through the detector to the photomultiplier tube (PMT), see

Figure 2.12. The PMT multiplies the size of the signal from the single photon and allows it to be measured by the electronics inside the detector. The SANDALS instrument shown in Figure 2.9 contains 633 ZnS detectors in arrays giving a continuous angular range of 3° to 40°. This provides a Q-range of 0.1-50 Å^{-1} leading to access of structures with length scales of 0.1-62.8 Å.
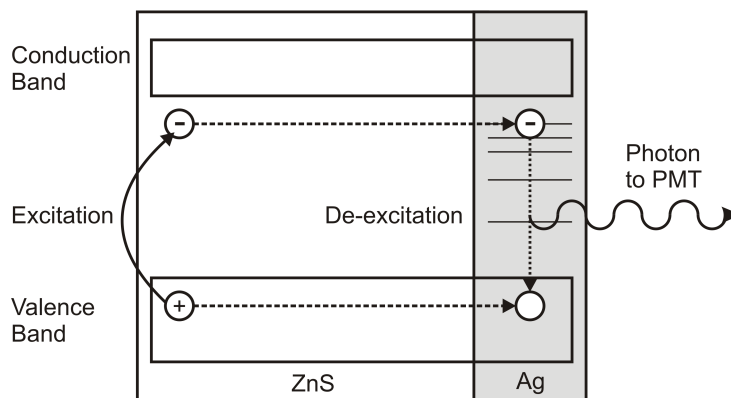
Figure 2.12: Schematic diagram showing the zinc-sulphide (ZnS) detectors used on the SANDALS instrument. Here, the energy released when a lithium atom absorbs a neutron causes an electron from the ZnS to become excited. This produces an exciton (electron and hole pair) which travels along the ZnS lattice until reaching a silver (Ag) atom. The Ag atom is an impurity activator and causes a photon to be released as the electron and hole re-combine. This photon is detected when a neutron is incident on the detector.

2.4.4 Processing Raw Neutron Diffraction Data

This section discusses the method used to process the raw neutron diffraction data to calculate the structure factor, $F(Q)$, and partial structure factors, $S_{\alpha\beta}(Q)$, discussed in Section 2.3.1. When using SANDALS, the samples are held within titanium-zirconium (TiZr) containers (see Figure 2.13) leading to a sample size to 35mm height $\times$ 35mm width $\times$ and 1mm thickness (a volume of around 1.3 cm^3). The raw data is measured as the number of counts recorded by each detector. Each count is due to the detection of one neutron. The use of time-of-flight measurements means that the data are of the form counts μs^{-1}. The data rate is given by normalising the counts μs^{-1} to the rate of neutron pulses to leave the data in units of counts μs^{-1} neutron pulse^{-1}.
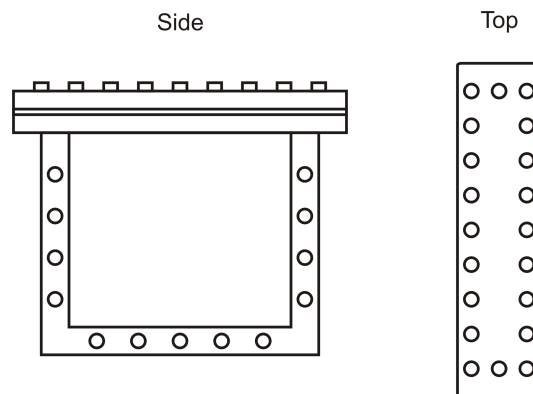
Figure 2.13: Schematic diagram of the flat-plate titanium zirconium containers used to hold samples. The side view shows the holes that are used to attach the sample can to the automatic sample changer. The top view shows the screws used to attach the top of the can to form an airtight seal.

In order to extract the structure factor from the experimental data, the following neutron diffraction experiments must be completed:

- Empty Instrument

- Vanadium Standard

- Empty Container

- Sample Data

These data sets are processed with the *Gudrun* routines (97) (based upon the algorithms in the widely used *ATLAS* package (98)). Alan Soper wrote the *Gudrun* codes with contributions from other members of the disordered materials group at ISIS (for example (99; 100)). The motivation for completing this procedure is to remove unwanted information in the signal (from the sample container and inelastic scattering *etc.*) and put the data on an absolute scale using,

$$\text{Corrected Result} = \frac{(\text{Sample Data} - \text{Empty Container})}{(\text{Vanadium Standard} - \text{Empty Instrument})} \qquad (2.24)$$

Before this can be applied, corrections must be made to eliminate the effects of faulty detectors. The removal of faulty detectors is performed using a routine known as *Purge*. Here, detectors are placed in groups and the standard deviations within each group are compared. A large standard deviation is caused by a noisy dataset and a very small

standard deviation would be caused by a weakly counting detector[1]. These are removed prior to further analysis in an iterative manner.

The next step in the data correction is the removal of effects due to attenuation. Here attenuation is used to mean both multiple scattering and absorption events. For most atom types, the total scattering cross-section, $\sigma^{tot}(\lambda)$, can be expressed as,

$$\sigma^{tot}(\lambda) = \sigma^s(\lambda) + \sigma^a(\lambda) \tag{2.25}$$

where $\sigma^s(\lambda)$ is the scattering cross-section and $\sigma^a(\lambda)$ is the absorption cross-section. For some systems the cross-sections are independent of wavelength, λ, and can be found in Sears Tables (92). There are exceptions to this case, which arise when there are large inelastic scattering signals, such as with hydrogen and deuterium. For these light atoms, the transmission cross-section, $\sigma^{trans}(\lambda)$, must be measured.

$$\sigma^{trans}(\lambda) = e^{-\rho \sigma^{tot}(\lambda) L} \tag{2.26}$$

where ρ is the sample density and L is the sample thickness. The use of a flat plate sample container allows L to be calculated simply because the thickness of the sample is the same across the whole neutron beam (see Figure 2.13). This calculation is more complicated when cylindrical sample containers are used (such as for high pressure studies) as the sample thickness varies across the neutron beam. All of the experiments detailed in this thesis were conducted at a pressure of 1 atm, therefore no equipment was required to generate this pressure. As such, flat plate sample containers were used for all the experiments detailed in this project. The measurement of $\sigma^{trans}(\lambda)$ is collected simultaneously with the other data sets. Therefore, if the density of the sample is known, and the transmission cross-section measured, the total scattering cross-section can be found using Equation 2.26. The effects of multiple scattering (when a neutron has interacted more than once within the sample) can be estimated using the theory outlined in the literature (99).

Each of the datasets is then normalised to remove the effect of changes in the levels of incident neutrons (known as neutron flux). The neutron flux in measured using a

---

[1]Here a noisy detector is defined as one with a standard deviation of more than 10 times the average standard deviation for a detector in the relevant group. Similarly a weakly counting detector will have a standard deviation of less than one tenth of the average

monitor, with very low efficiency, placed within the incident beam. The low efficiency of the monitor allows the flux to be measured whilst still allowing a large proportion of the neutrons to reach the sample to produce the diffraction pattern.

The measured diffraction data are then converted to an absolute scale using a vanadium standard. As mentioned in Section 2.2.1, vanadium provides a signal that is almost exclusively incoherent. As vanadium is a heavy metal, the corrections for inelasticity and multiple scattering can be completed relatively simply using Equation 2.25. This allows the calculation in Equation 2.24 to be completed, leaving the data on an absolute scale of (barns atom^{-1} sr^{-1}) [1]. These calculations and measurements replace the simple assumptions detailed in Section 2.3.1 and therefore allow access to the structure factor, $F(Q)$, given in Equation 2.16.

2.4.5 Data Handling for Glycerol-Water Studies

As stated previously, the aim of analysing the neutron diffraction data is to extract both the structure factor, $F(Q)$, and partial structure factors, $S_{\alpha\beta}(Q)$, discussed in Section 2.3.1. In this thesis there are two distinct atomic components in water and six distinct atomic components in glycerol molecules (see Figure 2.14). In the water molecule, the oxygen atom is labelled OW, and the hydrogen atom is labelled HW. In glycerol, the carbon atoms are labelled CC and CG, and refer to the central and distal carbon atoms respectively. The central oxygen is labelled OC and the distal oxygen atoms are labelled O. The hydrogen atoms are labelled H and HG for the hydroxyl and methyl hydrogen atoms respectively.

A full set of partial structure factors for this system of 8 different atomic labels ($N = 8$) would require the determination of,

$$\frac{N \cdot (N + 1)}{2} = 36 \tag{2.27}$$

different partial structure factors and radial distribution functions. Equation 2.27 can be understood by thinking about a sample that contains only water. In that sample there would be two different atoms, hydrogen and oxygen, and three possible partial structure factors: oxygen-oxygen, oxygen-hydrogen, and, hydrogen-hydrogen. In Section 2.2 it

---

[1]Here "sr" stands for steradian, which is a measure of solid angle. This can be pictured as the proportion of the surface of a sphere that is taken up multiplied by 4π .
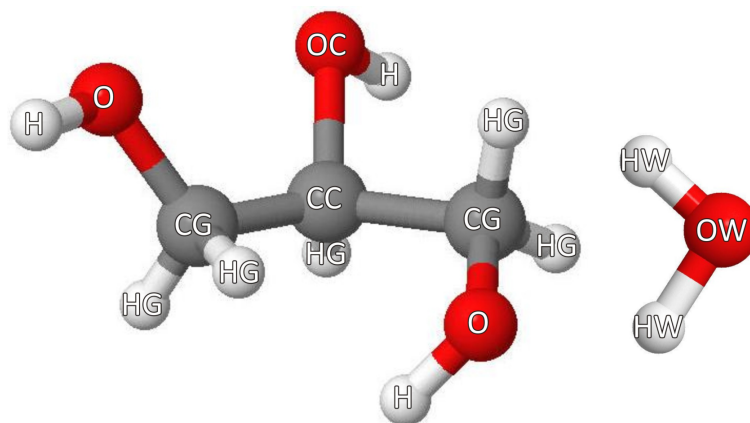
Figure 2.14: The glycerol (left) and water (right) molecules showing the atomic labels. In water, the oxygen atom is labelled OW and the hydrogen atom is labelled HW. In glycerol, the central carbon atom is labelled CC and the distal carbon atoms are labelled CG. The oxygen atoms are labelled OC and O, and refer to the central and distal oxygen atoms respectively. The hydroxyl hydrogen atoms are labelled H and the methyl hydrogen atoms are labelled HG.

was shown that different isotopes produce different signals. This can be harnessed by completing a number of experiments on the same system using two different isotopes of hydrogen.

Table 2.4: Isotopes Used

Sample No.	Sample Name	Description
i	Glycerol-D8-D2O	fully deuterated glycerol with D_2O
ii	Glycerol-D5-H2O	carbonyl atoms are deuterium and hydroxyl atoms are hydrogen with Milli-Q water
iii	Glycerol-D5HD3-HDO	1:1 mixture of samples i and ii with a 1:1 mixture of Milli-Q water and D_2O
iv	Glycerol-H8-H2O	fully protiated glycerol with Milli-Q water
v	Glycerol-HD8-HDO	1:1 mixture of samples i and iv with a 1:1 mixture of Milli-Q water and D_2O

Table 2.4 shows the different isotopic substitutions used for each of the aqueous glycerol samples. A similar range of isotopic substitutions was used for the pure glycerol experiments. These different experiments allow access to some of the partial structure factors, but not all 36. The reason that a full set of partial structure factors cannot be found is two-fold: it is very costly to use isotopic substitution of carbon or oxygen when compared to hydrogen, and, the differences in the scattering lengths are minimal for

these atoms. For example, the scattering length for ^{12}C is 6.65 fm and for ^{13}C is 6.19 fm (a difference of 7 %) and for ^{16}O is 5.80 fm and ^{17}O is 5.78 fm (a difference of 0.4 %). These differences are much smaller than the 44 % difference between hydrogen (3.74 fm) and deuterium (6.67 fm). Therefore, it is unlikely that much useful information could be extracted by completing such expensive additional experiments, so they were not included. A method is needed that allows all 36 of the partial structure factors to be extracted from the 5 isotopically different experiments. This technique (described in Section 2.5) is known as Empirical Potential Structure Refinement (EPSR) and uses computational modelling to extract these partial structure factors.

2.5 Computational Modelling

This section describes the computational modelling program, Empirical Potential Structure Refinement (EPSR). In a similar manner to *Gudrun*, EPSR was created by Alan Soper with contributions from the Disordered Materials Group at ISIS (101–104). The aim of the following section is to focus on the key points of EPSR, as an exhaustive account of the technique is well beyond the scope of this thesis.

EPSR is a form of Monte Carlo simulation that is used to produce an atomistic level model of the system under consideration. The EPSR model is then compared to the experimental data and iteratively modified until agreement with the experimental structure factors is found. The EPSR model is then interrogated to study the structure and bonding of the system of interest.

Figure 2.15 shows a summary of the main steps that are completed when using EPSR. Sections 2.4.4 and 2.4.5 describe how the data are corrected and how the experimental structure factors are extracted (Figure 2.15(a)). Section 2.5.1 describes the method of producing a simple model and calculating the structure factor of the model (Figure 2.15(b)). The process that is used to produce an empirical potential, which drives the simulated structure factor towards that taken from the experiment (Figure 2.15(c)), is then discussed.
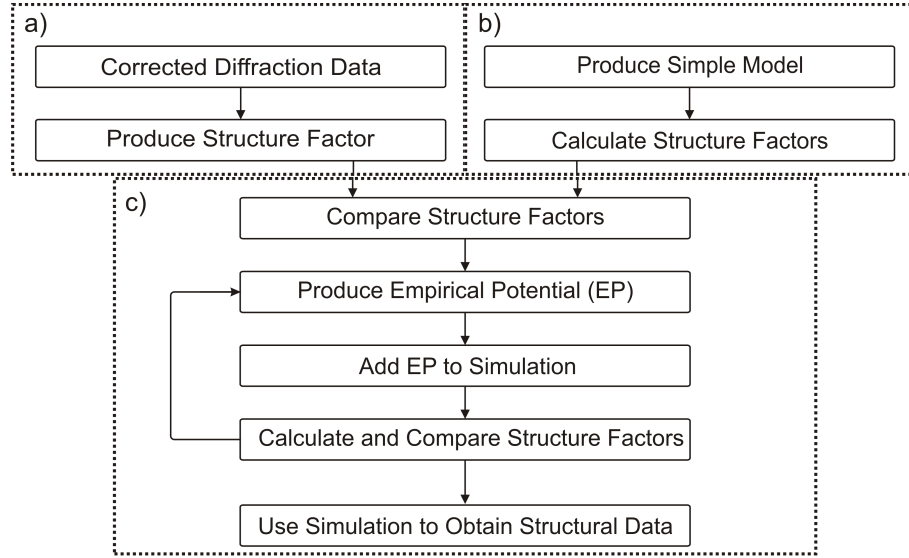
Figure 2.15: Flow diagram showing the steps involved in EPSR. (a) Neutron diffraction data is corrected and the structure factors are extracted. (b) A simple model is produced using reference potentials. The simulated structure factor is then calculated. (c) The model is driven towards the experimental data by modifying the potentials between the atoms. Once agreement between the experimental and simulated structure factors is found the simulation is used to extract the relevant information.

2.5.1 Producing a Model Using Empirical Potential Structure Refinement (EPSR)

The EPSR process begins with a standard Monte Carlo simulation of the system. The first step is to define a reference potential (U_{ref}),

$$U_{ref} = U_{intra} + U_{inter} \qquad (2.28)$$

where U_{intra} is the intramolecular potential and U_{inter} in the intermolecular potential. This will be combined with an empirical potential (U_{emp}) to produce the total potential (U_{tot}) used in Section 2.5.3. U_{intra}, is defined as,

$$U_{intra}(r_{ij}) = C \sum_{i} \sum_{\alpha\beta \neq \alpha} \frac{(r_{\alpha_i\beta_i} - d_{\alpha\beta})^2}{2w_{\alpha\beta}^2} \qquad (2.29)$$

where C is a constant, $d_{\alpha\beta}$ is the average separation and $r_{\alpha_i\beta_i}$ is the actual separation, of atoms i and j which are of atom types α and β respectively. The broadening function

$w_{\alpha\beta}^2$ is given by,

$$w_{\alpha\beta}^2 = \frac{d_{\alpha\beta}}{\sqrt{\mu_{\alpha\beta}}} \tag{2.30}$$

where $\mu_{\alpha\beta}$ is the reduced mass of the atom pair and is calculated using,

$$\mu_{\alpha\beta} = \frac{M_\alpha M_\beta}{M_\alpha + M_\beta} \tag{2.31}$$

$w_{\alpha\beta}^2$ has the effect of smearing the molecule structure and accounting for thermal fluctuations[1].

Within EPSR, intra-molecular bond angles are not explicitly defined. A bond angle $\overline{ABC}$ is defined by the two bonded pairs $\overline{AB}$ and $\overline{BC}$ and a pseudo-bond $\overline{AC}$. Therefore, adding a pseudo-bond between the first and last atoms imposes a bond angle. This bond angle naturally has a range of possible angles due to the smearing of the bond lengths as described by Equation 2.29. Dihedral angles can be defined in a similar way and this is discussed in greater detail in Chapter 3.

The inter-molecular potential, U_{inter}, between two particles, i & j of type α & β respectively, as a function of radial distance, r_{ij}, is based on the Lennard-Jones 12-6 potential along with Coulomb terms and is defined as,

$$U_{inter}(r_{ij}) = 4\epsilon_{\alpha\beta}\left[\left(\frac{\sigma_{\alpha\beta}}{r_{ij}}\right)^{12} - \left(\frac{\sigma_{\alpha\beta}}{r_{ij}}\right)^6\right] + \frac{q_\alpha q_\beta}{4\pi\epsilon_0 r_{ij}} \tag{2.32}$$

here, ϵ_0 is the permittivity of free space, q_α is the charge on atom α, $\sigma_{\alpha\beta}$ is the inter-particle distance at which the potential is zero, and, $\epsilon_{\alpha\beta}$ is the distance at which the potential between atoms α and β has its minimum value, see Figure 2.16.

The Lennard-Jones parameters, which are defined for each atom type, are combined using Lorentz-Berthelot mixing rules to provide (33),

$$\sigma_{\alpha\beta} = \frac{1}{2}(\sigma_\alpha + \sigma_\beta)$$
$$\epsilon_{\alpha\beta} = (\epsilon_\alpha \epsilon_\beta)^{\frac{1}{2}} \tag{2.33}$$

EPSR uses periodic boundary conditions. That is, when a particle leaves one side of the simulation box (all boxes used for this work are cubic) it re-enters on the opposite

---

[1]This broadening of the bond lengths in shown in Figure 3.7(b).
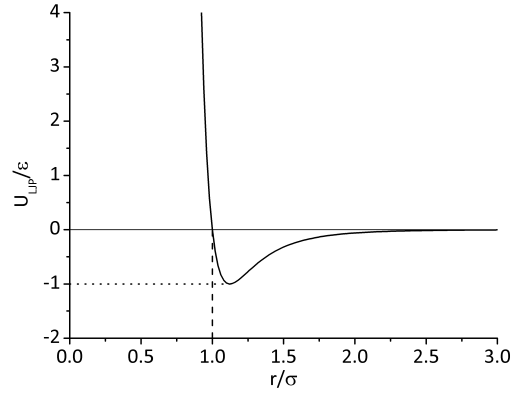
Figure 2.16: The Lennard-Jones potential (U_{LJP}) as a function of radial distance (r). The radial distance where U=0 is given by σ and the potential minimum is given by ϵ.

side. This holds the number of particles in the simulation constant throughout the simulation. EPSR deals with the long-range Coulomb potentials in a similar way to the reaction field method (105). In the reaction field method, a particle is assumed to be at the centre of a sphere over which it can have an influence. Outside of this sphere there is a uniform background potential. Therefore, the truncation factor for the Coulomb potentials, $T_c(r)$, is given as,

$$T_c(r) = \left(1 - \frac{r}{r_{maxpt}}\right)^4 \left(1 + \frac{8r}{5r_{maxpt}} + \frac{2r^2}{5r_{maxpt}^2}\right) \Theta(r_{maxpt} - r) \qquad (2.34)$$

where $\Theta(r_{maxpt} - r)$ is the Heaviside function which is a step function that equals zero for $r_{maxpt} < r$ and one for $r_{maxpt} > r$. Therefore, Equation 2.34 only acts on the Coulomb potentials at separations above r_{maxpt}.

The non-Coulomb part of the potential is given by the Lennard-Jones potential from Equation 2.32, and the empirical potential of Equation 2.36. This part of the potential is truncated smoothly by multiplying the potential by a truncation factor, $T(r)$, given by,

$$T = \begin{cases} 1 & r < r_{minpt} \\ 0.5 & \left(1 + \cos \pi \left(\frac{r - r_{minpt}}{r_{maxpt} - r_{minpt}}\right)\right) r_{minpt} < r < r_{maxpt} \\ 0 & r > r_{maxpt} \end{cases} \qquad (2.35)$$

In all of the work detailed in this thesis, r_{maxpt} is set at 12 Å, and is the distance at which the Coulomb potential truncation begins and the maximum distance for the non-

Coulombic potentials. The distance at which the non-Coulombic potentials begin to be truncated is given by r_{minpt} and is set to 9 Å. When using EPSR, reference potentials are obtained from literature sources, such as the Optimised Potentials for Liquid Simulation (OPLS) (32), chemical structure optimisation software, or other sources. The potentials used for glycerol in this study have been taken from the Ghemical software (106) and the water potentials are taken from the Simple Point Charge (SPC) model (107). The potentials and molecular geometry used can be found in Appendix A, and are discussed in greater detail in Chapter 3.

Standard Monte Carlo steps with the Metropolis condition are used to bring the simulation to equilibrium (34). Here, up to four possible types of small movement are permitted; whole molecule translation, whole molecule rotation, molecular side-chain rotation and atomic translation. For side-chain rotations, the axis of rotation is defined when the molecule is set up. A movement is accepted based on the Metropolis condition, which states that when the change in potential energy due to the movement, ΔU is negative, the movement is accepted. When ΔU is positive, the movement is accepted with a probability of $e^{-\frac{\Delta U}{kT}}$. This procedure continues until equilibrium is reached.

Once equilibrium has been reached, the structure factor that would be produced if a neutron diffraction experiment were run on the EPSR simulation box is calculated using Equation 2.16. To complete this, values are required for each of the RDFs ($g_{\alpha\beta}(r)$), the atomic concentrations (c_α) and scattering lengths (b_α). The RDFs and atomic concentrations are taken from the EPSR simulation. To find the values of the scattering lengths the presence of hydrogen/deuterium exchange must be included. Here, a hydrogen atom that is covalently bound to one molecule is replaced by a deuterium atom, or *vice versa*. In the EPSR simulations detailed in this thesis, the hydrogen atoms that are susceptible to exchange are those on the water molecules and the hydroxyl groups of the glycerol molecules. Here, it is assumed that the hydrogen/deuterium exchange is not dependent on the molecule that the hydrogen/deuterium atom is covalently bound to. Therefore, the proportion of water hydrogen atoms (HW in Figure 2.14) that are hydrogen is equal to the proportion of hydroxyl hydrogen atoms (H in Figure 2.14) that are hydrogen. This provides the values of (b_α) required to calculate the simulated structure factors. These simulated structure factors ($D(Q)$) are then compared to the experimentally measured structure factors ($F(Q)$), and an empirical potential is added

to the EPSR simulation. The empirical potential and its production are described in the following sections.

2.5.2 The Empirical Potential

This section contains a description of the empirical potential, U_{emp}, and how it is produced. The aim of U_{emp} is to account for differences between the experimentally measured structure factor, $F(Q)$, and the simulated structure factor, $D(Q)$. The empirical potential is given by a series of power exponential functions of the form,

$$U_{emp}(r) = kT \sum_i C_k \, p_{n_k}(r, \sigma_r) \tag{2.36}$$

where $k = 0, 1, 2, 3, 4, \ldots i$, T is the temperature, C_k are constants described below, σ_r is a width function with a value of 0.01 Å and, p_{n_i} is given by,

$$p_n(r, \sigma) = \frac{1}{4\pi\rho\sigma^3(n+2)!} \left(\frac{r}{\sigma}\right)^n e^{-\left[\frac{r}{\sigma}\right]} \tag{2.37}$$

An important factor is that Equation 2.37 has a direct three-dimensional Fourier Transform in Q-space given by,

$$
\begin{aligned}
P_n(Q, \sigma) &= 4\pi\rho \int p_n(r) e^{i\mathbf{Q}\cdot\mathbf{r}} d\mathbf{r} \\
&= \frac{1}{(n+2)\left(\sqrt{1+Q^2\sigma^2}\right)^{(n+4)}} \left[2\cos(n\alpha) + \frac{(1-Q^2\sigma^2)}{Q\sigma}\sin(n\alpha)\right]
\end{aligned} \tag{2.38}
$$

here $\alpha = tan^{-1}(Q\sigma)$. This allows the coefficients, C_k to be estimated directly from the diffraction data. Here, a series of the form,

$$U_{emp}(Q) = \sum_i C_k P_{n_i}(Q, \sigma_Q) \tag{2.39}$$

where σ_Q is a width function with a value of 0.003 Å, is fitted to the difference between the experimentally measured and simulated data in Q-space.

An inter-molecular empirical potential, $U_{emp}^{\alpha\beta}$, is added between each of the atomic pairs $\alpha\beta$. Here, the simulated partial structure factors are calculated using Equation

2.17 and the RDFs taken from the EPSR simulation. The experimental partial structure factors are estimated using the method of Soper (103). This allows coefficients $C_k^{\alpha\beta}$ to be produced for each of the partial structure factors and radial distribution functions. These coefficients are then used in Equation 2.36 to produce the empirical potential used in the simulation. The total potential between atoms of type α and β is then given by the summation of the potentials described in Equations 2.29, 2.32 and 2.36

$$U_{tot}(r) = U_{intra}(r) + U_{inter}(r) + U_{emp}(r) \tag{2.40}$$

Once the empirical potential has been added to the system, the differences between the experimentally measured structure factor, $F(Q)$, and the new simulated structure factor, $D(Q)$, are calculated. The next step is to iteratively improve the empirical potential, which is described below.

2.5.3   Refining the Potentials

/Applications/TeX/My Thesis in John's Format/Methods/Chapter2.tex

The loop shown in Figure 2.15(c) denotes the repeated production of the coefficients C_k, shown in Equation 2.39. This loop is repeated until one of two possible criteria is reached: the difference between the coefficients from the mth iteration and the $(m+1)^{th}$ iteration reaches zero, or, the absolute value of the empirical potential reaches a defined limit. In all of the work detailed within this thesis, the empirical potential has reached the defined limit. In an ideal world there would be no need to limit the size of the empirical potential, the data would be perfect and the simulation would eventually find a result that gave the same result as the experiment. This, however, is not possible as some artefacts remain in the neutron diffraction result. For the empirical potential to fit to these artefacts, some unphysical features, such as atomic overlap, would be introduced. Therefore, a limit on the empirical potential is introduced to prevent unphysical features from arising. Once the empirical potential has reached this limit, the quality of the fit can be measured using the R-Factor. The R-Factor is given by,

$$R = \frac{1}{M} \sum_i \frac{1}{n_Q(i)} \sum_Q [D(Q) - F(Q)]^2 \tag{2.41}$$

here, $n_Q(i)$ is the number of Q values found in data set i and M is the number of data sets used (*i.e.* the different isotopic substitutions). This method of calculating the quality of fit is discussed in greater detail in Chapter 3. The next step is to acquire ensemble averages of the structure of the EPSR simulation box. The RDFs can be calculated from these ensemble averages. These RDFs are used to constrain auxiliary routines, which measure the intermolecular bond angle distributions, coordination numbers (see Equation 2.18) and molecular cluster sizes. It is these auxiliary routines that form the basis of the results listed in Table 2.5 and discussed in Chapters 3, 4, 5, and, 6.

Table 2.5: Auxiliary Routines

Routine Name	Description	Where Routine Used
COORD	Calculates co-ordination numbers	3.3.2, 3.3.3, 4.4.3 and 6.3.2
TRIANGLES	Measures the included angle between three atoms	3.3.4, 4.3.3 and 6.2.4
TORANGLES	Determines the dihedral angle between four atoms. A full description can be found in Sections 3.1.1 and 3.2.1	3.2.2, 4.2.1 and 6.1.3
CLUSTERS	Calculates cluster size distributions See Section 5.1.3 for a full description	5.2.1, 5.2.2, 5.3.1, 5.3.2, 6.4.1 and 6.4.2

2.6   Methods Summary

This chapter describes the motivation behind using the combination of neutron diffraction with isotopic substitution and EPSR to study aqueous glycerol. Section 2.1 shows that structure can be found by measuring the interaction of a wave with a sample. Section 2.2 explains that neutron scattering is sensitive to the position of hydrogen atoms and that the Fourier Transform of the diffraction pattern can be used to calculate the structure of a sample. Section 2.3 shows how the partial differential scattering cross-sections can be found from the total scattering cross-section. Section 2.4 explains why neutron diffraction is chosen over other neutron-based techniques to find the structure and details the specific properties of the instrument used in this study. Finally, Section 2.5 describes the method of producing a computational model to extract all of the re-

quired data. The following chapters use the methods detailed here to investigate the structure of aqueous glycerol solutions.

Chapter 3

The Structure of Pure Glycerol

3.1 Context

Research into the structure of pure glycerol in the liquid state is of great interest (see Sections 1.1 and 1.1.3).The interaction between intra- and inter-molecular interactions determine liquid structure (19). Therefore, the question for the pure liquid glycerol is: is the structure dominated by intra- or inter- molecular interactions? This question is investigated here by comparing previously published data, including results regarding the crystal structure of glycerol found using X-ray diffraction (60) and the gas phase results of computational calculations (61), with results produced using a combination of neutron diffraction and computational modelling on the liquid.

This study of the structure of pure glycerol in the liquid state is important with regard to the investigation of aqueous glycerol. The structure of pure water has been studied many times using neutron diffraction and EPSR (101; 102; 108)[1], however, this technique had not been used to probe pure glycerol. Therefore, the structure of pure glycerol is investigated here using neutron diffraction and EPSR. This enables modifications within the structure of glycerol (or water) upon mixing to be found. The structure of glycerol is particularly interesting because all of the covalent bonds within the molecule are single (see Figure 2.14). Therefore, glycerol can be considered as a saturated molecule. This means that only one electron is shared with each neighbouring atom, and that each of these bonds has considerable rotational freedom. Consequently, glycerol molecules can adopt a large range of different structural conformations. The

---

[1]In fact water has been investigated using EPSR since before it was called EPSR. The original name for the program was Empirical Potential Monte Carlo.

method used to define these structures is discussed in Section 3.1.1 and the relevant results are shown in Section 3.2.

In Section 1.1.1, the importance of hydrogen bonding is introduced and Chapter 2 details the methods that are used to access this information. The hydrogen bonding of pure glycerol has been studied previously using computational (58; 64–69) and experimental methods (63), however, these studies have produced contradictory results (see Tables 3.1 and 3.2). This may be due to the different criteria that were used to classify a hydrogen bond, as such the respective results are discussed below. Section 3.1.2 focuses on intra-molecular hydrogen bonding and Section 3.1.3 addresses inter-molecular hydrogen bonding. Section 3.3 describes the criteria that have been used for this study and details the results that have been found. The main body of this chapter has been published previously (1).

3.1.1   Intra-Molecular Structure of Glycerol

Before discussing the intra-molecular structure of glycerol it is important to understand the method that is used to define this structure. A method used to classify the structure of glycerol is based upon the dihedral angles found within the molecule (59). A dihedral angle (denoted φ) is defined using the intersection between two planes setup within the molecule (see Figure 3.1). The first plane is defined using the vectors $\overline{AB}$ and $\overline{BC}$ and the second plane is defined using the vectors $\overline{BC}$ and $\overline{CD}$ (see Figure 3.1(a)). Here, it is the backbone conformation that is of particular interest. Therefore, the heavy atoms (carbon and oxygen) are used for this classification. One dihedral angle is formed by each of the distal oxygen-carbon-carbon-carbon quartets (denoted as O-CG-CC-CG in Figure 2.14). These angles are defined regardless of the hydrogen atom positions. Each of the dihedral angles is assigned a Greek letter based on the criteria of Bastiansen (59) given by,

$$
\begin{aligned}
\alpha &= 120^\circ < \varphi < 240^\circ \\
\beta &= 240^\circ < \varphi < 360^\circ \\
\gamma &= 0^\circ\ \ < \varphi < 120^\circ
\end{aligned}
$$

(3.1)
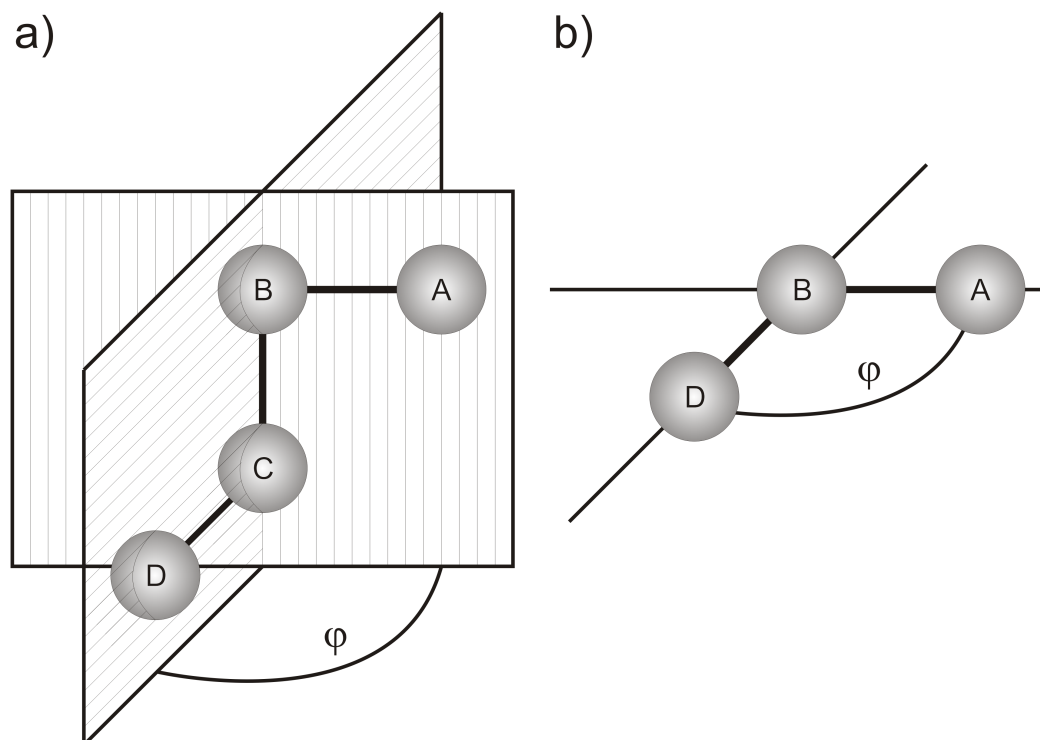
Figure 3.1: A diagram showing the calculation of a dihedral angle ($\overline{ABCD}$) in a simple four atom molecule. The four atoms are joined by three vectors: $\overline{AB}$, $\overline{BC}$ and $\overline{CD}$. (a) The two planes are given by pairs of vectors. The first plane is shown by vertical lines and is produced using the two vectors, $\overline{AB}$ and $\overline{BC}$. Similarly the second plane is constructed using the two vectors, $\overline{BC}$ and $\overline{CD}$. (b) The four atom molecule viewed along the $\overline{BC}$ vector. The atom labelled C is no longer visible as it is covered by the atom labelled B. Here, the angle φ can be clearly seen.

The structure of glycerol can be defined using Equation 3.1, along with measurements of the dihedral angles, to describe the molecule using the appropriate two letter expression. This leaves six possible conformations for the glycerol molecule, $\alpha\alpha$, $\alpha\beta$, $\alpha\gamma$, $\beta\beta$, $\beta\gamma$, and, $\gamma\gamma$. These are shown in Figure 3.2, in this figure, the hydrogen atoms are not shown on the molecules to aid clarity. There are only six conformations using this nomenclature because heterogeneous pairs, such as $\alpha\gamma$ and $\gamma\alpha$, are indistinguishable from one another. This nomenclature has been used in previous studies to investigate the structure of glycerol. This includes experimental investigations (57; 60; 62) and computational calculations (58; 61; 64–66). An X-ray diffraction study of crystalline glycerol found that glycerol molecules were of the $\alpha\alpha$ conformation (60). The structure of a crystal is much more well defined than that of a liquid (see Section 1.2.2) and therefore this is the accepted crystal structure of glycerol. The liquid phase, however, is less well defined. This is likely to have lead to the contradictory results within the
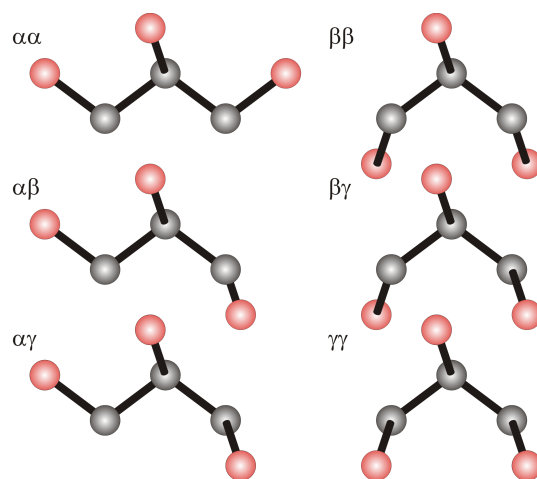
Figure 3.2: The six possible conformations of glycerol as defined by the dihedral angles described in Equation 3.1. Each of the two distal oxygen-carbon-carbon-carbon dihedral angles is defined as φ and given a letter α, β or γ leading to the conformations $\alpha\alpha$, $\alpha\beta$, $\alpha\gamma$, $\beta\beta$, $\beta\gamma$, and, $\gamma\gamma$.

literature.

Early neutron diffraction experiments of liquid glycerol were conducted at the Institut Laue-Langevin in the 1980s (57; 62). Both of these studies used a single, fully deuterated sample of liquid glycerol. The difference between the two studies being the diffractometer that was used. The D2 instrument allows a Q-range of up to 12 Å^{-1} (57) and the D4B diffractometer has a maximum Q value of 16 Å^{-1} (62). In these studies, χ^2 fitting was used to find an intra-molecular structure that gave a good agreement with the experimental data. Interestingly, these studies gave contradictory results with the conformation being described as $\alpha\alpha$ (57) and subsequently $\alpha\gamma$ (62). The difference between these two results could be due to the inter-molecular interactions not being included in the fitting procedure. A more recent neutron spectroscopy study was completed on fully deuterated glassy glycerol, which found that the conformation was $\beta\gamma$ at a temperature of 180 K (109). This study was completed using the MARI instrument at ISIS (mentioned in Section 2.4.2). The conclusions that can be drawn from these experimental studies are restricted due to the inability to separate the signals from different atoms unambiguously.

Purely computational methods have also been used to study liquid glycerol. Chelli *et al.* conducted a molecular dynamics study (64) using the AMBER molecular mechanics force-field (110). They found that the conformation of glycerol was made up of 48 % $\alpha\alpha$

and 46 % $\alpha\gamma$ (64). In a more recent density functional theory (DFT) based simulation study, Chelli *et al.* used B3-LYP functionals to optimise the structure of glycerol (65). The results from the DFT study broadly agreed with the previous result stating that 97 % of the molecules are either $\alpha\alpha$ or $\alpha\gamma$ (70 % $\alpha\alpha$ and 27 % $\alpha\gamma$) (65). The difference between these two investigations can be ascribed to the different methods used. The earlier study used molecular dynamics simulations alone (64), whereas the more recent study compared the structures that are taken from the DFT simulations with those found in IR spectroscopy measurements (65). Interestingly, the most stable (lowest energy) conformation for a single glycerol molecule was found to be $\gamma\gamma$ in a further study by Chelli *et al.* (61).

The state of the art of neutron diffraction measurements, and the associated modelling to extract the structure, has moved on significantly since the work of Champeney and Dore (57; 62). Consequently, an experimental determination of the intra-molecular structure was required. Modern neutron diffraction experiments, such as those described in this thesis, can exploit isotopic substitution (see Section 2.2) to allow the signals from different atom types to be distinguished from each other. The results of this study of liquid glycerol at room temperature are shown in Section 3.2.2.

3.1.2   Intra-Molecular Bonding in Liquid Glycerol

Hydrogen bonds (introduced in Section 1.2.3) are thought to be integral to the understanding of pure and aqueous glycerol. The hydrogen bond is, however, a complex phenomenon being partially electrostatic and partially covalent (111; 112). Therefore, a broad range of criteria have been used to define a hydrogen bond. This section introduces the definitions that have been used previously as criteria for an intra-molecular hydrogen bond within liquid glycerol. The following section details the criteria that have been used to define inter-molecular hydrogen bonds in liquid glycerol. Section 3.3.1 contains the definition that has been used for the present study of glycerol and its aqueous mixtures.

Computational simulations of liquid glycerol have suggested that the molecule forms intra-molecular hydrogen bonds, and that these stabilise the structure of the liquid. These previous studies have used a range of simulation based techniques (58; 64–66; 68) and are summarised in Table 3.1 and Figure 3.3. Root and Berne (68) conducted a
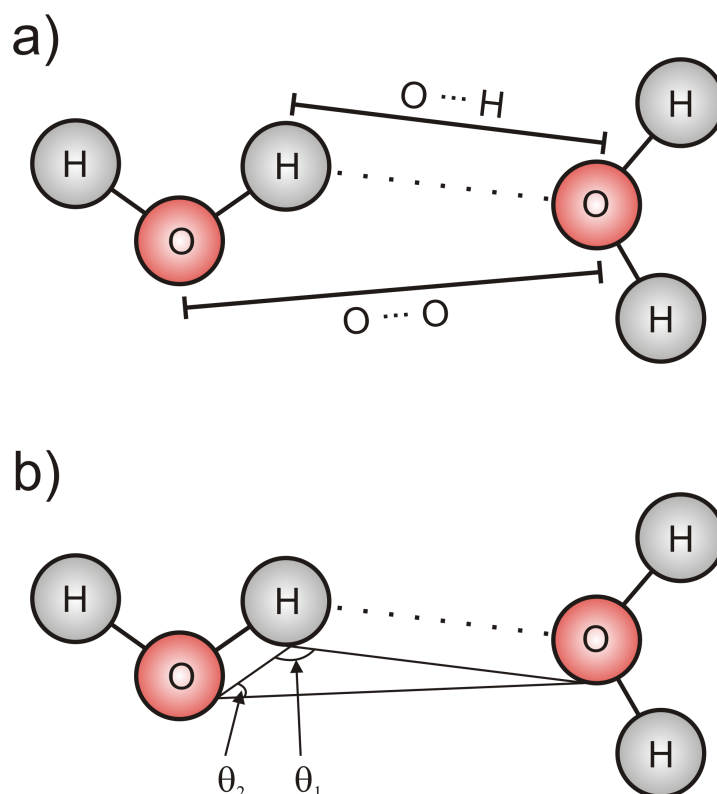
Figure 3.3: A diagram showing the different hydrogen bond criteria that have been used in previous studies. Here, two water molecules are used. The criteria are shown for separate molecules but equally hold for intra-molecular hydrogen bonding. (a) Distance criteria for the oxygen-hydrogen separation shown as "O$\cdots$H" and oxygen-oxygen separation are denoted "O$\cdots$O". (b) Angular contraints for oxygen-hydrogen$\cdots$oxygen are shown by θ_1 and hydrogen-oxygen$\cdots$oxygen angles are shown by θ_1.

simulation of 256 molecules at an average temperature of 298 K (the same temperature as the neutron diffraction experiments detailed in this chapter). They defined a hydrogen bond as having an oxygen-hydrogen$\cdots$oxygen angle of more than 135° and an oxygen-hydrogen separation of less than 2.55 Å. Chelli *et al.* also found the presence of intra-molecular hydrogen bonds (58; 64). Here, an intra-molecular hydrogen bond is defined as having an oxygen-hydrogen separation of less than 2.45 Å. Interestingly, no angular constraint was used for an intra-molecular hydrogen bond. A later study also suggested that intra-molecular hydrogen bonds act to stabilise the glycerol conformation (65). The cut-off in the more recent study was an oxygen-hydrogen separation of less than 2.50 Å and the inter-molecular hydrogen bond number was not calculated. In a DFT based simulation study, Zhuang and Dellago also found that intra-molecular hydrogen bonds

were formed (66). In their work they defined a hydrogen bond as having an oxygen-oxygen separation of less than 3.5 Å and a hydrogen-oxygen$\cdots$oxygen angle of no larger than 35°. This angular definition is subtly different from that mentioned previously. The results of the present study into the existence (or non existence) of intra-molecular hydrogen bond is given in Section 3.3.2.

Table 3.1: Intra-Molecular Hydrogen Bond Definitions and Results

Reference	Hydrogen Bond Definition	Average Hydrogen Bonds per Molecule
(67)	O$\cdots$H Separation $\leq$ 2.40 Å	0.16
(68)	O$\cdots$H Separation $\leq$ 2.55 Å and O-H$\cdots$O angle $\geq$ 135 °	0.16 at 0.1MPa 0.16 at 700 MPa
(58; 64)	O$\cdots$H Separation $\leq$ 2.45 Å	1 - 2
(65)	O$\cdots$H Separation $\leq$ 2.50 Å	1 - 3
(66)	O$\cdots$O Separation $\leq$ 3.50 Å and H-O$\cdots$O angle $\leq$ 35 °	0.80

3.1.3   Inter-Molecular Bonding in Liquid Glycerol

Similar to intra-molecular hydrogen bonds, the inter-molecular hydrogen bonding between glycerol molecules has been of significant scientific interest. This is due, in part, to the existence of an extended hydrogen bond network, which has been suggested to be the reason behind glycerol's macroscopic properties such as the viscosity of glycerol and its aqueous mixtures (113). Inter-molecular hydrogen bonding has been investigated by the computational studies detailed in Section 3.1.2 (58; 64; 66–68). It has also been the subject of a classical molecular dynamics study that makes no mention of intra-molecular bonding (69), as well as being used to explain X-ray diffraction measurements (63). The hydrogen bond definitions used in previous studies are detailed in Section 3.1.2. Padro *et al.* used a threefold hydrogen bond definition. In their work, a hydrogen bond is defined as having an oxygen-oxygen separation of less than 3.50 Å, an oxygen-separation of less than 2.60 Å and a hydrogen-oxygen$\cdots$oxygen angle of less than 30°. Table 3.2 and Figure 3.3 show the hydrogen bond definitions used by each of the simulation and experimental investigations. It can be seen that there is a large variation between the values that are calculated with the fewest hydrogen bonds being

3.09 (67) and the largest being 5.70 (66; 69).

Sarker and Joarder performed a re-analysis of X-ray diffraction measurements on pure glycerol from the literature for their study in 1996 (63). The Fourier transform of these results were taken and showed a prominent peak between 2.8 and 3.0 Å, which was attributed to hydrogen bonding. This peak was found to agree well with the peak that was calculated for a system where each glycerol molecule forms 6.5 hydrogen bonds with an average oxygen-oxygen separation of 2.95 Å (63). Section 3.3.3 details the results found using a combination of neutron diffraction and computational modelling.

Table 3.2: Inter-Molecular Hydrogen Bond Definitions and Results

Reference	Hydrogen Bond Definition	Average Hydrogen Bonds per Molecule
(67)	O$\cdots$H Separation $\leq$ 2.40 Å	3.09
(68)	O$\cdots$H Separation $\leq$ 2.55 Å and O-H$\cdots$O angle $\geq$ 135 $^\circ$	3.26 at 0.1MPa 3.68 at 700 MPa
(69)	O$\cdots$O Separation $\leq$ 3.50 Å O$\cdots$H Separation $\leq$ 2.60 Å and O-H$\cdots$O angle $\geq$ 135 $^\circ$	5.70
(58; 64)	O$\cdots$H Separation $\leq$ 2.45 Å O-H$\cdots$O angle $\geq$ 145 $^\circ$	3.40
(66)	O$\cdots$O Separation $\leq$ 3.50 Å and H-O$\cdots$O angle $\leq$ 35 $^\circ$	5.70
(63)	O$\cdots$ O Separation $\leq$ 2.95 Å	6.5

3.2 Investigating Intra-Molecular Structure within Liquid Glycerol

3.2.1 Defining Intra-Molecular Structure Using EPSR

As described in Section 2.5, bond angles ($\overline{ABC}$) are not explicitly defined within EPSR. Instead, a pseudo bond is included between the first and last atoms ($\overline{CA}$). This bond does not represent a physical bond between these atoms but constrains the angle $\overline{ABC}$ due to the law of cosines, which states:

$$\overline{CA}^2 = \overline{AB}^2 + \overline{BC}^2 - 2\overline{AB}\,\overline{BC}\ cos(\overline{ABC}) \tag{3.2}$$

Equation 3.2 shows that if the lengths $\overline{AB}$, $\overline{BC}$ and $\overline{CA}$ are defined then the angle, $\overline{ABC}$, is given. This technique, however, does not allow a dihedral angle to be defined. This is explained using Figure 3.4. Within EPSR a dihedral angle ($\overline{ABCD}$) is defined using a pseudo bond between the atoms A and D (see Figure 3.1). Figure 3.4(a) shows that this is insufficient to define a dihedral angle. The pseudo bond constrains the distance between atoms A and D, however, this does not constrain the dihedral angle; atom D could be at any position on the grey dotted line. Figure 3.4(b) shows that if an extra pseudo bond is included then a dihedral angle can be defined more precisely. The pseudo-bond constrains the distance between atoms E and D; atom D could be at any position on the grey dashed line. Therefore, the two pseudo-bonds ($\overline{AD}$ and $\overline{ED}$) restrain the position of atom D to be on both the dotted and dashed lines. This allows one dihedral angle to be defined.

Figure 3.5 shows the two pseudo-bonds that are required to define the oxygen-carbon-carbon-carbon dihedral angle. Here, the dihedral angle $\overline{O - CG - CC - CG}$ is defined by the pseudo-bonds $\overline{O - CG}$ and $\overline{O - OC}$. Two dihedral angles are required to define the conformation of the glycerol molecule (see section 3.1.1). Therefore, a second pair of pseudo-bonds ($\overline{CG - O}$ and $\overline{OC - O}$) is required to constrain the molecule to a conformation as defined by Equation 3.1 and shown in Figure 3.2. The conformations of the glycerol molecules are constrained using the angles shown in Table 3.3. These angles are then converted to the pseudo-bonds within EPSR and this ensures that the molecule conformation fits the definitions of Bastiansen (59) described in Equation 3.1.

Table 3.3: Dihedral Angles used to Constrain the Glycerol Molecules within EPSR

EPSR Model	$\overline{O\,CG\,CC\,CG}$ (°)	$\overline{O\,CG\,CC\,OC}$ (°)	$\overline{CG\,CC\,CG\,O}$ (°)	$\overline{OC\,CC\,CG\,O}$ (°)
$\alpha\alpha$	180	60	180	-60
$\alpha\beta$	180	60	60	180
$\alpha\gamma$	180	60	60	-60
$\beta\beta$	-60	180	60	180
$\beta\gamma$	-60	180	60	-60
$\gamma\gamma$	60	60	60	-60

The definitions shown in Table 3.3 were used along with the potentials and bond
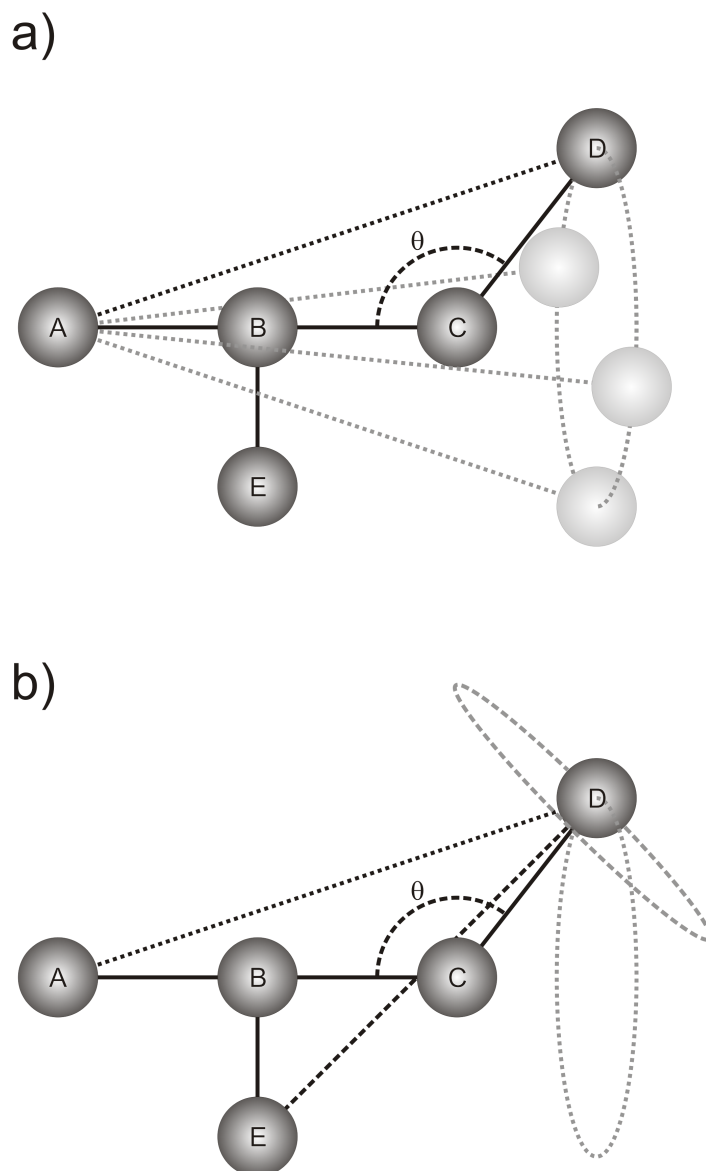
Figure 3.4: A diagram showing the pseudo-bonds that are required to define a dihedral angle using EPSR. (a) A pseudo-bond (black dotted line) is added between the first atom A and the last atom D of the $\overline{ABCD}$ dihedral angle. This bond $\overline{AD}$ constrains the distance between these two atoms. As there is no angular constraint on the bond, the atom D can be at any point on the edge of the cone shown by the grey dotted lines and atoms. The atom D can be anywhere on the circular dotted line. (b) A second pseudo-bond is added between atoms E and D (shown by a dashed line). Now the position of the atom D must lie on both the dashed and dotted lines. This constrains the dihedral angle $\overline{ABCD}$.

angles described in Tables A.1, A.2, and A.3 to form the starting point for the EPSR

analysis of the pure glycerol neutron diffraction data. This leaves six models, namely,
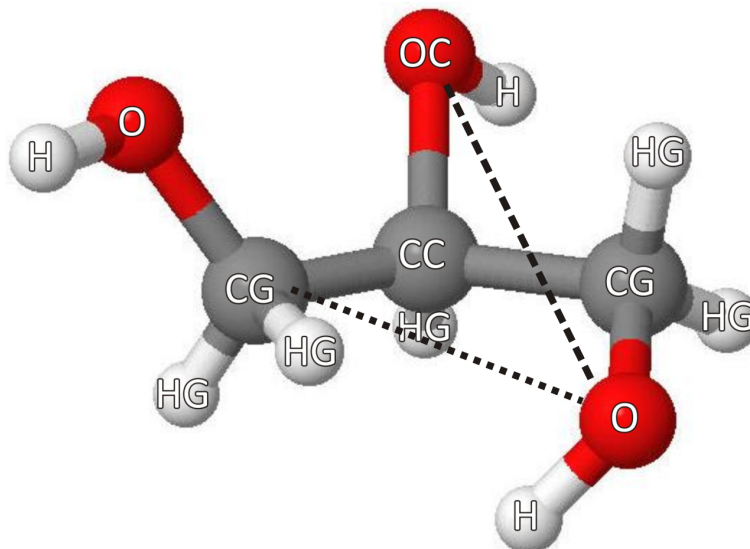
Figure 3.5: The glycerol molecule used within EPSR. When a dihedral angle $(\overline{O - CG - CC - CG})$ is defined in EPSR, a pseudo-bond is added to the molecule (shown by the dotted line $\overline{O - CG}$). A second pseudo-bond (dashed line $\overline{O - OC}$) is required to constrain the conformation of the molecule.

$\alpha\alpha$, $\alpha\beta$, $\alpha\gamma$, $\beta\beta$, $\beta\gamma$, and, $\gamma\gamma$. A seventh setup was produced where the dihedral angles were not defined; this model is referred to as "No Fixed Dihedrals" in the following description. The first test to perform is designed to ensure that the definitions from Table 3.3 provide a robust constraint on the conformation of the molecules in the EPSR simulation. This was completed by measuring the proportion of molecules that were of each conformation after equilibration of the EPSR simulation box.

Table 3.4: Glycerol Conformations after Equilibrium is Reached

Conformation	$\alpha\alpha$	$\alpha\beta$	$\alpha\gamma$	$\beta\beta$	$\beta\gamma$	$\gamma\gamma$
$\alpha\alpha$	**85.7**	0.0	12.1	0.0	0.0	2.2
$\alpha\beta$	0.0	**83.5**	10.4	0.0	4.3	1.8
$\alpha\gamma$	6.5	7.1	**82.2**	0.0	0.1	4.1
$\beta\beta$	0.0	0.0	0.0	**69.4**	30.2	0.4
$\beta\gamma$	0.0	7.8	1.1	7.4	**80.5**	3.2
$\gamma\gamma$	0.7	1.1	10.4	0.4	7.9	**79.5**
No Fixed Dihedrals	37.0	23.4	18.5	5.6	5.6	9.9

Table 3.4 shows that not all of the glycerol molecules are of the required conformation, however, around 70 to 85 % of the molecules are of the desired structure. This allows the difference between the conformations to be probed while maintaining the

level of disorder that is present in a liquid sample[1]. This mechanism for constraining the dihedral angles within the glycerol molecules, that are used in the EPSR analysis, allows the structure of liquid glycerol to be probed.

Interestingly, the simulation where the dihedral angles are allowed to rotate freely provides a result that is not completely dissimilar to the computational results of Chelli *et al.* (64; 65). That is, the "No Fixed Dihedrals" model and the work of Chelli *et al.* contain a large proportion of molecules that have at least one dihedral angle that falls in to the α region as well as the $\alpha\alpha$ conformation being the most prevalent conformer of glycerol.

3.2.2   Investigating Intra-Molecular Structure of Liquid Glycerol Using EPSR

The method described in Section 3.2.1 was used for each of the seven EPSR setups detailed in Table 3.4. Every simulation contained one thousand glycerol molecules at the experimentally measured atomic number density of 0.115 atoms Å^{-3}, equal to 1.261 g cm^{-3} (44; 72). Each of the simulation boxes was equilibrated, using Monte Carlo steps, before the empirical potential was added to drive the simulation as close as possible to agreement with the experimentally measured interference scattering cross sections[2]. The quality of the fit to the experimental data is given using the R-Factor, as described in Equation 2.41 from Section 2.5.3,

$$R = \frac{1}{M} \sum_i \frac{1}{n_Q(i)} \sum_Q [D(Q) - F(Q)]^2 \tag{2.41}$$

here, $F(Q)$ is the experimentally measured structure factor, $D(Q)$ is the simulated structure factor, $n_Q(i)$ is the number of Q values found in data set i, and, M is the number of data sets used (different isotopic substitutions). The R-factors for each of the seven EPSR setups shown in Table 3.4 are given in Table 3.5. Here, a lower R-factor is given by an EPSR simulation that provides a closer fit to the neutron diffraction data. It can be seen that the closest fit to the data is found using the $\alpha\beta$ setup. It is interesting that the "No Fixed Dihedrals" setup does not converge to the result given by $\alpha\beta$ setup. One might expect that the empirical potential should drive the system composed of

---

[1]This level of disorder is discussed in Section 3.3.2 and shown in Figure 3.7(b)

[2]For more detail on the steps used within EPSR see Figure 2.15 and Section 2.5

glycerol molecules with the fewest intra-molecular constraints to the closest fit to the experimental data. However, Table 3.4 shows that the "No Fixed Dihedrals" setup produces a range of different dihedral angles and Table 3.5 shows that this range does not produce the closest fit to the neutron diffraction data. This suggests that the "No Fixed Dihedrals" setup has reached a local minimum in the potential energy surface and that the empirical potential is not sufficient to drive the simulation to the close fit given by the $\alpha\beta$ setup.

Table 3.5: Fits to the data taken from the various EPSR setups

Conformation	R-Factor ($\times 10,000$)
$\gamma\gamma$	3.429
$\beta\gamma$	2.448
No Fixed Dihedrals	2.233
$\beta\beta$	2.090
$\alpha\alpha$	1.986
$\alpha\gamma$	1.931
$\alpha\beta$	1.734

The fit of the EPSR simulation to the experimental data can be further investigated by calculating the Q dependence of the fit. This is measured by taking the sum over the different isotopic substitutions of the residual between the simulated and measured structure factors for each of the EPSR setups as a function of the exchanged wave vector, Q (shown in Figure 3.6). Figure 3.6, again, confirms that the $\alpha\beta$ conformation provides the closest fit to the experimental data. This result is discussed in Section 3.4.

3.3 Investigating Hydrogen Bonding in Liquid Glycerol

3.3.1 Defining a Bond

Many different criteria have been suggested for the definition of a hydrogen bond (some of these are listed in Tables 3.1 and 3.2). These include limitations on the separations between different atoms; the oxygen-hydrogen separation (for example (58; 64)), and, the oxygen-oxygen separation (*e.g.* (66)). This raises the question, which hydrogen bond criteria should be used for the work in this thesis?

A definition of a hydrogen bond that does not include a hydrogen atom is question-
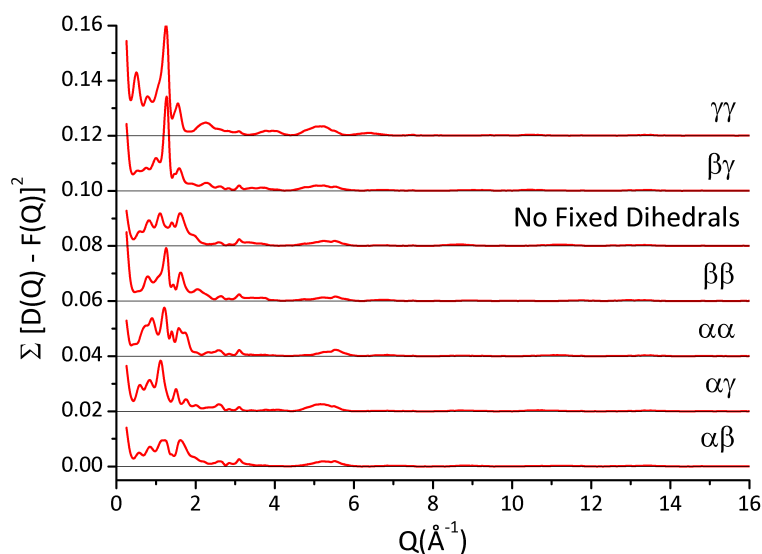
Figure 3.6: The sum of the residuals squared for each of the seven EPSR setups to the experimental data is shown as a function of the exchanged wave vector, Q. Here, the fit is shown as the sum over all isotopic substitutions of the residual between the simulated and experimental structure factors squared.

able. This can be explained by looking at a recently published IUPAC[1] definition of a hydrogen bond (111; 112), which states

> "The hydrogen bond is an attractive interaction between a hydrogen atom
> from a molecule or a molecular fragment XH in which X is more electroneg-
> ative than H, and an atom or a group of atoms in the same or a different
> molecule, in which there is evidence of bond formation."

This suggests that the separation between the hydrogen atom and the more electronegative atom (in the case of aqueous glycerol the oxygen) is a more accurate method of assigning a hydrogen bond. Other studies have also included a minimum bond angle (68). The angular dependence on the bond is included because the strength of a hydrogen bond is dependant on how straight the bond is. That is, how close to 180° the O-H· · ·O angle is.

As stated earlier, measuring and defining angles within a simulation is computationally costly. Therefore, the criterion that is used in this thesis is based on the oxygen-hydrogen separation, given by the relevant radial distribution functions (RDFs). An appropriate RDF is defined as having a first peak at around 1.8 Å and the number of

---

[1]IUPAC stands for the International Union of Pure and Applied Chemistry

hydrogen atoms that are found within this shell provides the number of hydrogen bonds. This number is found by integrating under this peak using Equation 2.18.

$$n_{\alpha\beta} = 4\pi\rho c_\beta \int_{rmin}^{rmax} r^2 g_{\alpha\beta}(r)\mathrm{d}r \qquad (2.18)$$

Here, $n_{\alpha\beta}$ is known as the coordination number, and, $rmax$ is given by the trough immediately after the first peak within the RDF. The coordination number gives the average number of atoms of type β around each atom of type α. The method that is used to calculate the average number of hydrogen bonds per molecule from the coordination numbers is shown in Section 3.3.3.

3.3.2 Investigating Intra-Molecular Hydrogen Bonding in Liquid Glycerol

The intra-molecular RDFs for the oxygen-oxygen distribution is shown in Figure 3.7(a) and the oxygen-hydrogen RDF is shown in Figure 3.7(b). From Figure 3.7 it can be seen that the distal oxygen-central oxygen (O-OC) peaks of Figure 3.7(a), as well as the distal oxygen-hydroxyl hydrogen (O-H) and central oxygen-hydroxyl hydrogen (O-H) peaks of Figure 3.7(b), have a spread around the values specified within EPSR[1]. This broadening is attributed to the $w_{\alpha\beta}^2$ function defined in Equations 2.29, 2.30 & 2.31 and described in Section 2.5.1.

Figure 3.7(a) shows that the distal oxygen-central oxygen (O-OC) RDF has peaks at around 2.8 Å and around 3.7 Å and the distal oxygen-distal oxygen (O-O) RDF has a peak at around 4.3 Å. The peak in the O-OC RDF at around 2.8 Å is of particular interest as this is indicative of hydrogen bonding. Interestingly this peak would fall entirely within the 3.5 Å cut-off used in a previous simulation based study (66). As a result of this, one could say that the first peak in the O-OC RDF shown in Figure 3.7(a) indicates that intra-molecular hydrogen bonding occurs in glycerol. Figure 3.7(b) shows a prominent peak at around 1.0 Å in both the central oxygen-hydroxyl hydrogen (OC-H) and distal oxygen-hydroxyl hydrogen (O-H) intra-molecular RDFs. These peaks are due to the covalently bound hydrogen atoms which define the hydroxyl groups (see Table A.2 and Figure 3.5)[2]. Both RDFs in Figure 3.7(b) show a diffuse second feature with a

---

[1]The labels given to the glycerol atoms are shown in Figure 3.5.

[2]The peak position is 0.967 Å as this is the specified average bond length when the molecule
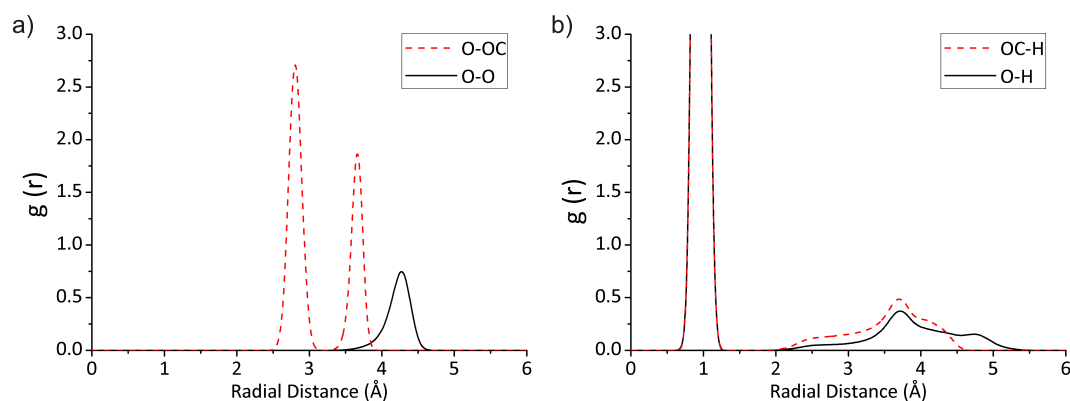
Figure 3.7: The intra-molecular radial distribution functions (RDFs) for oxygen-oxygen pairs (a) and the oxygen-hydrogen pairs (b). It can be seen that the distal oxygen-central oxygen RDF (O-OC) shows a peak at around 2.8 Å. This is the separation that would be expected if there were a hydrogen bond between these two atoms. For the two atoms to be forming a hydrogen bond a hydrogen atom must be found between the oxygen atoms. This atom will be covalently bonded to one of the oxygen atoms and therefore be around 1.0 Å away (see Table A.2). Therefore the hydrogen atom must be around 1.8 Å away from the other oxygen atom (2.8 - 1.0 = 1.8). The lack of a peak in either of the oxygen-hydrogen RDFs at around 1.8 Å shows that this data provides little evidence for the presence of intra-molecular hydrogen bonds.

peak position at around 3.7 Å.

If intra-molecular hydrogen bonding were present, then a peak would be expected to be found in the oxygen-hydrogen RDF at around 1.8 Å (114). As can be seen in Figure 3.7(b), there is no peak in the oxygen-hydrogen RDF at around 1.8 Å. Therefore, using the criterion for a hydrogen bond described in Section 3.3.1, there is little evidence for intra-molecular hydrogen bonding in this study. This shows that the EPSR analysis of intra-molecular hydrogen bonding does not support the studies detailed in Table 3.1. As stated in Section 3.1.3, the hydrogen bond network of glycerol has been proposed as the mechanism behind its macroscopic behaviour (113). Therefore, the following section shows the results of an investigation in to the inter-molecular hydrogen bonding of liquid glycerol.

3.3.3 Inter-Molecular Hydrogen Bond Number in Liquid Glycerol

In a similar way to Section 3.3.2, the RDFs are plotted to investigate the inter-molecular hydrogen bonding in liquid glycerol. Figure 3.8 shows the inter-molecular RDFs for all of the oxygen-oxygen pairs (Figure 3.8(a)) and the oxygen-hydroxyl hydrogen pairs (Figure is setup.

3.8(b)). Clear peaks can be seen in each of the oxygen-oxygen RDFs at around 2.8 Å and in the oxygen-hydroxyl hydrogen RDFs at 1.8 Å. The number of hydrogen bonds is
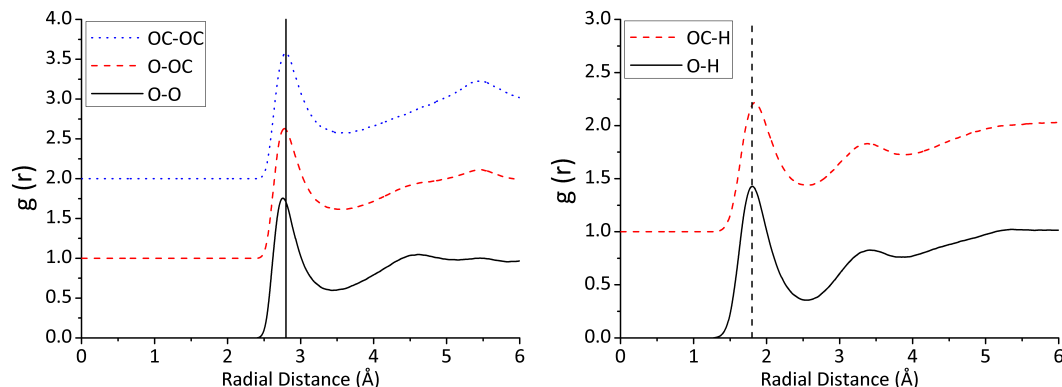
Figure 3.8: The inter-molecular radial distribution functions (RDFs) for oxygen-oxygen pairs (a) and the oxygen-hydrogen pairs (b). It can be seen that all of the oxygen-central oxygen RDFs show a peak at around 2.8 Å. This is the separation that would be expected if there were a hydrogen bond between these two atoms and is shown by the solid vertical line. The peak within the oxygen-hydrogen RDF at around 1.8 Å confirms the presence of inter-molecular hydrogen bonding and is highlighted using a dashed vertical line.

quantified using Equation 2.18 (shown in Section 3.3.1) and the coordination numbers are shown in Table 3.6.

Table 3.6: Inter-molecular Hydrogen Bonds found in Pure Glycerol

Atom 1	Atom 2	r_{max}	Coordination Number	Contribution to Hydrogen Bonds per molecule
O	H	2.50	0.96	1.92
OC	H	2.50	0.92	0.92
H	O	2.50	0.64	1.92
H	OC	2.50	0.31	0.92
Total				5.68

The number of hydrogen bonds that each molecule forms as an acceptor is calculated by measuring the number of hydrogen atoms, from different molecules, that are within the first coordination shell around each of the oxygen atoms. There are two distal oxygen atoms (O) and one central oxygen atom (OC) in each glycerol molecule (see Figure 3.5). Therefore, the number of hydrogen atoms around each "O" atom is doubled, and added to the number around each "OC" atom to yield the total number of occupied acceptor sites per glycerol molecule (1.92 + 0.92 = 2.84).

The number of hydrogen bonds that each molecule forms as a donor can be calculated in a similar way. There are three hydroxyl hydrogen atoms (H) per glycerol molecule. Each "H" atom forms an average 0.64 hydrogen bonds to a distal oxygen atom. Consequently, there are 1.92 hydrogen bonds where a hydroxyl hydrogen atom is acting a donator to a distal oxygen (0.64 x 3 = 1.92). Equivalently, the number of hydrogen bonds of the form hydroxyl hydrogen-central oxygen per molecule is given by the number per hydroxyl hydrogen atom multiplied by three, 0.92[1]. The total number of donator sites per glycerol molecule is given by the sum of these bond types (1.92 + 0.92 = 2.84).

This shows that glycerol forms a total of 5.68 hydrogen bonds per molecule (2.84 as a donor and 2.84 as an acceptor). This value is substantially higher than the value of inter-molecular hydrogen bonds found by most of the pure simulation studies detailed in Table 3.2 (58; 64; 67; 68), and is in agreement with the molecular dynamics simulations of Padro $et\,al.$ (69) and Zuang and Dellago (66). The total number of hydrogen bonds, however, is similar for the data shown in Table 3.6 and the work of Chelli $et\,al.$ (58; 64). They find that each glycerol molecule forms between 1 and 2 intra-molecular hydrogen bonds and 3.40 inter-molecular hydrogen bonds. This leads to a total of between 4.40 and 5.40 hydrogen bonds.

The total number of hydrogen bonds formed by glycerol in the work of Root and Stillinger (67) and the later study of Root and Berne (68) is 3.25 and 3.42 respectively. The lower number of hydrogen bonds formed can be ascribed to the partial charges on the relevant atomic sites. In their work, the charge on the hydroxyl oxygen atom was $-0.38\,e$ and the charge on the hydroxyl hydrogen atom was $+0.38\,e$[2] (67; 68). Table 3.7 details the charges that are used on the hydrogen and oxygen atom found in a hydroxyl group for a range of simulations. These include, the Optimised Potentials for Liquid Simulations (OPLS) force field (115) as used by Padro $et\,al.$ (69), those used in the work of Root and co-workers (67; 68), Chelli $et\,al.$ (58; 64), and those used throughout this thesis (see Table A.1 in Appendix A). Table 3.7 shows that the work of Root and co-workers (68) uses a partial charge on the oxygen atom that is substantially lower than

---

[1]The reason that this does not equal 0.93 is because the value of the H-OC coordination number is 0.307 and is rounded up in Table 3.6.

[2]Here, e is the elementary charge which is the charge on a single proton and is equal to 1.602×10^{-19}C.

Table 3.7: Partial Charges on Hydroxyl Group Atoms

Reference	Oxygen Atom	Hydrogen Charge (e)	Oxygen Charge (e)	Oxygen Charge/ Hydrogen Charge
(115)	All	0.435	-0.700	-1.61
(68)	All	0.380	-0.380	-1.00
(58; 64)	Distal	0.396	-0.585	-1.48
	Central	0.396	-0.581	-1.47
This thesis	All	0.392	-0.624	-1.59

for other studies (58; 64; 115). This suggests that the low number of total hydrogen bonds shown in Tables 3.1 and 3.2 is due to the oxygen atoms being less electronegative than other studies.

Another interesting point from Tables 3.1 and 3.2 is that the total number of hydrogen bonds found by the simulation study of Zuang and Dellago (66) and X-ray diffraction measurements of Sarker and Joader (63) are also in agreement. These studies state that each glycerol molecule forms as average of 6.50 hydrogen bonds. Here, Sarker and Joader do not distinguish between intra- and inter-molecular hydrogen bonding, and the work of Zuang and Dellago states that each glycerol molecule forms 0.80 intra-molecular and 5.70 inter-molecular hydrogen bonds; a total of 6.50. Both of these studies used the oxygen-oxygen separation as part of the criteria for a hydrogen bond. It is instructive to use a similar atomic separation cut-off as Zuang and Dellago to calculate the number of hydrogen bonds found in the data presented in this thesis. This provides a value of 7.94 "hydrogen bonds" per molecule[1]. This calculation shows that the number of oxygen atoms in the first coordination shell around an oxygen atom consists of at least 2.26 atoms that are not forming a hydrogen bond[2]. Therefore, the reason that the EPSR result is lower than these results could be due to the different criteria used for a hydrogen bond. Tables 3.1 and 3.2 show that the hydrogen bond angle is often used as part of the criteria to define a hydrogen bond. Therefore, the following section contains an analysis of the angular distribution of the hydrogen bonding within liquid glycerol.

---

[1]The values for this calculation can be found in Table B.1 in Appendix B.
[2]The number 2.26 is the difference between the number of hydrogen atoms and oxygen atoms in their respective coordination shells around an oxygen atom

3.3.4   Inter-Molecular Hydrogen Bond Structure of Liquid Glycerol

The strength of a hydrogen bond can be judged by two factors (see Section 1.2.3). A short hydrogen bond is considered to be a strong hydrogen bond, and the further away from 180° the oxygen-hydrogen···oxygen angle is the weaker the bond will be. A limitation with using EPSR is that it is not possible to measure the bond angle and bond length simultaneously, consequently, averages of these values must be used. The RDFs shown in Figure 3.8 display the average separations of the relevant atoms. Figure 3.9 shows the distribution of the oxygen-hydrogen···oxygen bonds and Figure 3.10 shows the oxygen···oxygen···oxygen distribution within pure glycerol.
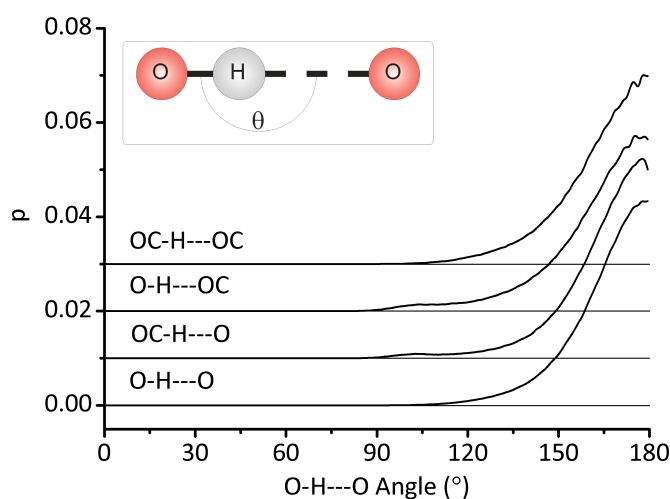
Figure 3.9: A plot of the proportion (p) of oxygen-hydrogen···oxygen (O-H···O) atomic triplets as a function of the angle formed between the three atoms. It can be seen that each of the distributions is very similar. Inset, a schematic diagram to show the system being studied.

In this study, the triplet bond angle $\overline{ABC}$ is calculated for all sets of three atoms that conform to specified length ranges. These criteria limit the length of the bonds $\overline{AB}$ and $\overline{BC}$ and are taken from the RDFs in Figures 3.7 and 3.8 in a similar way to those used to measure the coordination numbers. Specifically, minimum distances (r_{min}) are chosen based on a radial distance before the peak of interest. The maximum distances (r_{max}) are specified based on the position of either the trough after this peak or the point where the relevant RDF goes to zero.

Figure 3.9 is constructed using the intra-molecular $\overline{oxygen-hydrogen}$ and inter-molecular $\overline{hydrogen-oxygen}$ bonds. The r_{max} value for the intra-molecular bond is

set at 1.30 Å, as this is the point that both of the oxygen-hydrogen RDFs in Figures 3.7(b) go to zero. The radial distance cut-offs for the inter-molecular oxygen-hydrogen bonds are taken from Figure 3.8(b), and are the same as those used to calculate the oxygen-hydrogen coordination numbers (see Table 3.6). Importantly, all of the hydrogen bonds that are being measured using the coordination numbers in Section 3.3.3 have a triplet bond angle which is close to being straight (*i.e.* 180°) and have a similar angular distribution. This information forms an important baseline for the study of hydrogen bond angles in aqueous glycerol found in the following chapters.
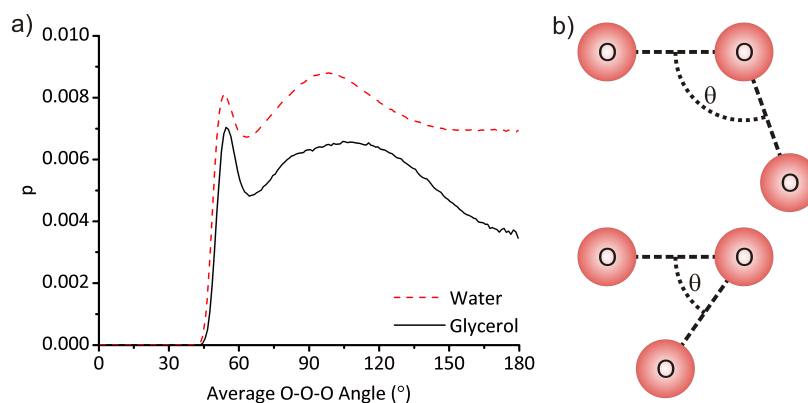
Figure 3.10: (a) A plot of the proportion (p) of oxygen···oxygen···oxygen (O-O-O) atomic triplets as a function of the angle formed between the three atoms. The solid black line refers to the result taken from pure glycerol and the red dashed line shows the data that is produced using previously published data taken using a pure water sample (108). A peak can be seen in both distributions at around 109.5° and shows that the oxygen atoms within pure glycerol form a tetrahedral structure. The peaks at 55° can be attributed to non-bonded oxygen atoms. (b) A schematic diagram to show the arrangement of oxygen atoms that would lead to the peaks in the in part (a). (b) top shows an arrangement at 109.5° and bottom shows the oxygen triplet with an included angle of 55°.

Figure 3.10 contains purely inter-molecular information and, as such, is produced using the inter-molecular $\overline{oxygen - oxygen}$ bond lengths taken from Figure 3.8(a). The peak that can be seen at around 55° can be attributed to oxygen atoms that are within the first coordination shell of one (or both) of the other oxygen atoms, but does not form a hydrogen bond to either (116). It is these oxygen atoms that account for the difference between the oxygen-hydrogen and oxygen-oxygen coordination numbers. A broad peak is also shown at around the tetrahedral angle of 109.5° in Figure 3.10. As a result, the oxygen atoms that are part of a hydrogen bond network are at a range of angles distributed around a tetrahedral arrangement. Interestingly, the distribution

is not completely dissimilar to that taken from previously published pure water data
(108). This suggests that the structure of glycerol-glycerol hydrogen bonds is similar to
water-water hydrogen bonds in the respective pure liquids.

3.4   Concluding Remarks

This chapter describes an investigation into the structure of pure liquid glycerol. Section
3.1.1 details the method that is used to define dihedral angles and how these can be used
to classify the structure of glycerol using the nomenclature put forward by Bastiansen
(59). The results of some previous studies are discussed in Section 3.1. The intra-
molecular structure is discussed in Section 3.2 with the method that is required to
produce the six different conformations of the glycerol molecule within EPSR being
discussed in Section 3.2.1. Section 3.3 details an investigation of the inter-molecular
structure and bonding between glycerol molecules.

It is shown in Section 3.2.2 that changes in the quality of the fit of the EPSR
simulation to the neutron diffraction data are found when different glycerol conforma-
tions are used. These results show that the $\alpha\beta$ conformation provides the closest fit
to the experimental data. Previous studies have found that the most stable (lowest
energy) conformation for an isolated glycerol molecule is the $\gamma\gamma$ structure (61). A glyc-
erol molecule in the $\gamma\gamma$ conformation would be expected if intra-molecular interactions
were dominating in the pure liquid. The crystal structure of glycerol has been found
to be the $\alpha\alpha$ conformation (60). The result that the liquid structure is closer to the
crystal structure than the gaseous structure suggests that inter-molecular forces are a
more important factor in determining the molecular conformation of the liquid than the
intra-molecular interaction. This is a possible explanation for the difference between
these results and those of previous neutron diffraction studies (57; 62). The research
conducted in the 1980s used one sample, and limited the fitting of the data to the
intra-molecular structure of glycerol. The research detailed in this chapter employed
five isotopically different samples, and the data was fitted using both intra- and inter-
molecular interactions. Thus the approach used in this thesis allows access to both intra-
and inter-molecular interactions in liquid glycerol, which was not possible in the earlier
studies. Interestingly, however, the $\alpha\beta$ conformation did not provide a good fit to the

aqueous glycerol systems (discussed in later chapters). The best fit to all of the data was found using the "No Fixed Dihedrals" setup. This result is in fair agreement the molecular conformations from the simulation based studies of Chelli *et al*. (64; 65) and is discussed in Section 4.1.1.

Sections 3.1.2 and 3.1.3 detail the previous studies that have been completed, their different findings regarding bonding and how these results were reached. Based on the work presented here, the existence of intra-molecular hydrogen bonding within glycerol molecules was questioned in Section 3.3.1. The method that is used throughout this thesis to calculate hydrogen bond number was introduced in Section 3.3.3. This technique is used to calculate the number of inter-molecular hydrogen bonds that are formed by each glycerol molecule. This analysis shows that glycerol forms an average 5.68 inter-molecular hydrogen bonds per molecule (2.84 as an acceptor and 2.84 as a donor). This result is substantially higher than previously reported by simulation only studies (58; 64; 67; 68) and similar to an experimental study (63) and simulation based studies (66; 69). The total number of hydrogen bonds found by Chelli *et al*., however, is not substantially different from the result described in this chapter. Chelli *et al*. find a total of between 4.40 and 5.40 hydrogen bonds per glycerol molecule. The differences between the work reported within this thesis and that of Root and co-workers (67; 68) can be attributed to the partial charges that have been used (see Table 3.7).

Finally, Section 3.3.4 explains how triplet bond angles can be extracted from EPSR data, and shows the structure of the hydrogen bond network within glycerol. It is shown that the hydrogen bonds are predominantly straight by measuring the included angles of oxygen-hydrogen$\cdots$oxygen triplets. Measurements of the oxygen$\cdots$oxyegn$\cdots$oxygen included angles shows that the oxygen atoms are arranged in a manner that is similar to that found in pure water. The following chapters use this information on pure glycerol to study the structural changes that occur when glycerol and water are mixed at a range of concentrations and temperatures.

Chapter 4

Structural Modifications on Mixing of Aqueous Glycerol at Room Temperature

4.1 Context

From the earliest uses of cryoprotection it has been thought that the cryoprotective action of glycerol is due to its ability to modify the structure of water in some way (29; 71; 75; 76). However, an experimental determination of the effect of glycerol on the structure of water has been lacking. Such a study is detailed here.

This chapter begins with a description of the glycerol model that has been used throughout this investigation (see Section 4.1.1). Within Section 1.4.3 some theories regarding the modification of the structure of water due to mixing with glycerol are discussed (75–79). These theories are discussed in greater detail in Sections 4.1.2 and 4.1.3. The results of the present study regarding these theories are split into two sections. Section 4.2 discusses the intra-molecular structure of glycerol. This is followed by an examination of the inter-molecular structure of the water-water (Sections 4.3.1, 4.3.2 and 4.3.3), glycerol-glycerol (Section 4.3.4) and glycerol-water (Section 4.3.5) interactions. This chapter finishes with a discussion of the modifications to the inter-molecular bonding of glycerol and water as a function of concentration (Section 4.4). A large proportion of the work in this chapter has been previously published (2–4). The earliest of these articles details an investigation of aqueous glycerol at a mole fraction of $X_g = 0.80$.

This article studied the effect of adding water to glycerol (2). The second article inves-
tigated the structural modifications to water when glycerol is added to form a mixture
with a glycerol mole fraction of Xg = 0.05 (3). The most recent article characterises the
structure and mixing of aqueous glycerol across the complete concentration range (4).
The results in this chapter concentrate on the structural modifications that are found
as a function of concentration[1].

4.1.1   The Intra-molecular Structure of Aqueous Glycerol

In Section 3.1.1 the method used to quantify the structure of glycerol is introduced.
This nomenclature has been used to find the structure of glycerol that gave the closest
fit to the neutron diffraction data from a pure glycerol sample. It was found that the
$\alpha\beta$ conformation gave the closest fit to the experimental data for pure liquid glycerol
(see Section 3.2.2 and Towey *et al.* (1)).

Similarly, when investigating the aqueous glycerol data, the model that gave the
closest fit on average across the concentration range was used. The $\alpha\beta$ setup gave
an average R-Factor of 2.063×10^{-4} and the "No Fixed Dihedrals" setup provided
an average of 1.963×10^{-4}. Therefore, the "No Fixed Dihedrals" model was used for
each of the aqueous glycerol concentrations. Figure 4.1 shows the data taken from
neutron diffraction experiments along with the EPSR fit produced using the "No Fixed
Dihedrals" model. This model gives very similar results for pure glycerol when compared
to those discussed in Section 3.3. The total number of hydrogen bonds per glycerol
molecule is 5.71 for the "No Fixed Dihedrals" model and 5.68 for the $\alpha\beta$ setup. Also,
there is no evidence for intra-molecular hydrogen bonds found using either conformation.
These results show that using a different model for the glycerol molecule does not modify
the main results from Chapter 3.

Previous studies have been conducted to investigate the structure of glycerol in
aqueous environments. These studies have each used the nomenclature of Bastiansen
(59) (see Section 3.1.1) and include a purely spectroscopic study by van Koningsveld
(117), a study using a mixture of spectroscopic and simulation techniques (77) as well
as studies using simulation techniques alone (73; 74). The earliest of these studies of

---

[1]Chapter 5 includes a description of larger scale interactions specifically the molecular mixing
that is found as a function of concentration.
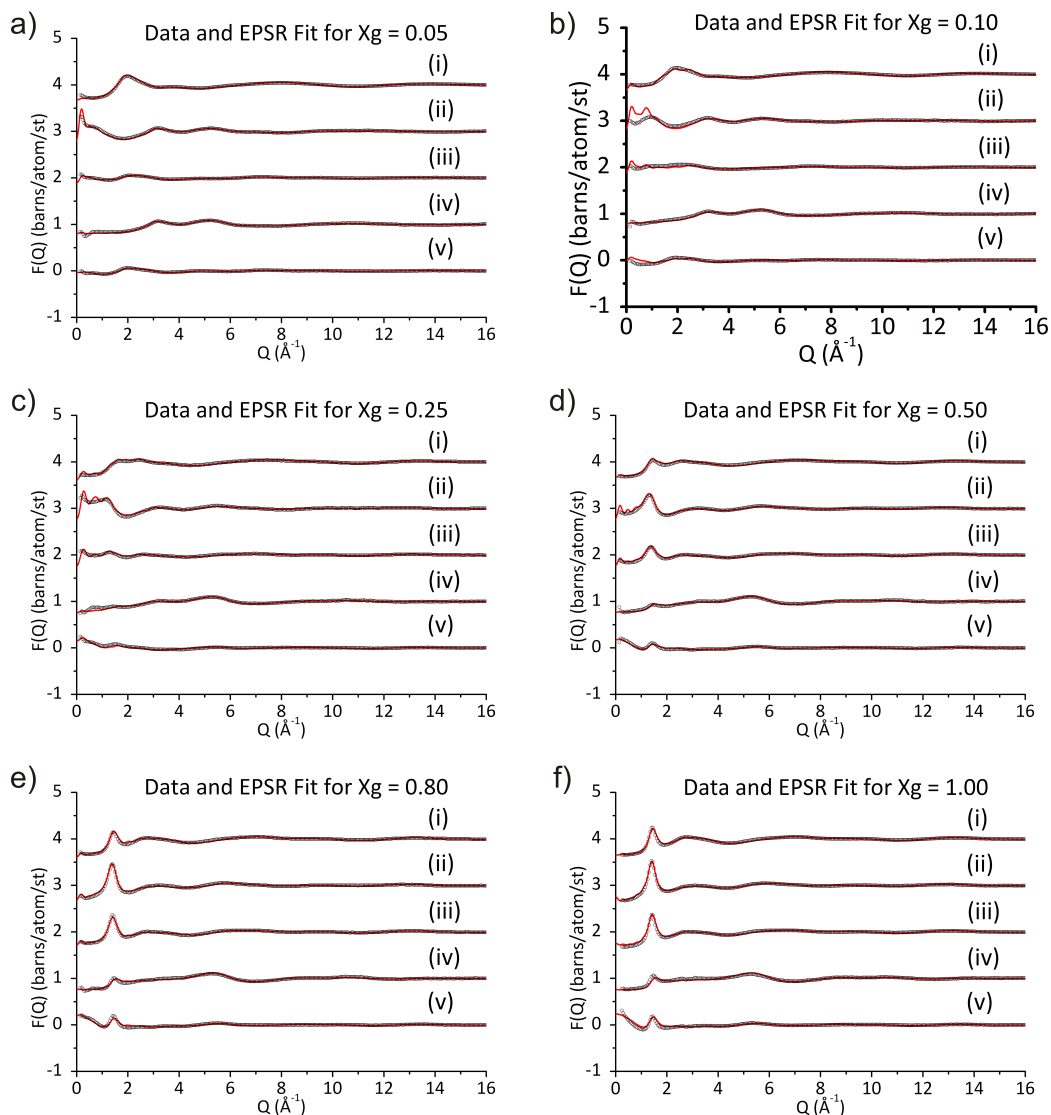
Figure 4.1: The experimental structure factors (black circles) and EPSR fitted structure factors (red lines) for each of the isotopic substitutions measured (see Table 2.4). These data are shown in order of increasing glycerol concentration: (a) Xg = 0.05,(b) Xg = 0.10,(c) Xg = 0.25,(d) Xg = 0.50,(e) Xg = 0.80, and,(f) Xg = 1.00 (pure glycerol). This confirms that the "No Fixed Dihedrals" EPSR models are in good agreement with the experimental data.

aqueous glycerol used nuclear magnetic resonance spectroscopy (NMR) to study mixtures of D_2O and glycerol (117). This study found that at a glycerol concentration of 5 %[1] the majority of the glycerol molecules were of either the $\alpha\alpha$, $\alpha\beta$ or $\alpha\gamma$ conformers with the $\alpha\gamma$ conformation being the most common[2]. A density functional theory (DFT)

---

[1]Unfortunately, van Koningsveld does not state whether this is a mass, volume or molar percentage. A 5 wt.% mixture is equal to a mole fraction of Xg = 0.0102 and a 5 vol.% mixture has a concentration of Xg = 0.0128.

[2]The values shown in Table 4.1 are the average proportions from this article.

based investigation has been conducted using a continuum model to represent the water
molecules (74). The calculated energies were then used to find the distribution of glycerol conformations found in the aqueous phase (74). The results of Callam *et al.* broadly
agreed with the results of van Koningsveld (117). Dashnau *et al.* performed an investigation that combined infra-red spectroscopy and molecular dynamics (MD) simulation
to study aqueous glycerol at concentrations of $0.03 \leq Xg \leq 0.27$. From their results
they found that the most common conformation was $\alpha\alpha$ (77). Yonge *et al.* conducted
a classical MD simulation of one glycerol molecule immersed in 235 water molecules (a
concentration of $Xg = 0.004$). They, in agreement with previous studies, found that the
$\alpha\gamma$ conformation was the most prevalent (73). The different results for the proportion
of glycerol molecules of each conformation are listed in Table 4.1. The results from the
present study are discussed in Section 4.2.1.

Table 4.1: Aqueous Glycerol Conformation Percentages

Reference	Concentration (Xg)	$\alpha\alpha$	$\alpha\beta$	$\alpha\gamma$	$\beta\beta$	$\beta\gamma$	$\gamma\gamma$
(117)	0.01	20	22	28	6	15	10
(74)	Infinite Dilution	20	20	30	5	15	10
(77)	$0.03 \leq Xg \leq 0.27$	40	20	30	0	5	5
(73)	0.004	17	31	33	2	15	3

Yonge *et al.* also found that glycerol conformations that are able to form intramolecular hydrogen bonds (namely $\beta\beta$ and $\gamma\gamma$) are the least populated (73). Other
studies have also investigated the presence of intra-molecular hydrogen bonds. Callam
et al. used DFT calculations to probe the conformation of aqueous and gaseous glycerol (74). They found that the conformation of aqueous glycerol is determined by the
presence of intra-molecular hydrogen bonds (74). In their study, Callam *et al.* did not
use explicit water molecules, but rather, used continuum models to mimic the effect of
hydrating the glycerol molecules. This result is questioned by a more recent classical
molecular dynamics simulation, which studied aqueous glycerol at five concentrations
up $Xg = 0.08$. In this more recent study, Weng *et al.* did not find any evidence for
intra-molecular hydrogen bonds (75). The presence of intra-molecular hydrogen bonds
has been investigated using neutron diffraction and EPSR. The results of this study are
detailed in Section 4.2.2.

4.1.2   The Inter-molecular Structure of Aqueous Glycerol

The structure of the water network within aqueous glycerol has been investigated previously (77; 78; 118; 119). Dashnau *et al.* have suggested that bulk-like water exists at glycerol concentrations under Xg = 0.15 (77). Politi *et al.* find a complementary result using molecular dynamics simulations (78). Here, the CHARMM27 force field (120; 121) is used along with TIP3P (122) water molecules. They too, have found that the water network is disrupted by the addition of glycerol. However, they state that this occurs at a lower glycerol concentration (Xg = 0.06) (78). In their work, Politi *et al.* use the loss of the tetrahedral structure of the water network as an indication that the water network has been disrupted (78). It has also been suggested that water-water hydrogen bonds become weaker (longer) as glycerol is added based on the changes to the infra-red absorption peaks (118). This result is in opposition to that of Parsons *et al.* who found that the presence of the carbon backbone of glycerol has little effect on the water structure as inferred from vapour pressure measurements (119). Modifications to the water structure are discussed in more detail within Section 4.3.

The interactions between water and glycerol molecules are also of importance when considering aqueous glycerol mixtures. Dashnau *et al.* have suggested that glycerol molecules form hydrophobic clusters with marked inter-molecular interaction between the CH$_2$ groups at concentrations above Xg = 0.60 (77). This result is in agreement with Parsons *et al.*, who suggest that glycerol molecules form clusters via the carbon backbone groups, with the hydroxyl (OH) groups available for inter-molecular hydrogen bonding (119). Macroscopic measurements have been used to investigate the interactions between water and glycerol (41; 44; 45; 71). These studies have suggested that the properties of aqueous glycerol can be attributed to the prevalence of mutual (glycerol-water) interactions (41; 44; 71) or the enhanced structure/rigidity within the system (45). Each of these theories can be investigated in the present thesis using the relevant radial distribution functions (RDFs). The theory of an enhancement of the structure of the system is discussed in Section 4.3 and the RDFs relating to mutual interactions are shown and discussed in Section 4.3.5.

It is also instructive to compare the structural modifications found when glycerol and water are mixed to those that have been previously found within different aqueous mixtures. Earlier investigations have studied the structural modifications due to dimethyl

sulfoxide (DMSO) (86), methanol (123; 124), proline (84) , sorbitol (85), tertiary butanol (tert-butanol) (125) the disaccharide sugar trehalose (82; 83), and, trimethylamine oxide (TMAO) (87) (see Figure 1.10). In each of these studies the second peak of the water oxygen-water oxygen RDF was found to be shifted upon addition of the solute. Shifts in this peak position have been attributed to a modification of the tetrahedrality of the system. The tetrahedrality of the water network in aqueous glycerol is investigated in Section 4.3.3. Tertiary butanol (125) and methanol (124; 126) have both been found to cluster via the hydrophobic methyl groups. This is of particular interest, as tertiary butanol and methanol are both small molecules that contain hydroxyl groups and methyl groups, making them amphiphilic in nature. Similarly, glycerol also contains hydroxyl and methyl groups, making it amphiphilic. Section 4.3.4 contains a discussion of whether a similar effect is seen in aqueous glycerol.

4.1.3 Inter-Molecular Bonding within Aqueous Glycerol

Previous studies of aqueous glycerol have investigated the hydrogen bonds that are present in this system (75–79). The results found by these studies are detailed below. Dashnau $et\,al.$ have used a combination of infra-red spectroscopy and molecular dynamics simulations to study aqueous glycerol across the complete concentration range. They found that the average number of hydrogen bonds formed by each water molecule decreases as glycerol is added (77). A more recent MD study found a similar trend at low glycerol concentrations ($0.003 \leq Xg \leq 0.133$) (76). A contradictory result was found by Politi $et\,al.$ who also used molecular dynamics simulations. Their MD study found that as glycerol concentration is increased, an increase in the number of water-glycerol hydrogen bonds per water molecule compensates for the loss of water-water hydrogen bonds (78). Conversely, Sethu Raman $et\,al.$ conducted a density functional theory based investigation of aqueous glycerol and found that each glycerol molecule is hydrated by four water molecules at each of nine concentrations of Xg ≤ 0.018 (79).

Interestingly, Weng $et\,al.$ have conducted molecular dynamics simulations of aqueous glycerol and state that glycerol forms more hydrogen bonds as an acceptor than a donator (75). This is unsurprising given the molecular structure of glycerol (see Figure 2.14). There are six lone pairs of electrons (two on each of the three oxygen atoms) each capable of accepting one hydrogen bond. A total of six hydrogen bonds as an acceptor.

These oxygen atoms each have one hydroxyl hydrogen atom capable of being donated in a hydrogen bond. A total of three hydrogen bonds as donator. Therefore, glycerol can form six hydrogen bonds as an acceptor and three as a donor. Section 4.4 contains a discussion of the results regarding inter-molecular hydrogen bonding that have been found using a combination of neutron diffraction and computational modelling.

4.2 The Intra-molecular Structure of Glycerol as a Function of Concentration

4.2.1 Glycerol Conformation on Aqueous Solution

The conformation of glycerol is a determining factor in its ability to form inter- and intra-molecular hydrogen bonds. Therefore, the intra-molecular structure of glycerol in aqueous environments has been studied previously (73; 74; 77; 117) (detailed in Table 4.1). Some general conclusions can be drawn from the previous studies: most of the glycerol molecules have at least one distal oxygen atom in the α position (70 - 90 %), the $\beta\beta$ is the least occupied conformation (0 - 6 %), and, the $\alpha\gamma$ conformation is often the most occupied (73; 74; 117) with the $\alpha\alpha$ the most common in one of the more recent studies (77). A comparison between these results and those reported in this thesis is given below. The results from the combination of neutron diffraction with isotopic substitution and computational modelling are detailed in Figure 4.2 and Table 4.2.

Table 4.2: Glycerol Molecules Containing at least One "α" Distal Oxygen

Reference	Concentration (Xg)	Percentage with at least One "α" Distal Oxygen
(117)	0.01	70
(74)	Infinite Dilution	70
(77)	$0.03 \leq Xg \leq 0.27$	90
(73)	0.004	81
This Work	0.05	75
"	0.10	72
"	0.25	77
"	0.50	81
"	0.80	82
"	1.00	78
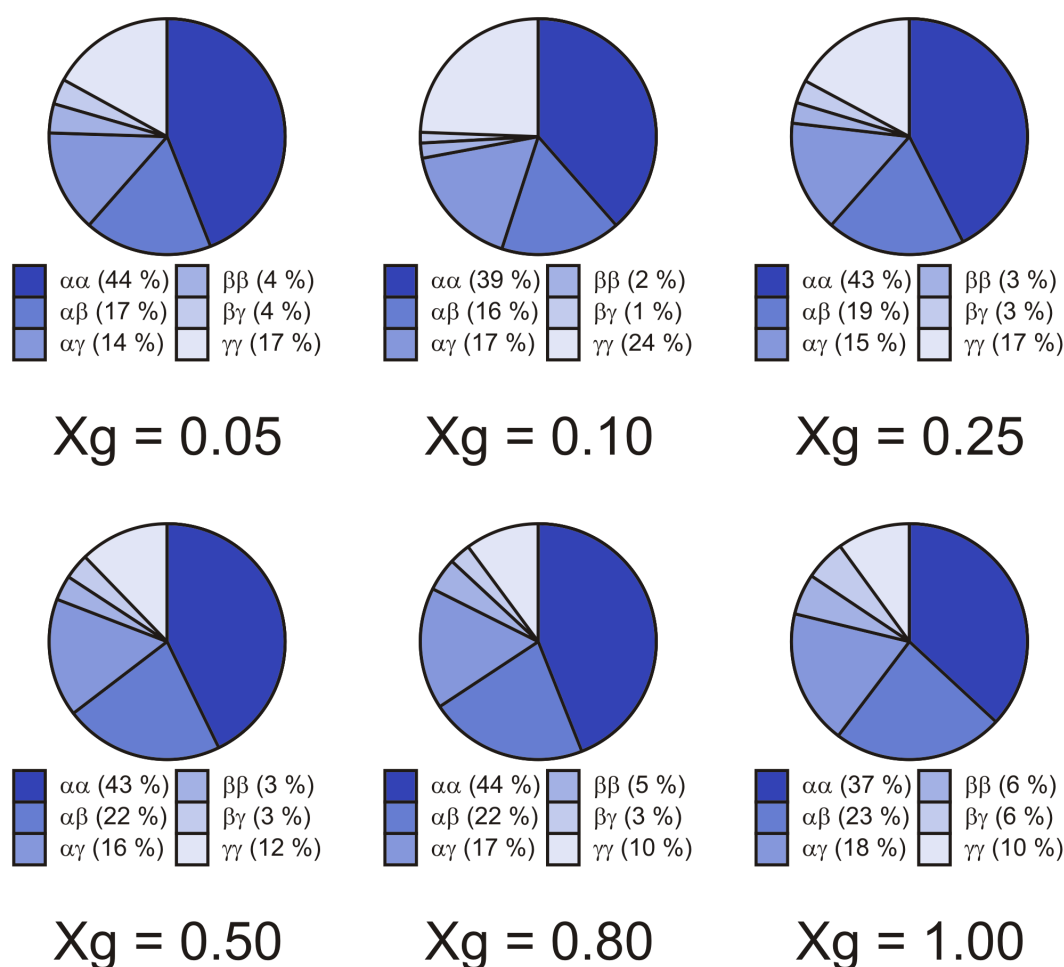
Figure 4.2: Pie charts indicating the proportion of the glycerol molecules that are of each of the conformations defined previously (see Section 3.1.1 and Figure 3.2), as a function of glycerol concentration. The data shown here are taken from the EPSR analysis of the neutron diffraction data shown in Figure 4.1.

From Figure 4.2 it can be seen that the proportion of the different conformations is not dramatically effected by the addition of water. In general there is a small decrease in the proportion of the $\alpha\alpha$ conformation at the expense of the $\alpha\beta$ structure, with increasing glycerol concentration, with the $\alpha\alpha$ conformation being the most common at all concentrations studied. This result is in agreement with a study using a combination of infra-red spectroscopy and computational modelling which also found that the $\alpha\alpha$ conformation was the most prevalent (77). Interestingly, other studies (73; 74; 117) have found a higher proportion of the $\alpha\beta$ and $\alpha\gamma$ structures than is reported here. However, the results in Table 4.2 show that most of the glycerol molecules (between 72 and 82 %) have at least one distal oxygen atom in the α configuration at each concentration

studied. This result is in agreement with the previous studies detailed in Table 4.1.

The least common conformations found, in the neutron diffraction and computational modelling study presented here, were the $\beta\beta$ and $\beta\gamma$ conformations. This low proportion of the $\beta\beta$ conformation is in agreement with all of the previous studies (73; 74; 77; 117) that are detailed in Table 4.1. The $\beta\gamma$ conformation, however, is found in higher proportions in many of the previous studies. The lower proportion of $\beta\gamma$ is accompanied by a higher proportion of the $\gamma\gamma$ structure in the work reported here when compared to the previous studies. It has been previously argued that glycerol molecules that are of the $\gamma\gamma$ conformation are able to form intra-molecular hydrogen bonds (73). The higher proportion of the $\gamma\gamma$ structure, therefore, could be an indication of the formation of such bonds. The following section describes the results that relate to the presence of intra-molecular hydrogen bonding.

4.2.2 Intra-molecular Hydrogen Bonding

Figure 4.3 shows the intra-molecular oxygen-hydrogen RDFs for glycerol molecules at each of the concentrations studied. It can be seen that none of these RDFs show a peak at 1.8 Å. From the definition of a hydrogen bond given in Section 3.3.1, this shows that there is no evidence for intra-molecular hydrogen bonding found in the glycerol molecules at any of the concentrations studied. The modifications in the peak height that are seen as a function of concentration are due to the way in which RDFs are normalised. The lowest peaks are seen in the pure glycerol data (Figure 4.3(f)) and the highest in the least concentrated solution (Figure 4.3(a)). Here, both distributions are produced by normalising using the distribution of atoms that would be found in an ideal mixture (see Equations 1.3 and 1.4 in Section 1.2.2). Therefore, the distribution of atoms in the pure glycerol data is divided by a larger number than for the most dilute mixture due to the proportion of glycerol molecules, and hence, has a lower peak height.

This result supports the molecular dynamics simulations of Yonge *et al.* (73) and Weng *et al.* (75) who both suggest that glycerol does not form intra-molecular hydrogen bonds in aqueous mixtures. The result is contradictory to the result of the density functional theory based study conducted by Callam *et al.* They found that the conformation of aqueous glycerol is determined by the presence of intra-molecular hydrogen bonds (74). It is conceivable that the lack of agreement between the work of Callam *et al.* and
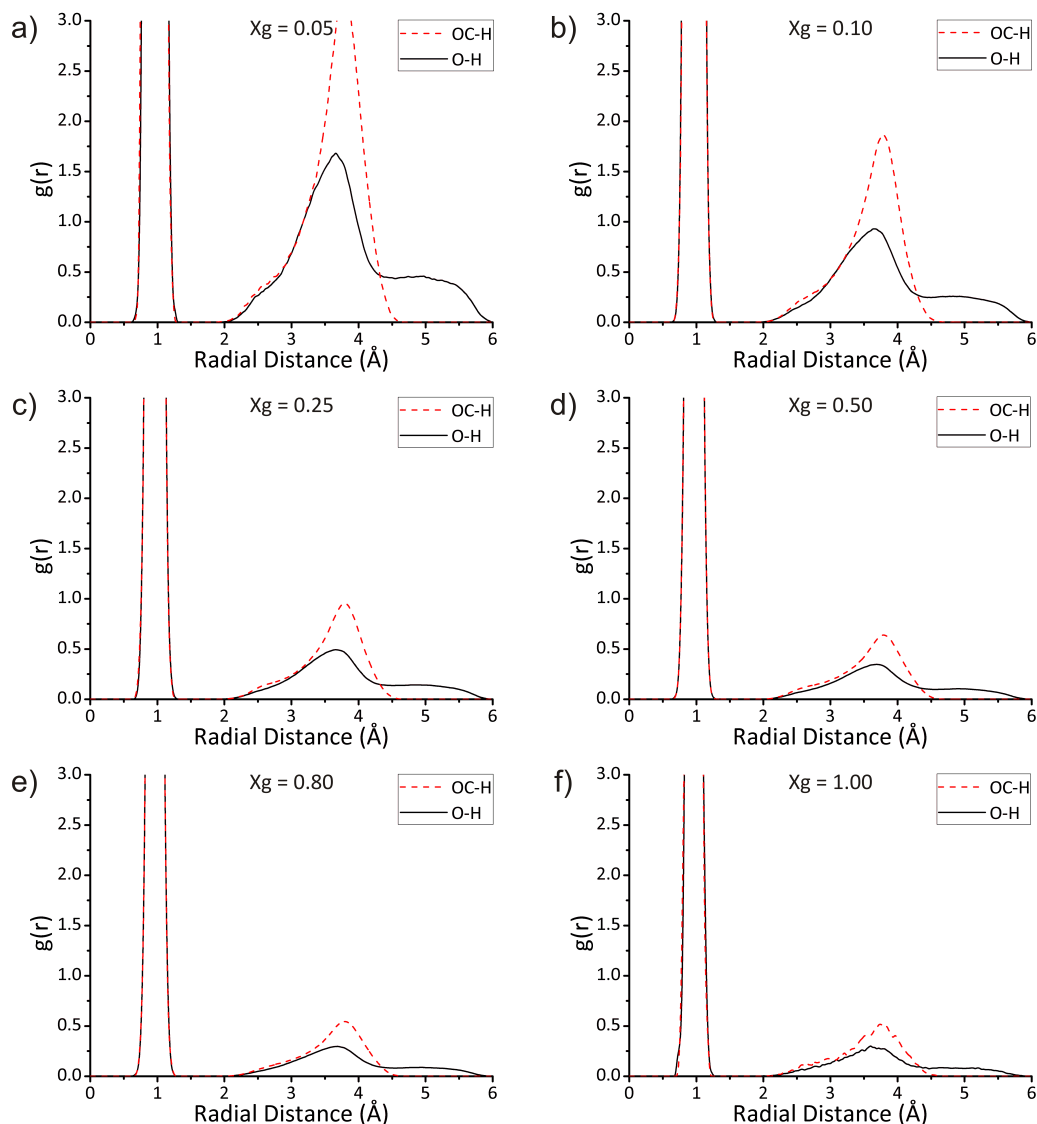
Figure 4.3: The intra-molecular RDFs for each of the oxygen-hydrogen pairs found within the glycerol molecules as a function of concentration. The distributions are shown in order of increasing glycerol concentration: (a) $Xg = 0.05$, (b) $Xg = 0.10$, (c) $Xg = 0.25$, (d) $Xg = 0.50$, (e) $Xg = 0.80$, and (f) $Xg = 1.00$ (pure glycerol). The decrease in the peak height with increasing glycerol concentration can be attributed to the RDFs being normalised to the average density of the relevant atoms (see Section 1.2.2).

that reported previously (73; 75), and within this thesis, could be due to the treatment of the water molecules. Callam $et\,al.$ use a continuum model for the water which allows a detailed study of intra-molecular interactions that are found in different conformations of glycerol. However, the use of this model for hydration is based on the assumption that the water molecules hydrating the glycerol molecules can be modelled as a uniform substance. The work of Yonge $et\,al.$ (73) and Weng $et\,al.$ (75) were both MD simulations using explicit water molecules with the TIP3P model (122). The work detailed in this

thesis uses explicit water molecules with the SPC model (107). From Figure 4.10 it can be seen that the hydration layer of water around glycerol is highly directional and structured, *i.e.* not a uniform continuum. This suggests that explicit water molecules should be used to accurately account for the interactions found in aqueous glycerol. The results in this section represent the first direct experimental structural investigation into the presence (or lack of) intra-molecular hydrogen bonding within glycerol molecules.

4.3 The Inter-Molecular Structure within Aqueous Glycerol as a Function of Concentration

4.3.1 Water-Water Interactions in Aqueous Glycerol Mixtures

To investigate the extent to which the water-water interactions are modified by the addition of glycerol, it is instructive to use the relevant RDFs. These RDFs are shown in Figure 4.4. The structure of the hydrogen-hydrogen pairs is shown in Figure 4.4(a), the oxygen-hydrogen correlation is shown in Figure 4.4(b), and, Figure 4.4(c) shows the oxygen-oxygen structure.

Figure 4.4 shows that the height of the first peak in each of the distributions increases as the glycerol concentration is increased. This is analogous to the effect shown with the intra-molecular structure of the glycerol molecules above (see Figure 4.3). The first hydrogen-hydrogen peak (Figure 4.4(a)) occurs at radial distances between 2.31 and 2.40 Å, and the second peak at distances between 3.78 and 3.90 Å. These changes equate to shifts of around 4 and 3 % respectively[1]. Therefore, the structure of the water hydrogen-water hydrogen pair is not significantly altered by the addition of glycerol. Here, a significant alteration in the peak position is defined as being larger than the difference between the RDFs taken from light and heavy water. The intermolecular oxygen-hydrogen peak is found at 1.74 in light water and 1.81 in heavy water (127), a modification of 3.9 %. Similarly, the oxygen-hydrogen first peak (Figure 4.4(b)) can be seen at positions between 1.68 and 1.80 Å. This peak is of particular interest as it confirms that water-water hydrogen bonds are present at all of the aqueous glycerol concentrations studied. The hydrogen bonding within aqueous glycerol is discussed in

---

[1]Here, the percentage shifts are calculated using the difference between the longest and shortest radial distance for the peak in question divided by the largest radial separation.
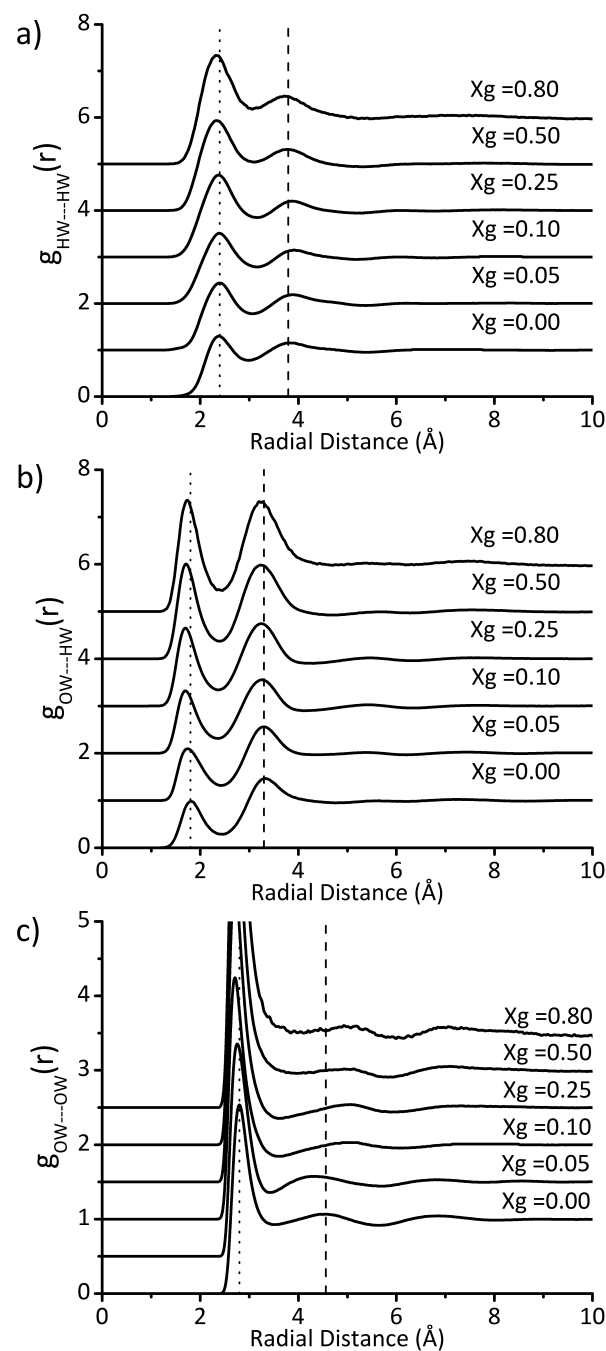
Figure 4.4: The inter-molecular RDFs for each of the water-water atomic pairs at each
of the glycerol-water concentrations studied. Here, Xg = 0.00 refers to a pure water
sample and is produced using previously published neutron diffraction data (108). For
each of the distributions the first peak position is indicated using a dotted line and the
second peak is shown with a dashed line. The peak positions are not altered by the
addition of glycerol for the hydrogen-hydrogen (a), and oxygen-hydrogen (b) functions.
For the oxygen-oxygen RDFs (c) the first peak is found at a relatively constant distance
at each glycerol concentration. Interestingly however, the second peak position is shifted
at low concentrations and is no longer present at high glycerol concentrations. N.B. The
scale of the y-axis is different in part (c).

greater detail in Section 4.4. The second peaks of the oxygen-hydrogen pairs are all at
positions between 3.21 and 3.30 Å. These small peak movements show that the structure
of the water oxygen-water hydrogen correlation is, also, not significantly altered with
the addition of glycerol.

The first peak of the oxygen-oxygen RDFs (Figure 4.4(c)) also shows limited de-
viations with concentration. For this peak, the lowest radial distance is 2.70 Å and
the largest separation is 2.76 Å. However, the second peak of the water oxygen-water
oxygen RDF is altered dramatically as a function of glycerol concentration. In the most
dilute aqueous glycerol solution ($X_g = 0.05$) the peak is shifted inward by 0.18 Å to
a position of 4.38 Å. Interestingly, at glycerol concentrations of $X_g \geq 0.10$, the second
peak is shifted to larger distances (from 4.56 Å in pure water to 5.01 Å) and becomes
less pronounced (see Figure 4.4(c)). It is instructive to compare the water-water struc-
tural modifications that are present in aqueous glycerol with those that have been found
previously in different aqueous mixtures. This is investigated in the following section.

4.3.2 Water-Water Interactions in a Range of Aqueous Mixtures

Other aqueous systems have been studied using neutron diffraction with isotopic sub-
stitution and EPSR. These previous investigations have studied a wide range of dif-
ferent solutes including: dimethyl sulfoxide (DMSO) (86), methanol (123; 124), proline
(84), sorbitol (85), tertiary butanol (tert-butanol) (125) the disaccharide sugar trehalose
(82; 83), and, trimethylamine oxide (TMAO) (87). The positions of the first and second
peaks that are found in the relevant water oxygen-water oxygen RDFs are detailed in
Table 4.3. Firstly, it can be seen that the position of the first peak is relatively constant
in each of these studies being found between 2.66 and 2.85 Å. This is consistent with
the results found for aqueous glycerol (see Figure 4.4(c)). There is, however, a marked
change in the position of the second water oxygen-water oxygen peak with many of the
solutes that have been studied.

In aqueous DMSO the second peak of the water oxygen-water oxygen RDF has
been shown to be shifted outward by at concentrations of $X_i = 0.048$ and 0.333[1] (86).
These concentrations are formed by having molecular ratios of 1 DMSO: 20 water and 1
DMSO : 2 water molecules respectively. The shift in the peak is also shown to be larger

---

[1]Here, X_i is used to denote the mole fraction of the solute, i, under investigation.

for the higher concentration DMSO mixture (0.59 Å) than at the lower concentration
(0.51 Å) (86). The amino acid proline has also been shown to cause an outward shift
of the water oxygen-water oxygen second peak, at concentrations of Xi = 0.048 and
0.091 (84). However, the peak position is similar to that of pure water in a proline-
water mixture at Xi = 0.063 being found at 4.53 Å. These changes in the second peak
position ($\pm < 0.10 \mathring{A}$) are small compared to the others found in Table 4.3 and are
comparable to those found in the first peak position. Sorbitol (85), TMAO (87) and
trehalose (82; 83) have all been shown to cause inward shifts of the water oxygen-water
oxygen RDF second peak. Sorbitol, at a concentration of Xi = 0.19 leads to an inward
shift of 0.50 Å (85). Similarly, an aqueous mixture of TMAO at a mole fraction of
0.052 leads to an inward shift of 0.30 Å (87). In aqueous trehalose the second peak of
the water oxygen-water oxygen RDF is found at 4.24 Å at Xi = 0.010 (82) and 4.34 Å
at Xi = 0.039 (83) (shifts of 0.32 Å and 0.22 Å respectively). Therefore, the second
peak position is shifted to larger distances as trehalose concentration is increased when
compared to more dilute aqueous trehalose mixtures (82; 83). The same effect as seen
when increasing the concentration of DMSO (86).
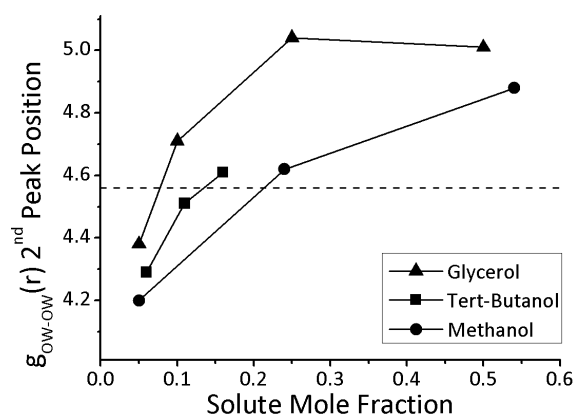
Figure 4.5: The radial distance of the second peak of the water oxygen-water oxygen
RDFs found in aqueous mixtures of glycerol (triangles), tertiary butanol (squares) and
methanol (circles) as a function of solute mole fraction. The dashed line shows the
position that is found in pure water. It can be seen that at low concentrations of
all three solutes the second peak is shifted to lower radial distances. As the solute
concentration is increased the peak is shifted to larger radial distances.

Aqueous mixtures of methanol (123; 124) and tert-butanol (125) show more complex
behaviour. At the lowest concentrations studied (Xi = 0.05 for methanol and Xi = 0.06
for tert-butanol) inward shifts are found (123; 125). Here, the second peak of the water

oxygen-water oxygen RDF is shifted inwards, relative to pure water, by 0.36 Å and
0.27 Å respectively. As the concentration is increased the peak position is shifted
gradually outward. The largest separations being 4.88 Å for methanol (124) and 4.61 Å
for tertiary butanol (125). The positions of these peaks are shown graphically in Figure
4.5.

Table 4.3: Water Oxygen-Water Oxygen RDF Peaks in Various Solutes

Solute	Mole Fraction (Xi)	1st Peak Position (Å)	2nd Peak Position (Å)	Reference
Pure Water	0.000	2.76	4.56	(5)
DMSO	0.048	2.79	5.07	(86)
"	0.333	2.75	5.15	(86)
Glycerol	0.050	2.76	4.38	(3)
"	0.100	2.73	4.71	(4)
"	0.250	2.70	5.04	(4)
"	0.500	2.71	5.01	(4)
"	0.800	2.73	n/a	(2)
Methanol	0.050	2.76	4.20	(123)
"	0.270	2.76	4.62	(124)
"	0.540	2.85	4.88	(124)
Proline	0.048	2.76	4.63	(84)
"	0.063	2.78	4.53	(84)
"	0.091	2.79	4.65	(84)
Sorbitol	0.190	2.66	4.06	(85)
Tert-Butanol	0.060	2.75	4.29	(125)
"	0.110	2.75	4.51	(125)
"	0.160	2.76	4.61	(125)
Trehalose	0.010	2.77	4.24	(82)
"	0.039	2.76	4.34	(83)
TMAO	0.052	2.75	4.26	(87)

From Figure 4.5 it can be seen that an increase in the concentration of glycerol,
tert-butanol , and methanol leads to an outward shift of the water oxygen-water oxygen
second peak. This result is similar to that shown for DMSO (86) and trehalose (82; 83).

This suggests that glycerol, tert-butanol, methanol, DMSO and trehalose all have a
similar effect of the structure of water as measured by the oxygen-oxygen RDFs.

4.3.3   The Tetrahedrality of Water Network

The position of the second peak in the water oxygen-water oxygen RDF is often sug-
gested as an indicator of the tetrahedrality (or lack thereof) within a system. This is
because the law of cosines can be used to calculate the ratio of the side lengths of a
triangle if the relevant angles are provided (see Equation 3.2). Using a tetrahedral an-
gle of $109.47°$, the ratio of side lengths is 1:1:1.633. Table 4.3 shows that the position
of the first peak is fairly insensitive to concentration and solute type being found at
around 2.80 Å. Consequently, a tetrahedral arrangement of oxygen atoms would have
a second peak at around 4.57 Å (2.80 Å × 1.633). Therefore, it is logical to measure
the angular distribution of water oxygen atom triplets. Here, the tetrahedrality of the
water network can be quantified by measuring the included angle formed by three water
oxygen atoms. This is achieved using a similar method to that outlined in Section 3.3.4.
Here, the included angle is measured for all triplets of atoms, which conform to specific
distance criteria. The separation cut-off is set as the radial distance of the first minimum
in the relevant water oxygen-water oxygen RDF (see Figure 4.4(c)). This distribution
$(N(\theta))$ is then divided by $\sin(\theta)$ to produce the density of triplet angles $(P(\theta))$. $\sin(\theta)$
is used here as this is the distribution that would be found in a completely random
system. Figure 4.6 shows the density of included angles formed by water oxygen triplets
(OW-OW-OW) as a function of angle for each of the aqueous glycerol systems studied
at room temperature along with the data taken from pure water (Xg = 0.00). Here, the
dashed lines indicate the perfect tetrahedral angle of $109.5°$.

From Figure 4.6 it can be seen that the tetrahedral nature of the water network
is lost at high glycerol concentrations (Xg $\geq$ 0.50). There is also an increase in the
height of the peak at around $50°$ with increasing glycerol concentration. This peak has
been attributed to oxygen atoms that are within the first coordination shell of another
oxygen atom, but do not form hydrogen bonds (116). These oxygen atoms are known
as interstitial atoms because they are occupying space within the first coordination
shell but are not forming hydrogen bonds to the central oxygen atom. The presence
of interstitial oxygen atoms suggests that the connectivity of the water network is lost
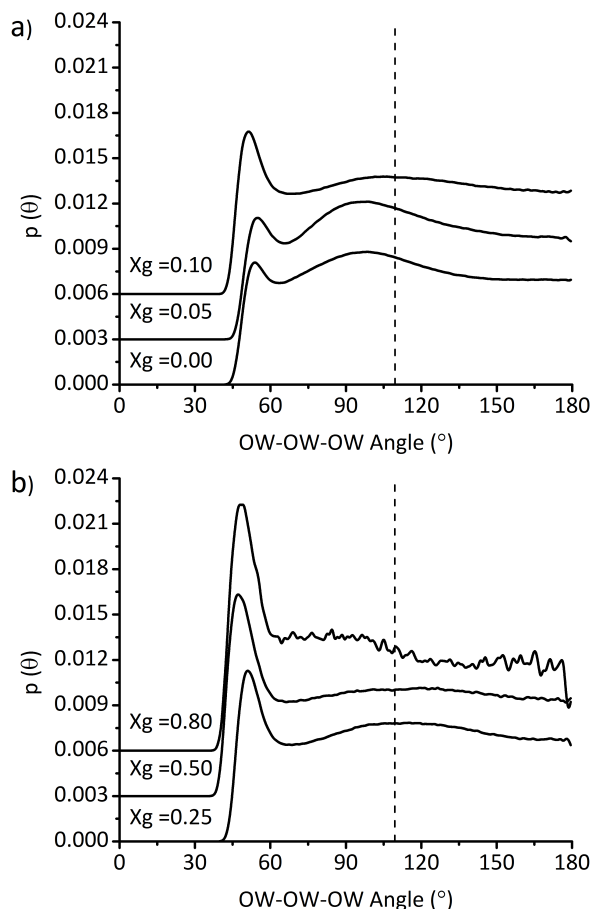
Figure 4.6: Plots of the density of water oxygen atomic triplets $(P(\theta))$ as a function of
the included angle (°) between them for each of the aqueous glycerol systems studied at
room temperature. These plots have been split in to the three most dilute systems (a)
and the three higher concentrations (b) to aid clarity. The dashed line at 109.5° shows
the angle that a perfect tetrahedron would form.

at concentrations of Xg $\geq$ 0.50. This effect has been seen at lower concentrations in
previous studies (77; 118). The concentration ranges where the glycerol and water
networks persist/are broken are discussed in greater detail in Chapter 5. A tetrahedral
angle can be defined as one where the angle $\left(\overline{ABC}\right)$ is given by,

$$cos\left(\overline{ABC}\right) = \frac{-1}{3} \tag{4.1}$$

$\left(\overline{ABC}\right)$ can be written as the as the angle between the jth and k^{th} bonds $\left(\overline{AB} \text{ and } \overline{BC}\right)$.
Deviations from this value can, therefore, be used to quantify the level of tetrahedrality
within a system. This approach has been used to construct tetrahedral order parameters.

Chau and Hardwick propose the following equation be used ([128]),

$$S_g = \frac{3}{32} \sum_{j=1}^{3} \sum_{k=j+1}^{4} \left[cos(\theta_{jk}) + \frac{1}{3} \right]^2 \tag{4.2}$$

where S_g is the angular component of the tetrahedrality parameter and θ_{jk} is the angle
between the jth and k^{th} bonds. The factor of 3/32 normalises the values of S_g to
be between zero and one. Here, a value of zero is given by a perfectly tetrahedral
arrangement and a value of one indicates an arrangement as far from tetrahedral as
possible. A similar approach has been proposed by Errington & Debenedetti ([129]) and
is given by,

$$q = 1 - \frac{3}{8} \sum_{j=1}^{3} \sum_{k=j+1}^{4} \left[cos(\theta_{jk}) + \frac{1}{3} \right]^2 \tag{4.3}$$

Here, the parameter has been rescaled such that $q = 1$ for a perfectly tetrahedral system
and $q = 0$ for an ideal gas distribution. Both the Sg and q factors provide the same
information with the difference between them being in the method of normalisation
of the two factors. The Sg factor is normalised to be between a perfect tetrahedral
arrangement and a structure that is as far from tetrahedral as mathematically possible.
This situation, although mathematically feasible, requires that the atoms are all at the
same position. This is an unphysical arrangement and therefore, the q factor will be
used throughout this thesis. The q factor is taken by measuring the sum over the 6
angles formed by the central oxygen atom and its four nearest neighbours. However, in
the glycerol-water mixtures that are studied here, it is likely that not all of these oxygen
atoms will be within the first coordination shell of the central oxygen atom. This would
lead to erroneous results. Therefore, a modification to Equation 4.3 must be made to
ensure that it is only the relevant oxygen atoms that are included in the calculation.
The $P(\theta)$ values that have been plotted in Figure 4.6 can be included in the calculation
([130]) using,

$$q = 1 - \frac{9}{4} \frac{\int_0^\pi sin\theta \left[cos(\theta_{jk}) + \frac{1}{3} \right]^2 P(\theta)d\theta}{\int_0^\pi sin\theta P(\theta)d\theta} \tag{4.4}$$

Here, the factor of 9/4 ensures that the normalisation of the q factor remains the same
as published by Errington & Debenedetti ([129]). The values of the q factors have been
calculated for each of the water oxygen triplets as a function of glycerol concentration
and are shown along with the value from pure water in Figure 4.7.
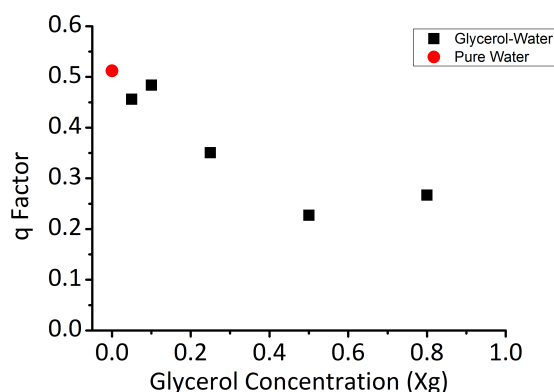
Figure 4.7: Tetrahedrality parameters (q) for water oxygen triplets calculated using Equation 4.4 as a function of glycerol concentration. The data taken from glycerol-water mixtures (black squares) are shown along with the q factor taken from previously published pure water data (red circles) (108).

Figure 4.7 shows that the q factor decreases with increasing glycerol concentration. At low concentrations ($Xg \leq 0.10$) the tetrahedrality of the water networks found in the glycerol-water mixtures is similar to that found in pure water at room temperature. At higher concentrations the tetrahedral nature of the water network is diminished. This result is similar to that found by Politi *et al.*, who used molecular dynamics simulations and found that the tetrahedral nature of the water network is lost at concentrations above $Xg = 0.06$ (78).

4.3.4 Glycerol-Glycerol Interactions in Aqueous Mixtures

It has been suggested that glycerol molecules associate via their methyl groups (77; 78). This feature has been seen in other amphiphilic molecules, such as tertiary butanol (125) and methanol (124; 126). The carbon-carbon and carbon-methyl hydrogen radial distributions are shown in Figure 4.8.

The lack of a change in the peak positions within the carbon-carbon RDFs as a function of concentration suggests that there is no change in the glycerol-glycerol association, as measured by the carbon-carbon interactions, with concentration. It is instructive to compare the carbon-carbon interactions found in aqueous glycerol with those found in other solutes. Figure 4.9 compares the results from previous studies of methanol (123; 124) and tert-butanol (125)[1]. The dilute glycerol data has been in-

---

[1]The data for the tert-butanol RDFs have been obtained using the Plotdigitizer software (see http://plotdigitizer.sourceforge.net/ for more information).
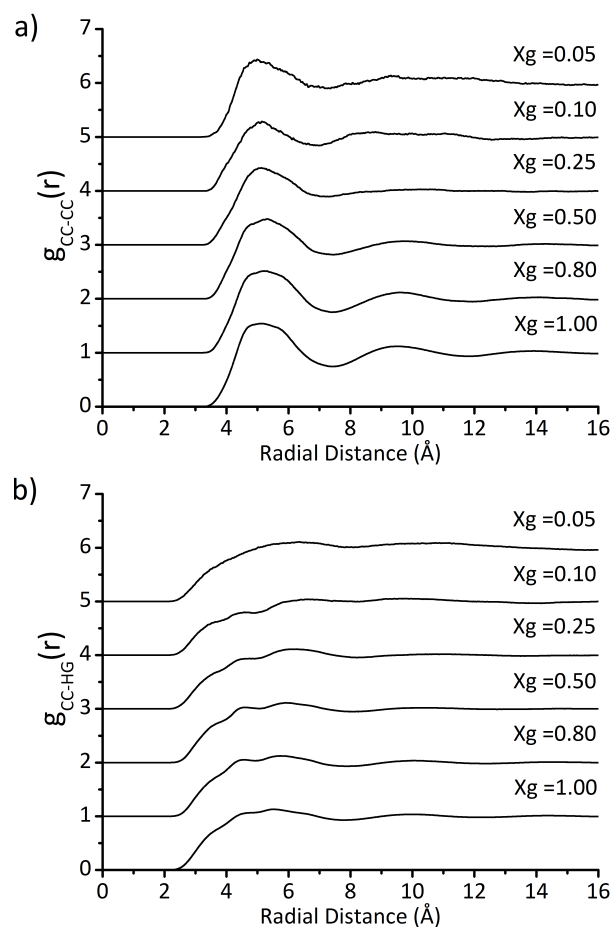
Figure 4.8: The inter-molecular RDFs for the central carbon-central carbon and central carbon-methyl hydrogen pairs. (a) The central carbon-central carbon RDFs at each of the concentrations studied. It can be seen that there is very little change in the peak positions as a function of concentration. Similarly the central carbon-methyl hydrogen RDFs (b) do not show a concentration dependence.

cluded as these data are of comparable concentrations to those taken from previous studies. From Figure 4.9 it can be seen that the carbon-carbon interactions have a less pronounced structure in aqueous glycerol than in mixtures of methanol and tertiary butanol. In Section 1.2.2 the method that is used to calculate an RDF is introduced. It is stated that the distribution is given by the measured distribution divided by the "Ideal Distribution" (see Equations 1.3, 1.4 and 1.5). Here, the ideal distribution is calculated using the fraction of atoms that are of type β (denoted as c_β). Therefore, the values of c_β in each of these systems must be taken into account.

The relevant c_β values are given in Table 4.4. When the c_β values are similar the two RDFs are directly comparable. This is the case for the most dilute concentrations. Here, c_β values are 0.141 for glycerol, 0.159 for methanol, and, 0.139 for tertiary butanol. The
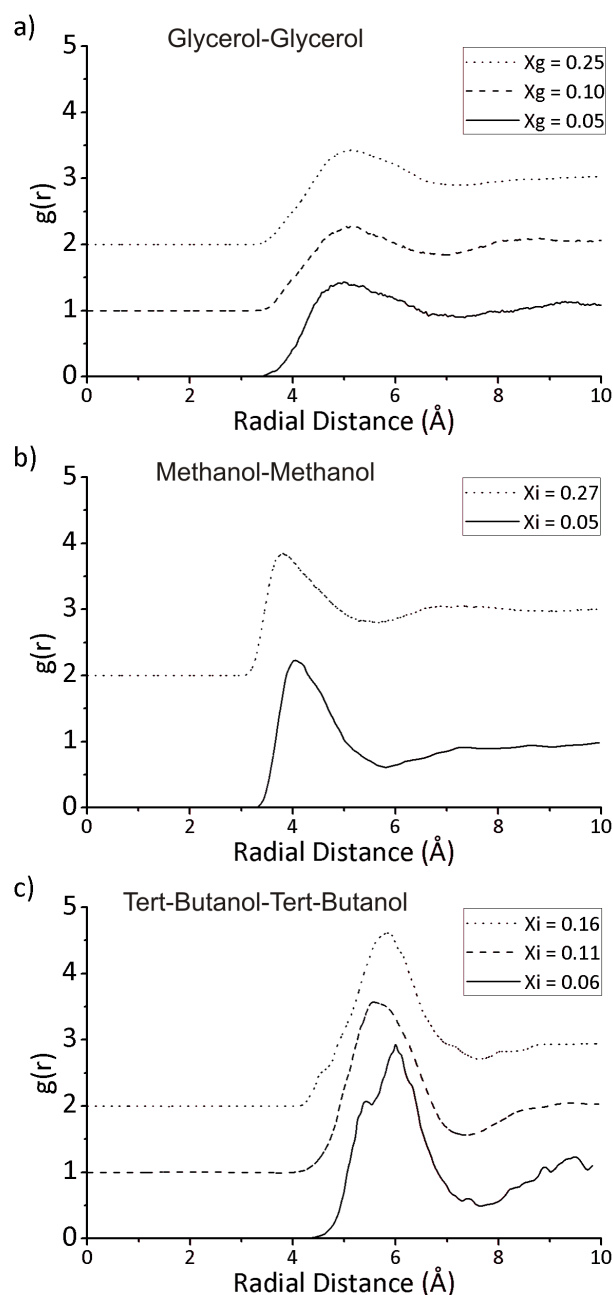
Figure 4.9: The inter-molecular RDFs for carbon-carbon interactions found in dilute aqueous solutions including: (a), glycerol-glycerol central carbon-central carbon RDFs, (b), methanol-methanol carbon-carbon RDFs, and, (c), tert-butanol-tert-butanol central carbon-central carbon RDFs. The carbon-carbon interactions are much more pronounced in aqueous methanol and tert-butanol than in glycerol-water mixtures.

heights of the first peak in the carbon-carbon RDFs for glycerol, methanol and tertiary butanol are 1.44, 2.23 and 2.94, respectively. This suggests that the carbon-carbon interactions are markedly more pronounced in aqueous methanol and tertiary butanol when compared to those found in a glycerol-water mixture. The atomic number fractions (c_β) for the central carbon atoms found in aqueous glycerol and tertiary butanol are

Table 4.4: Fractions of Central Carbon Atoms in Various Systems

Solute	Relevant Atom	Mole Fraction	atomic number fraction
Glycerol	Central Carbon	0.25	0.0435
"	Central Carbon	0.10	0.0244
"	Central Carbon	0.05	0.0141
Methanol	Carbon	0.27	0.0709
"	Carbon	0.05	0.0159
Tert-Butanol	Central Carbon	0.16	0.0325
"	Central Carbon	0.11	0.0255
"	Central Carbon	0.06	0.0139

similar at concentrations of Xg = 0.10 and Xi = 0.11. Therefore, these RDFs can also
be directly compared. The height of the first peak in the glycerol central carbon-central
carbon RDF is at 1.29. The peak height for the tertiary-butanol central carbon-central
carbon RDF is found at 2.58. Again, this confirms that there is a more structured
association between the carbon atoms within tertiary butanol-water mixtures than is
found in aqueous glycerol. These results contradict the previous studies by Dashnau
et al. (77) who suggest that glycerol molecules form hydrophobic clusters and suggest
that glycerol-water interactions are different from those found in aqueous mixtures of
tertiary butanol (125) and methanol (123; 124). Glycerol-glycerol interactions via the
hydrophilic hydroxyl groups are discussed in Section 4.4.

4.3.5   Water-Glycerol Interactions in Aqueous Mixtures

Macroscopic measurements of aqueous glycerol have suggested that the properties of the
mixture can be attributed to the prevalence of mutual (*i.e.* glycerol-water) interactions
(41; 44; 71). These investigations have used the compressibility (71), excess molar
volume (44) and a combination of data such as vapour pressure and heats of mixing
(41). In each of these studies, the interactions between water and glycerol are predicted
to be due to the presence of hydrogen bonding.

Hydrogen bonding can be confirmed using the relevant oxygen-hydrogen RDFs that
are shown in Figure 4.10. In each of these RDFs a peak is found at around 1.80 Å.
This shows that hydrogen bonds are formed between water and glycerol molecules at

each of the concentrations studied. Indeed, the peak positions are not altered with a change in the concentration of the mixture. The range of radial positions of the first peak positions for the central glycerol oxygen-water hydrogen 4.10(a), distal glycerol oxygen-water hydrogen 4.10(b), and, water oxygen-glycerol hydroxyl hydrogen 4.10(c), are all 0.06 Å. The presence of mutual interactions across the concentration range is in agreement with previous macroscopic studies which suggest the prevalence of mutual interactions (41; 44; 71). However, the nature of the correlation between hydrogen bonding and macroscopic properties remains unclear. The hydrogen bonding found in these mixtures is discussed in greater detail in the following section.

4.4   Inter-Molecular Bonding in Aqueous Glycerol as a Function of Concentration

4.4.1   The Uncertainty in Coordination Numbers

In previous studies using EPSR, the error on a coordination number has been quoted as the standard deviation of each coordination number measurement (*e.g.* (1; 2; 4; 131; 132)). This is a measure of the uncertainty on each atom of type α being coordinated by a certain amount of atoms of type β. This is not, however, the value that is of interest for the investigation reported in this thesis. Here, the average number of hydrogen bonds formed by each molecule is investigated. Therefore, the pertinent value is the uncertainty on the average number of hydrogen bonds per molecule.

Figure 4.11 shows the way in which EPSR can overestimate the errors in a coordination number. This simple system contains three atoms and two snapshots shown in Figures 4.11(a) and 4.11(b). In Figure 4.11(a), atoms A and B both have a coordination number of one and atom C has a coordination number of zero. Therefore, the average coordination number across the three atoms is 0.667. Similarly, in Figure 4.11(b) atom A has a coordination number of zero and atoms B and C each have a coordination number of one. This also results in an average coordination number of 0.667. The standard deviation across the six measurements of the coordination number (three per snapshot) is 0.52. Therefore, the coordination number would be stated as 0.7 ± 0.5. This is not an accurate measure of the uncertainty on the average coordination number per atom, as both snapshots provide the same average. Therefore, a new method of calculating
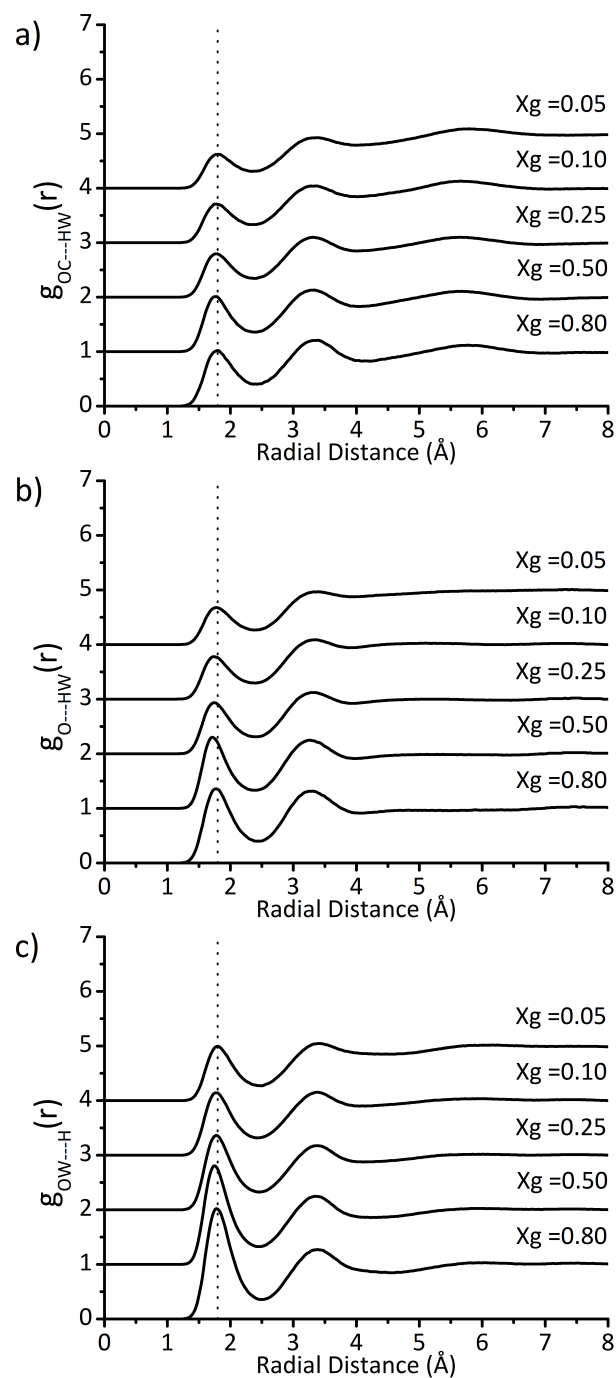
Figure 4.10: Inter-molecular RDFs showing the interactions between water hydrogen
atoms and glycerol oxygen atoms as well as water oxygen atoms and glycerol hydroxyl
hydrogen atoms as a function of glycerol concentration. Here, the central oxygen-water
hydrogen (a) distal oxygen-water hydrogen (b), and, water oxygen-hydroxyl hydrogen
(c) RDFs all show a peak at around 1.80 Å (dotted lines). This indicates that glycerol-
water and water-glycerol hydrogen bonds are present across the concentration range.

the uncertainty on the coordination numbers was used in this work. The simple code
(written using the Python language[1]) can be found in Appendix C. This code allows the

---

[1]See www.python.org for more information.
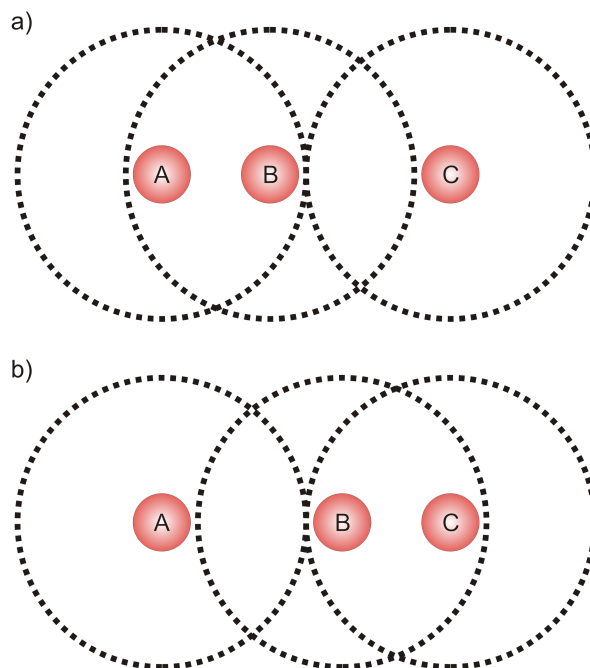
Figure 4.11: A schematic diagram showing two hypothetical snapshots from a simulation of 3 atoms. Here, the dotted lines around each atom represent the radial cut-off for the coordination number calculation. (a) Atoms A and B both have a coordination number of one, whereas the coordination number of C is zero giving an average of $0.667 = (1 + 1 + 0)/3$. (b) Atom A has a coordination number of zero, and atoms B and C both have a coordination number of one. Again, an average of $0.667 = (0 + 1 + 1)/3$.

average coordination numbers to be added to a text file with new data being appended to the file after subsequent EPSR iterations. This produces a text file that contains the coordination numbers measured after each EPSR iteration. From these data the spread of the average coordination number is used to calculate the relevant uncertainty (see Section 4.4.3). Figure 4.12 shows the number of water hydrogen atoms found in the first coordination shell around water oxygen atoms as a function of iteration along with the uncertainties that are produced by EPSR. It can be seen that the spread of the coordination numbers over 500 iterations is much smaller than the uncertainty taken from EPSR using the previous method. This is further evidence that the method used in previous studies to measure the uncertainty of coordination numbers (*e.g.* (1; 2; 4; 131; 132)) is a substantial overestimate.
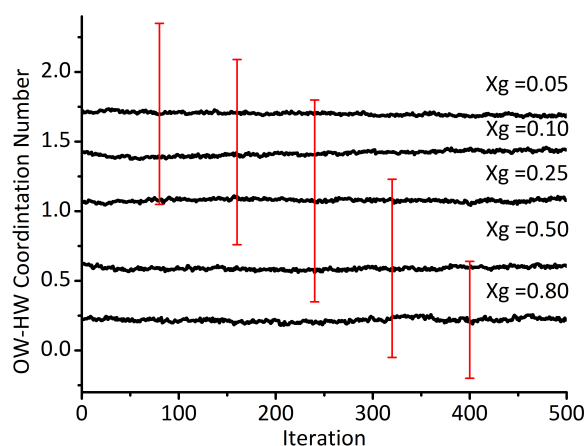
Figure 4.12: The average number of water hydrogen atoms found in the first coordination
shell around water oxygen atoms as a function of iteration for each of the glycerol-water
systems. The uncertainties taken from EPSR are shown with red error bars. It can be
seen that the error taken from EPSR is a gross over-estimate of the distribution of the
results.

4.4.2 Glycerol-Glycerol Hydrogen Bonding Interactions

To investigate the level of bonding within aqueous glycerol, it must first be confirmed
that bonding exists. Figures 4.4(b) and 4.10 show that there is a clear peak in the
oxygen-hydrogen RDFs at around 1.8 Å. This feature is indicative of hydrogen bonding.
This shows that water-water (Figure 4.4(b)) as well as water-glycerol and glycerol-water
hydrogen bonds (Figure 4.10) are formed at all of the concentrations studied. Figure
4.13 confirms the presence of glycerol-glycerol inter-molecular hydrogen bonds at each
of the concentrations studied. The RDFs shown in Figures 4.4(b), 4.10 and 4.13 can
be used to quantify the number of each type of hydrogen bond present as a function of
concentration. This is achieved using the method outlined in Section 3.3.1, where the
coordination numbers (see Equation 2.18) of hydrogen atoms around oxygen atoms are
calculated to find the number of hydrogen bonds formed.

4.4.3 Hydrogen Bond Number in Aqueous Glycerol at Room Temperature

In Section 3.3.3, the method used to calculate the number of hydrogen bonds per glycerol
molecule in the pure liquid is described (see Table 3.6). The number of each type of
hydrogen bond in the aqueous glycerol systems is calculated using a similar method.
The average number of hydrogen bonds formed by each of the glycerol molecules (G_{tot})
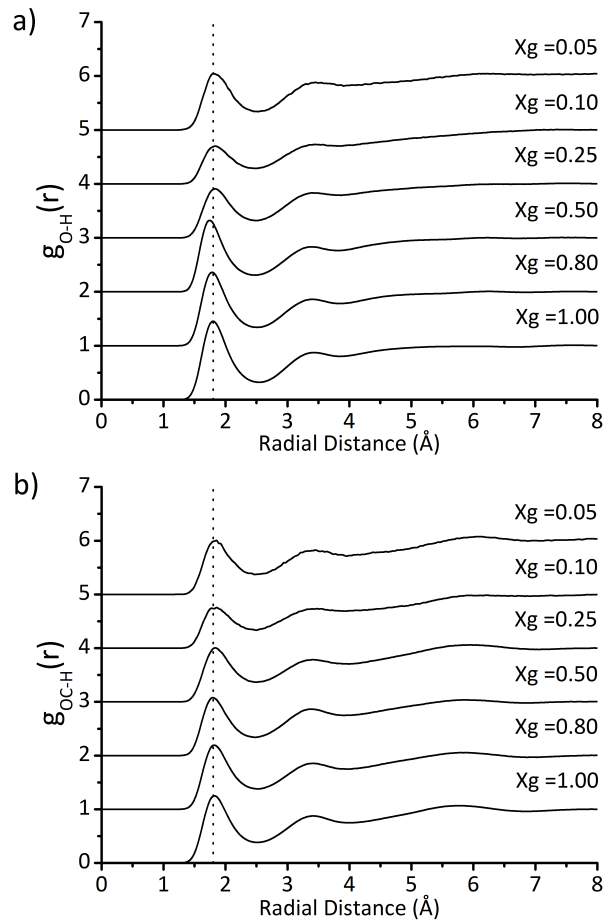
Figure 4.13: Glycerol-glycerol inter-molecular RDFs for each of the oxygen-hydroxyl hydrogen pairs at all concentrations studied. Part (a) shows the distal oxygen-hydroxyl hydrogen and part (b) shows the central oxygen-hydroxyl hydrogen distributions. The dotted lines show a radial distance of 1.8 Å. Each of the RDFs show a peak at around this distance, indicating that glycerol-glycerol hydrogen bonds are present across the complete concentrations range.

is given by,

$$G_{tot} = [G_{acc}] + [G_{don}]$$

$$= [n_{OC\,H} + n_{OC\,HW} + 2 \times (n_{O\,H} + n_{O\,HW})] + [3 \times (n_{H\,OC} + n_{H\,O} + n_{H\,OW})]$$

$$(4.5)$$

where the average number of acceptor and donator sites are given by G_{acc} and G_{don} respectively and $n_{\alpha\beta}$ is the average number of atoms of type β that are in the first coordination shell of atoms of type α. Similarly, the average number of hydrogen bonds

formed by each of the water molecules (W_{tot}) is given by,

$$W_{tot} = [W_{acc}] + [W_{don}]$$

$$= [n_{OW\ H} + n_{OW\ HW}] + [2 \times (n_{HW\ OC} + n_{HW\ O} + n_{HW\ OW})] \quad (4.6)$$

where the average number of acceptor and donator sites are given by W_{acc} and W_{don} respectively. The factors of two and three found in Equations 4.5 and 4.6 are due to the number of the relevant type of atom in each molecule. For example, there are two hydrogen atoms in each water molecule. Therefore, each of the coordination numbers that give the number of atoms around each water hydrogen atom, is multiplied by two in order to calculate the number around each water molecule. These hydrogen bonds can be further categorised as either homo (glycerol-glycerol or water-water) or hetero (glycerol-water or water-glycerol) using,

$$\text{Glycerol-Glycerol} = [n_{OC\ H} + 2 \times (n_{O\ H})] + [3 \times (n_{H\ OC} + n_{H\ O})]$$

$$\text{Glycerol-Water} = [n_{OC\ HW} + 2 \times (n_{O\ HW})] + [3 \times (n_{H\ OW})]$$

$$\text{Water-Water} = [n_{OW\ HW}] + [2 \times (n_{HW\ OW})] \quad (4.7)$$

$$\text{Water-Glycerol} = [n_{OW\ H}] + [2 \times (n_{HW\ OC} + n_{HW\ O})]$$

The values calculated with Equation 4.7 are used to produce Figure 4.14. The results shown in Figure 4.14 are in agreement with the molecular dynamics study of Politi $et\,al.$, who found that water-glycerol hydrogen bonds compensate for the loss of water-water hydrogen bonds at glycerol concentrations of below Xg = 0.06 (78). However, as the glycerol concentration is increased, there are insufficient water-glycerol hydrogen bonds to compensate for the loss of water-water hydrogen bonds. This result is in agreement with the MD simulations of Chen $et\,al.$ (76) and the investigation of Dashnau $et\,al.$ (77), who combined simulation and spectroscopy.

To investigate the significance of the changes in the number of hydrogen bonds per molecule, it is important to understand the uncertainties on the values that are calculated. The method introduced in Section 4.4.1 has been used to measure the uncertainty. Here, the average coordination numbers are calculated after each iteration of EPSR us-
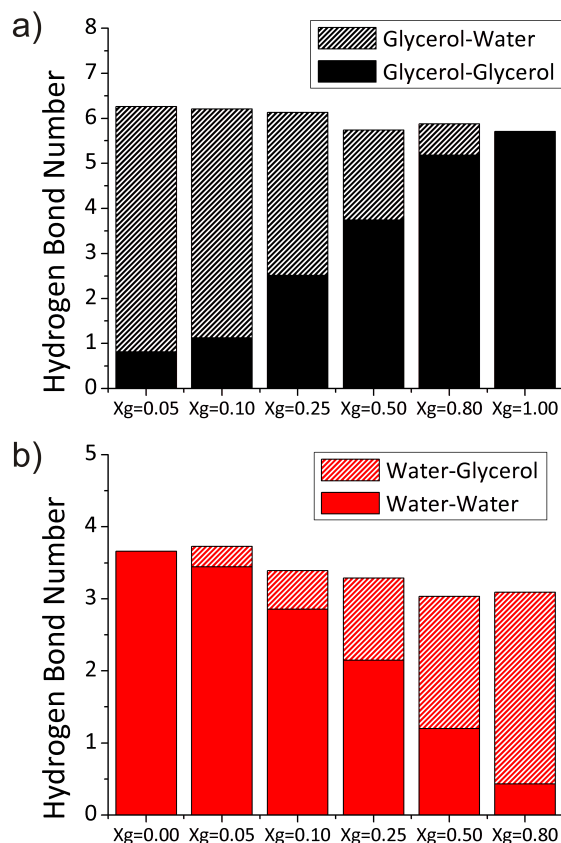
Figure 4.14: Bar charts showing the average number of hydrogen bonds per molecule at each of the different aqueous glycerol concentrations, plus data from pure water (Xg = 0.00) and pure glycerol (Xg = 1.00). (a) Glycerol-water (shaded region) hydrogen bonds compensate for the loss of glycerol-glycerol (solid region) with decreasing glycerol concentration. (b) Water-glycerol (shaded region) hydrogen bond number increases with increased glycerol concentration. This, however, is not sufficient to compensate for the loss of water-water hydrogen bonds with decreasing water concentration, except for at the lowest glycerol concentration (Xg = 0.05).

ing Equation 4.7. The error on each of these coordination numbers is denoted as $\delta \mathrm{X}$[1],

and is calculated using the range of the relevant values taken over five hundred iterations

(highest coordination number minus lowest coordination number). This number is then

divided by two to produce the uncertainty on the average number of hydrogen bonds

of each type (δGlycerol-Glycerol, δGlycerol-Water, δWater-Water & δWater-Glycerol

[1]Here, "X" represents one of the bond categories listed in Equation 4.7.

respectively). These values are combined in quadrature using,

$$\delta(G_{tot}) = \left[(\delta\text{Glycerol-Glycerol})^2 + (\delta\text{Glycerol-Water})^2\right]^{-1/2}$$

$$\delta(W_{tot}) = \left[(\delta\text{Water-Water})^2 + (\delta\text{Water-Glycerol})^2\right]^{-1/2} \tag{4.8}$$

where $\delta(G_{tot})$ and $\delta(W_{tot})$ are the uncertainties in the total number of hydrogen bonds
formed by glycerol and water respectively. The total number of hydrogen bonds formed
by each molecule type is calculated using Equations 4.5 and 4.6 and combined with the
error calculations using Equation 4.8 to produce Figure 4.15.
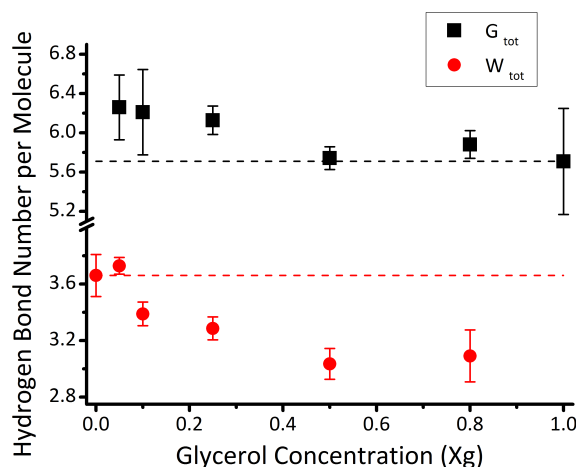
Figure 4.15: The average number of hydrogen bonds formed by each glycerol molecule
(G_{tot}) calculated using Equation 4.5 (black) and the average number of hydrogen bonds
formed by each water molecule (W_{tot}) found using Equation 4.6 (red). The error bars
are calculated using the spread of the relevant coordination numbers (see Equation 4.8).
Here, the dashed lines indicate the average number of hydrogen bonds formed in the
pure liquids.

Interestingly, at low glycerol concentrations each glycerol molecule forms more than
six hydrogen bonds (6.3 ± 0.3). This is higher than found for the pure liquid, which has a
hydrogen bond number of 5.7 ± 0.5. In the pure liquid, each hydroxyl hydrogen donates
an average of 0.95 hydrogen bonds and each hydroxyl oxygen accepts an average of 0.95
hydrogen bonds. The increase at low glycerol concentration could be due to one of
two processes: Each hydroxyl oxygen atom could be accepting more than one hydrogen
bond, or each hydroxyl hydrogen atom could be donated to more than one oxygen
atom (a process known as bifurcation or over-coordination (114)). Table 4.5 shows the
number hydrogen bonds accepted or donated per accepting or donating atom on each

glycerol molecule ($G_{acc}/3$ and $G_{don}/3$ respectively). From Table 4.5 it can be seen

Table 4.5: Glycerol Donator and Acceptor Values per Atom

Concentration (Xg)	$G_{acc}/3$	$G_{don}/3$	$(G_{acc} - G_{don})/3$
0.05	1.20	0.89	0.31
0.10	1.18	0.89	0.29
0.25	1.11	0.92	0.19
0.50	1.00	0.91	0.09
0.80	0.99	0.96	0.03
1.00	0.95	0.95	0.00

that glycerol accepts more hydrogen bonds per molecule than it donates at low glycerol concentrations (Xg $\leq$ 0.25). At higher glycerol concentrations, the difference between hydrogen bonds accepted and donated becomes comparable to the uncertainties on the number of hydrogen bonds per molecule (see Figure 4.15). This result is consistent with the molecular dynamics study of Weng *et al*. (75).

4.5 Conclusions of the Structure of Aqueous Glycerol at Room Temperature

This chapter describes the structural modifications that are found within water and glycerol as a function of concentration. It was found that a model produced using a glycerol molecule without dihedral angle constraints provided the closest fit to the neutron diffraction data across the concentration range (see Section 4.1.1). The use of this model does not greatly affect the results regarding intra- and inter-molecular hydrogen bonding described in Chapter 3. The model used in this chapter (and for the remainder of the work in this thesis) produces a spread of conformations that is in agreement with previous studies (73; 74; 77; 117) (see Table 4.1). Specifically, most of the glycerol molecules (72 - 82 %) have at least one distal oxygen atom in the α arrangement (see Figure 4.2). This spread of glycerol molecular structures was found not to be due to the formation of intra-molecular hydrogen bonds. This is confirmed by the oxygen-hydrogen intra-molecular RDFs shown in Figure 4.3, as there is not a peak in the region of 1.8 Å.

Section 4.3 describes an investigation of the inter-molecular structure within aque-

ous glycerol as a function of concentration. This investigation is split in to three parts
with the water-water, glycerol-glycerol, and water-glycerol structure described in Sections 4.3.1, 4.3.4, and 4.3.5, respectively. The water structure up to the first neighbour
remains relatively unperturbed at each of the concentrations studied. Similar effects
have been seen for the glycerol-glycerol and water-glycerol interactions. However, the
second neighbour structure of the water oxygen-water oxygen interaction is altered. This
leads to the water network becoming less tetrahedral as the glycerol concentration is
increased (see Section 4.3.3). The connectivity of the water network is discussed further
in Chapter 5.

Inter-molecular hydrogen bonding as a function of glycerol concentration is described
in Section 4.4, with a new method to calculate the uncertainty on the hydrogen bond
number being introduced in Section 4.4.1. It is shown that the formation of water-glycerol hydrogen bonds compensates for the loss of water-water hydrogen bonds at
the lowest glycerol concentration studied. Glycerol-water hydrogen bonds, however,
preserve the number of hydrogen bonds formed by each glycerol molecule at high glycerol
concentration, and increase the number formed as glycerol concentration is decreased
(see Figure 4.15). This increase is achieved by glycerol accepting more hydrogen bonds
than are donated (see Table 4.5). The following chapter describes the molecular scale
structure that is found in aqueous glycerol, and how this is modified with concentration.

Chapter 5

Molecular Scale Mixing in Aqueous Glycerol at Room Temperature

5.1 Context

The aim of this chapter is to investigate the relative strengths of the hetero and homo interactions by measuring the molecular scale structure of aqueous glycerol as a function of concentration. This chapter, therefore, builds upon the previous chapter where the presence, structure and quantity of hetero interactions (glycerol-water or water-glycerol) was investigated. Previously, macroscopic measurements have been used to infer the molecular scale interactions that are present (41; 42; 133–135). These are introduced in Section 5.1.1 with the various results that have been found previously being given in Section 5.1.2. The method that has been used in this research is introduced in Section 5.1.3. The mixing that is found is compared to two reference systems: the mixing that would be expected due to a purely packing effect (see Section 5.1.3), and, the predicted cluster distribution at the percolation threshold (see Section 5.3.1).

The results presented in this chapter begin with a discussion of the molecular mixing at the extremes of the concentration range (see Section 5.2.1). This is followed by an investigation of the mixing as a function of concentration in Section 5.2.2. Section 5.3.1 includes an introduction to a hypothetical cluster distribution that would be found at the percolation threshold. This distribution is then compared to the results taken from

neutron diffraction experiments within Section 5.3.2. The structure of the clusters is investigated in Section 5.3.3. Finally, a method that estimates the excess entropy of mixing based on cluster formation is investigated in Section 5.3.4. A large proportion of the work in this chapter has been previously published (2–4).

5.1.1   Introduction to Mutual Interactions

For many years the molecular scale interactions within liquid samples have been probed using macroscopic properties. For example, measurements of water vapour pressure (42), heat capacity (133) and heats of mixing (134) have been measured for aqueous glycerol at a range of different concentrations. These data have been used by Marcus to calculate various thermodynamic properties of the system such as the excess Gibbs energy (G^E) (41). This value is related to the Gibbs energy change (ΔG), which is a measure of whether or not a process is energetically favourable and thus will happen spontaneously. ΔG is given by,

$$\Delta G = \Delta H - T\Delta S \tag{5.1}$$

where ΔH is the enthalpy change and ΔS is the change in entropy, and T is the temperature. When ΔG is less than zero a process is energetically favourable and when ΔG is more than zero a process in energetically unfavourable. The process under investigation here is the mixing of water and glycerol therefore it is the energetics of mixing that are of interest.

In Section 1.2.2 the method of quantifying liquid structure is introduced. Here, insight is found by comparing the measured distribution of atoms with the distribution that would be found in an ideal system. A similar approach can be used for the macroscopic properties of the system by comparing the system to an ideal (model) system. In an ideal mixture (sometimes called an ideal solution) the enthalpy of mixing (ΔH) is given by,

$$\Delta H = 0 \tag{5.2}$$

It should be noted that this does not mean that there are no interactions between the different molecule types as is found in an ideal gas. Rather, it means that there is no change in these interactions on mixing. For a binary mixture of atoms of type α and

β this means that the hetero interactions ($U_{\alpha\beta}$) are the same strength as the homo interactions ($U_{\alpha\alpha}$ and $U_{\beta\beta}$). Formally,

$$2U_{\alpha\beta} = U_{\alpha\alpha} + U_{\beta\beta} \tag{5.3}$$

Ideal mixing can be defined using a number of macroscopically measurable properties. One example of this is contained within Raoult's law, which states

$$p^M = \sum_j Xj \cdot p_j^* \tag{5.4}$$

here, p^M is the measured vapour pressure of a mixture and p_j^* is the vapour pressure of the pure components. The combination of Equations 5.1 and 5.2 means that the Gibbs free energy of ideal mixing is given by,

$$\Delta G = -T\Delta S \tag{5.5}$$

Therefore, the change in the Gibbs energy upon mixing of an ideal solution is due to a change in the entropy of the system. Many of the assumptions of the ideal mixture hold in very dilute systems. However, this is not the reason why they are of interest in the current thesis. Ideal mixing is used as a point of reference to compare experimentally measured values. This is because deviations from ideal behaviour provide information regarding the relative strengths of the intermolecular forces within the mixture. These deviations from ideal behaviour are known as excess functions and can be quantified using,

$$Z^E = Z^M - \sum_j Xj \cdot Z_j^* \tag{5.6}$$

where Z is the property under investigation, Z^M is the experimentally measured value, Xj is the mole fraction of component j, Z_j^* is the value of the property in the pure component, and, Z^E is the excess function. Equation 5.5 shows that, for an ideal mixture, the enthalpy change due to mixing is zero. Therefore, any change in the enthalpy due to mixing is an excess function (H^E). This factor is also known as the heat of mixing and can be viewed as being due to three steps: the breaking of solvent-solvent bonds, the breaking of solute-solute bonds, and, the formation of solvent-solute

bonds. The breaking of the homo-interactions (solvent-solvent and solute-solute) are both endothermic processes. That is, there is a decrease in the enthalpy of the system which requires the addition of heat to the system. The formation of hetero-interactions (solvent-solute) is an exothermic process, in which, heat is given of by the system due to the formation of new bonds. The enthalpy of mixing is, therefore, the combination of these factors.

$$E_{hetero} > E_{homo} \; H^E > 0 \; \text{(Endothermic Mixing)}$$
$$E_{hetero} = E_{homo} \; H^E = 0 \; \text{(Ideal Mixing)} \tag{5.7}$$
$$E_{hetero} < E_{homo} \; H^E < 0 \; \text{(Exothermic Mixing)}$$

For aqueous glycerol the enthalpy of mixing (H^E) has been shown to be negative across the concentration range (134). This shows that the formation of hetero-interactions has a lower free energy (E_{hetero}) than is lost when homo-interactions are broken (E_{homo}). This shows that the formation of hetero-interactions leads to the system being in a lower energy state than would be found if the mixing was ideal (see Equation 5.6). This suggests that the mixing of water and glycerol is energetically favourable due to the hetero-interactions being more favourable than the homo-interactions. It has been argued that this factor is indicative of a system with a predominance of hetero-interactions over homo-interactions (41).

Anther macroscopic property of interest is the excess molar volume (V^E). This has been measured by Cristancho $etal.$ and Xu $etal.$ (44; 72). Here, the excess molar volume, V^E, is given by,

$$V^E = V^M - \sum_i Xi \cdot V_i^* \tag{5.8}$$

where V^M is the experimentally measured volume, Xi is the mole fraction of component i and V_i^* is the molar volume of the pure component. Both Cristancho $etal.$ and Xu $etal.$ found that the excess molar volume was negative across the concentration range (44; 72). This contraction on mixing has been argued to be due to strong hetero interactions (44; 72).

In Section 4.4 the presence of mutual interactions is confirmed by hetero hydrogen bonds being formed at each of the concentrations studied (see Figure 4.10). This is, however, highly unsurprising given that both water and glycerol are hydrogen bond

forming liquids. The molecular mixing regimes that are present in the system can provide information about the concentrations at which hetero or homo interactions are dominant. The following section introduces previous research into the mixing regimes found within aqueous glycerol.

5.1.2 Introduction to Molecular Mixing Regimes

The molecular scale mixing of aqueous glycerol has been investigated using a number of different techniques including, vapour pressure measurements (42), spectroscopy (38; 43; 80), and molecular dynamics simulations (77; 81). To $et\ al.$ used vapour pressure measurements to calculate the partial molar enthalpies of glycerol up to a concentration of $Xg = 0.55$ (42). Here, changes in the gradient of the partial molar enthalpy as a function of concentration are used as evidence for a change in the molecular mixing (42). To $et\,al.$ conclude that there are three different regimes: at glycerol concentrations of $Xg \leq 0.15$ the water-water interactions are gradually decreased; between $Xg = 0.15$ and 0.35 the mixture consists of two kinds of cluster each rich in either glycerol or water; and, extended glycerol clusters are found at concentrations above $Xg = 0.35$ (42).

Hayashi $et\,al.$ have used a combination of differential scanning calorimetry and broadband dielectric spectroscopy to study aqueous glycerol (43). Their study took measurements at concentrations of $0.05 \leq Xg \leq 1.00$ with intervals of 0.05 over a temperature range of 138 - 313 K and used previously published data for pure water ($Xg = 0.00$) (136). At glycerol concentrations of above $Xg = 0.60$ the spectrum is relatively unperturbed. This is attributed to the glycerol network being unperturbed (43). Water-water interactions are found at concentrations below $Xg = 0.60$ and ice nano-crystals are formed below $Xg = 0.20$. They conclude that this is due to water domains of increasing size with decreased glycerol concentration until they begin to form crystals at the lowest glycerol concentrations (43). Similar results have been reported by Banerjee & Bhat from an electron spin resonance (ESR) investigation (80). In ESR the microwave absorbance of an unpaired electron is measured. In systems where there are not any unpaired electrons (such as aqueous glycerol) a probe molecule, known as a tracer is included. In the work of Banerjee & Bhat, 2,2,6,6-tetramethyl-l-piperidine-l-oxy (TEMPO) molecules are used as the tracer (80). TEMPO is an organic free radical that contains a nitrogen-oxygen group. The coupling of the nitrogen and oxygen atoms within the TEMPO molecule

leads to spectra that have three peaks. Modifications to these spectra as a function of temperature are due to changes in the reorientation of the tracer molecule. The broadening of the triplet is used as a measure of the glass transition of the glycerol-water mixtures. Banerjee & Bhat measure the glass transition temperature as a function of glycerol concentration. They find that there are three regions with different gradients of glass transition temperature against glycerol concentration (80) and argue that these are indicative of the three mixing regimes proposed by Hayashi *et al*. (43).

Mudalige & Pemberton conducted a Raman spectroscopy investigation of glycerol-D_2O mixtures at concentrations of Xg = 0.02, 0.12 and 0.32 (38). Deuterated water was used to separate the oxygen-hydrogen signal from glycerol from the oxygen-deuterium of the water molecules. The oxygen-deuterium vibrational peak is used as an indication of the water network. It was found that at glycerol concentrations of Xg $\leq$ 0.12 the spectrum is similar to pure water (38). In the most concentrated glycerol-D_2O mixture however, the oxygen-deuterium vibrational peak structure is shifted to higher frequencies. This is explained as being due to D_2O monomers (38). The glycerol network was also studied by Mudalige & Pemberton. They use the CO-H vibrational modes and assign the mode at 3593 cm $^{-1}$ to glycerol monomers (38). From the integrated areas of the decomposed peak they find that at concentrations of Xg = 0.02, 0.12, and 0.32 glycerol monomers represent 10%, 3%, and 2% respectively.

Molecular dynamics simulations have also been used to study the mixing of aqueous glycerol (77; 81). Dashnau *et al*. have found that as glycerol concentration is increased more water-glycerol hydrogen bonds are formed at the expense of water-water hydrogen bonds. Once the concentration reaches Xg = 0.27 the water is forming a spanning two-dimensional hydration layer around the glycerol molecules with the water network being lost at concentrations above Xg = 0.27 (77). Kyrychenko & Dyubko have also used molecular dynamics to study aqueous glycerol at a concentration of Xg = 0.07. Interestingly, they find that water and glycerol are incompletely mixed with pronounced heterogeneity (81). This result could be due to the time scales studied in this investigation.

The results from each of these studies are in general agreement, with the mixing split into three regimes. At low glycerol concentrations the water network is largely unperturbed with the water molecules having similar characteristics to those in pure water.

Similarly, at high glycerol concentration the glycerol molecules form a continuous network. At intermediate concentrations however, the mixture forms an inhomogeneous and segregated structure (see Figure 1.9). Interestingly, aqueous methanol has been studied previously using EPSR at methanol mole fractions (Xm) of 0.05, 0.27, 0.54 and 0.70 (124). Dougan *et al.* use a similar cluster definition to that described in Section 5.1.3 and compare the results to the theoretical study detailed in Section 5.3. They found that both water and methanol form percolating clusters between concentrations of $0.27 \leq$ Xm ≤ 0.54 (124). It is suggested that this clustering could be a structural explanation for the thermodynamic properties of aqueous methanol (137). These connections are discussed in greater detail in Section 5.3.4. Many other aqueous systems have been studied using neutron diffraction and EPSR including trimethylamine oxide (TMAO) (87), the disaccharide sugar trehalose (82; 83), tertiary butanol (tert-butnanol) (125), sorbitol (85), proline (84), and, dimethyl sulfoxide (DMSO) (86). However, it is only aqueous glycerol and methanol that have been studied across the complete concentration range. The following section describes the method that is used to investigate the molecular scale mixing found in room temperature aqueous glycerol.

5.1.3 Measuring Molecular Mixing

The molecular mixing is measured using the "CLUSTERS" routine found within EPSR (102). Here, two water molecules are defined as being part of the same cluster if the inter-molecular oxygen-oxygen separation is less than the radial distance of the first minimum within the relevant RDF (see Figure 4.4(c)). Similarly, two glycerol molecules are defined as being part of the same cluster if any of the inter-molecular oxygen-oxygen separations are less than the relevant minimum in the RDF. The glycerol oxygen-glycerol oxygen radial distribution functions are shown in Figure 5.1.

This definition allows the number of clusters that contain i molecules ($M(i)$) as a fraction of the total number of clusters (M) to be plotted as a function of cluster size (here, $M = \sum_i M(i)$). This value is referred to as "Proportion of Clusters" and is calculated using,

$$\text{Proportion of Clusters} = \frac{M(i)}{M} \tag{5.9}$$

The motivation behind the use of the oxygen-oxygen distances rather than the oxygen-
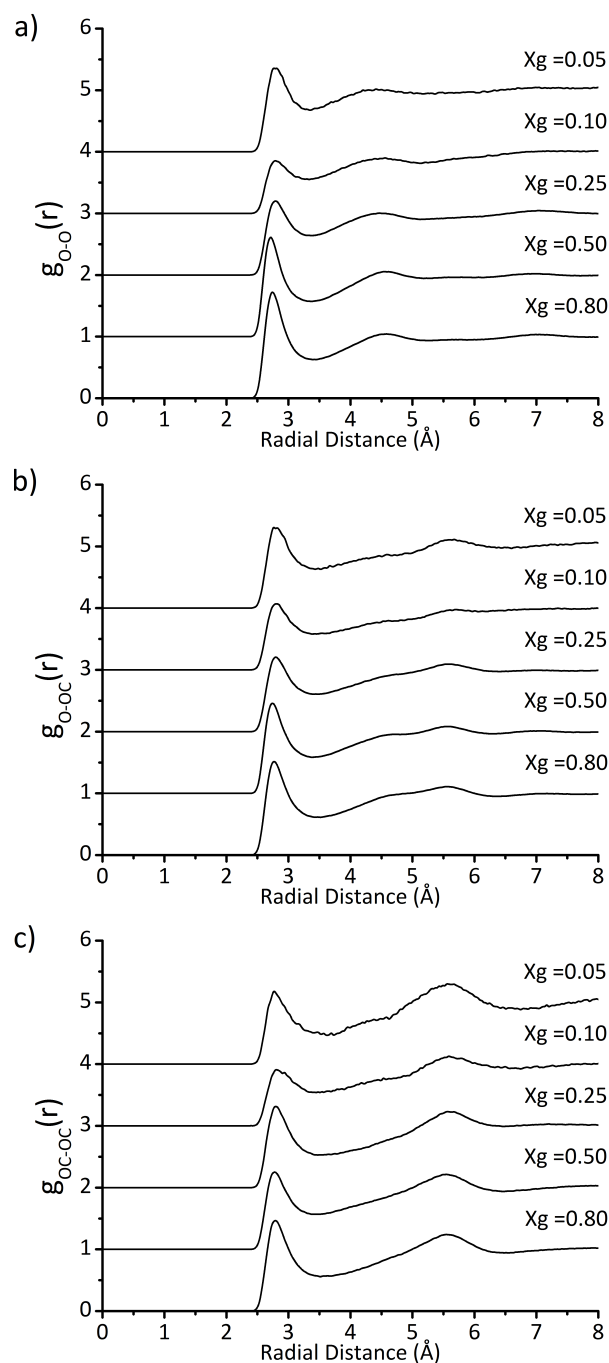
Figure 5.1: The inter-molecular radial distribution functions for each of the glycerol oxygen-glycerol oxygen atomic pairs at each of the glycerol-water concentrations studied. This includes; (a) the distal oxygen-distal oxygen functions, (b) the distal oxygen-central oxygen functions, and, (c) the central oxygen-central oxygen functions. It is the first minimum in each of these RDFs that are used as the radial distance cut-off when calculating the glycerol cluster sizes.

hydrogen separation is that it allows the comparison of the EPSR data with a model fluid. Here, the model fluid is composed of the same number of glycerol and water

molecules with the same atomic number density as the EPSR data[1] but the Coulombic and empirical potentials have been removed. The molecules in these simulations contain the same Lennard-Jones parameters and intra-molecular bond lengths and angles as the initial EPSR simulation to ensure a similar molecular structure. These simulations are known as "LJP Only" and form a mixture where the inter-molecular interactions are purely due to packing effects. The changes in cluster size as a function of concentration are discussed in Section 5.2.

5.2 Molecular Mixing in Room Temperature Aqueous Glycerol

5.2.1 Adding Water to Glycerol and Vice Versa

This section details results regarding the mixing of glycerol and water molecules at the extremes of the concentration range. This is achieved by the investigation of the molecular clusters found in a dilute glycerol mixture at a concentration of $Xg = 0.05$ and a concentrated aqueous glycerol mixture at $Xg = 0.80$. Here, the cluster size distribution found in the EPSR analysis of neutron diffraction data is measured. This is compared to the value found from a simulation of molecules that do not have the Coulombic and empirical potentials (LJP Only).

From Figure 5.2 it can be seen that there are smaller clusters of each molecule type measured in the EPSR data compared to the LJP Only simulations. This is highlighted by the largest cluster sizes. In dilute aqueous glycerol the largest cluster in the EPSR data contains 32 glycerol molecules whereas the largest glycerol cluster in the LJP Only simulation contains 168 molecules. In the concentrated mixture the largest water clusters contain 7 molecules in the EPSR analysis with the largest water cluster in the LJP Only simulation containing 16 molecules. These results suggest that the molecular mixing, as measured by the cluster size distribution, are due to the interactions between the molecules rather than a purely packing effect. Strikingly, these data also show that the glycerol-water is better mixed than is found in a randomly packed system.

Figure 5.2 shows the proportion of clusters that are of a particular size and therefore, further analysis of the data is required to find the proportion of molecules that are in

---

[1]See Appendix A for details
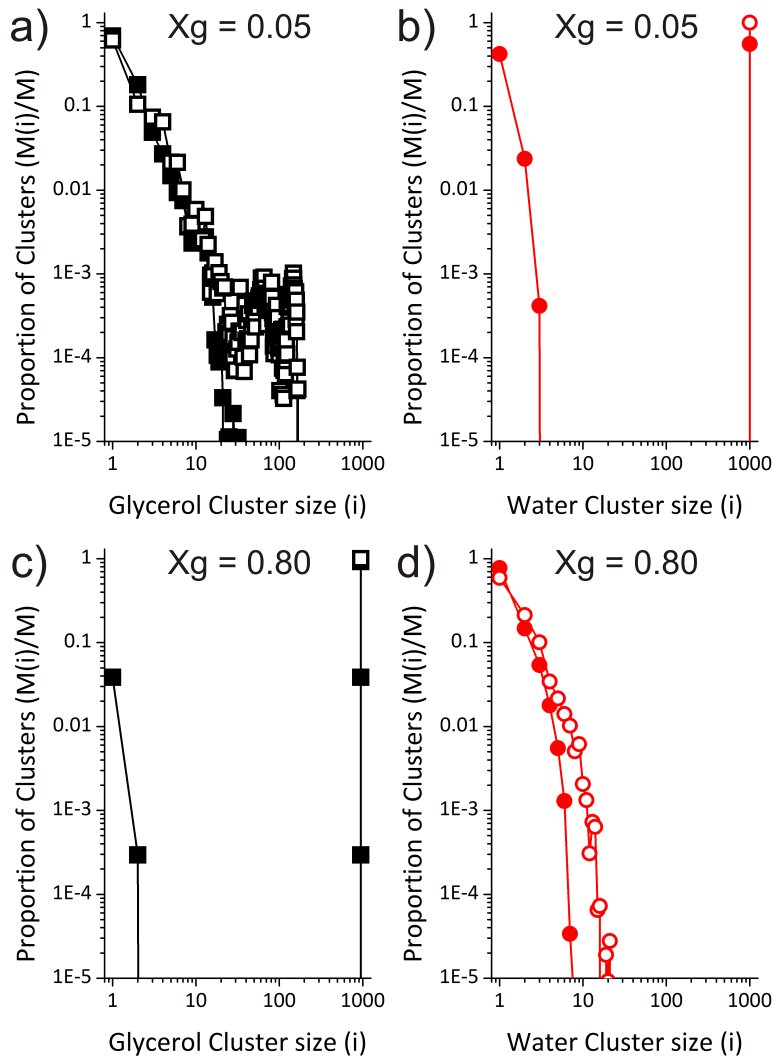
Figure 5.2: Glycerol (black squares) and water (red circles) molecular cluster size distributions. Here, the data taken from the EPSR analysis of neutron diffraction data (solid) is shown alongside data from a simulation of molecules containing only Lennard-Jones potentials (open). The cluster distributions found in the dilute aqueous glycerol mixture are shown in parts (a) and (b) with the results from the concentrated mixture shown in parts (c) and (d). The Lennard-Jones potential only simulation of the dilute mixture shows a single cluster of water (b). Similarly, there is a single glycerol cluster in LJP Only simulation of concentrated aqueous glycerol (c).

each cluster size $(N(i))$. This value is calculated using,

$$N(i) = \frac{i \cdot \dfrac{M(i)}{M}}{\sum\limits_{i} i \cdot \dfrac{M(i)}{M}} \tag{5.10}$$

This allows the proportion of molecules that are monomeric to be calculated for both the EPSR and LJP Only datasets (see Figure 5.3 and Table 5.1). Here, a monomeric

molecule is found in a cluster with a size of one. The proportion of molecules that are found in spanning clusters is also calculated. A spanning cluster is defined as one that either includes all of the molecules of the relevant type or one that reaches the limit of 999 molecules. For example, the EPSR simulation at a concentration of Xg = 0.80 is comprised of 948 glycerol molecules and 237 water molecules[1].
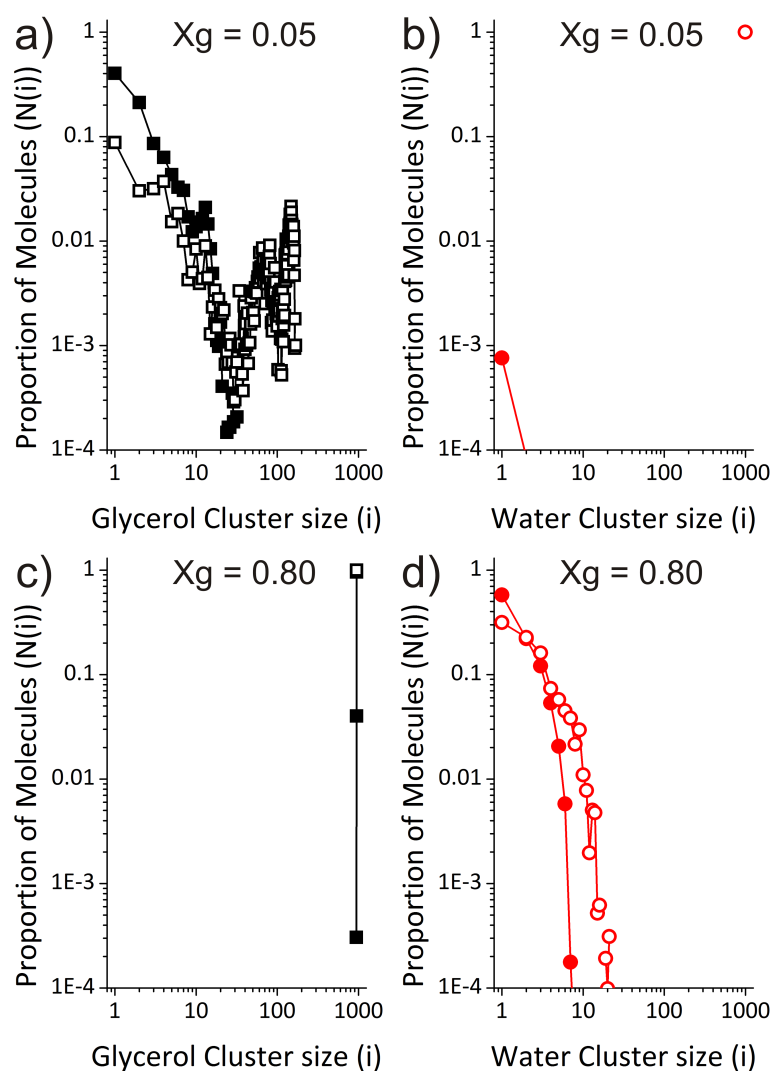
Figure 5.3: The proportion of glycerol (black squares) and water (red circles) molecules that are found in molecular clusters of size i. Data from the EPSR analysis of neutron diffraction data (solid) is shown along with the results taken from a simulation using only Lennard-Jones potentials (open). (a) Glycerol clusters and (b) water clusters at Xg = 0.05. (c) Glycerol clusters and (d) water clusters at Xg = 0.80. It can be seen that there are more molecules found in monomeric clusters of glycerol at Xg = 0.05 and water clusters at Xg = 0.80 for the EPSR analysis compared to the LJP Only simulation.

Table 5.1 shows that there are more glycerol monomers found in the EPSR analysis

---

[1]The total number of molecules present in the EPSR analysis can be found in Table A.7 within Appendix A

Table 5.1: Proportion of Monomers and Spanning Clusters

System	Molecule Type	Monomer Proportion	Spanning Proportion
Xg = 0.05 EPSR	Glycerol	0.403	0.000
Xg = 0.05 LJP Only	Glycerol	0.088	0.000
Xg = 0.05 EPSR	Water	0.001	0.999
Xg = 0.05 LJP Only	Water	0.000	1.000
Xg = 0.80 EPSR	Glycerol	0.000	0.960
Xg = 0.80 LJP Only	Glycerol	0.000	1.000
Xg = 0.80 EPSR	Water	0.578	0.000
Xg = 0.80 LJP Only	Water	0.315	0.000

of the data than the LJP Only simulation of the Xg = 0.05 system. Likewise, there are more monomeric water molecules found in the in the EPSR analysis of the data than the LJP Only simulation at a concentration of Xg = 0.80. This suggests that there is a preference for isolated water molecules in aqueous glycerol at high glycerol concentrations. Similarly, there is a preference for isolated glycerol molecules in dilute aqueous glycerol. These results suggest that at the extremes of the concentration range hetero interactions (glycerol-water and water-glycerol) are more energetically favourable than homo (glycerol-glycerol or water-water) interactions. This is further evidence that aqueous glycerol is better mixed than a randomly packed system. The following section extends this study by investigating the mixing found at intermediate concentrations.

5.2.2   Mixing at Intermediate Concentrations

Figures 5.4 and 5.5 show the cluster distributions for glycerol and water at intermediate concentrations ($0.10 \leq Xg \leq 0.50$). Again, the results taken from the EPSR analysis of the neutron diffraction data (solid) are shown along with data taken from the LJP Only simulations (open). Figure 5.4 shows that the glycerol clusters are smaller in each of the EPSR datasets than the LJP Only simulations. Interestingly, the largest glycerol cluster in the EPSR analysis of the Xg = 0.10 system contains 62 molecules, whereas the LJP Only simulation contains spanning clusters of 340 molecules (see Figure 5.4(a)). Similarly, there are much more molecules found in spanning glycerol clusters in the LJP Only simulation at a concentration of Xg = 0.25 compared to the EPSR analysis shown

in Figure 5.4(b) (99.2 % compared to 0.1 % [1]). The data taken at a concentration of $Xg = 0.50$ shows a similar trend to that found in more dilute mixtures (Figure 5.4(c)). Here, 21.9 % of the glycerol molecules are found in spanning clusters in the EPSR data and all of the glycerol molecules are found in a single spanning cluster in the LJP Only simulation. Therefore, the clusters of glycerol molecules are smaller in the EPSR data than in the LJP Only simulation at each of the concentrations shown in Figure 5.4.
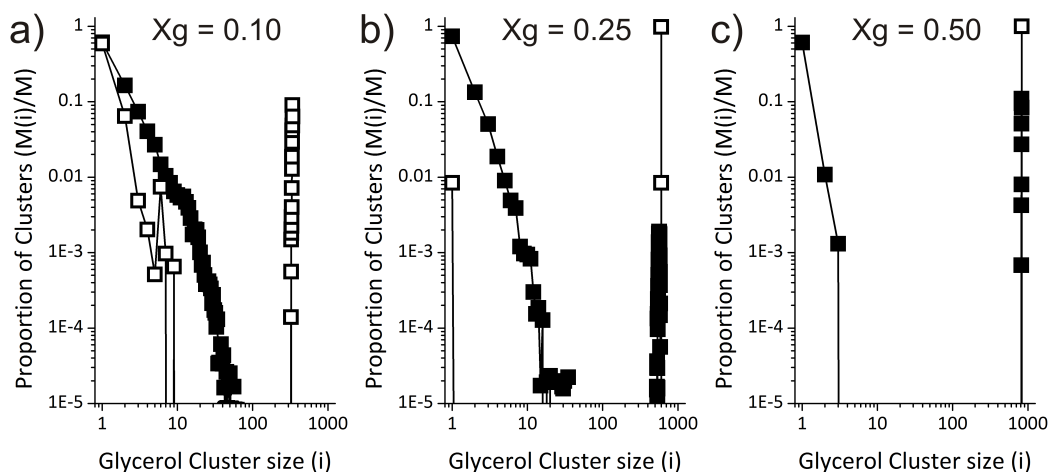
Figure 5.4: Glycerol cluster distributions in aqueous samples at intermediate concentrations; (a) $Xg = 0.10$, (b) $Xg = 0.25$, and, (c) $Xg = 0.50$. Here, the data taken from the EPSR analysis of neutron diffraction data is shown (solid squares) alongside data from a simulation of molecules containing only Lennard-Jones potentials (open squares).
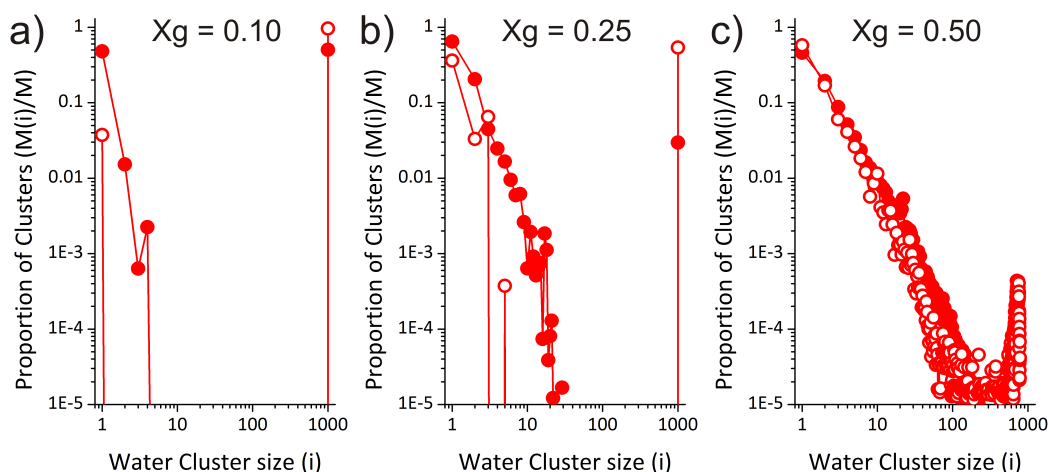
Figure 5.5: Water cluster distributions in aqueous samples at intermediate concentrations; (a) $Xg = 0.10$, (b) $Xg = 0.25$, and, (c) $Xg = 0.50$. Here, the data taken from the EPSR analysis of neutron diffraction data is shown (solid circles) alongside data from the LJP Only simulations (open circles).

[1]These values are calculated using Equation 5.10

The water cluster distributions at a concentration of Xg = 0.10 are shown in Figure 5.5(a). These data can be used to measure the proportion of molecules that are found in clusters of each size (see Equation 5.10). These calculations show that 99.99 % of the water molecules in the LJP Only simulation are found in spanning clusters. This is not, however, very different from the proportion found in the EPSR analysis, where 99.93 % of the water molecules are found in spanning clusters. A similar result is found at a glycerol concentration of Xg = 0.25 (see Figure 5.5(b)). Here, the proportion of water molecules found in spanning clusters is 99.88 % for the LJP Only simulation and 94.67 % for the EPSR analysis of the neutron diffraction data. There is, however, a clear difference between the EPSR result and that taken from the LJP Only simulation at a concentration of Xg = 0.50 (see Figure 5.5(c)). At this concentration, the largest water cluster found in the EPSR analysis contains 332 molecules and the largest in the LJP Only simulation contains 781 molecules. This shows that the water clusters in the LJP Only simulation are larger than those found in the EPSR data shown in Figure 5.5 across the complete concentration range.

Figures 5.2, 5.4 and 5.5 show that there are smaller clusters in the EPSR analysis at each concentration compared to the LJP Only simulations. This suggests that the molecular clustering is not purely due to a packing effect. These results indicate that homo interactions (water-water or glycerol-glycerol) are less favourable than hetero interactions (water-glycerol or glycerol-water).

5.3 Mixing Regimes as a Function of Concentration

5.3.1 Percolation Thresholds

In this section the mixing regimes are investigated using the theoretical percolation threshold. Jan has used a simulation technique to calculate the cluster size distribution that is found at the percolation threshold for a simple cubic lattice (138). In that work Jan used the critical concentration of 0.3116 (31.16% of the sites are occupied) in the cubic lattice of length 10,001 (138). This threshold is in good agreement with previous studies (139–144). Jan defined two cubes as being in the same cluster if they are found on adjacent sites of the cubic lattice. From this definition, the probability of a cluster

containing i cubes ($M(i)/M$) is given by (138),

$$\frac{M(i)}{M} = i^{-2.2} \tag{5.11}$$

In the work detailed in this thesis, cluster distributions which cross the line given by Equation 5.11 are defined as being indicative of a percolating network of molecules.
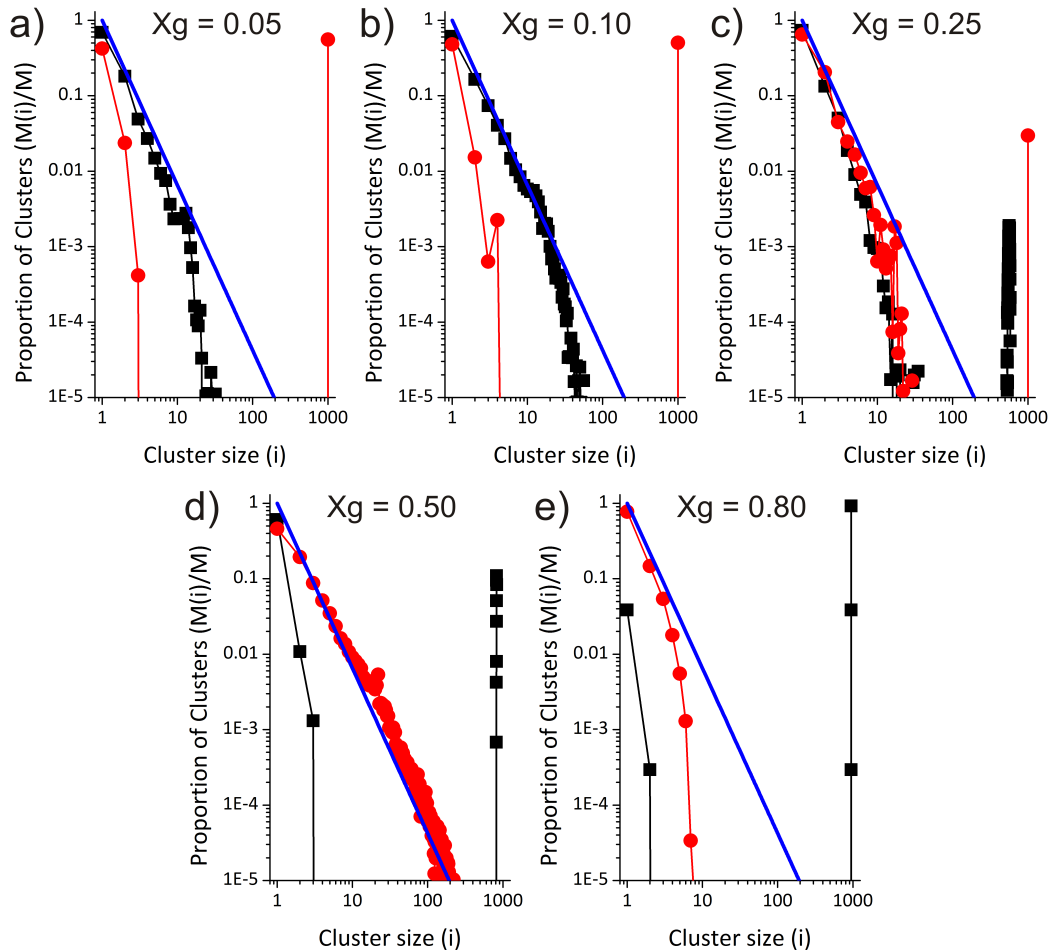
Figure 5.6: The cluster distributions for water (red circles) and glycerol (black squares) that are found at each of the aqueous glycerol concentrations studied. The mixtures shown here are at concentrations of (a) Xg = 0.05, (b) Xg = 0.10, (c) Xg = 0.25, (d) Xg = 0.50, and, (e) Xg = 0.80. Water molecules form percolating clusters at concentrations of Xg ≤ 0.50 and glycerol molecules form percolating clusters at concentrations of Xg ≥ 0.25.

The cluster distributions for water (red circles) and glycerol (black squares) are shown for each of the aqueous glycerol concentrations studied along with the theoretical percolation threshold given by Equation 5.11 (blue line) in Figure 5.6. It can be seen that the water molecules are forming percolating clusters at glycerol concentrations of

Xg $\leq$ 0.50 and glycerol molecules are forming percolating clusters at concentrations of Xg $\geq$ 0.25. Therefore, both glycerol and water are forming percolating clusters at intermediate concentrations (0.25 $\leq$ Xg $\leq$ 0.50).

The proportion of molecules that are found in clusters, which cross the percolation threshold, can also be calculated. Here, a cluster that satisfies the condition of $N(i) \geq i^{(-2.2)}$ is defined as having crossed the percolation threshold. Equation 5.10 is then used to calculate the proportion of the molecules that are found in each of these clusters. The sum of these proportions is then taken. This is the proportion of the molecules that are found in percolating clusters. These proportions are detailed in Table 5.2.

Table 5.2: Proportion of Molecules Found in Percolating Clusters

Concentration	Glycerol	Water
Xg = 0.05	0.000	0.999
Xg = 0.10	0.000	0.999
Xg = 0.25	0.940	0.947
Xg = 0.50	0.998	0.764
Xg = 0.80	1.000	0.000

Table 5.2, again, shows that a bi-percolating mixture is found at glycerol concentrations of 0.25 $\leq$ Xg $\leq$ 0.50. Interestingly, this is also the range that some thermodynamic extremes are found in aqueous glycerol (see Figure 5.7). The lowest melting temperature is found at Xg = 0.28 (88) and the most negative excess molar volume is found at Xg = 0.36 (72). There are differing results for the excess entropy (0.33 $\leq$ Xg $\leq$ 0.58), enthalpy (0.38 $\leq$ Xg $\leq$ 0.49) and Gibbs energy (0.38 $\leq$ Xg $\leq$ 0.49) (41) with most falling within the concentration range of bi-percolation. The possible links between molecular mixing and excess entropy are discussed in Section 5.3.4.

Figure 5.6 also shows that the glycerol cluster distribution is close to that expected for a random percolating system at Xg = 0.10 and clearly crosses the threshold at Xg = 0.25. This suggests that glycerol percolation begins at a concentration that is slightly higher than Xg = 0.10. Similarly, the water cluster distribution is very close to the threshold at a concentration of Xg = 0.50. From this, it can be concluded that the water clustering will cross the percolation threshold at a concentration that is not considerably higher than Xg = 0.50.
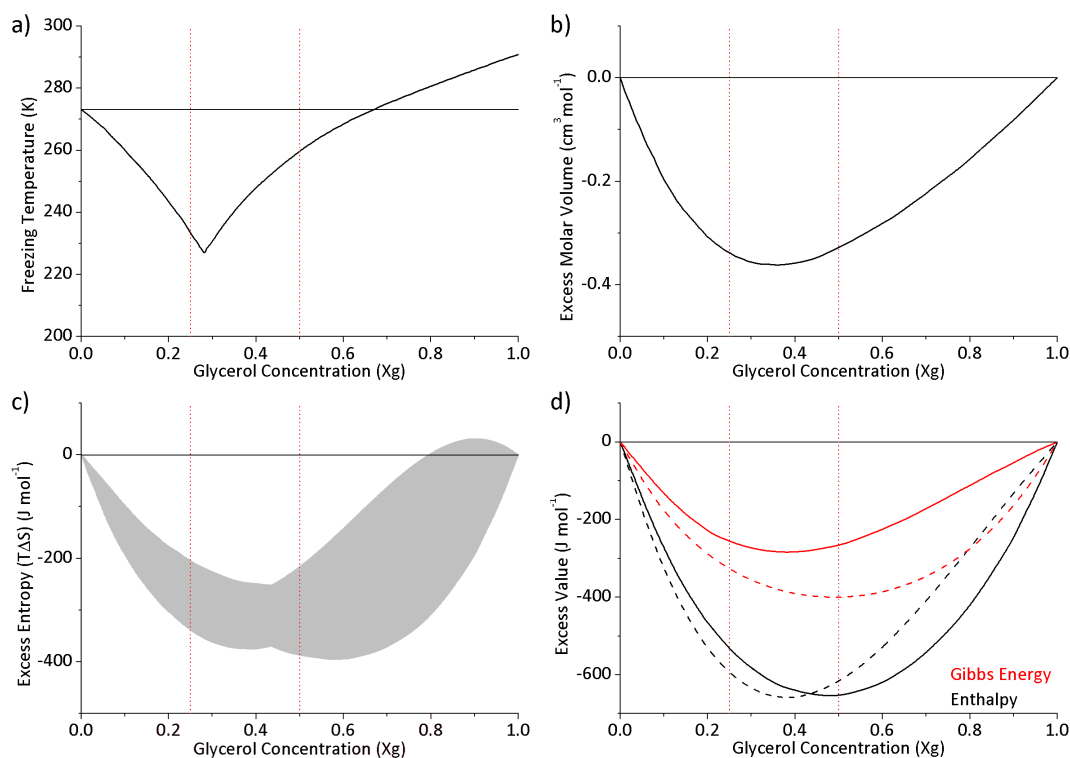
Figure 5.7: Experimental measurements of the thermodynamic properties of aqueous glycerol as a function of glycerol concentration (Xg). (a) freezing temperature (88), (b) excess molar volume (72), (c) excess entropy (41), and, (d) excess enthalpy and Gibbs energy (41). In each case, the boundaries of the concentration range that glycerol-water mixtures are forming a bi-percolating network are indicated by red dotted lines.

5.3.2   Mixing Regimes

It has been previously suggested the that water network has similar characteristics to pure water at low glycerol concentrations (38; 42; 43; 77; 80) (see region 1 in Figure 5.8). The cut-off for this mixing regime is found at concentrations of $0.12 \leq Xg \leq 0.20$. Interestingly, this is the region at which glycerol begins to form a percolating network. It is conceivable that it is the formation of a percolating glycerol network that is leading to the mixture no longer resembling pure water. Figure 5.8 also shows the concentrations above which glycerol-glycerol interactions have been shown to dominate (see region 3). This region was found to exist at concentrations above $Xg = 0.27$ in a study using IR spectroscopy and MD simulations (77) and above $Xg = 0.60$ using a combination of differential scanning calorimetry and broadband dielectric spectroscopy (43). Other investigations have found this region to begin at concentrations between these (38; 42; 80).

Different molecular mixing has been suggested to be found in the intermediate mixing
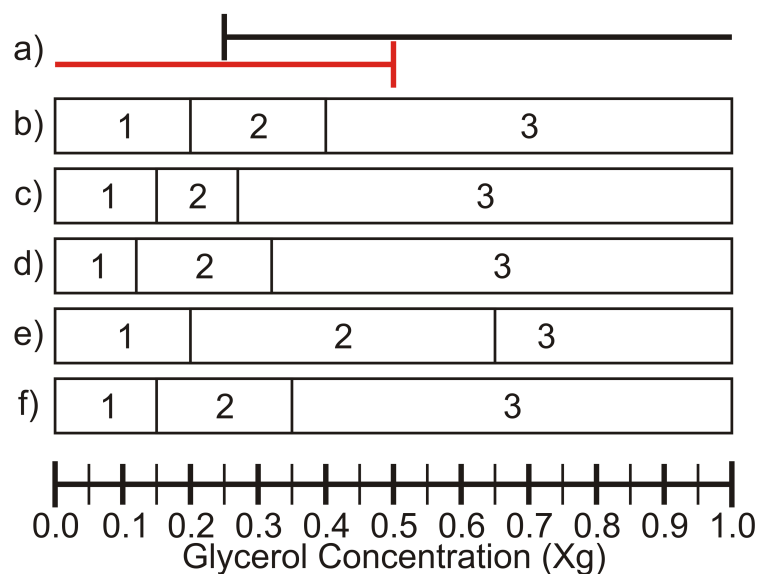
Figure 5.8: The concentrations at which water (red) and glycerol (black) form percolating clusters (a) along with the mixing regimes that have been found in previous studies (b) (80) (c) (77) (d) (38) (e) (43) (f) (42). Here, mixing region contains a water network similar to pure water, region 2 contains domains of high concentration of either component, and, region 3 contains pure-like glycerol.

regime (labelled as region 2 in Figure 5.8). To *et al.* have suggested that the system micro-segregates at concentrations of $0.20 \leq Xg \leq 0.35$ (42). Similarly, both Hayashi *et al.* and Banerjee & Bhat have both suggested that, at concentrations of $0.25 \leq Xg \leq 0.40$, domains of high water concentration are present (43; 80). However, above this concentration Hayashi *et al.* find that water-water interactions are still prominent up to $Xg = 0.60$ (43) whereas Banerjee & Bhat state that aqueous glycerol is homogeneously mixed at concentrations above $Xg = 0.40$ (80). Dashnau *et al.* have used MD simulations and find that at concentrations of $0.15 \leq Xg \leq 0.27$ the water molecules are forming a two-dimensional layer that is hydrating the glycerol molecules (77). The prevalence of water-glycerol hydrogen bonds shown in Figure 4.14 support the hypothesis of Dashnau *et al.* (77). However, the large clusters of both molecule types shown in Figure 5.6 could be seen as evidence for the micro-segregation reported by To *et al.* (42), Hayashi *et al.* (43), and, Banerjee & Bhat (80). The level of segregation of the clusters can be elucidated by investigating the structure of the molecular clusters found in aqueous glycerol. Such an investigation is detailed in the following section.

5.3.3 The Structure of the Clusters

The structure of the clusters shown in Section 5.2 can be investigated further by measuring the fraction of molecules found in the interface between clusters as a function of glycerol concentration. Here, a molecule is defined as being in the interface based on the intermolecular separation of unlike molecules. For a glycerol molecule to be defined as being in the interface the oxygen or hydroxyl hydrogen atom (O/OC or H) must be within 2.4 Å of a water hydrogen or oxygen atom (HW or OW) respectively. Similarly a water molecule with its oxygen or hydrogen atom (OW or HW) within 2.4 Å of a glycerol hydroxyl hydrogen or oxygen atom (H or O/OC) respectively is defined as being in the interface. The cut-off was set at 2.4 Å as this is the average distance to the first minimum in the oxygen-hydrogen radial distribution functions (see Figures 4.4(b), 4.10 and 4.13). These distances are used as the cut-offs for the coordination numbers used to calculate the hydrogen bond number (see Section 4.4). Figure 5.9 shows a two-dimensional schematic to explain how a surface fraction calculation can provide information regarding the structure of a cluster. It can be seen that a low surface fraction indicates a compact structure (Figure 5.9(a)) and a larger surface fraction is indicative of an elongated shape (Figure 5.9(c)).

The fraction of each type of molecule that is found in the surface is shown in Table 5.3. The total fraction of molecules found in the surface of clusters is calculated using the fraction of each molecule type found on the surface of clusters multiplied by its mole fraction. It can be seen that the fraction of each type of molecule found in the surface increases with decreasing concentration. The values shown in **bold type** are the limits of percolation (see Figure 5.6). Interestingly, 98.8 % of the glycerol molecules and 93.6% of the water molecules are found at the surface of clusters at the concentrations at which percolation begins.

Table 5.3: Proportion of Molecules Found in the Surface of Clusters

Concentration	Glycerol	Water	Total
Xg = 0.05	0.999	0.039	0.087
Xg = 0.10	0.999	0.093	0.184
Xg = 0.25	**0.988**	0.272	0.451
Xg = 0.50	0.655	**0.936**	0.796
Xg = 0.80	0.313	0.989	0.448
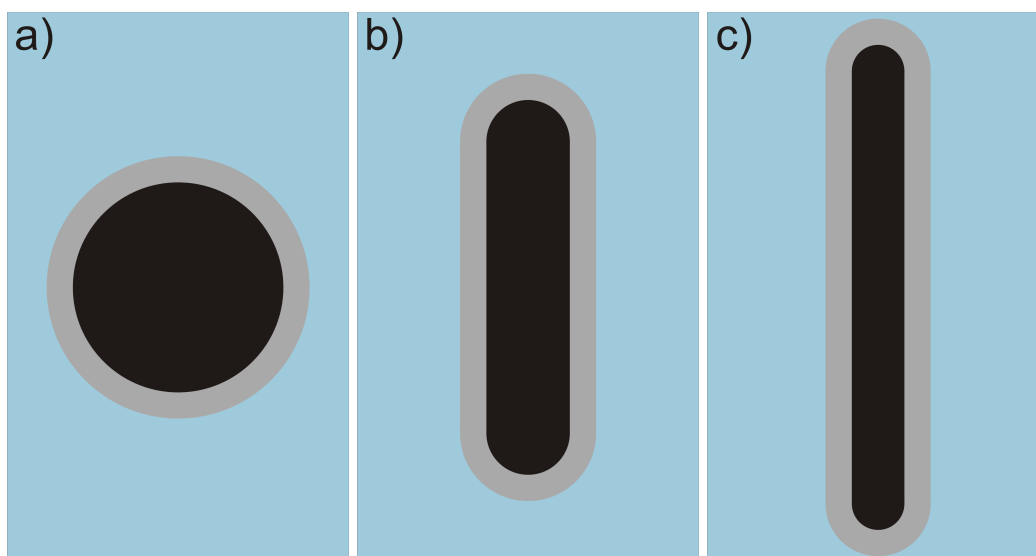
Figure 5.9: A diagram showing how the fraction of molecules found in the surface of clusters can provide information regarding the structure of the clusters. Here, the black region represents a cluster of molecules of type α inside a bath of blue molecules of type β. The grey region shows the area of molecules of type α that are in the interface between the α cluster and the β molecules. The total area covered by the bulk molecules (black) and surface molecules (grey) is equal in each of the different diagrams. The three different regimes are shown in order of increasing surface fraction; (a) 0.36, (b) 0.45, and, (c) 0.54. This shows that a low surface fraction ((a)) is indicative of a compact structure and a high surface fraction ((c)) indicates an elongated shape.

The high fraction of glycerol molecules found at the surface of clusters in the $Xg =$ 0.25 system suggests that these clusters are forming elongated structures such as strings or sheets. This result is contradictory to the work of Dashnau $et\ al.$ who state that water forms a two-dimensional hydration layer around glycerol at a concentration of $Xg = 0.27$ (77). Instead, it is the glycerol cluster that appears to be forming extended structures with high surface area around the water network. The lower surface fraction of the water molecules at this concentration suggests that the water network is forming a much more compact structure. It is conceivable that these compact water clusters could be the source of the water-water interactions measured by Banerjee & Bhat (80), Hayashi $et\ al.$ (43), and, To $et\ al.$ (42). The large total surface fraction found at $Xg =$ 0.50 can also be seen as evidence for the homogenous mixture measured by Banerjee & Bhat in the concentration range of $0.40 \leq Xg \leq 0.60$ (80). The finding of a homogenous mixture of water and glycerol is also reinforced by the similarity between the EPSR and LJP Only clusters seen in Figures 5.4(c) and 5.5(c). These similarities suggest that the molecules are forming clusters that are similar to those that would be found in a

randomly packed system.

5.3.4   Estimating Entropy from Molecular Mixing

The non-ideal characteristics of the mixing found in aqueous systems can reveal information regarding the molecular scale interactions that are present. Evidence for the non-ideal nature of the mixing of glycerol and water is shown by the excess thermodynamic properties (see Figure 5.7). A simple model to explain the excess entropy of mixing of alcohol-water systems was proposed by Soper *et al.* (137). This model uses information from EPSR analysis of neutron diffraction experiments to estimate the excess entropy of mixing by measuring the molecular scale clustering found within the system of interest. The aim of this section is to test the validity of that model for aqueous glycerol.

One feature of the mixing of alcohols and water is their negative excess entropy (145). This means that the change in entropy due to mixing is lower than would be found in an ideal system. The entropy associated with ideal mixing (S^{id}) is given by,

$$\Delta S^{id} = -k_B N \sum_j X_j \ln X_j \tag{5.12}$$

where, k_B is Boltzmann's constant, N is the total number of molecules and X_j is the mole fraction of component j. Experimental analysis of binary aqueous mixtures has shown that molecular clustering is present (2–4; 124; 126). To investigate the effect that this clustering has on entropy the calculation begins with a completely de-mixed solution. In this system the two components are separated by a sharp boundary and no mixing is found. The entropy of this system, relative to ideal mixing, is given by (137; 146),

$$\Delta S = -k_B N \sum_j X_j \ln \left(\frac{\overline{V}}{X_j V_j} \right) \tag{5.13}$$

where $\overline{V}$ is the average molar volume of the system and V_j is the molar volume of component j at a concentration of X_j. This de-mixed system forms a limiting case. To apply Equation 5.13 to a real mixture the interface between the two liquids must be taken into account. Here, a fraction of the molecules f_j of type j are defined as being within an ideally mixed interface. These molecules will not contribute to the

calculation in Equation 5.13 and, therefore, the entropy of mixing relative to an ideal mixture becomes,

$$\Delta S = -k_B N \sum_j X_j (1 - f_j) \ln \left(\frac{\overline{V}}{X_j V_j} \right) \qquad (5.14)$$

The definition of an interface molecule is similar to that introduced in Section 5.3.3. The oxygen-hydrogen separation was used to define the interface molecules with maximum separations of 1.75, 1.80 and 1.85 Å. It was shown that using an oxygen-hydrogen separation of 1.80 Å provides a close fit to the experimentally derived excess entropy of mixing for aqueous methanol (137; 146). Therefore, a similar method has been used to calculate the excess entropy of mixing for aqueous glycerol using Equation **??**. Here, the maximum separation of relevant oxygen and hydrogen atoms were set to 1.75, 1.80 and 1.85 Å. The calculated excess entropy values are shown in Figure 5.10 along with the experimentally determined values. The different results that have been measured for the excess entropy of mixing (41) are shown by the grey region.
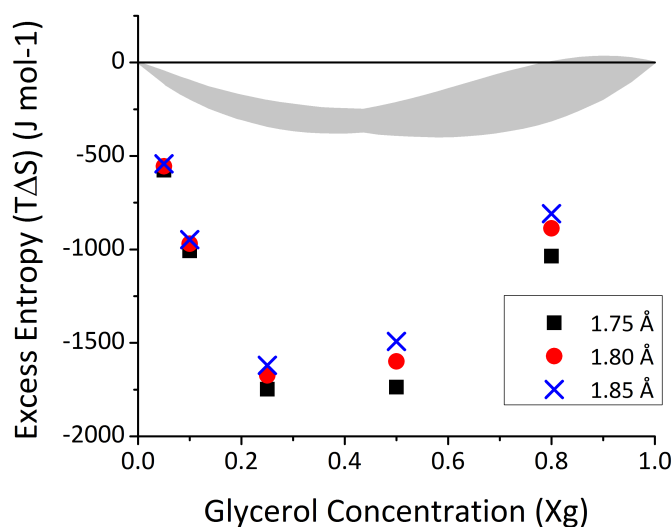
Figure 5.10: The range of experimentally derived excess entropy values (41) (grey) along with the values calculated using Equation 5.14. Here, three different radial cut-offs have been used to define a molecule being on the interface between clusters based on oxygen-hydrogen separations of 1.75 (black squares), 1.80 (red circles) and 1.85 (blue crosses) Å. It is shown that these calculations overestimate the excess entropy of mixing by a factor of around five.

Figure 5.10 shows that Equation 5.14 does not produce a reliable estimate for the excess entropy of mixing for glycerol-water systems. It is interesting to consider why a method would produce good agreement for methanol-water mixtures but not for aqueous

glycerol. This is likely to be due to the different molecular mixing that is found in the systems. The water molecular clusters that are found in the EPSR analysis of aqueous methanol at a concentration of Xm = 0.54 have been shown to be smaller than those found in a LJP Only simulation[1] (146). This suggests that methanol and water are less well mixed in the EPSR result than in a randomly packed system. The opposite effect has been seen with aqueous glycerol systems (see Figures 5.2, 5.4 and 5.5). The calculation of the excess entropy that is described here is based on a modification to the excess entropy that would be found in a completely de-mixed solution. Therefore, it is conceivable that the calculation will only provide reasonable results for a system that is partially de-mixed on the molecular scale. The calculations shown in this section suggest that the entropy model proposed by Soper *et al.* (137) is an oversimplification and fails for aqueous glycerol due to the system being more well mixed than the methanol-water system.

5.4 Conclusions Regarding the Molecular Scale Mixing in Aqueous Glycerol at Room Temperature

This chapter describes an investigation of the molecular mixing that is found within aqueous glycerol as a function of concentration. The method that has been used to assess the molecular mixing is introduced in Section 5.1.3. Section 5.2 describes an investigation of the molecular mixing that is present in aqueous glycerol. Here, the size of the clusters taken from EPSR analysis of neutron diffraction data is compared to random packing simulations. At the extremes of the concentration range (Xg = 0.05 and Xg 0.80) it was found that there are more monomeric molecules (glycerol and water respectively) than would be found if the molecular mixing was due to a packing effect alone (see Section 5.2.1). This indicates the presence of a preferential interaction between glycerol and water at these concentrations. The mixing at intermediate concentrations (Xg = 0.10, 0.25 & 0.50) is discussed in Section 5.2.2. This study confirms that smaller clusters are found in the EPSR analysis compared to the LJP Only simulations: a further indication of preferential interactions between water and glycerol. If there were a preference for homo interactions (water-water or glycerol-glycerol) over hetero

---

[1]See Section 5.1.3 for an introduction to LJP Only simulations.

interactions (water-glycerol and glycerol-water) the system would microsegregate and form clusters of larger size than is found in the LJP Only simulation.

Section 5.3 describes a comparison between the cluster distribution that is found using EPSR and a theoretical model for random percolation. Interestingly, within the range of $0.25 \leq Xg \leq 0.50$ the system forms a bi-percolating network with extended clusters of both glycerol and water (see Section 5.3.1). These results are then compared to previously published data in Section 5.3.2. The structure of these clusters is investigated by measuring the proportion of molecules that are found at the surface (see Section 5.3.3). Finally, a method to estimate the excess entropy of mixing is tested. It is found that a procedure that provides good agreement for methanol and water mixtures does not hold for aqueous glycerol. The following chapter discusses the results that are found when temperature is altered. These results are compared to the structural properties described in Chapter 4 and the mixing described in this chapter.

Chapter 6

The Structure of Aqueous Glycerol at Low Temperatures

6.1 Context

The aim of this thesis is to investigate the structure of a cryoprotectant solution. Therefore, it is important to understand the effects that a decrease in temperature has on this mixture. This chapter describes a study of the effects of cooling on the structure of pure and aqueous glycerol. To achieve this, the relevant structural information has been measured at low temperatures and is compared to that found at room temperature (see Chapters 3, 4 and 5). This chapter begins with a description of the EPSR analysis that has been employed to study the low temperature systems (Section 6.1.2).

The results that are described within the chapter are split in to four groups. The intra-molecular structure of glycerol is investigated in Section 6.1.3. This is followed by a study of the inter-molecular structure of the mixtures in Section 6.2. Section 6.3 contains an investigation of the hydrogen bonding that is present in these liquid mixtures. The final results section of this chapter discusses the molecular scale mixing that is found by comparing the results to a model system and measuring the fraction of molecules found at the surface of the clusters (see Section 6.4).

6.1.1 Low Temperature Experiments

The aim of this chapter is to investigate what modifications (if any) are present when aqueous glycerol is cooled. To this end, a number of neutron diffraction experiments

have been conducted at low temperatures. Here, low temperature refers to temperatures less than room temperature (25 °C or 298.15 K). Experimental data has been collected for glycerol-water mixtures at Xg = 0.10 and 262.15 K, Xg = 0.25 and 238.15 K and at Xg = 0.80 and 285.15 K. Pure glycerol has been studied at a temperature of 293.15 K. These temperatures have been chosen as they are close to, but above, the freezing temperature of the liquid mixture at the relevant concentration. The concentrations and temperature of each of the neutron diffraction experiments is shown in Figure 6.3 with the freezing temperature values taken from the literature (88).
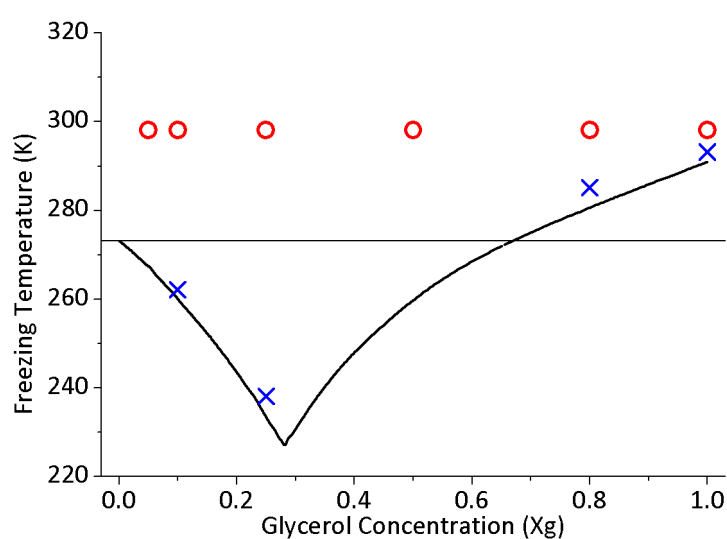
Figure 6.1: The freezing temperature of aqueous glycerol (88) is shown with a thick black line along with the concentrations and temperatures of the neutron diffraction experiments. The horizontal thin black line indicates a temperature of 273.15 K. The room temperature experiments are shown with red circles and the low temperature experiments are shown with blue crosses.

Previously, two other aqueous systems have been studied using a combination of neutron diffraction and EPSR at low temperatures (85; 126). Dougan *et al.* studied aqueous methanol at concentrations of Xm[1] = 0.27 and 0.54 at 238 and 190 K respectively (126) and compared these values to the published previously room temperature structures (124). Chou *et al.* investigated the structure of aqueous sorbitol at a mole fraction of 0.19 and temperatures of 298, 213, 173 and 100 K (85). In the methanol study of Dougan *et al.* the results from EPSR are compared to those from taken from molecular dynamics simulations. The results of the two datasets are broadly consistent with each other. Chou *et al.* also use small angle neutron scattering (SANS) to study

[1]Here, Xm is the mole fraction of methanol.

sorbitol-water mixtures[1]. They argue that the the SANS data suggest that there are voids within the system on the scale of hundreds of nanometres. This, although an interesting result, is not a length scale that will be addressed in this thesis and therefore it will not be discussed further.

Dougan *et al.* found that the peaks within the water oxygen-water oxygen RDF at Xm = 0.27 are sharpened on cooling, but not shifted when compared to the room temperature data. At Xm = 0.54, they found that the radial position of the second peak in the RDF is shifted inward on cooling. Interestingly, this is the opposite of the effect of increasing the methanol concentration at room temperature, which shifts the second peak outwards. This is attributed to the recovery of the tetrahedral nature of the water network upon cooling (126). They also found that the water molecules form larger clusters at the decreased temperatures. This, it is argued, is indicative of increased segregation of the mixture upon cooling (126). Chou *et al.* also found that the second peaks of the water oxygen-water oxygen RDFs were shifted inwards in each of the cooled aqueous sorbitol systems (85) when compared to the room temperature pure water data of Soper (108). They also looked at the water oxygen-water hydrogen coordination numbers in aqueous sorbitol at each of the temperatures that were studied, and found that there was an increase from 0.93 at 298 K to 1.08 at 100 K (85). Unfortunately, there is no mention of the water-sorbitol coordination numbers, thus the ability of water to from hydrogen bonds cannot be investigated using these values. From these studies it can be seen that with both methanol and sorbitol, the second peak of the water oxygen-water oxygen RDF is shifted inwards (85; 126). The results taken from the aqueous glycerol systems are compared to these results in Section 6.2.3. The increased segregation found in aqueous methanol is compared to the cluster distribution in glycerol-water in Section 6.4.

6.1.2   Low Temperature Density Values

Data regarding the density of aqueous glycerol at room temperature are available from the literature (44; 72) (listed in Table A.7 and shown graphically in Figure 5.7(b)). These data have been used in the setup of the EPSR programs that are used for the analysis

---

[1]see Section 2.1.3 for a description of the difference between small and wide angle measurements

of neutron diffraction data (see Chapters 3, 4 and 5). Unfortunately, this is not the case for the low temperature mixtures. There are, however, data at various concentrations and temperatures (12; 147). Therefore, a method to estimate the densities from those available in the literature must be found. The method that has been used here is to linearly extrapolate between the available data points to find the density at which the neutron diffraction experiments have been conducted[1]. Therefore, the density ρ at a concentration of X_j that lies between data points at concentrations of X_i and X_k with densities of ρ_i and ρ_k respectively, is given by,

$$\rho = \rho_i + [(X_k - X_i) \cdot (\rho_k - \rho_i)] \tag{6.1}$$

When the required data point lies between the temperatures found in the literature values of the density, the effect of temperature is also be included in the density estimation by similar linear extrapolation. For this calculation, the density change with temperature is assumed to be linear between experimental and extrapolated points.
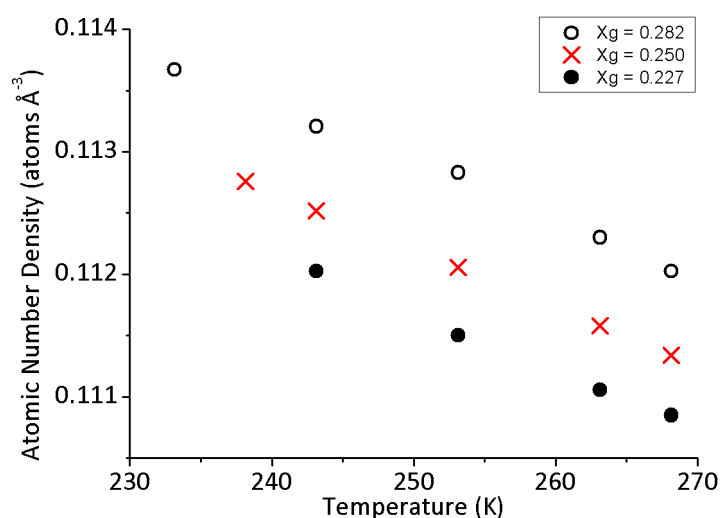
Figure 6.2: The atomic number densities of aqueous glycerol at sub zero temperatures. The experimental density values are shown with open and closed black circles and the extrapolated values are shown with red crosses.

This method is shown graphically in Figure 6.2. The estimations of the density of glycerol can be examined using the neutron diffraction data. Equation 2.13 in Section 2.3.1 states that the differential scattering cross section of the sample is dependant on the

---

[1]It should be noted that this method has been used previously (85).

number of scattering centres within the sample. Therefore, if the thickness of the sample is known, then the density can be found from the differential scattering cross section. In each of the experiments that are detailed in this thesis, standard sample containers have been used (see Figure 2.13). The density values calculated using Equation 6.1 are in agreement with the measured differential scattering cross sections from neutron diffraction. Therefore these densities were used as input values for the relevant EPSR setups. The quality of the fit of the neutron diffraction data to the EPSR simulations is discussed in the following section.

6.1.3   Glycerol Intramolecular Structure at Low Temperatures

The neutron diffraction data taken from the low temperature experiments detailed in Figure 6.1 are shown along with the simulated structure factors in Figure 6.3. It can be seen that the quality of the fit of the EPSR model to the experimental data is good at each of the concentrations studied. This can be quantified by measuring the R-Factors given by Equation 2.41. The average R-Factor for the low temperature data is 1.57 $\times 10^{-4}$, this value demonstrates that the fits are of a similarly high quality to those of the room temperature datasets, which had an average R-Factor of 1.96 $\times 10^{-4}$. The first piece of information that can be found from the EPSR analysis of the neutron diffraction data at low temperatures is the conformation of the glycerol molecules. To do this, the standard nomenclature for glycerol conformations (59) that was introduced in Section 3.1.1 and Figure 3.2 is used. From the room temperature data it was found that most of the glycerol molecules have at least one dihedral angle in the α conformation. The distribution of the glycerol conformations found at low temperatures are shown in Table 6.1 along with the data taken from the relevant room temperature systems.

The distribution of the glycerol conformations that are found at low temperatures are shown graphically in Figure 6.4. From these data it can be seen that most of the glycerol molecules in each of the systems have at least one of the distal oxygen atom in the α position. Specifically, in pure glycerol at 293.15 K, the value is 82 % compared to 78 % at 298.15 K. The most concentrated mixture (Xg = 0.80) has 83 % of the molecules containing at least one distal oxygen in the α position, an increase of 1 % when compared to the room temperature result. In the Xg = 0.25 mixture, 81 % of the molecules contain at least one α distal oxygen at lowered temperature, which is 4
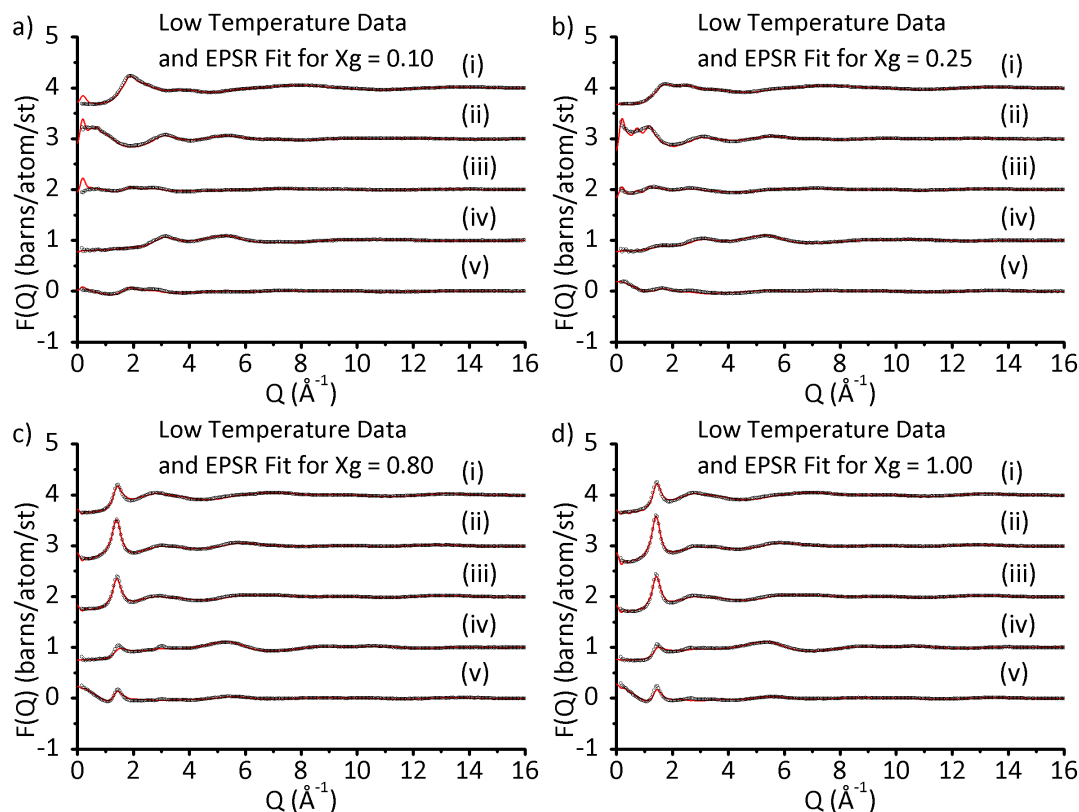
Figure 6.3: The experimental structure factors (black circles) and EPSR fitted structure factors (red lines) for each of the isotopic substitutions measured (see Table 2.4). These data are shown in order of increasing glycerol concentration: (a) Xg = 0.10,(b) Xg = 0.25, (c) Xg = 0.80, and,(d) Xg = 1.00 (pure glycerol). These data confirm that these EPSR models are in excellent agreement with the experimental data.

Table 6.1: Glycerol Conformation Percentages at Room and Low Temperatures

Concentration	Temperature (K)	$\alpha\alpha$	$\alpha\beta$	$\alpha\gamma$	$\beta\beta$	$\beta\gamma$	$\gamma\gamma$
Xg = 1.00	298	37	23	19	6	6	10
Xg = 1.00	293	44	22	16	4	3	11
Xg = 0.80	298	44	22	17	5	4	10
Xg = 0.80	285	45	24	14	4	3	10
Xg = 0.25	298	43	19	15	3	3	17
Xg = 0.25	238	47	18	16	2	4	13
Xg = 0.10	298	38	17	17	2	2	24
Xg = 0.10	262	37	21	20	3	4	15

% higher than at room temperature. Finally, in the most dilute cooled mixture (Xg = 0.10) 78 % of the glycerol molecules contain at least one distal oxygen in the α position
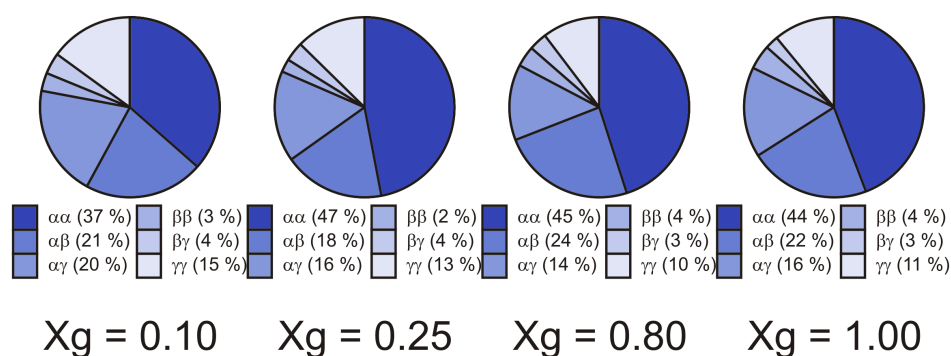
Figure 6.4: Pie charts indicating the proportion of the glycerol molecules that are of each of the conformations defined previously (see Section 3.1.1 and Figure 3.2) as a function of glycerol concentration at low temperatures. The data shown here are taken from the EPSR analysis of the neutron diffraction data shown in Figure 6.3.

(an increase of 6 %) over the room temperature result. Therefore, it can be concluded that there is a small increase in the proportion of the glycerol molecules that contain at least one "α" distal oxygen with a decrease in the temperature.

It has been argued previously that the conformational structure of glycerol is determined by the presence of intra-molecular hydrogen bonds (74). However, in Section 4.2.2 no evidence was found for intra-molecular hydrogen bonding in glycerol molecules at room temperature. Within this thesis, a hydrogen bond is defined as a sharp peak in the relevant oxygen-hydrogen RDF at a radial separation of around 1.80 Å. The intra-molecular oxygen-hydrogen RDFs for aqueous and pure glycerol at low temperatures are shown in Figure 6.5. It can be seen that no clear peaks are visible in any of the intra-molecular RDFs around 1.8 Å. Therefore, it is concluded that intra-molecular hydrogen bonds are not determining the conformation of glycerol at low temperatures. This result is consistent with that found at room temperature (see Section 4.1.1 and references (73)(75)) and suggests that the inter-molecular interactions between the molecules are the driving force behind the conformation of glycerol.
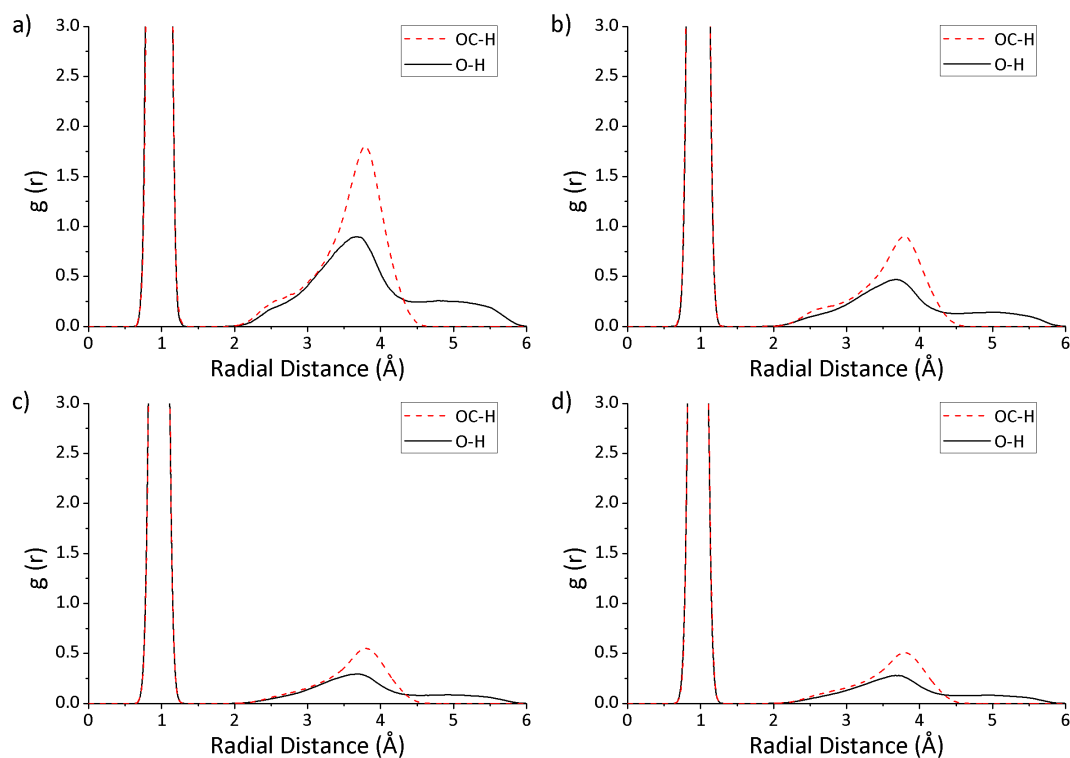
Figure 6.5: The intra-molecular radial distribution functions for glycerol taken from the EPSR analysis of neutron diffraction experiments at low temperatures. Here, the distal oxygen-hydroxyl hydrogen RDFs are shown with a solid black line and the central oxygen-hydroxyl hydrogen RDFs are shown with a dashed red line. The data are shown in order of increasing glycerol concentration with: (a) $Xg = 0.10$, (b) $Xg = 0.25$, (c) $Xg = 0.80$, and, (d) $Xg = 1.00$ (pure glycerol). The lack of a distinct peak in any of the RDFs at a distance of 1.8 Å indicates that intra-molecular hydrogen bonds are not formed at low temperatures.

6.2 The Inter-Molecular Structure within Aqueous Glycerol at Low Temperatures

In this section the inter-molecular structure is investigated using the heavier atoms in the system (oxygen and carbon). This analysis is split into four sections: firstly the glycerol-glycerol interactions are studied, the water-glycerol interactions are then investigated, the water-water pair correlations are analysed, and, finally the structure of the water network is studied.

6.2.1 Glycerol-Glycerol Interactions at Decreased Temperatures

Due to the amphiphilic nature of glycerol, the interactions between the molecules can be split in to two groups. The modifications within the backbone-backbone interactions

can be investigated using the carbon-carbon RDFs. To that end, Figure 6.6 shows the carbon-carbon radial distribution functions between glycerol molecules at low temperatures and compares them to those found at room temperature. The carbon-carbon interactions are shown in order of increasing glycerol concentration with the most dilute system (Xg = 0.10) shown in Figure 6.6(a), Xg = 0.25 in Figure 6.6(b), the most concentrated mixture (Xg = 0.80) in Figure 6.6(c), and pure glycerol in Figure 6.6(d). It can be seen that the low temperature RDFs are very similar to the room temperature distribution functions. This suggests that there are no marked changes in the hydrophobic backbone-backbone interactions within aqueous and pure glycerol when the temperature is lowered.
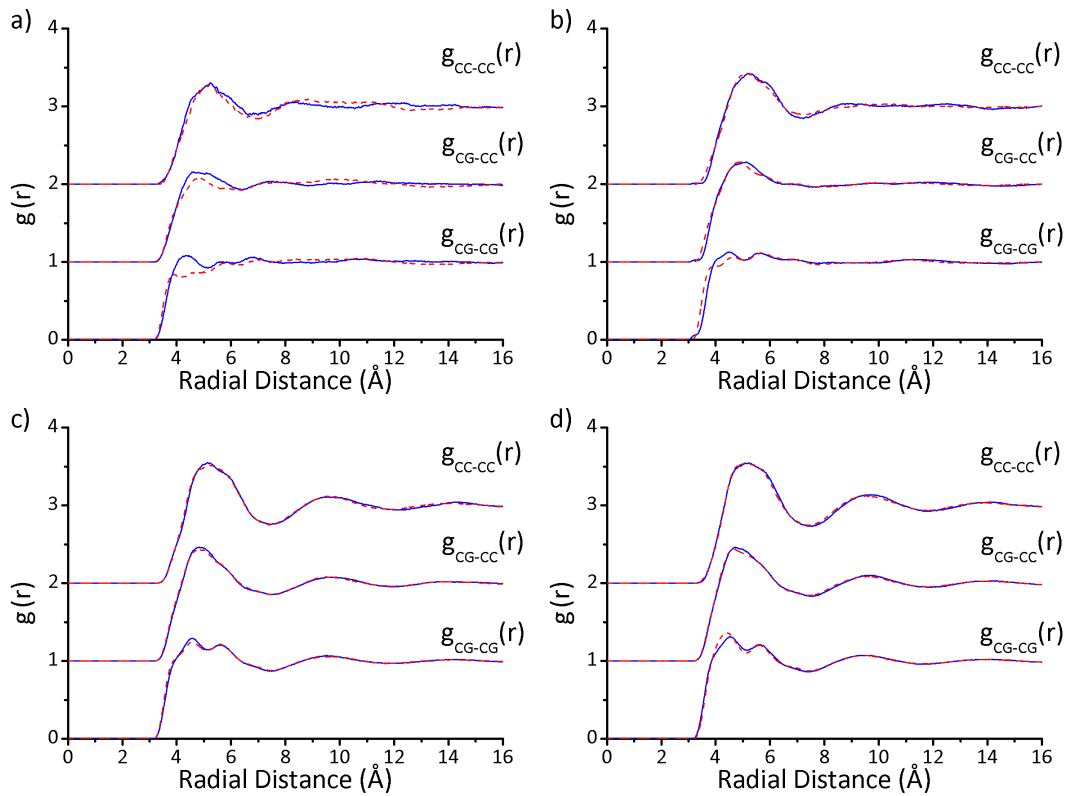
Figure 6.6: The inter-molecular carbon-carbon radial distribution functions from the EPSR analysis of neutron diffraction experiments at low temperatures. Here, the low temperature data is shown with a solid blue line and the room temperature data is shown with a dashed red line. The experiments were taken at concentrations of: (a) Xg = 0.10, (b) Xg = 0.25, (c) Xg = 0.80, and, (d) Xg = 1.00 (pure glycerol).

The changes in the hydrophilic interactions on cooling are investigated using the oxygen-oxygen radial distribution functions. Figure 6.7 shows each of the three oxygen-oxygen RDFs for low temperature and room temperature aqueous glycerol mixtures

(Figures 6.7(a), 6.7(b) & 6.7(c)) and pure glycerol (Figure 6.7(d)). Again, no clear modifications can be seen as the temperature is decreased. This shows that the lowering of the temperature does not cause any significant changes in interactions between the hydrophilic portions of the glycerol molecules. This, combined with the result shown in Figure 6.6, indicates that the glycerol-glycerol interactions measured using either the hydrophobic or hydrophilic interactions are not altered when the temperature is decreased.
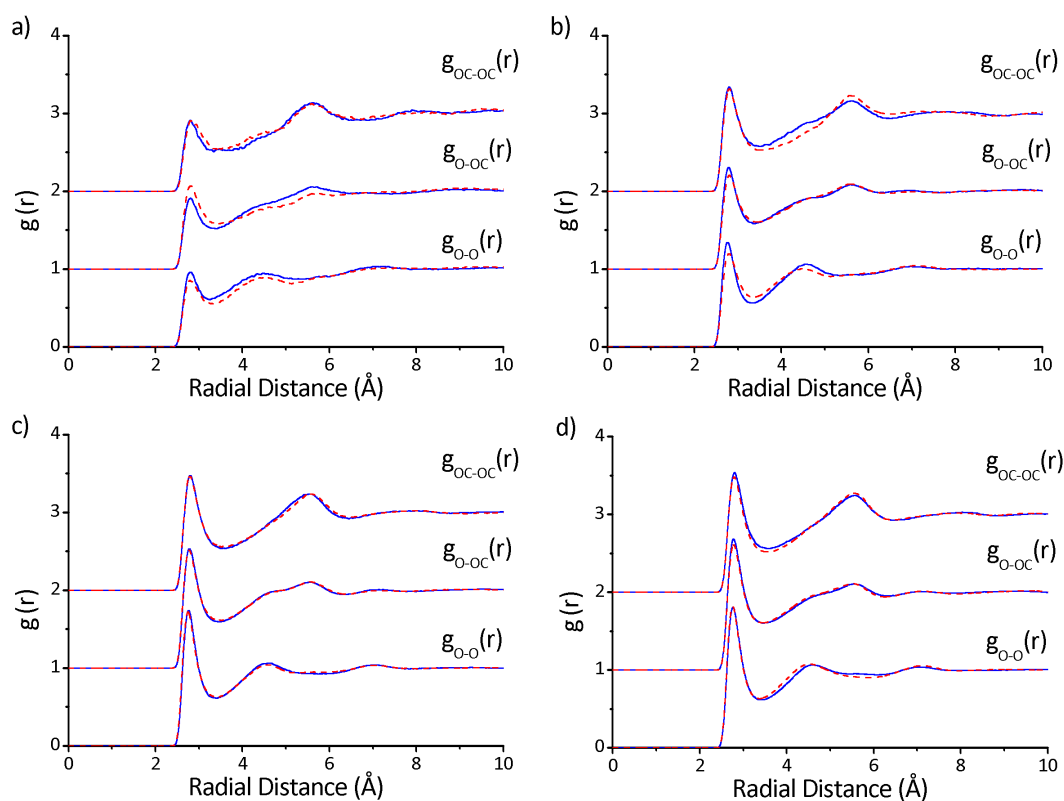
Figure 6.7: The inter-molecular glycerol oxygen-glycerol oxygen radial distribution functions from the EPSR analysis of neutron diffraction experiments at low temperatures. Here, the low temperature data is shown with a solid blue line and the room temperature data is shown with a dashed red line. The experiments were taken at concentrations of: (a) Xg = 0.10, (b) Xg = 0.25, (c) Xg = 0.80, and, (d) Xg = 1.00 (pure glycerol).

6.2.2 Water-Glycerol Interactions at Low Temperatures

The water-glycerol interactions are studied using the relevant oxygen-oxygen radial distribution functions. Here, the distal glycerol oxygen-water oxygen RDFs are shown in Figure 6.8(a) and the central glycerol oxygen-water oxygen RDFs are shown in Figure 6.8(b). It can be seen that the hetero (glycerol-water) oxygen-oxygen interactions are

are very similar at room and decreased temperatures for the most concentrated aqueous glycerol sample (Xg = 0.80). This is unsurprising as the temperature change at this concentration is the smallest of the aqueous samples (13 K). The largest change is seen in the first peak of the distal glycerol oxygen-water oxygen RDF at Xg = 0.25. Here, the peak position is higher, and the following trough is more pronounced in the low temperature system. Again, this effect is likely to be due to the magnitude of the temperature change in the Xg = 0.25 system, as the temperature has been reduced by 60 K. The peak positions are not altered at any of the concentrations when the temperature is decreased, with the largest shift in peak position on cooling being only 0.09 Å . This shows that the structure of the hetero interactions is not greatly altered when the temperature is decreased.
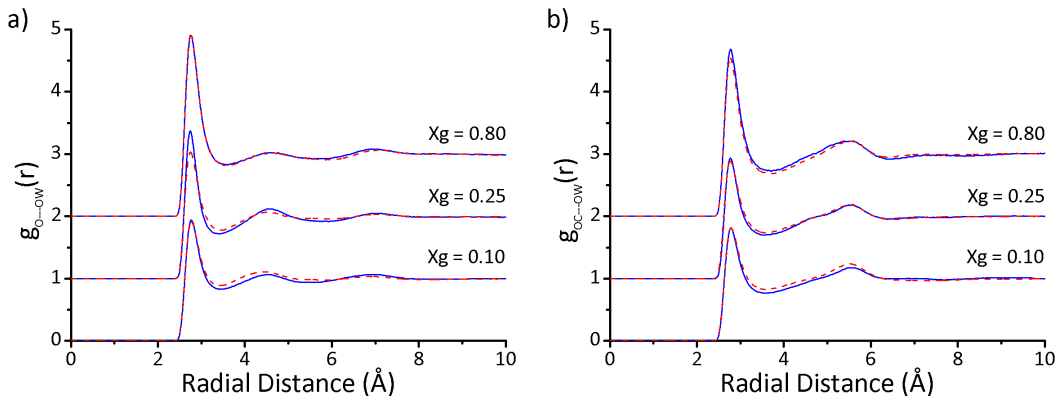
Figure 6.8: The inter-molecular glycerol oxygen-water oxygen radial distribution functions from the EPSR analysis of neutron diffraction experiments at low temperatures. (a) The distal glycerol oxygen-water oxygen RDFs and (b) shows the central oxygen-water oxygen RDFs. Here, the low temperature data is shown with a solid blue line and the room temperature data is shown with a dashed red line.

6.2.3 Water-Water Interactions at Decreased Temperatures

In this (and the following) sections, the changes in the structure of the water network due to a decrease in temperature are investigated. Here, the water network structure is investigated using the water oxygen-water oxygen radial distribution functions (see Figure 6.9). The position of the first peaks is not shown in Figure 6.9, as they do not change appreciably when the temperature is lowered[1]. This result is consistent with those seen in aqueous methanol (126) and sorbitol (85).

[1]The largest shift in first peak position in the water oxygen-water oxygen RDFs is only 0.03 Å .
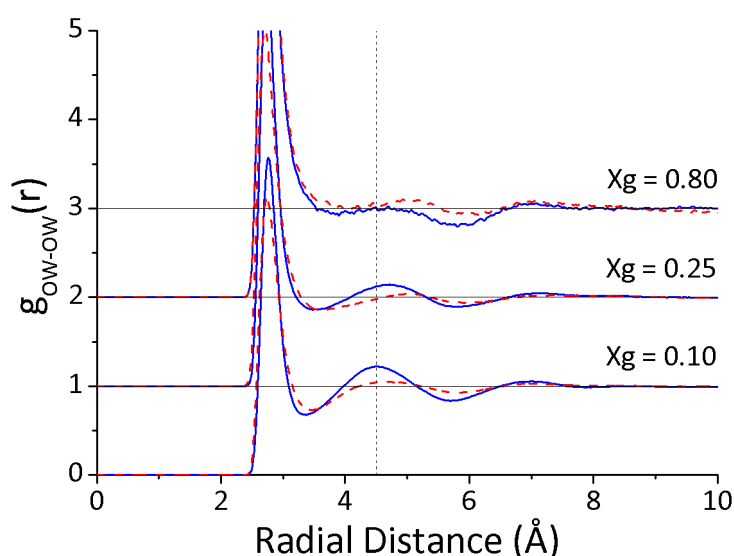
Figure 6.9: Water oxygen-water oxygen radial distributions taken from the EPSR analysis of the neutron diffraction data of aqueous glycerol samples at low (solid blue lines) and room (dashed red lines) temperatures. The distance of 4.50 Å is shown with a vertical dashed line. It can be seen that the second peaks of the RDFs taken from the dilute low temperature mixtures are markedly more pronounced than those taken at room temperature.

In the most concentrated glycerol solution, the second peak is less clear than each of the other concentrations. This is due, in part, to there being far fewer water molecules in this system (see Tables A.1 and A.4 within Appendix A). The diffuse nature of the second peak also suggests that there is not an extended water network at this glycerol concentration when the mixture is cooled. The molecular mixing found at the lower temperatures is discussed in Section 6.4. For both the intermediate ($Xg = 0.25$) and dilute ($Xg = 0.10$) concentrations there are clear changes in the second peak of the water oxygen-water oxygen RDFs. The height of the second peak in the $Xg = 0.10$ mixture is 1.221 for the low temperature system, which is larger than the peak at room temperature which has a height of 1.049. The height of the second peak in the $Xg = 0.25$ mixture is at 1.114 in the low temperature system and 1.040 at room temperature. This shows that the second peaks in both the $Xg = 0.10$ and $Xg = 0.25$ mixtures are more pronounced at low temperatures than at room temperature.

The position of the second peak is also affected by the temperature of the mixtures. In the $Xg = 0.25$ system, the second peak is shifted inwards from 5.04 Å to 4.71 Å, a shift of 0.33 Å. The second peak of the $Xg = 0.10$ system is also shifted inward by

0.24 Å when the temperature is decreased. The difference in the magnitude of the inward shift of the second peaks could be due to the different sizes of the temperature changes. The Xg = 0.25 mixture is cooled by 60 K, whereas the Xg = 0.10 system is cooled by 36 K. An inward shift is also seen when aqueous sorbitol (85) and methanol (126) are cooled. These shifts are similar to those that have been found from X-Ray diffraction measurements of the structure of pure water upon cooling (54; 55) (see Figure 1.8(a)). These data show that the presence of glycerol in the system does not prevent the changes in water structure that are associated with cooling, but does allow the water to remain liquid at greatly decreased temperatures. The position of the second peak in the oxygen-oxygen RDFs has previously been seen as being indicative of the tetrahedral nature of the system. Therefore, the following section includes an investigation of how the changes in the water-water RDFs upon cooling discussed in this section lead to a change in the tetrahedrality of the water network.

6.2.4   Water Network Tetrahedrality at Low Temperatures

The tetrahedrality of the water network has been probed using two techniques in this section. The first technique requires the angular distribution of the water oxygen atoms to be measured. Here, the included angle is measured for all sets of the three water oxygen atoms that conform to to specified distance criteria (as described in Section 4.3.3). The values taken from the low temperature systems (solid lines) are shown with those taken from the room temperature analysis (dashed lines) in Figure 6.10.

From these data it can be seen that, at low glycerol concentrations, there is an increase in the proportion of water oxygen triplets that have an included angle around the tetrahedral angle of 109.5° (dotted line) at the expense of triplets that have an included angle around 55°. These low angle triplets have been attributed to the presence of interstitial oxygen atoms in the water network (116). These interstitial oxygen atoms are not part of the hydrogen bond network, but are close enough to other oxygen atoms to be included in the angular distribution calculation (116). Therefore, it can be concluded that there is an increase in the proportion of oxygen atoms that form a tetrahedral structure accompanied by a decrease in the proportion of interstitial oxygen atoms in the Xg = 0.10 (Figure 6.10(a)) and Xg = 0.25 (Figure 6.10(b)) systems upon cooling. The most concentrated system (Xg = 0.80) does not show this effect (see Figure
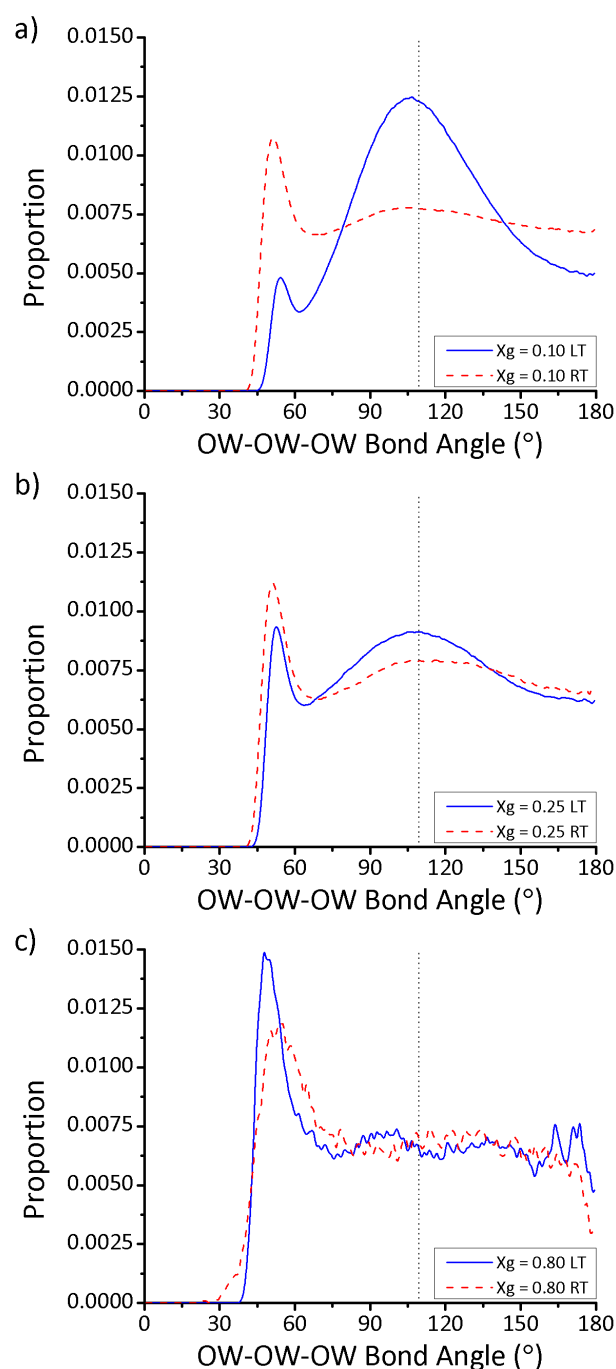
Figure 6.10: The proportion of water oxygen triplets that form an included angle as a function of angle. Here, data are shown for each of the aqueous glycerol systems that have been studied at low temperature (solid blue lines) along with the results taken from the room temperature mixtures (dashed red lines). The concentrations shown are: (a) $X_g = 0.10$, (b) $X_g = 0.25$, and, (c) $X_g = 0.80$. The dotted line in each plot indicates the perfect tetrahedral angle of $109.5°$. It can be seen that there is an increase in the proportion of triplets with an included angle close to the tetrahedral angle for the $X_g = 0.10$ and $X_g = 0.25$ systems.

6.10(c)). Here, there is an increase in the number of interstitial water oxygen atoms on cooling, with an inward shift of the peak at around $55°$. This could be attributed to the

low concentration of water in this system preventing an extended water network from forming. The water network is discussed in greater detail in Section 6.4.

The tetrahedral nature of a system can be quantified using tetrahedral order parameters (see Section 4.3.3). The parameter that is calculated here is the q parameter proposed by Errington & Debenedetti (129). These values are calculated using Equation 4.3. The results for the low temperature mixtures are shown with the values calculated for the room temperature systems in Table 6.2 and Figure 6.11.

Table 6.2: Water Network Tetrahedrality at Room and Low Temperatures

Concentration (Xg)	Temperature (K)	Tetrahedrality Parameter q
0.10	298.15	0.601
0.10	262.15	0.687
0.25	298.15	0.537
0.25	238.15	0.583
0.80	298.15	0.550
0.80	285.15	0.528
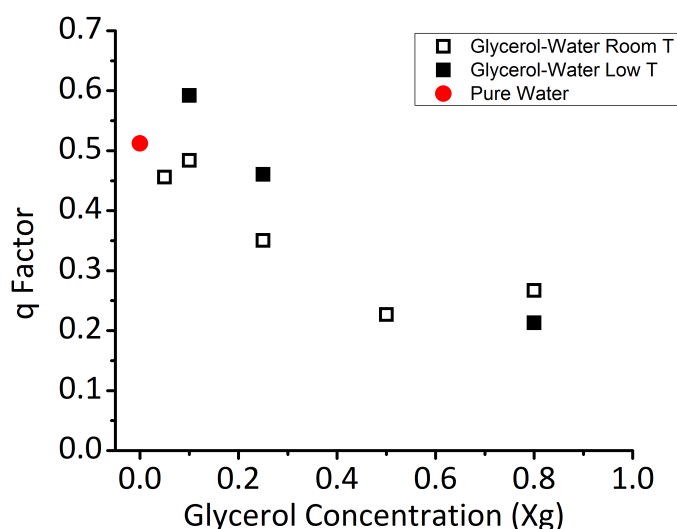
Figure 6.11: Tetrahedrality parameters for water oxygen-water oxygen-water oxygen atomic triplets in each of the aqueous glycerol systems at room temperature (open black squares), low temperatures (filled black squares), and pure water at room temperature (red circle). It can be seen that there is an increase in the tetrahedrality parameter for each of the dilute systems on cooling.

From Table 6.2 and Figure 6.11 it can be seen that each of the low temperature systems have higher q values when compared to the room temperature results. The most dilute system (Xg = 0.10) shows an increase of the q value of 0.086. For Xg = 0.25, the value of the q parameter is 0.046 higher in the decreased temperature system than at room temperature. Interestingly, the q parameter decreases by 0.022 for the most concentrated mixture (Xg = 0.80). From the data in this section it can be concluded that the water network in both the Xg = 0.10 and Xg = 0.25 mixtures is closer to a tetrahedral structure in the low temperature systems than was found at room temperature.

6.3   Inter-Molecular Bonding within Aqueous Glycerol at Decreased Temperatures

6.3.1   Confirming Low Temperature Hydrogen Bonding

The hydrogen bonding within the low temperature aqueous and pure glycerol systems is investigated within this section. Therefore, it is logical to begin with a reminder of the definition of a hydrogen bond that is used in this thesis (introduced in Section 3.3.1). Any radial distribution function, between a relevant hydrogen atom and an electronegative atom, with a peak at a radial distance of around 1.80 Å is considered to be indicative hydrogen bonding. The relevant electronegative atoms within aqueous glycerol are the distal and central oxygens of the glycerol molecules (O and OC respectively) and the oxygen of the water molecule (OW)[1]. The pertinent hydrogen atoms are those found on either the hydroxyl groups of glycerol (H) or the water molecules (HW). Therefore, it is the RDFs between these atoms that are investigated in this section. Figure 6.12 shows the oxygen-hydrogen RDFs involving the hydroxyl hydrogen atoms of glycerol and Figure 6.13 displays those involving the water hydrogen atoms.

From Figure 6.12 it can be seen that there are clear peaks at around 1.80 Å in each of the glycerol hydroxyl hydrogen-oxygen RDFs for all of the low temperature systems studied. This shows that glycerol hydroxyl hydrogen atoms act as hydrogen bond donors in all of the low temperature mixtures. Moreover, the radial distribution functions for the low temperature systems are very similar to those found at room temperature. This

[1]See Tables A.1 and A.4 in Appendix A.

suggests that the hydrogen bonds that are formed at low temperatures are of a similar structure to those observed at room temperature. Indeed, the position of the first peak in all of the RDFs shown in Figure 6.12 are shifted on cooling by only ≤ 0.03 Å. Therefore, the data shown in Figure 6.12 show that glycerol hydroxyl hydrogen atoms form hydrogen bonds as donors in the low temperature studies. It also shows that these hydrogen bonds have a similar structure when compared to those at room temperature. The number of hydrogen bonds formed is investigated in Section 6.3.2.

Each of the water hydrogen-oxygen radial distribution functions (O-HW, OC-HW, and OW-HW) taken from the EPSR analysis of the low temperature aqueous glycerol systems are shown in Figure 6.13. All of these distributions contain a prominent peak at a radial distance of around 1.80 Å. This peak indicates the presence of hydrogen bonding and shows that the water hydrogen atoms form hydrogen bonds as donors with each of the three different oxygen atom types in the system. Figure 6.13(a) shows that the structure of the water hydrogen-distal glycerol oxygen RDFs taken from the low temperature mixtures are very similar to those found in the room temperature systems. This suggests that cooling these aqueous mixtures has little effect on the structure of the hydrogen bonds formed between distal glycerol oxygen atoms and water hydrogen atoms. The structure of the hydrogen bonds formed between the hydrogen atoms found on water molecules and the central glycerol oxygen atoms are shown in Figure 6.13(b). Again, these radial distribution functions show that the results taken from the low and room temperature systems are very similar. This observation, combined with that shown in Figure 6.13(a), indicates that the structure of the hydrogen bonds between water hydrogen atoms and the oxygen atoms found on glycerol molecules are not dramatically altered by cooling. The number of hydrogen bonds that are formed is discussed in Section 6.3.2.

Figure 6.13(c) shows the RDFs for water hydrogen-water oxygen interactions. It can be seen that there are more substantial changes in the structure of the water hydrogen-water oxygen radial distributions on cooling than is seen in either the: glycerol hydrogen-glycerol oxygen (Figures 6.12(a) and 6.12(a)); glycerol hydrogen-water oxygen (Figure 6.12(c)); or, the water hydrogen-glycerol oxygen RDFs (Figures 6.13(a) and 6.13(b)). This feature can be quantified by measuring the radial position and height of the relevant peaks and troughs within the radial distribution functions (see Table 6.3). The largest
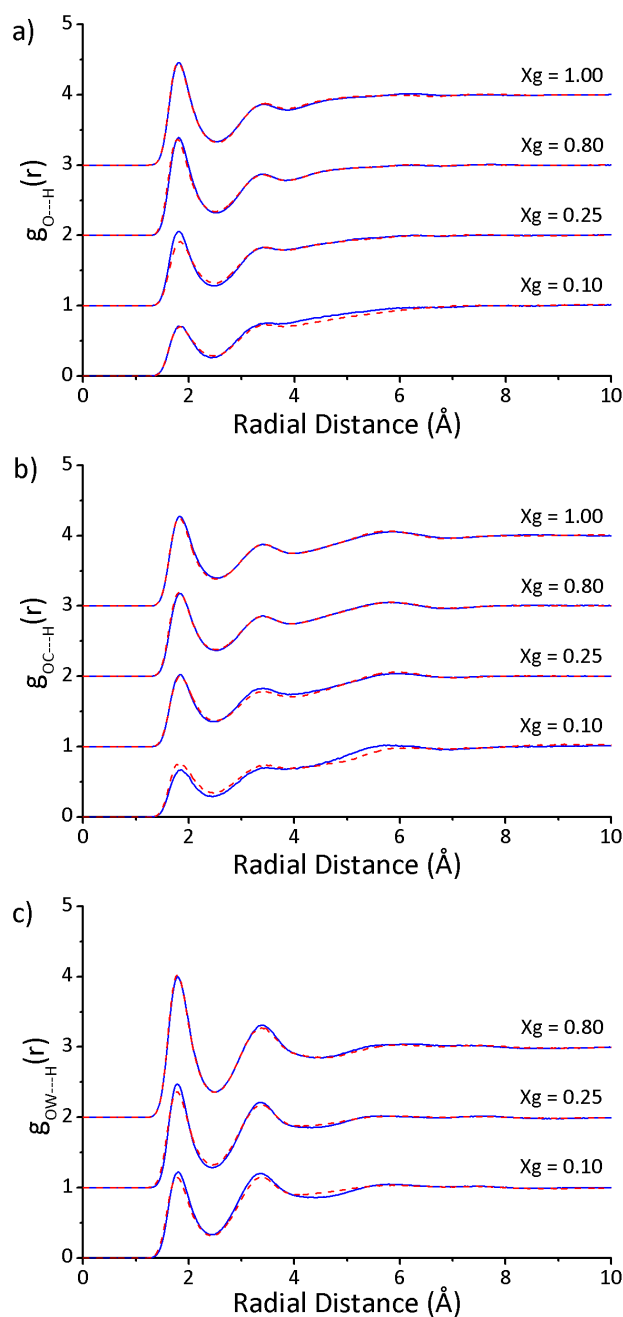
Figure 6.12: Inter-molecular glycerol hydroxyl hydrogen-oxygen radial distribution functions found in each of the low temperature studies (solid blue lines) along with those taken from the room temperature data (dashed red line). Included are: (a) distal oxygen-hydroxyl hydrogen, (b) central oxygen-hydroxyl hydrogen, and, (c) water oxygen-hydroxyl hydrogen. All of these RDFs show a peak at 1.80 Å which is indicative of hydrogen bonding.

change in the height of a trough can be found at $X_g = 0.10$. Here, the trough is found at a height of 0.313 at room temperature and at 0.180 at 262 K (a decrease of 0.133). A significant change is also seen at $X_g = 0.25$. Here, the trough is found at a height of 0.341 at room temperature and 0.266 at 238 K, a decrease of 0.075. The decrease in
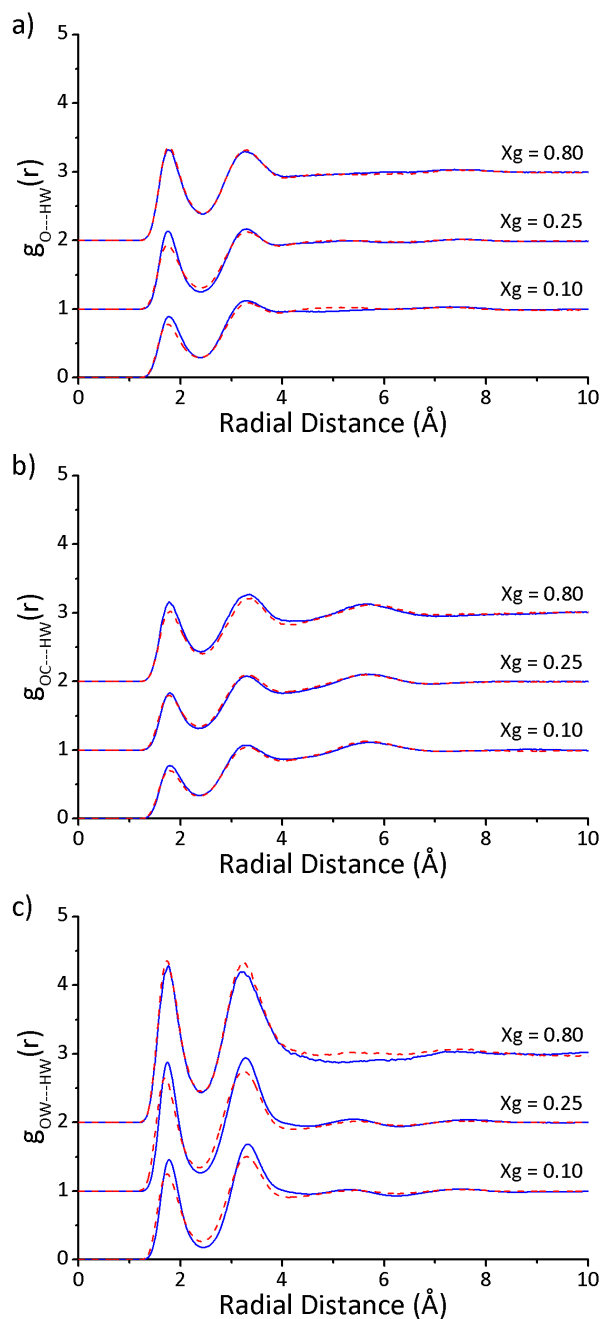
Figure 6.13: Inter-molecular water hydrogen-oxygen radial distribution functions for each of the low temperature studies (solid blue lines) and those taken from the room temperature data (dashed red line). These include: (a) distal oxygen-water hydrogen, (b) central oxygen-water hydrogen, and, (c) water oxygen-water hydrogen. All of these RDFs show a peak at 1.80 Å which indicatives that hydrogen bonds are formed.

the trough position seen for the Xg = 0.80 system is much less pronounced being only 0.014. The changes in the water hydrogen-water oxygen RDFs in dilute aqueous glycerol systems are more substantial than any others seen in the oxygen-hydrogen RDFs. This indicates that, at low glycerol concentrations, the water hydrogen-water oxygen RDF

Table 6.3: Water Hydrogen-Water Oxygen RDF Peak Positions

Concentration (Xg)	Temperature (K)	First Peak		First Trough	
		Distance (Å)	Height	Distance (Å)	Height
0.10	298	1.68	1.323	2.37	0.313
0.10	262	1.77	1.464	2.46	0.180
0.25	298	1.71	1.655	2.37	0.341
0.25	238	1.74	1.882	2.37	0.266
0.80	298	1.74	2.363	2.34	0.449
0.80	285	1.77	2.303	2.40	0.435

is modified more than any other hydrogen-oxygen RDF. These functions are found to have sharper first peaks as evidenced by the trough following the peak being found at a lower point. This shows that the water-water hydrogen bonds in low concentrations of aqueous glycerol are more well defined than those found at room temperature.

6.3.2 Quantifying Low Temperature Hydrogen Bonding

In Figures 6.12 and 6.13, the presence of inter-molecular hydrogen bonding within pure and aqueous glycerol at low temperatures was confirmed. These bonds can be further investigated by measuring the number of each type of hydrogen bond that are present. This is achieved by integration under the relevant peak within the oxygen-hydrogen RDFs to find the applicable coordination numbers (see Equation 2.18). These are then combined to find the total number of hydrogen bonds formed by either molecule type. The average number of hydrogen bonds formed by each glycerol molecule (G_{tot}) is calculated using Equation 4.5, and the average number per water molecule (W_{tot}) is found using Equation 4.6. The uncertainties in these hydrogen bond numbers is calculated using the method outlined in Section 4.4.1. The values that are taken from the EPSR analysis of the low temperature systems (solid blue symbols) are compared to those found at room temperature (open red symbols) in Figure 6.14.

From Figure 6.14 it can be seen that there is an increase in the average total number of hydrogen bonds formed by each glycerol molecule as the concentration is decreased at low temperatures with $G_{tot} = 5.85 \pm 0.46$ in pure glycerol to 6.62 ± 0.26 at Xg $= 0.10$. Similarly, there is an increase in W_{tot} as the water concentration is increased from
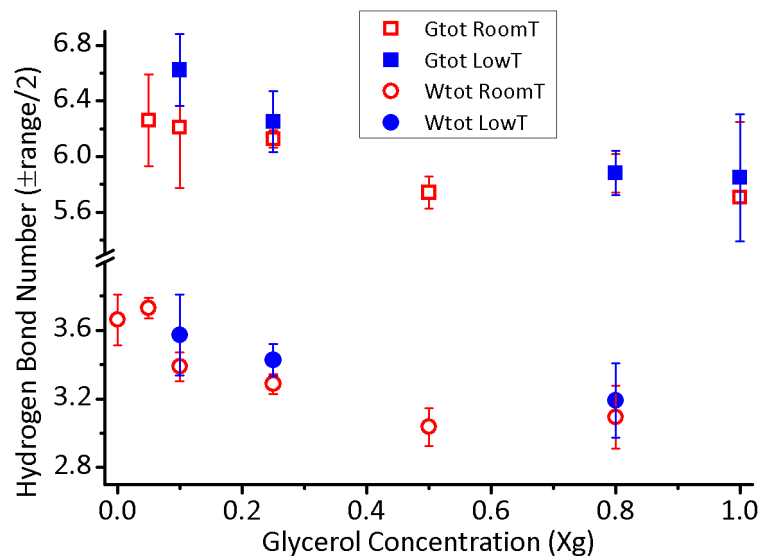
Figure 6.14: The average total number of hydrogen bonds formed by glycerol (G_{tot}) and water (W_{tot}) are shown with squares and circles respectively. The room temperature data (RoomT) is shown in red and low temperature data (LowT) is indicated by blue symbols. It can be seen that more hydrogen bonds are formed in the low temperature systems than at room temperature. These increases are, however, within the uncertainties.

3.19 ± 0.22 at Xg = 0.80 to 3.57 ± 0.24 at Xg = 0.10. This increase in the number of hydrogen bonds with decreasing glycerol concentration could be due to steric effects. Glycerol molecules contain hydrophobic carbon backbones and therefore, a decrease in the glycerol concentration leads to less hydrophobic regions within the mixture. It is conceivable that the decrease in the number of hydrophobic groups allows more hydrogen bonds to be formed in this system.

The next quantity to investigate is the relationship between the room and low temperature hydrogen bond numbers. From Figure 6.14 it an be seen that both G_{tot} and W_{tot} are higher in the low temperature systems than was found at room temperature. The largest of these increases is found in G_{tot} at Xg = 0.10. Here, the number of hydrogen bonds increases from 6.21 ± 0.43 to 6.62 ± 0.26 on cooling. However, this increase of 0.41 hydrogen bonds per molecule is within the uncertainty on these values and, therefore, is not a significant increase. This shows that the number of hydrogen bonds formed by either water (W_{tot}) or glycerol (G_{tot}) is not significantly modified upon cooling. Chou et al. have reported an increase in the number of water-water hydrogen bonds in aqueous sorbitol when the mixture is cooled (85). However, it is difficult to compare their results to those presented here as the number of sorbitol-water hydrogen

bonds is not included in their publication, and neither are the uncertainties on these values.

6.4 Molecular Mixing within Aqueous Glycerol at Decreased Temperatures

In this section the molecular scale mixing of aqueous glycerol at low temperatures is investigated. Here, the method outlined in Section 5.1.3 will be used to measure the number of clusters that contain i molecules ($M(i)$) as a fraction of the total number of clusters (M). The radial cut-offs used to define a cluster are taken from Figures 6.7, 6.8, and, 6.9. These distributions are then compared to two reference systems and the room temperature data discussed in Chapter 5. Finally the structure of the clusters is investigated.

6.4.1 Are Low Temperature Clusters due to Molecular Packing?

Firstly the clustering found in low temperature aqueous glycerol is compared to a simulation of the mixture which has been produced using only the Lennard-Jones potentials. This system is at the appropriate atomic number densities and box sizes to be comparable to the EPSR setups (see Appendix A) and is known as the LJP Only simulation. Figure 6.15 shows the glycerol clusters that are found at low temperatures at each of the three aqueous glycerol concentrations studied, as well as the cluster distributions taken from the LJP Only simulations. It can be seen that at Xg = 0.10 there are spanning clusters of 340 molecules in the LJP Only simulation (grey circles in Figure 6.15(a)). The largest cluster found in the EPSR analysis contains only 63 molecules. In the Xg = 0.25 mixture, 3 % of the clusters within the EPSR analysis contain at least 90 % of the glycerol molecules (black squares in 6.15(b)). For the LJP Only simulation, however, over 99 % of the clusters contain at least 90 % of the glycerol molecules. At a concentration of Xg = 0.80, all of the glycerol molecules in the LJP Only simulation are found in a single spanning cluster (see Figure 6.15(c)). The clusters in the EPSR analysis, however, are found at a wide range of different sizes. Therefore, at each of the low temperature concentrations studied, the EPSR analysis shows smaller glycerol clusters than the LJP Only simulations.
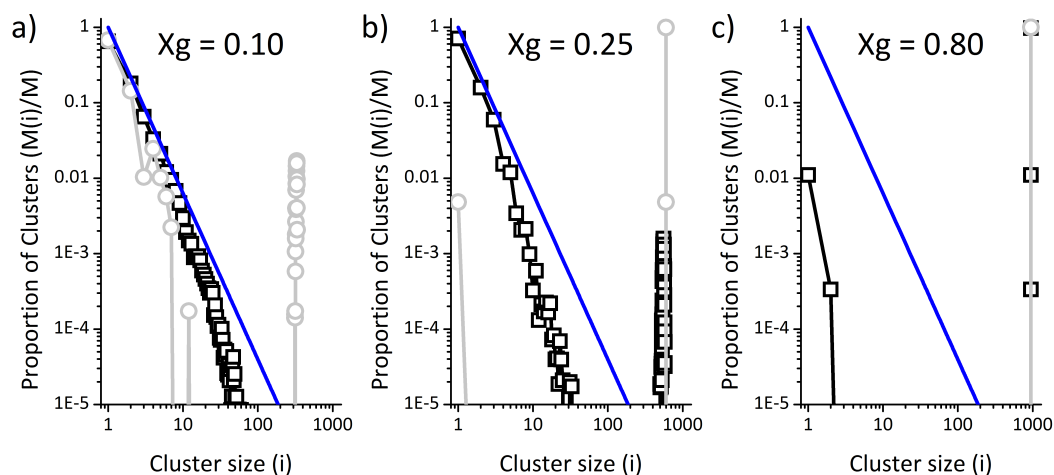
Figure 6.15: The glycerol cluster distributions taken from the EPSR analysis of the neutron diffraction data at low temperatures (black squares) along with those taken from the LJP Only simulation (grey circles) and the cluster distribution that would be found at the percolation threshold (blue line). Here, data are shown at three concentrations: (a) Xg = 0.10, (b) Xg = 0.25, and, (c) Xg = 0.80. The LJP Only simulation forms percolating clusters at all concentrations, but the EPSR data only shows percolating clusters at concentrations of Xg ≥ 0.25.
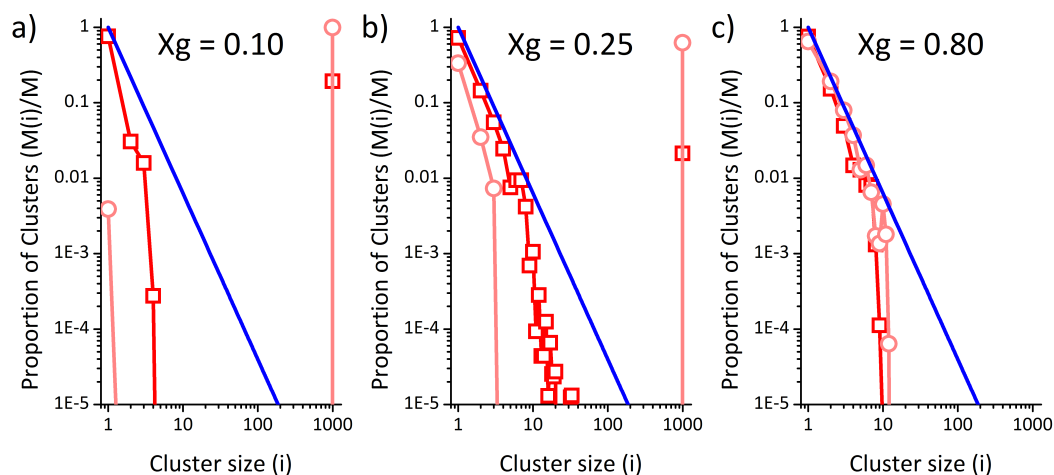
Figure 6.16: The water cluster distributions taken from the EPSR analysis of the neutron diffraction data at low temperatures (red squares) and those taken from the LJP Only simulation (light red circles) and the cluster distribution that would be found at the percolation threshold (blue line). Here, data are shown at three concentrations: (a) Xg = 0.10, (b) Xg = 0.25, and, (c) Xg = 0.80. The LJP Only simulations and the EPSR data show percolating clusters at concentrations of Xg ≤ 0.25.

The water clusters taken from the EPSR analysis of neutron diffraction data collected at three glycerol-water concentrations at low temperatures are shown in Figure 6.16. Again, these are shown with the distributions taken from the relevant LJP Only simulations. The water cluster size distribution at a concentration of Xg = 0.10 is shown

in Figure 6.16(a). It can be seen that spanning clusters of ≥ 999 water molecules are found in both the EPSR and LJP Only data. These clusters account for 19.3 % of those found in the EPSR analysis, whereas 99.6 % of the clusters found in the LJP Only simulation contain at least 999 water molecules. A similar scenario is found at $Xg = 0.25$ (Figure 6.16(b)). Here, 62.4 % of the water clusters found in the LJP Only simulation are spanning clusters and the EPSR analysis shows that only 2.1 % of the water clusters are spanning. Interestingly, the proportion of the clusters found in both the EPSR analysis and the LJP Only simulation of the $Xg = 0.80$ system are very similar (Figure 6.16(c)). Both systems do not contain any spanning clusters, with the largest cluster found in the EPSR analysis containing 10 water molecules and the largest in the LJP Only simulation being 12 water molecules. Therefore, Figure 6.16 shows that a higher proportion of larger water clusters found in the EPSR data compared to the LJP Only simulation at concentrations of $Xg = 0.10$ and 0.25 systems. The water cluster sizes found in the EPSR analysis of the $Xg = 0.80$ system are close to those found in a randomly packed system.

Figures 6.15 and 6.16 show that the cluster distributions found in the EPSR analysis of the low temperature aqueous glycerol systems are smaller than those found in the LJP Only simulations. This shows that the clustering that is found in these systems is not purely due to molecular packing. This result is similar to that found at room temperature (see Section 5.2). The low temperature mixing is compared to that found at room temperature in the following section.

6.4.2 The Effect of Temperature on Molecular Mixing

In this section the cluster distributions shown in Section 6.4.1 are compared to those found at room temperature (see Chapter 5). Figure 6.17 shows the glycerol clusters found at low temperatures (black squares) along with those found at room temperature (grey crosses). From these data it can be seen that the cluster distributions for glycerol are very similar at room and low temperatures. Therefore, temperature does not have a marked effect on the clustering of glycerol molecules in aqueous glycerol.

The water cluster distributions found in room and low temperature EPSR analysis of the neutron diffraction experiments are shown in Figure 6.18. Here, the low temperature results are represented by red squares and the room temperature data are shown with
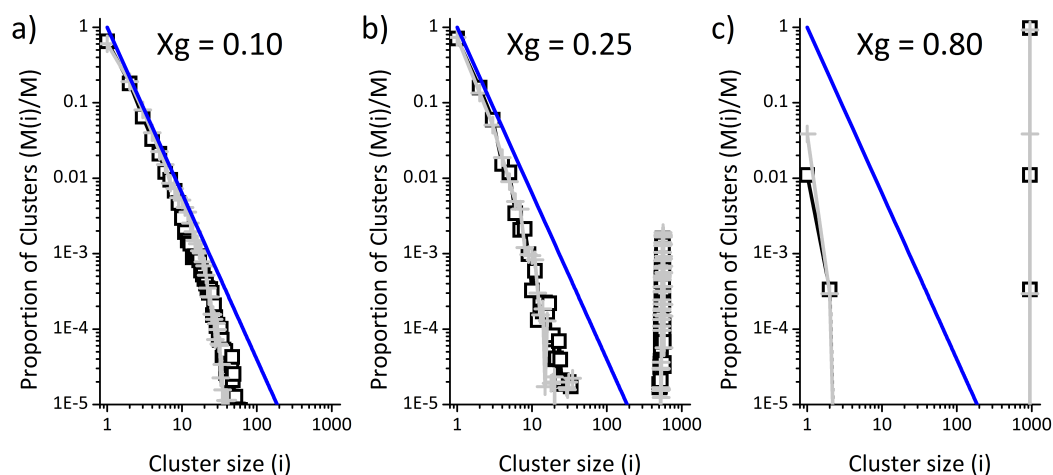
Figure 6.17: The glycerol cluster distributions taken from the low temperature (black squares) and room temperature (grey crosses) EPSR analyses of neutron diffraction data, and the cluster distribution that would be found at the percolation threshold (blue line). Here, data are shown at three concentration: (a) Xg = 0.10, (b) Xg = 0.25, and, (c) Xg = 0.80. The distributions are shown to be very similar at each of the concentrations studied.
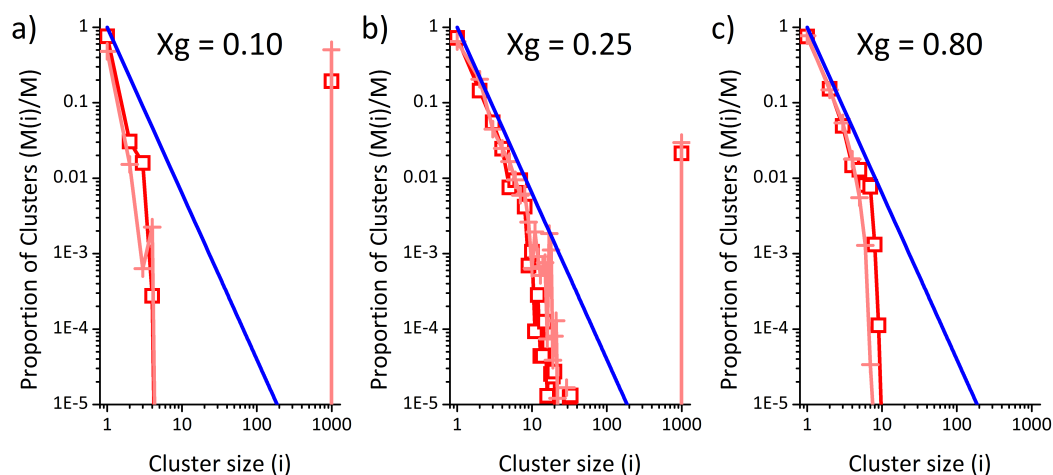
Figure 6.18: The water cluster distributions taken from the low temperature (red squares) and room temperature (light red crosses) EPSR analyses of neutron diffraction data, and the cluster distribution that would be found at the percolation threshold (blue line). Here, data are shown at three concentration: (a) Xg = 0.10, (b) Xg = 0.25, and, (c) Xg = 0.80. The distributions are shown to be very similar at concentrations of Xg = 0.25 and 0.80. However, there is a decrease in the number of spanning clusters in the Xg = 0.10 system on cooling.

light red crosses. The cluster distributions at Xg = 0.25 and 0.80 show that, at these concentrations, the water cluster sizes are not modified on cooling. There is, however, a clear difference in the distributions that are found in the Xg = 0.10 system (see Figure 6.18(a)). Here, 19.3 % of the water clusters found at low temperature are spanning

clusters. However, at room temperature 50.3 % of the water clusters are spanning clusters. Equation 5.10 has been used to calculate the proportion of molecules that are found in clusters from the cluster size proportions. This is used to understand the importance of this difference. From this calculation it is found that 99.54 % of the water molecules are found in spanning clusters at low temperature. This is a decrease of only 0.38 % when compared to the room temperature data.

Figures 6.17 and 6.18 show that the cluster distributions of both glycerol and water that are found in aqueous glycerol are very similar at low and room temperatures. The largest change is found in the water clusters at Xg 0.10, where there is a decrease of 0.38 % in the proportion of water molecules found in spanning clusters. This result is the opposite to that found by Dougan *et al*. when they studied aqueous methanol systems (126). They find that the proportion of spanning clusters increases by a factor of around 10 at the expense of intermediate size clusters (126). Figure 4.9 in Section 4.3.4 shows that the carbon-carbon interactions are significantly less pronounced in aqueous glycerol than in aqueous methanol. This suggests that the methanol molecular clustering occurs via the hydrophobic methyl groups, and that glycerol aggregation occurs via the hydrophilic hydroxyl groups. This different method of clustering could lead to the different relationship between clustering and temperature seen in aqueous glycerol and methanol.

6.4.3   Cluster Percolation at Low Temperatures

The molecular scale clustering of aqueous glycerol can be further investigated by measuring the proportion of molecules that are found in percolating clusters. Here, the definition introduced in Section 5.3.1 will be used to define a percolating cluster. Therefore, any cluster with a proportion that exceeds the value given by Equation 5.11 (from the work of Jan (138)) is described as being indicative of percolation. Figure 6.19 shows the proportion of molecules of each kind that are found in percolating clusters in the low temperature aqueous glycerol systems. It can be seen that the water molecules are forming percolating clusters (red circles) at concentrations of Xg $\leq$ 0.25. The glycerol molecules are forming percolating clusters at Xg $\geq$ 0.25. Therefore, a bi-percolating mixture is formed at a concentration of Xg = 0.25. Figure 6.17(a) shows that the glycerol cluster distribution at Xg = 0.10 is close to the percolation threshold. This suggests

that a small increase from Xg = 0.10 would lead to the glycerol molecules forming a percolating structure. From Figure 5.11 it can be concluded that the concentration region of bi-percolation found at room temperature is still present when aqueous glycerol is cooled.
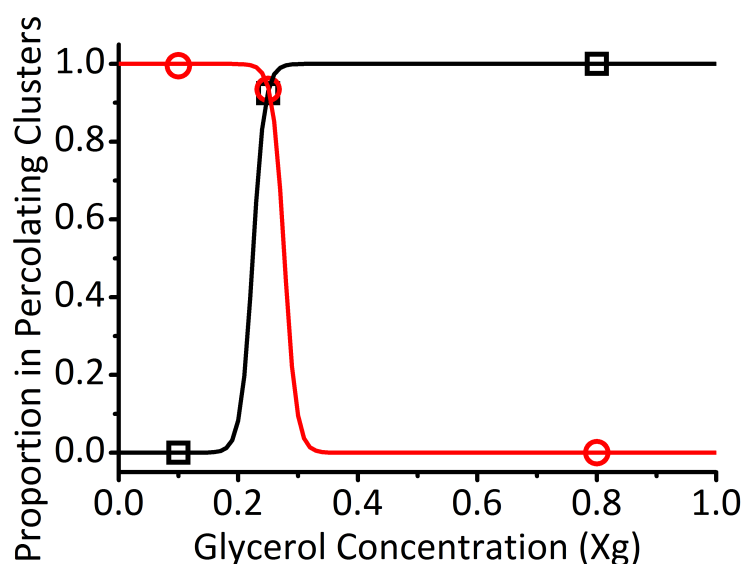
Figure 6.19: The proportion of glycerol (black squares) and water (red circles) found in percolating clusters as a function of glycerol concentration for the low temperature aqueous glycerol systems studied. Glycerol is shown to be forming percolating clusters at concentrations of Xg $\geq$ 0.25 and water is forming percolating clusters at concentrations of Xg $\leq$ 0.25. Therefore, at a concentration of Xg = 0.25 both glycerol and water are forming percolating clusters.

6.4.4   The Structure of Low Temperature Clusters

The final method that is used to investigate the structure of the clusters is to measure the proportion of the molecules that are found at the surface of the clusters. Here, a molecule is defined as being on the surface of a cluster if it has an oxygen atom that is within 2.40 Å of a hydrogen atom of a different molecule type or *vice versa*[1]. Figure 6.20(a) shows the proportion of glycerol (squares) and water (circles) found at the surface of clusters at low (blue) and room (red) temperatures. It can be seen that these data are very similar. This suggests that cooling does not alter the structure of either glycerol or water clusters. These data are used to find the total fraction of molecules found in

---

[1]See Section 5.3.3 for full a description.

the surface of clusters (Surf_{tot}) using,

$$\text{Surf}_{tot} = \sum_i \text{Surf}_i \cdot X_i \tag{6.2}$$

where Surf_i is the fraction of molecules of type i that are found at the surface of clusters and X_i is the mole fraction of molecule i. The values for the total proportion of molecules found at the surface are also similar for the low and room temperatures (Figure 6.20(b)). These data, combined with that shown in Figures 6.15, 6.16 and 6.19 show that the molecular mixing found at room temperature is still present at low temperatures.

Interestingly, at a concentration of Xg = 0.25, over 98 % of the glycerol molecules and around 28 % of the water molecules are at the cluster surface at both room or low temperature. Therefore, even though the glycerol is forming a percolating network at this concentration, the structure of the clusters is such that 98 % of these molecules are bonded to the surrounding water network. This could be a signature that the glycerol molecules are forming a sheath around the water molecules at this concentration. It is conceivable that this layer of glycerol prevents bulk water and ice from forming when the mixture is cooled.
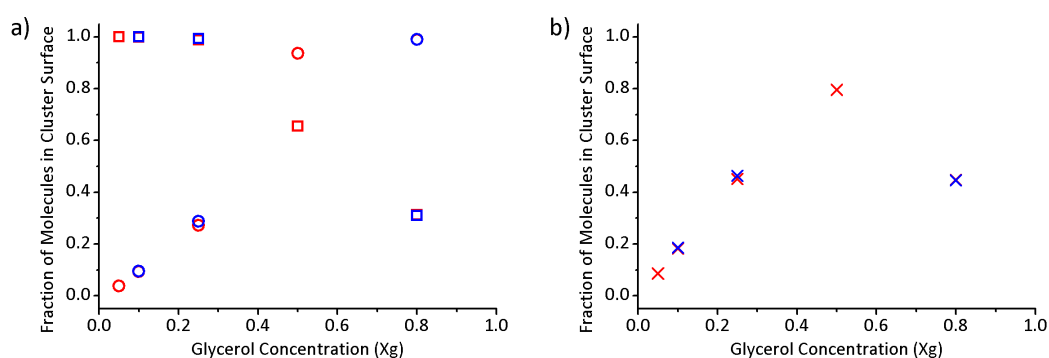
Figure 6.20: The fraction of molecules that are found at the surface of clusters in the low temperature (blue) and room temperature (red) aqueous glycerol mixtures as a function of glycerol concentration (Xg). (a) The fraction of water (circles) and glycerol (squares) molecules found at the surface of clusters. (b) The total fraction of molecules (crosses) found at the surface of clusters.

6.5 Conclusions Regarding the Low Temperature Structure of Glycerol and Aqueous Glycerol

This chapter details a study of the structure of pure and aqueous glycerol at low temperatures. Here, a low temperature system refers to one that is below 25 °C and the neutron diffraction experiments that have been conducted are shown in Figure 6.1. In order to analyse these data the density of the mixtures has been estimated using linear interpolation between values taken from the literature (12; 147). This method is described in Section 6.1.2. The fit of the EPSR simulation has been confirmed (Figure 6.3) and has been interrogated. Comparison of these results with those described in Chapters 3, 4 and 5 allows the structural modifications on cooling to be found. These structural properties are divided into four sections: intra-molecular structure and bonding, inter-molecular structure, inter-molecular bonding, and, molecular scale mixing.

It was found that the distribution of the conformations of glycerol were not dramatically altered by the decrease in temperature (see Table 6.1 and Figure 6.4). Intra-molecular hydrogen bonding was investigating using the relevant oxygen-hydrogen RDFs (Figure 6.5). No evidence was found for intra-molecular hydrogen bonding within the glycerol molecules. These results show that the intra-molecular structure of glycerol is not appreciably modified when either aqueous or pure glycerol is cooled to temperatures close to the melting point at the relevant concentrations.

Section 6.2 includes an investigation of the inter-molecular interactions that are found at low temperatures. These data are compared to the values that are found at room temperature. It is shown the glycerol-glycerol interactions as measured by the carbon-carbon (Figure 6.6) and oxygen-oxygen (Figure 6.7) RDFs are not modified due to the cooling of the system. Similarly, the glycerol-water interactions are investigated using the glycerol oxygen-water oxygen RDFs in Figure 6.8 and are shown not to change when the temperature is decreased. There are, however, clear modifications to the water-water interactions on cooling. This is shown by the sharpening and inward movement of the second peak of the water oxygen-water oxygen RDFs in Figure 6.9 at glycerol concentrations of Xg = 0.10 and 0.25. This modification to the water structure upon cooling is similar to that seen on the cooling of pure water (54; 55), aqueous methanol (126), and, aqueous sorbitol (85). In Section 6.2.4 these shifts in the position of the

second peak are shown to be indicative of a modification in the tetrahedrality of the water network (see Figure 6.10). The increase in the tetrahedral nature of the system on cooling is quantified using both the q parameter proposed by Errington & Debenedetti (129) within Table 6.2.

The hydrogen bonds that are formed in the low temperature systems are investigated in Section 6.3. The formation of hydrogen bonds are confirmed by the presence of a clear peak at a radial distance of around 1.80 Å within the inter-molecular oxygen-hydrogen RDFs. Glycerol-glycerol hydrogen bonds are shown in Figures 6.12(a) and 6.12(b), glycerol-water hydrogen bonds are shown in Figures 6.12(c), 6.13(a) and 6.13(b), and water-water hydrogen bonds are shown in Figure 6.13(c). These RDFs are used to quantify the hydrogen bonding in Section 6.3.2. It is found that the changes in the number of hydrogen bonds that are formed are within the uncertainties of these values. This suggests that the temperature change investigated here does not lead to a modification in the number of hydrogen bonds formed within aqueous glycerol.

Finally, molecular scale mixing is investigated in Section 6.4. Figure 6.15 and 6.16 show that the clusters formed in the EPSR analysis are significantly smaller than those found in the LJP Only simulation for both glycerol and water respectively. The glycerol cluster distribution is shown not to be modified on cooling in Figure 6.17. Figure 6.18(a) shows that there is a small decrease in the number of spanning water clusters at a concentration of Xg = 0.10. The water clusters at Xg = 0.25 and 0.80 are shown to be unaffected by cooling (see Figures 6.18(b) and 6.18(c) respectively). Interestingly, this result is different to that found for aqueous methanol (126). It is also shown that aqueous glycerol forms a bi-percolating structure at Xg = 0.25 (Figure 6.16). This structure is accompanied by a high proportion of glycerol molecules being found in the surface of these clusters (Figure 6.19).

Therefore, it can be concluded that the cooling of pure and aqueous glycerol to temperatures above the relevant melting temperature does not have a dramatic effect on the structure of the system. The most notable change comes in an increase in the tetrahedrality of the water network. However, this increase in tetrahedrality is prevented from leading to ice formation by the well mixed nature of aqueous glycerol.

Chapter 7

Conclusions and Future Work

This chapter provides a summary of the important work that has been detailed in Chapters 3, 4, 5 and 6, as well as introducing future areas that could be investigated.

7.1   Concluding Remarks

This thesis details a thorough investigation into the structure of aqueous glycerol across the complete concentration range at room and low temperatures. These results have been found using a combination of neutron diffraction and computational modelling. This has allowed fundamental insights into the intra- and inter-molecular structure, the hydrogen bonding, and molecular mixing that is present. Changes in these properties are measured as a function of both temperature and concentration.

No evidence for intra-molecular hydrogen bonding was found in glycerol. This shows that the conformation of the glycerol molecules is determined by inter-molecular rather than intra-molecular bonding. It is also shown that the hydrogen bonding ability of water is relatively unperturbed when glycerol is added. Glycerol and water molecules have been shown to form a very well mixed solution at each of the concentrations studied. Strikingly, it has been shown that these molecular clusters of glycerol and water are smaller than would be seen in a randomly packed mixture.

The structure of both glycerol-glycerol and glycerol-water interactions are not altered when the solutions are cooled. The water-water structure is, however, dramatically modified when the temperature is decreased. This leads to a marked increase in the tetrahedrality of the water network with the water molecules forming a structure similar

to that found in ice. Within these systems the glycerol molecules are forming a sheath around the water molecules with a large proportion of the glycerol molecules bonded to water molecules. This mixing regime leads to the glycerol molecules preventing water from forming the large clusters that are needed to for water to form ice.

From these results it is concluded that the cryoprotective action of glycerol is due to its ability to form a very well mixed aqueous solution. This prevents large water clusters from forming. This mixing is maintained when the solution is cooled, leading to the prevention of ice formation. This alleviates the problems caused by freeze dehydration and intra-cellular ice formation during cryopreservation.

7.2 Future Work

The work detailed in this thesis addresses the structure of an important binary mixture in the liquid state. To broaden the impact of this work it is important that it should be used as the starting point for future investigations. The suggestions below relate to investigations that would enhance the scientific importance of the research detailed in this thesis.

7.2.1 Links Between Macroscopic Properties and Molecular Structure

In Figure 5.7 the thermodynamic properties of aqueous glycerol are shown. It would be interesting to find a link between these macroscopic properties and the molecular level structure that is described in detail in this thesis. Previously, it has been shown that the molecular level de-mixing of aqueous methanol can be used to calculate the excess entropy of mixing (137). Conversely the thermodynamic properties of aqueous glycerol have been used to infer molecular scale structure (41). An extension of the current research could include a thorough investigation of the links between molecular scale bonding and cluster formation and the macroscopically measured properties of the system.

7.2.2 Temperature Regimes

The use of vitrification as a tool for cryoprotection was introduced in 1940 by Luyet and Gehenio (148) and this set the foundation for successful work by Greg Fahy and co-

workers in the 1980s (149). Encapsulating a biomolecule in a vitrified system does not, however, guarantee successful cryopreservation. Indeed, it has been shown that the rate of temperature change has an effect on the viability of cryopreserved biomolecules and organisms after thawing (see reference (21) and those within). It has been previously shown that the thermal history of glycerol can effect the structure of the glass that is formed (150). Littau *et al* showed that cooling rates of 0.2 K min^{-1} and 600 K min^{-1} produce markedly different dynamic properties measured using two photon echo and hole burning spectroscopy (150). Therefore, it would be interesting to study the effects of the rate of temperature change on aqueous glycerol structure.

7.2.3 Biologically Relevant Solutions

The aim of the research detailed in this thesis was to investigate the structure of an important cryoprotectant molecule in aqueous mixtures. To enhance the scientific impact of this work it should be used as the starting point for a study of the interactions between aqueous glycerol and relevant biomolecules. Indeed, a neutron diffraction experiment has been performed to study the structure of an important biological molecule in aqueous glycerol. Here, the amino acid glutamine has been studied in aqueous mixtures at temperatures of 297.15 and 277.15 K. The glycerol is at a mole fraction of 0.10 and the mole fraction of glutamine is 0.003. This work will build upon the the aqueous glycerol studies that are detailed in this thesis and elsewhere (1–4) as well as recent work by Rhys *et al* looking at the structure of aqueous glutamine (151).

Appendix A

Reference Potentials and Geometry

A.1   Glycerol Reference Potentials and Geometry

Table A.1: Glycerol Potentials

Atom Label	ϵ (kJ mol^{-1})	σ (Å)	Mass (a.m.u.)	q(e)	Atom Type
OC	0.650	3.100	16	-0.624	Oxygen
O	0.650	3.100	16	-0.624	Oxygen
CC	0.800	3.700	12	0.107	Carbon
CG	0.800	3.700	12	0.107	Carbon
H	0.000	0.000	1	0.392	Hydrogen
HG	0.000	0.000	1	0.063	Hydrogen

Table A.2: Glycerol Bond Lengths

Atom 1	Atom 2	Bond Length (Å)
O	CG	1.450
O	H	0.969
OC	H	0.969
OC	CC	1.449
CG	CC	1.538
CG	HG	1.084
CC	HG	1.084

Table A.3: Glycerol Bond Angles

Atom 1	Atom 2	Atom 3	Angle (°)
CG	O	H	109.91
CC	OC	H	108.33
O	CG	CC	108.88
CC	CG	HG	110.17
O	CG	HG	109.51
HG	CG	HG	108.57
CG	CC	CG	111.20
OC	CC	CG	108.72
CG	CC	HG	109.61
OC	CC	HG	108.96

A.2 Water Reference Potentials and Geometry

Table A.4: Water Potentials

Atom Label	ϵ (kJ mol^{-1})	σ (Å)	Mass (a.m.u.)	q(e)	Atom Type
OW	0.650	3.166	16	-0.82	Oxygen
HW	0.000	0.000	1	0.41	Hydrogen

Table A.5: Water Bond Lengths

Atom 1	Atom 2	Bond Length (Å)
HW	OW	1.000

Table A.6: Water Bond Angles

Atom 1	Atom 2	Atom 3	Angle (°)
HW	OW	HW	109.47

A.3   EPSR Parameters

Table A.7: Room Temperature EPSR Parameters

Xg	No. Glycerol	No. Water	No. Atoms	ρ (Atoms Å^{-1})
1.00	1,000	0	14,000	0.11500
0.80	948	237	13,983	0.11445
0.50	825	825	14,025	0.11280
0.25	600	1,800	13,800	0.10970
0.10	340	3,060	13,940	0.10560
0.05	200	3,800	14,200	0.10320
0.00	0	1,000	3,000	0.10000

Table A.8: Room Temperature EPSR Box Sizes

Xg	Box Length (Å)	Volume (Å^3)
1.00	49.56	121,739
0.80	49.62	122,176
0.50	49.91	124,335
0.25	50.11	125,798
0.10	50.92	132,008
0.05	51.63	137,597
0.00	31.07	30,000

Table A.9: Low Temperature EPSR Parameters

Xg	No. Glycerol	No. Water	No. Atoms	ρ (Atoms Å^{-1})
1.00	1,000	0	14,000	0.11545
0.80	948	237	13,983	0.11515
0.25	600	1,800	13,800	0.11289
0.10	340	3,060	13,940	0.10680

Table A.10: Low Temperature EPSR Box Sizes

Xg	Box Length (Å)	Volume (Å^3)
0.80	49.50	121,265
0.25	49.52	121,433
0.10	49.63	122,243
0.05	50.73	130,524

Appendix B

Calculating Hydrogen Bond Number Using Oxygen-Oxygen Separation

Table B.1: Inter-molecular Hydrogen Bonds Calculated Using Oxygen-Oxygen RDFs

Atom 1	Atom 2	r_{max}	Coordination Number	Contribution to Hydrogen Bonds per molecule
O	O	3.50	1.78	1.78 x 2 = 3.56
O	OC	3.50	0.88	0.88 x 2 = 1.76
OC	O	3.50	1.76	1.76 x 1 = 1.76
OC	OC	3.50	0.85	0.85 x 1 = 0.85
Total				7.94

Appendix C

Calculating The Uncertainty Hydrogen Bond Number

```
#input filename
finput = "nodi_spc_o_h.COORD.dat"
#output filename
foutput = "results.dat"


#open file for reading
FIN=open(finput,"r")
#open file for writing (appending mode)
FOUT=open(foutput,"a")


#the whole file is saved (in RAM) as an array of strings(lines)
allLines = FIN.readlines()


i=0 #just a boolean


for line in allLines: #takes a line at a time from the array
if i==1:
FOUT.write(line) # writes lines into the output file, only if i=1
if (line[0]=='q'): #if first letter of a line is 'q', then i becomes 1 and
```

```
#will never change again

i=1


#closing both files

FIN.close()

FOUT.close()
```

References

[1] J.J. Towey, A.K. Soper, and L. Dougan, "The structure of glycerol in the liquid state: A neutron diffraction study", *Physical Chemistry Chemical Physics* **13**(20), pp. 9397 – 9406 (2011). iii, 68, 92, 113, 115, 179

[2] J.J. Towey, A.K. Soper, and L. Dougan, "Preference for isolated water molecules in a concentrated glycerol-water mixture", *Journal of Physical Chemistry B* **115**(24), pp. 7799 – 7807 (2011). iii, 91, 92, 105, 113, 115, 124, 143

[3] J.J. Towey and L. Dougan, "Structural examination of the impact of glycerol on water structure", *Journal of Physical Chemistry B* **116**(5), pp. 1633 – 1641 (2012). iii, 92, 105

[4] J.J. Towey, A.K. Soper, and L. Dougan, "Molecular insight into the hydrogen bonding and micro-segregation of a cryoprotectant molecule", *Journal of Physical Chemistry B* **116**(47), pp. 13898 – 13904 (2012). iii, 91, 92, 105, 113, 115, 124, 143, 179

[5] J.J. Towey, A.K. Soper, and L. Dougan, "What happens to the structure of water in cryoprotectant solutions?", *Faraday Discussions* **167**(Accepted Manuscript) (2013). iii, 105

[6] J. Sjostrom, R. Bergman, C. Wadell, T. Moberg, J. Swenson, and J. Mattsson, "Effects of water contamination on the supercooled dynamics of a hydrogen-bonded model glass former", *Journal of Physical Chemistry B* **115**, pp. 1842 – 1847 (2011). 2

[7] P.G. Debenedetti and F.H. Stillinger, "Supercooled liquids and the glass transition", *Nature* **410**, pp. 259 – 267 (2001). 2

[8] P.H. Yancey, M.E. Clark, S.C. Hand, R.D. Bowlus, and G.N. Somero, "Living with water-stress - evolution of osmolyte systems", *Science* **217**(4566), pp. 1214 – 1222 (1982). 2

[9] J. Wuttke, J. Hernandez, G. Li, G. Coddens, H.Z. Cummins, F. Fujara, W. Petry, and H. Sillescu, "Neutron and light-scattering study of supercooled glycerol", *Physical Review Letters* **72**(19), pp. 3052 – 3055 (1994). 2

[10] C. Polge, A.U. Smith, and A.S. Parkes, "Revival of spermatozoa after vitrification and dehydration at low temperatures", *Nature* **164**(4172), pp. 666 – 666 (1949). 2, 4, 5

[11] R.L. Cook, H.E. King, C.A. Herbst, and D.R. Herschbach, "Pressure and temperature-dependent viscosity of 2 glass-forming liquids - glycerol and dibutyl phthalate", *Journal of Chemical Physics* **100**(7), pp. 5178 – 5189 (1994). 2

[12] E. Green and J.P. Parke, "The density and viscosity of glycerol solutions at low temperatures", *Journal of the Society of Chemical Industry* **58**(40), pp. 319T – 320T (1939). 2, 150, 175

[13] A. Singhabhandhu and T. Tezuka, "A perspective on incorporation of glycerin purification process in biodiesel plants using waste cooking oil as feedstock", *Energy* **35**, pp. 2493 – 2504 (2010). 3

[14] J. F. Izquierdo, M. Montiel, I. Pales, P. R. Outon, M. Galan, L. Jutglar, M. Villarrubia, M. Izquierdo, M. P. Hermo, and X. Ariza, "Fuel additives from glycerol etherification with light olefins: State of the art", *Renewable and Sustainable Energy Reviews* **16**, pp. 6717 – 1724 (2012). 3

[15] M. Gupta and N. Kumar, "Scope and opportunities of using glycerol as an energy source", *Renewable and Sustainable Energy Reviews* **16**, pp. 4551 – 4556 (2012). 4

[16] E. Santacesaria, G. Martinez Vicente, M. Di Serio, and R. Tesser, "Main technologies in biodiesel production: State of the art and future challenges", *Catalysis Today* **195**, pp. 2 – 13 (2012). 4

[17] J.R.M. Almeida, L.C.L. Favaro, and B.F. Quirino, "Biodiesel biorefinery: Opportunities and challenges for microbial production of fuels and chemicals from glycerol waste", *Biotechnology for Biofuels* **5**, pp. 48 (2012). 4

[18] F. Yang, M.A. Hanna, and R. Sun, "Value-added uses for crude glycerol-a byproduct of biodiesel production", *Biotechnology for Biofuels* **5**(13) (2012). 3, 4

[19] P.A. Egelstaff, *An Introduction to the Liquid State*, Oxford Series on Neutron Scattering in Condensed Matter. Oxford Univ. Press New York, U.S.A. 2nd edition (1992). 4, 67

[20] G.M. Fahy, B. Wowk, J. Wu, and S. Paynter, "Improved vitrification solutions based on the predictability of vitrification solution toxicity", *Cryobiology* **48**(1), pp. 22 – 35 (2004). 4

[21] B.J. Fuller, "Cryoprotectants: The essential antifreezes to protect life in the frozen state", *Cryoletters* **25**(6), pp. 375 – 388 (2004). 5, 6, 26, 179

[22] K. Muldrew and L.E. McGann, "Mechanisms of intracellular ice formation", *Biophysical Journal* **57**(3), pp. 525 – 532 (1990). 5

[23] A.U. Smith, "Prevention of haemolysis during freezing and thawing of red bloodcells", *Lancet* **2**(6644), pp. 910 – 911 (1950). 5, 6

[24] P. Mazur, "Cryobiology - freezing of biological systems", *Science* **168**(3934), pp. 939 (1970). 6

[25] J.E. Lovelock, "The mechanism of the protective action of glycerol against haemolysis by freezing and thawing", *Biochimica et Biophysica Acta* **11**(1), pp. 28 – 36 (1953). 6

[26] T. Nash, *Cryobiology* , pp. 179 – 211, Academic Press New York, U.S.A. (1966). 6

[27] I. Bernemann, N. Hofmann, R. Spindler, A. Szentivanyi, and B. Glasmacher, "Strategy to improve cryopreservation protocols", *Cryoletters* **29**(1), pp. 83 (2008). 6

[28] R.A. Lobo, "Current concepts - potential options for preservation of fertility in women", *New England Journal of Medicine* **353**(1), pp. 64 – 73 (2005). 6

[29] A.M. Karow and W.R. Webb, "Toxicity of various solute moderators used in hypothermia.", *Cryobiology* **1**(4), pp. 270 – 273 (1965). 6, 91

[30] J.P. Hansen and I.R. McDonald, *The Theory of Simple Liquids*, Academic Press London, U.K. 3 edition (2006). 7

[31] J. Henin, W. Shinoda, and M.L. Klein, "United-atom acyl chains for charmm phospholipids", *Journal of Physical Chemistry B* **112**(23), pp. 7008 – 7015 (2008). 15

[32] W.L. Jorgensen, D.S. Maxwell, and J. Tiradorives, "Development and testing of the opls all-atom force field on conformational energetics and properties of organic liquids", *Journal of the American Chemical Society* **118**(45), pp. 11225 – 11236 (1996). 15, 62

[33] M.P. Allen and D.J. Tildesley, *Computer Simulation of Liquids*, Oxford Univ. Press (1987). 15, 31, 60

[34] N. Metropolis, A.W. Rosenbluth, M.N. Rosenbluth, A.H. Teller, and E. Teller, "Equation of state calculations by fast computing machines", *Journal of Chemical Physics* **21**, pp. 1087 – 1092 (1953). 15, 62

[35] P.H. Poole, F. Sciortino, U. Essmann, and H.E. Stanley, "Phase-behavior of metastable water", *Nature* **360**(6402), pp. 324 – 328 (1992). 16

[36] D.T. Limmer and D. Chandler, "The putative liquid-liquid transition is a liquid-solid transition in atomistic models of water. ii", *Journal of Chemical Physics* **138**(21), pp. 214504 (2013). 16

[37] B. Guillot, "A reappraisal of what we have learnt during three decades of computer simulations on water", *Journal of Molecular Liquids* **101**(1 - 3), pp. 219 – 260 (2002). 16

[38] A. Mudalige and J.E. Pemberton, "Raman spectroscopy of glycerol/d2o solutions", *Vibrational Spectroscopy* **45**(1), pp. 27 – 35 (2007). 17, 24, 127, 128, 139, 140

[39] J.M. Vanderkooi, J.L. Dashnau, and B. Zelent, "Temperature excursion infrared (teir) spectroscopy used to study hydrogen bonding between water and biomolecules", *Biochimica et Biophysica Acta-Proteins and Proteomics* **1749**(2), pp. 214 – 233 (2005). 17

[40] D.A. Schmidt and K. Miki, "Structural correlations in liquid water: A new interpretation of ir spectroscopy", *Journal of Physical Chemistry A* **111**(40), pp. 10119 – 10122 (2007). 17

[41] Y. Marcus, "Some thermodynamic and structural aspects of mixtures of glycerol with water", *Physical Chemistry Chemical Physics* **2**(21), pp. 4891 – 4896 (2000). 17, 23, 24, 95, 112, 113, 123, 124, 126, 138, 139, 144, 178

[42] E.C.H. To, J.V. Davies, M. Tucker, P. Westh, C. Trandum, K.S.H. Suh, and Y. Koga, "Excess chemical potentials, excess partial molar enthalpies, entropies, volumes, and isobaric thermal expansivities of aqueous glycerol at 25 degrees c", *Journal of Solution Chemistry* **28**(10), pp. 1137 – 1157 (1999). 18, 24, 123, 124, 127, 139, 140, 142

[43] Y. Hayashi, A. Puzenko, and Y. Feldman, "Slow and fast dynamics in glycerol-water mixtures", *Journal of Non-Crystalline Solids* **352**(42-49), pp. 4696 – 4703 (2006). 18, 24, 127, 128, 139, 140, 142

[44] D.M. Cristancho, D.R. Delgado, F. Martínez, M.A.A. Fakhree, and A. Jouyban, "Volumetric properties of glycerol and water mixtures at several temperatures and correlation with the jouyban-acree model", *Revista Colombiana de Ciencias Químico Farmacéuticas* **40**(1), pp. 92 – 115 (2011). 18, 23, 24, 78, 95, 112, 113, 126, 149

[45] S.P. Moulik and D. Basu, "Interaction of binary-mixtures of associated liquids (glycerol-water system)", *Indian Journal of Chemistry Section A-Inorganic Bioinorganic Physical Theoretical and Analytical Chemistry* **16**(10), pp. 815 – 820 (1978). 18, 95

[46] D. Chandler, "Interfaces and the driving force of hydrophobic assembly", *Nature* **437**(7059), pp. 640 – 647 (2005). 19

[47] J.G Davis, K.P. Gierszal, P. Wang, and D. Ben-Amotz, "Water structural transformation at molecular hydrophobic interfaces", *Nature* **491**(7425), pp. 582 – 585 (2012). 19

[48] F. Bruni, R. Mancinelli, and M.A. Ricci, "How safe is to safely enter in the water no-man's land?", *Journal of Molecular Liquids* **176**, pp. SI 39 – 43 (2012). 19

[49] F. Uhlig, O. Marsalek, and P. Jungwirth, "Electron at the surface of water: Dehydrated or not?", *Journal of Physical Chemistry Letters* **4**(2), pp. 338 – 343 (2013). 19

[50] P. Wernet, D. Nordlund, U. Bergmann, M. Cavalleri, M. Odelius, H. Ogasawara, L.A. Naslund, T.K. Hirsch, L. Ojamae, P. Glatzel, L.G.M. Pettersson, and A. Nilsson, "The structure of the first coordination shell in liquid water", *Science* **304**, pp. 995 – 999 (2004). 19

[51] C. Huang, K.T. Wikfeldt, T. Tokushima, D. Nordlund, Y. Harada, U. Bergmann, M. Niebuhr, T.M. Weiss, Y. Horikawa, M. Leetmaa, M.P. Ljungberg, O. Takahashi, A. Lenz, L. Ojamae, A.P. Lyubartsev, S. Shin, L.G.M. Pettersson, and A. Nilsson, "The inhomogeneous structure of water at ambient conditions", *Proceedings of the National Academy of Sceinces of the United States of America* **106**(36), pp. 15214 – 15218 (2009). 19

[52] A.K. Soper, "Recent water myths", *Pure and Applied Chemistry* **82**(10), pp. 1855 – 1867 (2010). 19

[53] T.D. Kühne and R.Z. Khaliullin, "Electronic signature of the instantaneous asymmetry in the first coordination shell of liquid water", *Nature Communications* **4**, pp. 1450 (2013). 19

[54] J. Morgan and B.E. Warren, "X-ray analysis of the structure of water", *Journal of Chemical Physics* **6**(11), pp. 666 – 673 (1938). 19, 20, 29, 159, 175

[55] A.H. Narten and H.A. Levy, "Liquid water - molecular correlation functions from X-ray diffraction", *Journal of Chemical Physics* **55**(5), pp. 2263 – 2269 (1971). 20, 21, 29, 159, 175

[56] A.K. Soper, "The radial distribution functions of water and ice from 220 to 673 K and at pressures up to 400 MPa", *Chemical Physics* **258**(2 - 3), pp. 121 – 137 (2000). 20, 21, 29

[57] D.C. Champeney, R.N. Joarder, and J.C. Dore, "Structural studies of liquid d-glycerol by neutron diffraction", *Molecular Physics* **58**(2), pp. 337 – 347 (1986). 20, 22, 69, 70, 71, 88

[58] R. Chelli, P. Procacci, G. Cardini, R.G. Della valle, and S. Califano, "Glycerol condensed phases part i. a molecular dynamics study", *Physical Chemistry Chemical Physics* **1**(5), pp. 871 – 877 (1999). 20, 22, 68, 69, 71, 72, 73, 74, 79, 84, 85, 89

[59] O. Bastiansen, "Intra-molecular hydrogen bonds in ethylene glycol, glycerol, and ethylene chlorohydrin", *Acta Chemica Scandinavica* **3**(4), pp. 415 – 421 (1949). 21, 68, 75, 88, 92, 151

[60] H. van Koningsveld, "Crystal structure of glycerol and its conformation", *Recueil des Travaux Chimiques des Pays-Bas* **87**(3), pp. 243 – 249 (1968). 21, 67, 69, 88

[61] R. Chelli, F.L. Gervasio, C. Gellini, P. Procacci, G. Cardini, and V. Schettino, "Conformational distribution of gas-phase glycerol", *Journal of Physical Chemistry A* **104**(47), pp. 11220 – 11222 (2000). 21, 22, 67, 69, 71, 88

[62] M. Garawi, J.C. Dore, and D.C. Champeney, "Structural studies of liquid d-glycerol. 2. molecular-conformation and long-range correlations", *Molecular Physics* **62**(2), pp. 475 – 487 (1987). 22, 69, 70, 71, 88

[63] S. Sarkar and R.N. Joarder, "Intermolecular ordering of hydrogen-bonded liquid glycerol", *Physics Letters A* **222**(3), pp. 195 – 198 (1996). 22, 68, 73, 74, 85, 89

[64] R. Chelli, P. Procacci, G. Cardini, and S. Califano, "Glycerol condensed phases part ii. a molecular dynamics study of the conformational structure and hydrogen bonding", *Physical Chemistry Chemical Physics* **1**(5), pp. 879 – 885 (1999). 22, 68, 69, 70, 71, 72, 73, 74, 78, 79, 84, 85, 89

[65] R. Chelli, F.L. Gervasio, C. Gellini, P. Procacci, G. Cardini, and V. Schettino, "Density functional calculation of structural and vibrational properties of glyc-

erol", *Journal of Physical Chemistry A* **104**(22), pp. 5351 – 5357 (2000). 22, 71, 72, 73, 78, 89

[66] W. Zhuang and C. Dellago, "Dissociation of hydrogen chloride and proton transfer in liquid glycerol: An ab initio molecular dynamics study", *Journal of Physical Chemistry B* **108**(51), pp. 19647 – 19656 (2004). 22, 69, 71, 73, 74, 79, 81, 84, 85, 89

[67] L.J. Root and F.H. Stillinger, "Short-range order in glycerol - a molecular-dynamics study", *Journal of Chemical Physics* **90**(2), pp. 1200 – 1208 (1989). 22, 73, 74, 84, 89

[68] L.J. Root and B.J. Berne, "Effect of pressure on hydrogen bonding in glycerol: A molecular dynamics investigation", *Journal of Chemical Physics* **107**(11), pp. 4350 – 4357 (1997). 22, 71, 73, 74, 80, 84, 85, 89

[69] J.A. Padro, L. Saiz, and E. Guardia, "Hydrogen bonding in liquid alcohols: a computer simulation study", *Journal of Molecular Structure* **416**(1-3), pp. 243 – 248 (1997). 22, 68, 73, 74, 84, 89

[70] E. Guardia, J. Marti, J.A. Padro, L. Saiz, and A.V. Komolkin, "Dynamics in hydrogen bonded liquids: water and alcohols", *Journal of Molecular Liquids* **96-7**(SI), pp. 3 – 17 (2002). 22

[71] R.J. Fort and W.R. Moore, "Adiabatic compressibilities of binary liquid mixtures", *Transactions of the Faraday Society* **61**, pp. 2102 – 2111 (1965). 23, 24, 91, 95, 112, 113

[72] L. Xu, X.G. Hu, and R.S. Lin, "Volumetic properties of glycerol with n,n-dimethylformamide and with water at 25 and 35 degrees C", *Journal of Solution Chemistry* **32**(4), pp. 363–370 (2003). 23, 24, 78, 126, 138, 139, 149

[73] A.B. Yongye, B.L. Foley, and R.J. Woods, "On achieving experimental accuracy from molecular dynamics simulations of flexible molecules: Aqueous glycerol", *Journal of Physical Chemistry A* **112**(12), pp. 2634 – 2639 (2008). 23, 92, 94, 97, 98, 99, 100, 121, 153

[74] C.S. Callam, S.J. Singer, T.L. Lowary, and C.M. Hadad, "Computational analysis of the potential energy surfaces of glycerol in the gas and aqueous phases: Effects of level of theory, basis set, and solvation on strongly intramolecularly hydrogen-bonded systems", *Journal of the American Chemical Society* **123**(47), pp. 11743 – 11754 (2001). 23, 92, 94, 97, 98, 99, 121, 153

[75] L.D. Weng, C. Chen, J.G. Zuo, and W.Z. Li, "Molecular dynamics study of effects of temperature and concentration on hydrogen-bond abilities of ethylene glycol and glycerol: Implications for cryopreservation", *Journal of Physical Chemistry A* **115**(18), pp. 4729 – 4737 (2011). 23, 91, 94, 96, 99, 100, 121, 153

[76] C. Chen, W.Z. Li, Y.C. Song, and J. Yang, "Hydrogen bonding analysis of glycerol aqueous solutions: A molecular dynamics simulation study", *Journal of Molecular Liquids* **146**, pp. 23 – 28 (2009). 23, 91, 96, 118

[77] J.L. Dashnau, N.V. Nucci, K.A. Sharp, and J.M. Vanderkooi, "Hydrogen bonding and the cryoprotective properties of glycerol/water mixtures", *Journal of Physical Chemistry B* **110**(27), pp. 13670 – 13677 (2006). 23, 25, 92, 94, 95, 96, 97, 98, 99, 107, 109, 112, 118, 121, 127, 128, 139, 140, 142

[78] R. Politi, L. Sapir, and D. Harries, "The impact of polyols on water structure in solution: A computational study", *Journal of Physical Chemistry A* **113**(26), pp. 7548 – 7555 (2009). 23, 95, 96, 109, 118

[79] M.S. Raman, V. Ponnuswamy, P. Kolandaivel, and K. Perumal, "Ultrasonic and dft study of intermolecular association through hydrogen bonding in aqueous solutions of glycerol", *Journal of Molecular Liquids* **142**(1-3), pp. 10 – 16 (2008). 23, 91, 96

[80] D. Banerjee and S.V. Bhat, "Vitrification, relaxation and free volume in glycerol-water binary liquid mixture: Spin probe esr studies", *Journal of Non-Crystalline Solids* **355**(50-51), pp. 2433–2438 (2009). 24, 127, 128, 139, 140, 142

[81] A. Kyrychenko and T.S. Dyubko, "Molecular dynamics simulations of microstructure and mixing dynamics of cryoprotective solvents in water and in the presence of a lipid membrane", *Biophysical Chemistry* **136**(1), pp. 23 – 31 (2008). 25, 127, 128

[82] S.E. Pagnotta, M.A. Ricci, F. Bruni, S.E. McLain, and S. Magazu, "Water structure around trehalose", *Chemical Physics* **345**(2 - 3), pp. 159 – 163 (2008). 26, 29, 96, 103, 104, 105, 129

[83] S.E. Pagnotta, S.E. McLain, A.K. Soper, F. Bruni, and M.A. Ricci, "Water and trehalose: How much do they interact with each other?", *Journal of Physical Chemistry B* **114**(14), pp. 4908 – 4909 (2010). 26, 27, 28, 96, 103, 104, 105, 129

[84] S.E. McLain, A.K. Soper, A.E. Terry, and A. Watts, "Structure and hydration of l-proline in aqueous solutions", *Journal of Physical Chemistry B* **111**(17), pp. 4568 – 4580 (2007). 26, 27, 28, 96, 103, 104, 105, 129

[85] S.G. Chou, A.K. Soper, S. Khodadadi, J.E. Curtis, S. Krueger, M.T. Cicerone, A.N. Fitch, and E.Y. Shalaev, "Pronounced microheterogeneity in a sorbitol-water mixture observed through variable temperature neutron scattering", *Journal of Physical Chemistry B* **116**(15), pp. 4439 – 4447 (2012). 26, 28, 29, 96, 103, 104, 105, 129, 148, 149, 150, 157, 159, 167, 175

[86] S.E. McLain, A.K. Soper, and A. Luzar, "Orientational correlations in liquid acetone and dimethyl sulfoxide: A comparative study", *Journal of Chemical Physics* **124**(7), pp. 074502 (2006). 26, 29, 96, 103, 104, 105, 129

[87] F. Meersman, D. Bowron, A.K. Soper, and M.H.J. Koch, "Counteraction of urea by trimethylamine n-oxide is due to direct interaction", *Biophysical Journal* **97**(9), pp. 2559 – 2566 (2009). 26, 28, 29, 96, 103, 104, 105, 129

[88] L.B. Lane, "Freezing points of glycerol and its aqueous solutions", *Industrial and Engineering Chemistry* **17**(9), pp. 924 (1925). 30, 138, 139, 148

[89] C. Hammond, *The Basics of Crystallography and Diffraction*, Oxford Univ. Press (2001). 31

[90] D.S. Sivia, *Elementary Scattering Theory: For X-ray and Neutron Users*, Oxford Univ. Press (2011). 31

[91] L. de Broglie, "Waves and quanta", *Nature* **112**, pp. 540 – 540 (1923). 36

[92] V.F. Sears, "Neutron scattering lengths and cross sections", *Neutron News* **3**(3), pp. 26 – 37 (1992). 38, 40, 55

[93] W.H. McMaster, N. Kerr Del Grande, J.H. Mallett, and J.H. Hubbell, *Compilation of X-ray Cross Sections*, U.S. Dept. of Commerce (1969). 38, 40

[94] T. Young, *A Course of Lectures on Natural Philosophy and the Mechanical Arts* volume 2, Johnson (1807). 41

[95] J. Chadwick, "Possible existence of a neutron", *Nature* **129**, pp. 312 – 312 (1932). 45

[96] J. Chadwick, "The existence of a neutron", *Proceedings of the Royal Society of London Series A-Containing Papers of a Mathematical and Physical Character* **136**(830), pp. 692 – 708 (1932). 45

[97] A.K. Soper, "Gudrunn and gudrunx: Programs for correcting raw neutron and X-ray diffraction data to differential scattering cross section", *RAL Report vol. RAL-TR-2011-013* (2011). 54

[98] A.K. Soper, S. Howells, and A.C. Hannon, "Atlas - analysis of time-of-flight diffraction data from liquid and amorphous samples", *RAL Report RAL-89-046* (1989). 54

[99] A.K. Soper, "Multiple-scattering from an infinite-plane slab", *Nuclear Instruments and Methods in Physics Research* **212**(1-3), pp. 337 – 347 (1983). 54, 55

[100] A.K. Soper, "Inelasticity corrections for time-of-flight and fixed wavelength neutron diffraction experiments", *Molecular Physics* **107**(16), pp. 1667 – 1684 (2009). 54

[101] A.K. Soper, "Empirical potential monte carlo simulation of fluid structure", *Chemical Physics* **202**(2-3), pp. 295 – 306 (1996). 58, 67

[102] A.K. Soper, "Tests of the empirical potential structure refinement method and a new method of application to neutron diffraction data on water", *Molecular Physics* **99**(17), pp. 1503 – 1516 (2001). 67, 129

[103] A.K. Soper, "Partial structure factors from disordered materials diffraction data: An approach using empirical potential structure refinement", *Physical Review B* **72**(10), pp. 104204 (2005). 64

[104] A.K. Soper, "On the uniqueness of structure extracted from diffraction experiments on liquids and glasses", *Journal of Physics-Condensed Matter* **19**(415108) (2007). 58

[105] G. Hummer, D.M. Soumpasis, and M. Neumann, "Computer-simulation of aqueous na-cl electrolytes", *Journal of Physics-Condensed Matter* **6**, pp. A141 – A144 (1994). 61

[106] T. Hassinen and M. Perakyla, "New energy terms for reduced protein models implemented in an off-lattice force field", *Journal of Computational Chemistry* **22**(12), pp. 1229 – 1242 (2001). 62

[107] H.J.C. Berendsen, J.R. Grigera, and T.P. Straatsma, "The missing term in effective pair potentials", *Journal of Physical Chemistry* **91**(24), pp. 6269 – 6271 (1987). 62, 101

[108] A.K. Soper, "Joint structure refinement of X-ray and neutron diffraction data on disordered materials: Application to liquid water", *Journal of Physics-Condensed Matter* **19**(335206) (2007). 67, 87, 88, 102, 109, 149

[109] J. Dawidowski, F.J. Bermejo, R. Fayos, R.F. Perea, S.M. Bennington, and A. Criado, "Coherent neutron scattering response from glassy glycerol", *Physical Review E* **53**(5), pp. 5079 – 5088 (1996). 70

[110] P. CIEPLAK, C.I. BAYLY, I.R. GOULD, K.M. MERZ, D.M. FERGUSON, D.C. SPELLMEYER, T. FOX, J.W. CALDWELL, and P.A. KOLLMAN, "A 2nd generation force-field for the simulation of proteins, nucleic-acids, and organic-molecules", *Journal of the American Chemical Society* **117**(19), pp. 5179 – 5197 (1995). 70

[111] E. Arunan, G.R. Desiraju, R.A. Klein, J. Sadlej, S. Scheiner, I. Alkorta, D.C. Clary, R.H. Crabtree, J.J. Dannenberg, P. Hobza, H.G. Kjaergaard, A.C. Legon, B. Mennucci, and D.J. Nesbitt, "Defining the hydrogen bond: An account (iupac technical report)", *Pure and Applied Chemistry* **83**(8), pp. 1619 – 1636 (2011). 71, 80

[112] E. Arunan, G.R. Desiraju, R.A. Klein, J. Sadlej, S. Scheiner, I. Alkorta, D.C. Clary, R.H. Crabtree, J.J. Dannenberg, P. Hobza, H.G. Kjaergaard, A.C. Legon, B. Mennucci, and D.J. Nesbitt, "Defining the hydrogen bond (iupac recommendations 2011)", *Pure and Applied Chemistry* **83**(8), pp. 1637 – 1641 (2011). 71, 80

[113] R. Bohmer and G. Hinze, "Reorientations in supercooled glycerol studied by two-dimensional time-domain deuteron nuclear magnetic resonance spectroscopy", *Journal of Chemical Physics* **109**(1), pp. 241 – 248 (1998). 73, 82

[114] L. Pauling, *The Nature of the Chemical Bonb*, Oxford Univ. Press 3 edition (1960). 82, 120

[115] W.L. Jorgensen, "Optimized intermolecular potential functions for liquid alcohols", *Journal of Physical Chemistry A* **90**(7), pp. 1276 – 1284 (1986). 84, 85

[116] A.K. Soper, "Water: Two liquids divided by a common hydrogen bond", *Journal of Physical Chemistry B* **115**, pp. 14014 – 14022 (2011). 87, 106, 159

[117] H. van Koningsveld, "A conformational study on glycerol in a d2o solution by means of 220 mc-pmr data", *Recueil des Travaux Chimiques des Pays-Bas* **89**(8), pp. 801 – 812 (1970). 92, 93, 94, 97, 98, 99, 121

[118] Y. Kataoka, N. Kitadai, O. Hisatomi, and S. Nakashima, "Nature of hydrogen bonding of water molecules in aqueous solutions of glycerol by attenuated total reflection (atr) infrared spectroscopy", *Applied Spectroscopy* **65**(4), pp. 436 – 441 (2011). 95, 107

[119] M.T. Parsons, P. Westh, J.V. Davies, C. Trandum, E.C.H. To, W.M. Chiang, E.G.M. Yee, and Y. Koga, "A thermodynamic study of 1-propanol-glycerol-h2o at 25 degrees c: Effect of glycerol on molecular organization of h2o", *Journal of Solution Chemistry* **30**(11), pp. 1007 – 1028 (2001). 95

[120] A.D. MacKerell, D. Bashford, M. Bellott, R.L. Dunbrack, J.D. Evanseck, M.J. Field, S. Fischer, J. Gao, H. Guo, S. Ha, D. Joseph-McCarthy, L. Kuchnir, K. Kuczera, F.T.K. Lau, C. Mattos, S. Michnick, T. Ngo, D.T. Nguyen, B. Prodhom, W.E. Reiher, B. Roux, M. Schlenkrich, J.C. Smith, R. Stote, J. Straub,

M. Watanabe, J. Wiorkiewicz-Kuczera, D. Yin, and M Karplus, "All-atom empirical potential for molecular modeling and dynamics studies of proteins", *Journal of Physical Chemistry B* **102**(18), pp. 3586 – 3616 (1998). 95

[121] B.R. Brooks, R.E. Bruccoleri, B.D. Olafson, D.J. States, S. Swaminathan, and M. Karplus, "Charmm - a program for macromolecular energy, minimization, and dynamics calculations", *Journal of Computational Chemistry* **4**(2), pp. 187 – 217 (1983). 95

[122] W.L. Jorgensen, J. Chandrasekhar, J.D. Madura, R.W. Impey, and M.L. Klein, "Comparison of simple potential functions for simulating liquid water", *Journal of Chemical Physics* **79**(2), pp. 926 – 935 (1983). 95, 100

[123] S. Dixit, A.K. Soper, J.L. Finney, and J. Crain, "Water structure and solute association in dilute aqueous methanol", *Europhysics Letters* **59**(3), pp. 377 – 383 (2002). 96, 103, 104, 105, 109, 112

[124] L. Dougan, S.P. Bates, R. Hargreaves, J.P. Fox, J. Crain, J.L. Finney, V. Reat, and A.K. Soper, "Methanol-water solutions: A bi-percolating liquid mixture", *Journal of Chemical Physics* **121**(13), pp. 6456 – 6462 (2004). 96, 103, 104, 105, 109, 112, 129, 143, 148

[125] D. Bowron, J.L. Finney, and A.K. Soper, "Structural investigation of solute-solute interactions in aqueous solutions of tertiary butanol", *Journal of Physical Chemistry B* **102**(18), pp. 3551 – 3563 (1998). 96, 103, 104, 105, 109, 112, 129

[126] L. Dougan, R. Hargreaves, S.P. Bates, J.L. Finney, V. Reat, A.K. Soper, and J. Crain, "Segregation in aqueous methanol enhanced by cooling and compression", *Journal of Chemical Physics* **122**(17), pp. 174514 (2005). 96, 109, 143, 148, 149, 157, 159, 172, 175, 176

[127] A.K. Soper and C.J. Benmore, "Quantum differences between heavy and light water", *Physical Review Letters* **101**(065502) (2008). 101

[128] P.L. Chau and A.J. Hardwick, "A new order parameter for tetrahedral configurations", *Molecular Physics* **93**(3), pp. 511 – 518 (1998). 108

[129] J.R. Errington and P.G. Debenedetti, "Relationship between structural order and the anomalies of liquid water", *Nature* **409**(6818), pp. 318 – 321 (2001). 108, 161, 176

[130] A.K. Soper, *Personal Communication* (2013). 108

[131] D. Bowron, J.L. Finney, and A.K. Soper, "Structural characteristics of a 0.23 mole fraction aqueous solution of tetrahydrofuran at 20 °C", *Journal of Physical Chemistry B* **110**(41), pp. 20235 (2006). 113, 115

[132] S. Imberti and D. Bowron, "Formic and acetic acid aggregation in the liquid state", *Journal of Physics-Condensed Matter* **22**(40), pp. 404212 (2010). 113, 115

[133] N.M. Murthy and S.V. Subrahmanyam, "Behaviour of excess heat capacity of aqueous non-electrolytes", *Indian Journal of Pure Applied Physics* **15**, pp. 485–489 (1977). 123, 124

[134] N. Bennani, A. Coronas, and M. Prevost, "Water-glycerol mixtures - thermodynamic data to absorption cycle simulation", *Journal de Chimie Physique et de Physico-Chimie Biologique* **86**(11 - 12), pp. 2125 – 2148 (1989). 124, 126

[135] K. Gekko and S.N. Timasheff, "Mechanism of protein stabilization by glycerol - preferential hydration in glycerol-water mixtures", *Biochemistry* **20**(16), pp. 4667 – 4676 (1981). 123

[136] Y. Hayashi, A. Puzenko, I. Balin, Y.E. Ryabov, and Y. Feldman, "Relaxation dynamics in glycerol-water mixtures. 2. Mesoscopic feature in water rich mixtures", *Journal of Physical Chemistry A* **109**, pp. 9174 – 9177 (2005). 127

[137] A.K. Soper, L. Dougan, J. Crain, and J.L. Finney, "Excess entropy in alcohol-water solutions: A simple clustering explanation", *Journal of Physical Chemistry B* **110**, pp. 3472 – 3476 (2006). 129, 143, 144, 145, 178

[138] N. Jan, "Large lattice random site percolation", *Physica A* **266**, pp. 72 – 75 (1999). 136, 137, 172

[139] J. Skvor and I. Nezbeda, "Percolation threshold parameters of fluids", *Physical Review E* **79**(4), pp. 041141 (2009). 136

[140] Y.J. Deng and H.W.J. Blote, "Monte carlo study of the site-percolation model in two and three dimensions", *Physical Review E* **72**(1), pp. 016126 (2005).

[141] H.G. Ballesteros, L.A. Fernandez, V. Martin-Mayor, A.M. Sudupe, G. Parisi, and J.J. Ruiz-Lorenzo, "Scaling corrections: Site percolation and ising model in three dimensions", *Journal of Physics A-Mathematical and General* **32**(1), pp. 1 – 13 (1999).

[142] C.D. Lorenz and R.M. Ziff, "Universality of the excess number of clusters and the crossing probability function in three-dimensional percolation", *Journal of Physics A-Mathematical and General* **31**(40), pp. 8147 – 8157 (1998).

[143] M. Acharyya and D. Stauffer, "Effects of boundary conditions on the critical spanning probability", *International Journal of Modern Physics C* **9**(4), pp. 643 – 647 (1998).

[144] P. Grassberger, "Numerical studies of critical percolation in 3-dimensions", *Journal of Physics A-Mathematical and General* **25**(22), pp. 5867 – 5888 (1992). 136

[145] H.S. Frank and M.W. Evans, "Free volume and entropy in condensed systems .3. Entropy in binary liquid mixtures - partial molal entropy in dilute solutions - structure and thermodynamics in aqueous electrolytes", *Journal of Chemical Physics* **13**(11), pp. 507 – 532 (1945). 143

[146] L. Dougan, J. Crain, J.L. Finney, and A.K. Soper, "Molecular self-assembly in a model amphiphile system", *Physical Chemistry Chemical Physics* **12**(35), pp. 10221 – 10229 (2010). 143, 144, 145

[147] L.W. Bosart and A.O. Snoddy, "New glycerol tables - tables for specific gravity and percent of glycerol - thermal expansion of aqueous solutions in terms of specific gravity", *Industrial and Engineering Chemistry* **19**(1), pp. 506 – 510 (1927). 150, 175

[148] B.J. Luyet and P.M. Gehenio, *Life and Death at Low Temperatures*, Normandy, Mo.,Biodynamica, (1940). 178

[149] G.M. Fahy, D.R. MacFarlane, C.A. Angell, and H. Meryman, "Vitrification as an approach to cryopreservation", *Cryobiology* **21**(4), pp. 407 – 426 (1984). 179

[150] K.A. Littau, A. Elschner, and M.D. Fayer, "Thermal history and temperature-dependent photon echo and hole burning linewidths in low temperature glycerol glasses", *Chemical Physics Letters* **175**(3), pp. 149 – 155 (1990). 179

[151] N.H. Rhys, A.K. Soper, and L. Dougan, "The hydrogen-bonding ability of the amino acid glutamine revealed by neutron diffraction experiments", *Journal of Physical Chemistry B* **116**(45), pp. 13308 – 13319 (2012). 179